The LISA Three-Backlink Experiment: Ultra-Stable Optical Bench Construction and Non-Reciprocity Investigation

M. Sc. Lea Bischof

2023

In der vorliegenden Arbeit wurde gegenüber der am 5. September 2022 bei der QUEST-Leibniz-Forschungsschule der Gottfried Wilhelm Leibniz Universität Hannover eingereichten Version an vereinzelten Stellen Tipp- und Grammatikfehler korrigiert sowie vereinzelt ergänzente Satzabschnitte im Sinne eines besseren Verständnisses ergänzt.
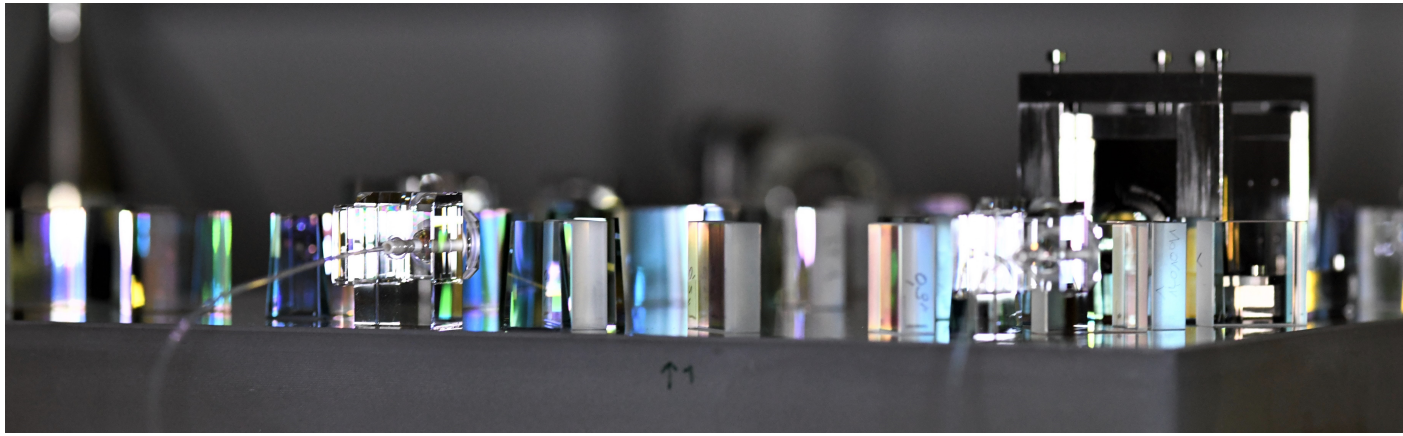
The LISA Three-Backlink Experiment:
Ultra-Stable Optical Bench Construction
and Non-Reciprocity Investigation

Max Planck Institute for Gravitational Physics

Albert Einstein Institute

Leibniz Universität Hannover

LISA Consortium

"'- yer a wizard.'"

Rowling, J. K. (2000). *Harry potter and the philosopher's stone.*
p.60, Bloomsbury Publishing, First published in Great Britain in 1997

Abstract

The Laser Interferometer Space Antenna (LISA) will be a future gravitational wave observatory in space. It will consist of three spacecraft forming a triangular constellation using laser links. The angles of the constellation will change due to orbital dynamics and require a compensation mechanism in each spacecraft. For this purpose, they each house two independently movable optical benches that are optically connected with each other via the so-called Backlink to exchange the laser light between the benches. The Backlink's non-reciprocity is described by the differential phase stability of its counter-propagating beams and requires a noise level below $\frac{\text{pm}}{\sqrt{\text{Hz}}}$ in the LISA measurement band. The experimental study of such a Backlink is the topic of this thesis, by constructing and commissioning an experiment to investigate three different Backlink implementations; the Three-Backlink Experiment. The LISA requirement can only be tested if the experiment is also pm-stable, which is reached by using quasi-monolithic optical benches with optical components glued onto a glass-ceramic baseplate. The first part of the thesis describes the construction of the complex optical benches, which house in total eight interferometers and four fiber-couplings with entangled construction requirements. A beam measurement and alignment tool, the Calibrated Quadrant Singleton, is investigated and characterized as an essential tool for the construction process. Alignment strategies were developed for the demanding construction steps and are presented in a conceptual form, so they are applicable in future optical bench constructions. The construction of the two benches is successfully completed. They are characterized for their relevant performance parameters and implemented in their experimental infrastructure.

The second part of this thesis focuses on the Three-Backlink Experiment's commissioning and noise analysis. The three different Backlink implementations enable a distinction of their individual noise couplings and contributions. The parameter of interest in the Backlink's measurement is the non-reciprocity which reaches the requirement of $1\frac{\text{pm}}{\sqrt{\text{Hz}}}$ in the frequencies above $0.3\,\text{Hz}$ for two Backlink implementations; the direct fiber implementation and the free-beam Backlink. Technical limitations in the current phase read-out measurement system limit the third Backlink implementation, the frequency-separated fiber Backlink. Backscatter at the direct fiber Backlink implementation enables the coupling of laser frequency noise and temperature to the non-reciprocity measurements. The observed couplings probe existing models and agree with their predicted noise coupling via Backlink backscatter. A free-beam connection between the two stationary optical benches is established with a closed piezo-mirror control loop that ensures pm-stability above $0.3\,\text{Hz}$.

An upper limit for the performance of all three Backlinks is measured; the non-reciprocity is at $1.7\frac{\text{pm}}{\sqrt{\text{Hz}}}$ above $0.3\,\text{Hz}$, below $10\frac{\text{pm}}{\sqrt{\text{Hz}}}$ above $0.01\,\text{Hz}$, and at the frequencies below at $3\frac{\text{nm}}{\sqrt{\text{Hz}}}$. At the current state, without motion between the optical benches, the free-beam implementation is operating with the lowest non-reciprocity noise contribution.

The Three-Backlink Experiment offers a unique LISA-like test-bed on two optical benches enabling the study of coupling of different noises in the individual Backlink implementations. This thesis provides the key part of the test-bed, the optical benches, verifies the concept of the three Backlink's disentanglement, and includes an analysis and modeling of its limiting noise sources.

Keywords: *(quasi-)monolithic optical bench construction, UV-glue, LISA Backlink, laser interferometry, non-reciprocity, gravitational wave detection, fiber backscatter, Three-Backlink Experiment*

Contents

Acronyms

3BL Three-Backlink Experiment.

ADC Analog-to-Digital Converter.

ADPLL All Digital Phase-Locked Loop.

AEI Albert Einstein Institut.

ALO Additional Local Oscillator.

BaliLo Backlink-Locking PM.

BaliRo Backlink-Readout PM.

BEAST BEam Alignment Support Tool.

BN Beatnote.

bs beamsplitter.

CABAM CMM-Assisted Beam Alignment and Measurement.

CIC Cascaded Integrator-Comb.

CMM Coordinate Measurement Machine.

CQP Calibrated Quadrant Photodiode Pair.

CQS Calibrated Quadrant Photodiode Singleton.

CTE Coefficient of Thermal Expansion.

DAC Digital-to-Analog Converter.

DFBL Direct Fiber Backlink.

DPS Differential Power Sensing.

DWS Differential Wavefront Sensing.

EM Engineering Model.

EOM Electro-optic modulator.

FBBL Free-Beam Backlink.

fios Fiber Injector Optical Sub-assembly.

FMA Fiber Mount Assembly.

FSFBL Frequency Separated Fiber Backlink.

GW Gravitational Wave.

LED light-emitting diode.

LFN Laser Frequency Noise.

LIGO Laser Interferometer Gravitational-Wave Observatory.

LISA Laser Interferometer Space Antenna.

MOSA Moving Optical Subassemblies.

NCO Numerical Controlled Oscillator.

pbs polarizing beamsplitter.

PD Photodiode.

PER Polarization Extinction Ratio.

PM Phasemeter.

PR Photoreceiver.

PRDS Phase Reference Distribution System.

QPD Quadrant Photodiode.

RIN Relative Intensity Noise.

s/c Spacecraft.

TDI Time-Delay Interferometry.

TIA Transimpedance Amplifier.

TIfo Test-Interferometer.

TM Test Masses.

TTL Tilt to Length.

UGF Unity Gain Frequncy.

UV ultraviolet.

List of Figures

List of Tables

LISA and the Backlink

Ground-based gravitational-wave detectors, [Ber+21; Col+15; Abe+22], have detected several Gravitational Waves (GWs) since the first detection of *GW150914* in 2015 [Abb+16]. GWs are dynamical changes, often called ripples, in spacetime that propagate essentially inviolated though the universe [AS+17; Tho95]. About 90 GW signals have been discovered from compact binary coalescences such as mergers of black hole and neutron star binaries in a mass range of one to a few hundred solar masses [The+21]. These sources emit GWs that reach the earth causing a stretch or compression of space in the order of 10^{-21} [Abb+16]. Precise laser interferometer-based measurements between test-masses enable the observation of these length changes. While the detected signals already provide rich insights, detection of heavier mass objects or detection of galactic binaries and their study is needed for a broader understanding of the universe. These sources are predicted in the lower frequency range, which is not accessible by detectors on the earth which will be eventually limited by seismic and Newtonian noise below 1 Hz [CM22]. A space mission can overcome this limitation and offer a wider range of feasible test-mass distances. The Laser Interferometer Space Antenna (LISA) is a future gravitational wave detector in space designed to measure GWs in the frequency range of 0.1 mHz to 0.1 Hz [AS+17].

One of LISA's critical subsystems is the Backlink. It describes the component that optically connects two optical benches with a low non-reciprocity and is described in the following. This thesis aims to provide an experimental setup for testing different Backlink implementations and verify them in an experiment. This chapter overviews the LISA mission and its Backlink in Section 1.1. Similar to ground-based detectors, LISA will use laser interferometry to measure the small length changes caused by GWs. This technique and the associated need for stable optical benches are introduced in Section 1.2. A brief insight into the LISA measurement principle with a focus on the non-reciprocity of the Backlink is given in Section 1.3. Section 1.4 presents past Backlink experiments and how they led to an improved testing environment, the Three-Backlink Experiment (3BL) (in Section 1.5).

1.1 LISA

The instrumental design of LISA has been ongoing for about 30 years, leading LISA closer to its expected launch date in the 2030s [Geh19]. LISA is formed by a constellation of three satellites following the earth in a cartwheel motion while forming a triangle with 2.5 million km armlength, as shown in Figure 1.1a. Each Spacecraft (s/c) houses two free-floating Test Massess (TMs), one for each arm, which follows a geodesic around the sun. The s/c around the TM senses its movement and follows, shielding the TM from external disturbances. The distance between the TMs of one arm changes characteristically in the order of pm to nm [AS+17] for a passing GW. While all single arms are tracked independently with laser interferometers, they are combined in post-processing to
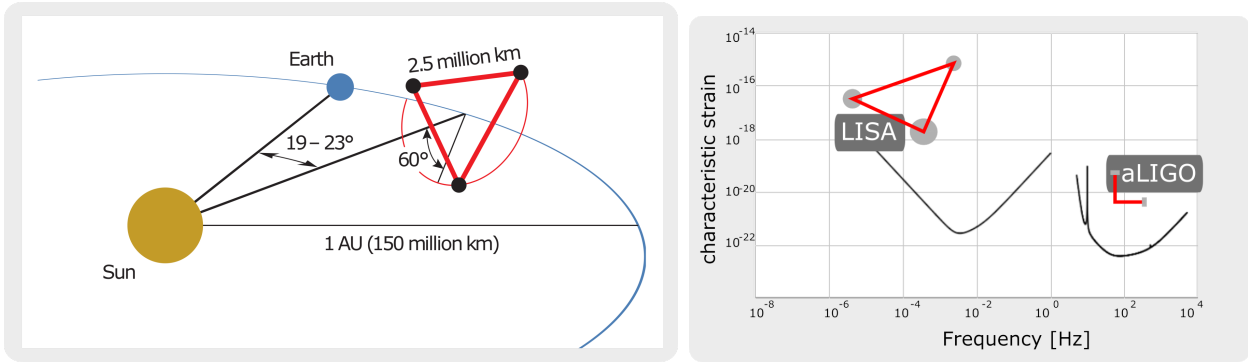
(a) LISA satellites following their orbits behind the earth around the sun. The constellation forms a triangle that performs a cartwheel motion.
Picture credit: [AS+17].

(b) Strain Sensitivity for LISA and advanced LIGO, covering disjointed frequency ranges. Sensitivity curves from [MCB14]. The different detector geometries are indicated for the triangular LISA and the L-shaped aLIGO. The sketches are not to scale.

Fig. 1.1.: LISA orbit and its sensitivity curve compared to one currently active ground based detector.

create a Sagnac-configuration for observing the noise floor and two quasi-Michelson Interferometers. They allow the observation of the two GW polarization states and jointly with the changing orientation of LISA enables the sky localization of the source [AS+17]. GWs emitted from massive black hole binaries can be located depending on the source distance up to a few square degrees [LH09].

LISA will detect sources in a lower frequency range than ground-based detectors, where various objects and discoveries are expected: heavier black holes, redshift larger than 20, and the study of the fundamental nature of gravity. LISA might see unforeseen events and help to understand the black hole population of the universe [AS+17]. Furthermore, LISA can enhance the ground-based detector network by providing an early alert for signals that cross both frequency ranges. Some black hole binaries emit signals that stay in the LISA band for many years before the merger is detectable on the ground [Ses16].

The challenge for LISA addressed in this thesis lies in changes in the armlength and angle of the constellation caused by the impact of solar system celestial dynamic on the s/c's orbits. The baseline orbits balance a minimal breathing angle and armlength change with an acceptable distance to earth for communication [AS+17]. Even with this optimized orbit design, the angle changes by $\pm 1°$, and a Dopplershift of $\pm 5\,\text{MHz}$ is introduced between the s/c [AS+17]. This constant angular change must be compensated, and two possible implementations are presented in the following section. One essential constraint is to maintain the optical connection between the LISA arms in each s/c, needed for the post-processing technique called **Time-Delay Interferometry (TDI)**. Sophisticated shifting of the individual arm measurements in post-processing synthesizes the aforementioned Michelson Interferometers with virtual equal-armlength, in which the otherwise dominant noise contribution of Laser Frequency Noise (LFN) cancels. Further details about TDI can be, for example, found in [Ott15], [Har21].

1.1.1 Telescope and In-field Pointing

The two proposed solutions for compensating the angular breathing are called "telescope pointing" and "in-field pointing". For the latter, each s/c houses one optical bench, and the steering happens inside the two telescopes that each emits and receives the light of one arm. One mirror of each telescope is steerable to guide the emitted laser beam and compensate for the angular motion. In this case, each s/c requires only one TM and can use a second one for redundancy. The challenge lies in the steerable mirror, which is part of the measurement path. Its path-length stability is crucial not to degrade the scientific measurement sensitivity [Koe18]. Additionally, the telescope design needs to consider scattered light occurrences, simulated in [Liv+17], showing the challenge of reaching the requirements with an in-field pointing telescope design. The approach is further investigated by [Koe18].

In the case of telescope pointing, the point of steering is shifted to the optical bench as a whole. Each s/c houses two optical benches, both steerable with the Moving Optical Subassemblies (MOSA), according to the angle between the arms. Therefore, the telescope remains stable, reducing the dynamics of scattered light. This shifts the problem to a different optical path that becomes dynamic, the so-called Backlink; the necessary connection between these two optical benches in each s/c. The Backlink and its performance are crucial for the implementation of telescope pointing [Sal+09].

The official term for the Backlink is the Phase Reference Distribution System (PRDS), as it delivers the phase reference from one bench to the other and vice versa. Literature, including this thesis, typically uses the term 'Backlink'. As part of the critical measurement chain of LISA, its noise contribution is required to stay below the requirement in the order of $\frac{\text{pm}}{\sqrt{\text{Hz}}}$. The goal of $1\,\frac{\text{pm}}{\sqrt{\text{Hz}}}$ will be used throughout this thesis for the Backlink's so-called "non-reciprocity", which is discussed further in Section 1.1 and in Section 3.2. Telescope pointing and its required Backlink are baseline for the LISA mission [LIG18].

1.2 Laser Interferometry

Similar to ground-based detectors, laser interferometry is the selected tool to measure the small distance changes created by GWs in LISA. Its design sensitivity aims to measure GWs with a strength, called "strain", down to $h \sim 10^{-21}$ in the frequency band between $0.1\,\text{mHz}$ to $0.1\,\text{Hz}$, as illustrated in Figure 1.1b. The detectors sensitivity for a strain h depends on the armlength L and the detectable length change according to $\Delta L/L = h/2$ [Sal+09]. With a LISA armlength of $2.5\,\text{million km}$ the instrument has to detect length changes in the order of $10\,\text{pm}$.

By using heterodyne laser interferometry with a laser wavelength λ, this pathlength change corresponds to a phase change $\Delta\varphi$ via

$$\Delta l = \Delta\varphi \cdot \frac{\lambda}{2\pi}, \tag{1.1}$$

where $\Delta\varphi$ is extracted from the interferometric measurement as explained in the following.

For a **Mach-Zehnder interferometer** like in Figure 1.2, two light fields $\vec{E}_1$ and $\vec{E}_2$

$$\vec{E}_1 = \vec{g}_1 \cdot a_1 \cdot \cos(\omega_1 t + \varphi_1) \text{ and } \vec{E}_2 = \vec{g}_2 \cdot a_2 \cdot \cos(\omega_2 t + \varphi_2)$$
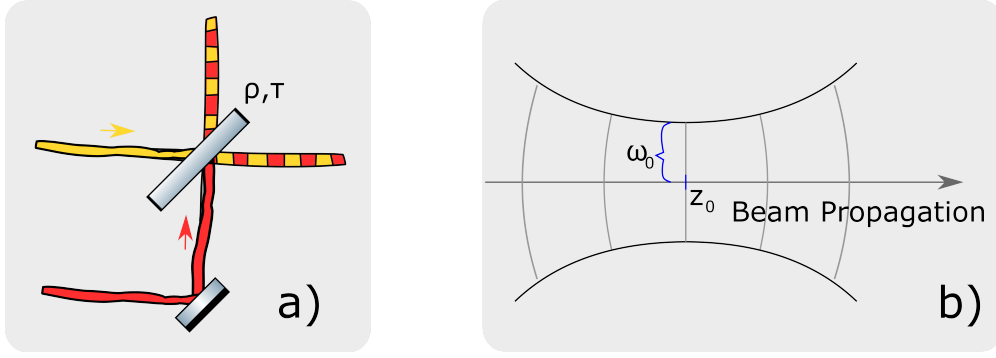
Fig. 1.2.: a) Heterodyne interference of two laser beams with different frequencies at an interference beamsplitter with values ρ and τ. b) A Gaussian Beam with beam waist ω_0 at position z_0 and indicated wavefronts.

with different frequencies ω_1 and ω_2, and amplitudes a_1 and a_1 are interfered at a beamsplitter (bs) with a reflectivity of ρ^2 and transmission of τ^2. Interference beamsplitters are typically chosen with a reflectivity of 0.5. Without loss of generality, it is assumed that $\varphi_1 = 0$ and $\varphi_2 = \Delta\varphi$ and all geometrical properties and the polarization state are described in $\vec{g}$, which is dropped in the further calculations. The resulting beatnote's (BN) signal at the output of one beamsplitter port has an intensity I_{BN} as the square of the interfered electric fields:

$$I_{\mathrm{BN}} \propto \frac{c\epsilon_0 n}{4} \cdot |\vec{E_1} + \vec{E_2}|^2. \tag{1.2}$$

This includes the speed of light c, the vacuum permittivity ϵ_0, and the refractive index n of the propagation medium. When detecting the intensity using a Photodiode (PD) with active area A and the responsivity $\mathcal{R}$, the measured photocurrent i_{PD} can be calculated as

$$i_{PD} = \mathcal{R} \cdot \int dA \; I_{\mathrm{BN}}, \tag{1.3}$$

and further transformed to a voltage by a Transimpedance Amplifier (TIA). The chain of PD and TIA is referred to as a Photoreceiver (PR). The **resulting voltage signal** consists of an AC and a DC part, where only the AC part includes the phase information $\Delta\varphi(t)$ and has an amplitude A_v:

$$v(t) = A_v(\cos\left[\Delta\omega t + \Delta\varphi(t)\right]). \tag{1.4}$$

Finally, the voltage is digitized with a Digital-to-Analog Converter (DAC). A more detailed derivation of the signals can be found, for example, in [Isl18] on which the presented approach is based on.

Before undergoing the described interference, the light field $\vec{E}$ will collect an additional phase while **propagating** through fibers, vacuum, air, and components according to Equation 1.1. The optical pathlength

$$l = n \cdot s$$

is given by the refractive index n and the geometrical pathlength s. Changes of n caused by stress or temperature, especially in a fiber, introduce a phase change.

The given interference description omits any geometrical mismatch, reducing the beam modes' overlap. This quality is described by the **heterodyne efficiency** η. More commonly used in the laboratory is the related **contrast**, which additionally depends on the power levels of the interfered

beams 1 and 2. It can be measured with the maximal and minimal voltage levels on an oscilloscope, proportional to the powers P:

$$c = 2 \frac{\sqrt{P_1 P_2}}{P_1 + P_2} \sqrt{\eta} = \frac{V_{min} - V_{max}}{V_{min} + V_{max}}. \tag{1.5}$$

The dependence of the contrast on the geometric misalignment and the interfering beam's mode is presented in [WH14].

Another quantity that reduces the contrast between two interfered beams is a mismatched in their **polarization** states, which can be introduced in a fiber (see Section 1.2.3).

Light beams described in this thesis refer to **Gaussian beams** in a TEM00-like fiber mode, LP01 [VG12]. They are emitted from different kinds of fiber couplers and described via a beam waist ω_0 at a position z_0, shown in Figure 1.2.

1.2.1 Phasor Basics

The previous section gave a brief overview of the basics of laser interferometry. For the experiment in this thesis, the interferometric signal's phase is most relevant, which is proportional to the pathlength change according to Equation 1.1. Phasor diagrams provide a visualization of the signal and its phase and enable presenting four descriptions that appear throughout this thesis: the extraction of the nominal signal's phase and amplitude via IQ-Demodulation, how phase noise caused by spurious beams affects the nominal read-out phase, partial counteraction of the latter by balanced detection, and how noise is investigated with π-measurements.

Phasor Signal

A signal proportional to $\cos(\Delta\omega t + \varphi)$, like the heterodyne interference in Equation 1.4, can be described by a phasor. It is represented in polar coordinates in the imaginary and real plane, as depicted in Figure 1.3 via $\vec{A} = A \cdot \exp(i\varphi)$. The coordinate system is defined as rotating with the signal's angular frequency $\Delta\omega$, which makes the phasor stationary. The phase φ corresponds to the angle towards the real plane, and the phasor's length is the amplitude A of the signal.

(a) Phasor.   **(b)** Phase error.   **(c)** Two bs ports.
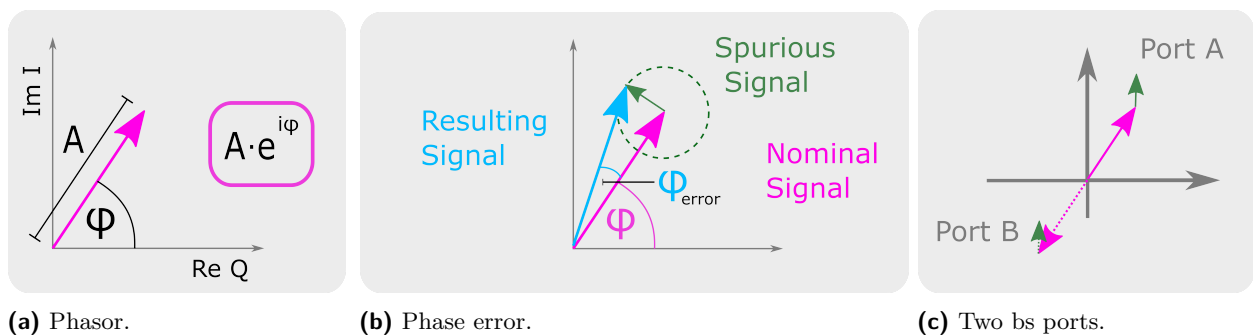
Fig. 1.3.: a) Signal with phase φ and amplitude A illustrated as phasor. b) phase error φ_{error} created by a spurious interference on top of the signal. c) Two ports of the interference beamsplitter. The interfered signal is phase shifted by π, the pre-interfered signal is not.

IQ-Demodulation

The accumulated phase from the signal in Equation 1.4 at frequency $\Delta\omega$ can be read out with the so-called "IQ-demodulation". As depicted in Figure 1.3a, the phasor can be represented by two components with 90° phaseshift, the so-called "in-phase" I and "quadrature" Q. They are extracted by mixing the measured signal $v(t)$ with a signal at the frequency $\Delta\tilde{\omega}$ and low-pass filtering (Lp) afterwards. The resulting sine and cosine mixed signals are the I and Q values:

$$I = \mathrm{Lp}[v(t) \cdot \cos(\Delta\tilde{\omega} \cdot t)] \text{ and } Q = \mathrm{Lp}[v(t) \cdot \sin(\Delta\tilde{\omega}\cdot)],$$

from which the amplitude A and phase φ of the signal are reconstructed via:

$$A \propto \cdot\sqrt{I^2 + Q^2} \text{ and } \varphi = \arctan(Q/I). \tag{1.6}$$

Further information can be found, for example, in [Ger14].

Phase Noise caused by Spurious Beams

Equivalent to a nominal signal, also interference with a spurious light beam can be described by a phasor. Secondary reflections at non-perfect anti-reflective coatings or backscatter inside a fiber can create spurious beams. For example, a detailed distinction between different kinds of spurious beams can be found in [Isl18]. In the heterodyne read-out scheme used in this thesis, only the interference between the spurious signal at frequency ω_1 with a beam at frequency ω_2 is relevant. The spurious interference with a beam at frequency ω_1 results in an additional DC component. The spurious beam potentially has a different phase which is further influenced by different external sources compared to the nominal signal. Thus, the spurious signal in the phasor diagram fluctuates anywhere in the circle at the top of the nominal phasor; see Figure 1.3b. The measured signal in blue contains the nominal signal's phase φ and the phase error φ_{error}. In [Isl18] a description of this phase error for small spurious interference amplitudes is derived via trigonometry and geometry: Spurious beams that interfere with one of the nominal beams or each other cause a phase error when detected at the Photoreceiver (PR) at the beatnote frequency. This error depends on the dynamic of the spurious light φ_{SLS} and can be approximated for a small spurious signal via [Isl18]:

$$\varphi_{\mathrm{error}} \approx \frac{a_{\mathrm{SLS}}}{a_{\mathrm{nominal}}} \cdot \sin\left(\varphi_{\mathrm{SLS}}\right) = \sqrt{\frac{\eta_{\mathrm{SL}} \cdot P_{SLS}^{\omega_1} \cdot P^{\omega_2}}{\eta_{\mathrm{nominal}} \cdot P^{\omega_1} \cdot P^{\omega_2}}} \cdot \sin\left(\varphi_{\mathrm{SLS}}\right). \tag{1.7}$$

The a_i's denote the heterodyne amplitudes for the spurious light signal (SLS) and the nominal signal, and P_i the powers of the involved beams; the spurious light (SL) at frequency ω_1 and the nominal beams at frequencies ω_1 and ω_2. The heterodyne efficiency of these interferences is given by η_i. For worst-case estimations, η_{SLS} is typically assumed to equal 1. The phase error can be simulated when a model of these dynamics and the power ratios are available, as is applied in the later chapters. The noise coupling is non-linear and can be reduced by either a reduction of the power, a suppression of the coupling mechanism, or a reduced dynamic of the spurious phase.

(a) Balanced detection. **(b)** π-measurement.
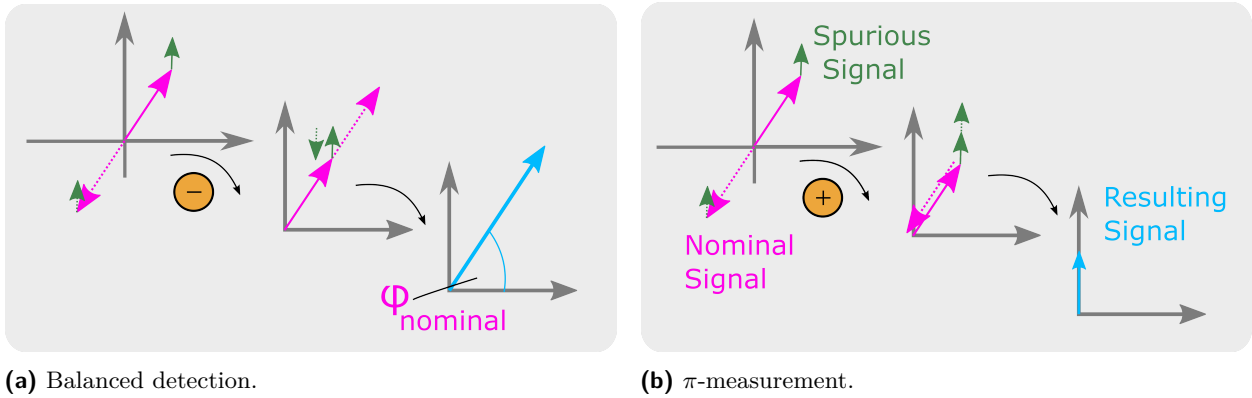
Fig. 1.4.: Combinations of the measured signals at the two interferometer ports. The nominal signal in pink, the spurious in green and their resulting signal in blue. a) for balanced detection, the phasors are subtracted and therefore the spurious signal is removed. b) the phasors are added up in the π-measurement, resulting only in noise.

Balanced Detection

The phasor diagram in Figure 1.4a illustrates the description of the post-processing technique balanced detection. This method reduces the influence of spurious light beams and their interference at the nominal frequency. It suppresses spurious interferences between beams at the two nominal frequencies, that happened before the main interference beamsplitter. Figure 1.4a shows the signal at both ports of the interference beamsplitter. Because of energy conservation, the two nominal phasors have a phase shift of π. It does not appear in the spurious signal because this has interfered at an earlier point and is instead split by the beamsplitters ratio. Also illustrated is the difference between the two measured signals in both ports. It annihilates the spurious signal while the amplitudes of the signal's phasors are added up, and the phase remains unchanged. The actual signal's phase is thus recovered from the measured signal. For example, balanced detection suppresses noise contributions from Backlink-fiber backscatter [Fle12] and 1f- RIN [Wis+22]. It can therefore support diagnosing the source of a spurious signal. The achievable suppression of the spurious interference with balanced detection is limited when the signal's amplitudes in both ports are unequal. Normalization of the signals and a variation of their ratio can optimize the noise suppression [Ste08].

Pi-Measurements

The two ports of an interference beamsplitter are useful for balanced detection to reduce the influence of spurious signals in post-processing by subtracting the PR's signals. They can also be used in so-called π-measurements to investigate the noise floor in the experiment. Figure 1.4b shows that the nominal signals cancel and the spurious signals remain when both phasors are added. π-measurements are usually implemented by extracting the individual phases of the ports and subtracting them, which results in π, hence the name. The residual deviations are caused by a spurious signal, which is not necessarily removable with balanced detection. The application of this diagnostic technique is described in Section 3.3.

1.2.2 Optical Benches

Measuring length changes at pm-precision, laser interferometers are also sensitive to noise sources in that order of magnitude. As an example, the geometrical pathlength s over an interferometer baseplate changes temperature dependent by δs [Kil06]:

$$\delta s = \alpha \cdot s \cdot \delta T, \tag{1.8}$$

with the Coefficient of Thermal Expansion (CTE) α of the baseplates material and the temperature noise δT. In a set-up with $45\,\mathrm{cm}$ long arms and a thermal stability of $10^{-5}\,\mathrm{K}/\sqrt{\mathrm{Hz}}$, an interferometer built on an *aluminum* baseplate with an CTE of about $23 \cdot 10^{-6}\,/\mathrm{K}$ [DL92] would experience a pathlength noise of $10^{-10}\,\mathrm{m}/\sqrt{\mathrm{Hz}}$. Using the nickel-iron composition *invar* with an especially low CTE in the order of $10^{-6}\,/\mathrm{K}$ [DL92], this noise is with $4.5 \cdot 10^{-12}\,\mathrm{m}/\sqrt{\mathrm{Hz}}$ still above the LISA requirement of $1\,\frac{\mathrm{pm}}{\sqrt{\mathrm{Hz}}}$. For a glass ceramic like *zerodur* (ZERODUR® by the company Schott AG) or *clearceram* by OHARA GmbH, with a CTE in the order of $10^{-8}/\mathrm{K}$[Har+21; Isl18], the pathlength variation is as low as $4.5 \cdot 10^{-14}\,\mathrm{m}/\sqrt{\mathrm{Hz}}$. Accordingly, these materials are chosen for optical benches. To ensure the same stability in the optics, the interferometers are built monolithic or quasi-monolithic. For space applications, *hydroxide-catalysis bonding*, also known as *silicate bonding*, has remarkable stability, which is relevant for the launch of a space mission. A bonding solution is used to etch the optic and optical bench surfaces, which are then connected by a strong chemical bond. Its bonding time of less than $60\,\mathrm{s}$ makes this a demanding technique for interferometer alignments [Deh12],[van+08]. A similar, less strong contact is achieved in the *optical contacting* mechanism, where two optics, polished to at least $\lambda/10$ (for $\lambda = 633$) are attached by van der Waals forces [Deh12], and no alignment is possible after contact. A third option is using glue cured with UV-light that significantly extends the possible alignment time.

Many experiments for LISA have been previously built (quasi-)monolithically. The optical bench of the LISA pathfinder mission, the predecessor space mission for LISA technology tests [Fit10], was built using hydroxide-catalysis bonding. The previous Backlink experiment described in [Fle12] was bonded with the same method [Ste08]. For the Hexagon experiment at the AEI Hannover, which tests phasemeter performances, a combination of hydroxide-catalysis bonding and optical contacting was applied [Deh12]. The gluing technique was tested in a Mach-Zehnder Interferometer in [Ger+17] operated in vacuum. The contrast achieved during the alignment remained unchanged after four months. Without any hint that the bond would degrade after more time, this technique was chosen for the 3BL described in this thesis and addressed in detail in Chapter 2.

The technique of optical contacting has the advantage that the component can be removed by applying a reasonable force. The alignments with hydroxide-catalysis bonding or glue are permanent and thus more stable. Accordingly, a significant amount of care has to be taken during the alignment of the optics because any placement mistake can potentially corrupt the whole construction. One of the demands is a precise alignment, for example, to achieve optimized interference. The heterodyne efficiency or contrast of Equation 1.5 depends further on the geometrical misalignment between the beams, [WH14], which have typical $\frac{1}{\mathrm{e}^2}$-intensity radii of about $500\,\mathrm{\mu m}$. Accordingly, misalignments in the order of $10\,\mathrm{\mu m}$ and $10\,\mathrm{\mu rad}$ critically reduce their overlap.

1.2.3 Optical Fibers

Optical fibers are typically made from silica glass and propagate light based on total internal reflection [VG12]. Their central core is surrounded by a cladding, a coating, and additional protective layers [Roh22]. The thesis at hand uses single-mode polarization maintaining fibers that propagate only one mode and retain the injected polarization state. The latter is achieved by areas with different indexes of refraction, forming two distinct axes, called 'fast' and 'slow' axis. The most common ones are *polarization-maintaining and absorption-reducing* (PANDA) fibers [VG12]. An in-coupled beam is aligned with a quarter and a half waveplate to a linear polarization state that conforms with the slow axis of the fiber. This alignment and the polarization-maintaining of the fiber are not perfect and are described via the Polarization Extinction Ratio (PER) [VG12], which is the ratio of the two polarization states. Imperfect alignment together with stress or changes in the Verdet constant of the fiber by temperature or magnetic fields introduce unwanted polarization [Fle12], shifting power to create parasitic interferences.

The intensity distribution in a single-mode fiber is described with the LP01 mode [VG12], close to a Gaussian mode. Similar to its importance for interference, the efficiency of light coupling into a fiber is optimized when the incoming mode is the same as the fiber's mode, which can be reached with an appropriate lens system [CKO21].

Thorough investigations of backscatter happening in a fiber and different coupling mechanisms have been performed in the PhD thesis of J.M. Rohr at the AEI in Hannover [Roh22]. For different fiber types, the amount of backscatter relative to the input power was measured and is used in simulations in this thesis. The fibers used in the fiber Backlink connections in the 3BL are the Nufern PM 980-XP with a core diameter of 5.5 µm and a 245 µm coating diameter. The fiber's core diameter is assumed to be inversely proportional to its amount of backscatter [Roh22]; therefore, the fiber with the smallest core diameter of 6 µm (Fujikura fibers type SM98-PS-U40D) in [Roh22] is taken as a conservative reference. A value of 6.4 ppm/m was measured and thus 7 ppm/m are assumed in Chapter 3 as a conservative approach. The amount of backscatter has been measured for fiber coupling efficiencies between 50-90%, with the dependency of the backscatter amount on the coupling efficiency being unknown. The 3BL has different coupling efficiencies in each Backlink which might cause disagreement between measurements and simulation and should be studied in detail in the future. Since backscatter typically increases with damage in fibers, the concern of increased backscatter caused by radiation damage during flight arose. Accordingly, the backscatter of fibers after being exposed to radiation was measured. No increase was found; hence it was concluded to be uncritical for LISA [Roh22]. The measurements in [Roh22] also investigated the coupling coefficients from the temperature environment to the transmitted phase. This coupling was found to depend on the coating diameter. For the 3BL fibers, this is 245 µm, which is similar to the *Nufern* PM1060L fibers with a measured value of 35-50 rad/K/m. Fibers with a jacket typically have a higher coupling [LBJ81]. Thus, because of the additional wrapping in FEP (Fluorinated ethylene propylene) of the 3BL fibers, the upper value of 50rad/K/m is used in simulations in Chapter 3.
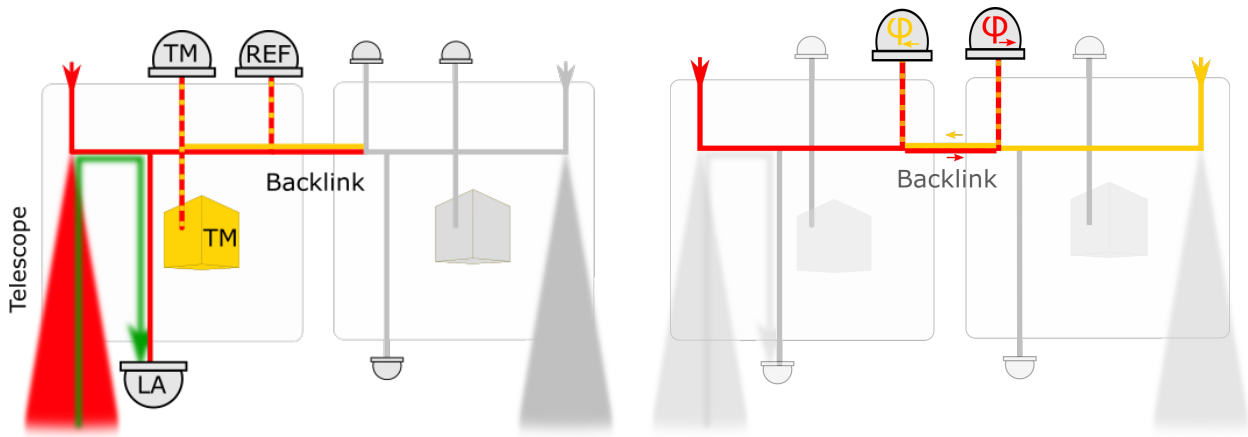
(a) The three interferometers on each bench are the long arm (LA), testmass (TM) and reference interferometer (REF).

(b) The benches are connected via a backlink, where a potentially different phase is collected and measured in different directions.

Fig. 1.5.: A simplified sketch of the two benches inside one LISA s/c. The local laser is send to the distance s/c with the telescope and to the local interferometers.

1.3 LISA Measurement Principle and the Backlinks Non-Reciprocity

Each LISA s/c hosts two optical benches with a telescope, each of which emits the light to the distance spacecraft and receives the counter-propagating beam. Due to the long distance, the low power of this beam requires a phase-locked copy of it to be sent back instead of a passive back-reflection like in a Michelson-Interferometer [AS+17]. The changing armlength between the s/c discussed before creates unequal armlength through which LFN couples, which in turn requires the TDI algorithm. Each optical bench houses a laser, which is additionally exchanged with the adjacent bench via the Backlink, as illustrated in Figure 1.5a. To measure the relative motion between the test masses along one arm, its measurements are divided into three parts, called 'split interferometry concept' [Ott15] or 'strap down scheme' [Fit10]: A measurement between the TM and its s/c, a measurement from the s/c to the distant s/c, and again an s/c to TM measurement. In each s/c three interferometers are placed on each bench; The **long arm interferometer** reads out the distance to the other s/c and contains the gravitational wave signal. The **TM interferometer** tracks the TM movement and the **reference interferometer** measures the differential noise of the two local lasers on the same s/c [LIG18].

These measurements are combined and post-processed with TDI to extract the GW signal and remove limiting noises. As for example presented in [Ott15], these combinations include a term $\varphi - \tilde{\varphi}$. By propagating from bench 1 to bench 2, the light collects the phase φ, and $\tilde{\varphi}$ for the other direction. This is shown in Figure 1.5b where the propagation direction is indicated with arrows. If $\varphi = \tilde{\varphi}$, there is no phase difference in each direction, and the system is called reciprocal. Since this term is part of the LISA measurements that contains the scientific data, the level of reciprocity, or, contrary, of non-reciprocity, is critical for the LISA performance. A non-reciprocal pathlength noise below $1 \frac{\text{pm}}{\sqrt{\text{Hz}}}$ is required.

Different physical effects causing non-reciprocal phase noise are the Sagnac and Faraday effect and dispersion changes induced by temperature fluctuations or unequal frequencies exchanged
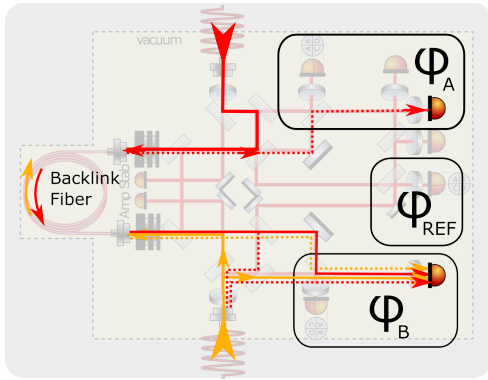
(a) Schematic of the experiment with a bidirectionally used Backlink fiber on one optical bench. The backlink backscatter is shown in dashed lines for the upper TX-beam, while the lower beam path show scatter at both fibers for visibility.
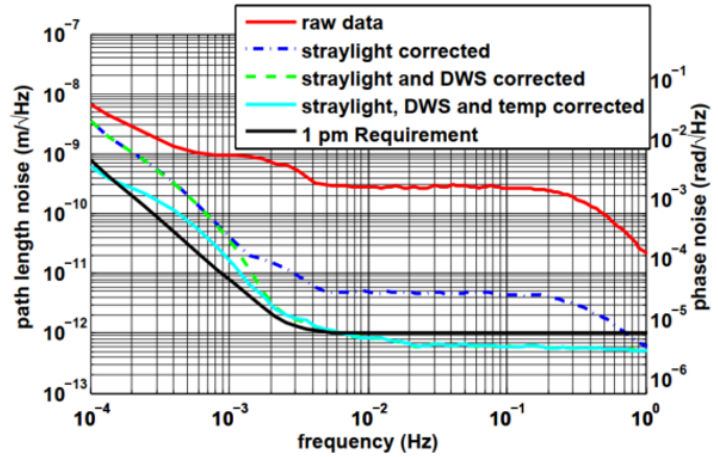
(b) Results of the experiment with different stages of corrections applied. The requirement is reached with straylight, DWS and temperature corrections [Fle+18].

Fig. 1.6.: a) Figure based on a Figure by [Fle+18]. b) [Fle+18].

in both directions. These have been studied theoretically by [Fle12] and concluded to be below the LISA requirement. As explained in detail in the next section, another non-reciprocal effect was limiting the Backlink's experimental investigations so far: In a fiber implementation, parts of the light in the order of $1\,\mathrm{ppm/m}$ that enter the fiber are stochastically backscattered. Because the nominal light is exchanged in both directions, the spurious light also enters the measurement interferometer causing an effective non-reciprocity.

This summarizes the requirement for the LISA Backlink to a non-reciprocity below the $\frac{\mathrm{pm}}{\sqrt{\mathrm{Hz}}}$-requirement. This includes non-reciprocal effects inside the Backlink and backscatter that affects the measurement in a non-reciprocal way. The exact requirement is subject to change in the mission design, and this thesis assumes a 1pm-requirement as a conservative limit for the combined non-reciprocal effects [LIG18; Mar21]. Additionally, the Backlink must tolerate the breathing angle of $\pm 1\,°$ between the optical benches.

1.4 Previous Backlink Measurements

The straightforward solution for the Backlink implementation is a polarization-maintaining, single-mode fiber. Accordingly, this approach was tested in an experiment at the AEI in Hannover. The first experiment implemented a Sagnac-Interferometer [Fle06] because of the reciprocal nature of this design. However, the set-up was limited by a high noise floor, attributed to the required Electro-optic modulator (EOM) [Ste08].

The subsequent experiment was a LISA-like set-up, shown in Figure 1.6a. Two light beams at different frequencies propagate through a fiber in both directions and interfere behind it with the mutual local beam. This allows extracting the phase difference for both propagation directions and thus the non-reciprocal phase noise (see Section 1.5.1 for more details). The experiment was built using hydroxide-catalysis bonding but used commercially available alignable fiber couplers [Ste08]. The limiting noise factors of the experiment were found to be inherent to the design of the Backlink

implementation but not to a fiber as a Backlink per se. The primary noise source was fiber backscatter from the Backlink fiber and the TX-fiber, as illustrated in Figure 1.6. All TX and Backlink fibers backscatter the incoming light and reflect it back into the measurement interferometers [Fle12], [Fle+18]. Figure 1.6b shows the measured non-reciprocity dominated by this spurious light. Several post-correction strategies, and especially a noise subtraction by a factor of more than 100 via balanced detection (see Section 1.2.1), were applied to reach the $\frac{\text{pm}}{\sqrt{\text{Hz}}}$-regime. The experiment concluded that a fiber is a possible Backlink candidate for LISA, while there is much room for further improvement, as described in the following.

One important conclusion is the necessity of decreasing the two primary sources of backscatter, at the TX-fiber and at the Backlink fiber. Backscatter happening at the TX-fibers is reducible by applying attenuation stages. The nominal beam is attenuated once and the backscatter twice, achieving a gain in the backscatter-to-nominal beam ratio. The effectiveness was proven in [Hen13]. Conveniently, this feature is included in LISA because most of the local laser power is sent via the telescope to the distant s/c. Therefore, attenuation after the TX-fiber is a set design choice for LISA.

Attenuation stages on both sides of the Backlink fiber were long believed to be inefficient [Fle12]. However, as shown in Chapter 4 this is a pressing solution for the final LISA Backlink implementation and its current baseline [Ger+19].

Several Backlink implementations have been studied in simulations by [Die13], [Hen13] and [Isl18]. The goal was to further decrease the backscatter influence from the TX-fiber and overcome the backscatter problem at the Backlink fiber. Examples are using additional frequencies to avoid backscatter at the measurement frequency and using steerable mirrors instead of a fiber. The latter is combined with polarization separation, which was tested in the course of TM-read out by [Deh12]. The three most promising candidates were chosen for testing in the 3BL with the additional trade-off of feasibility regarding the number of components. This experiment is the core of this thesis and will be introduced in the next section.

1.5 The Three Backlink Experiment

As implied by its name, the Three-Backlink Experiment (3BL) consists of three possible implementations of a LISA-Backlink; a direct fiber, a frequency separated fiber, and a Backlink connection with a free beam. Furthermore, the 3BL is built on two separate benches, which can be rotated to emulate the actual movement of the MOSAs in the LISA s/c. The different ways of reducing the backscatter limitation found in the previous Backlink experiment, the measurement principle, and the design of the 3BL will be explained in this section, based on the work in [Isl18].

The three Backlink candidates in the 3BL were designed based on the findings of the first Backlink measurements by R. Fledderman. As discussed later in Section 4.1, this experiment was presumably limited by the coupling of the thermal environment via the backscatter at the TX-fibers. This noise will be significantly lower in LISA, based on the design choice of an additional attenuator in front of the Backlink fiber, also discussed in Section 4.2, which will reduce the power ratio in Equation 1.7. The dynamics included in the equation will be further reduced by a lower thermal
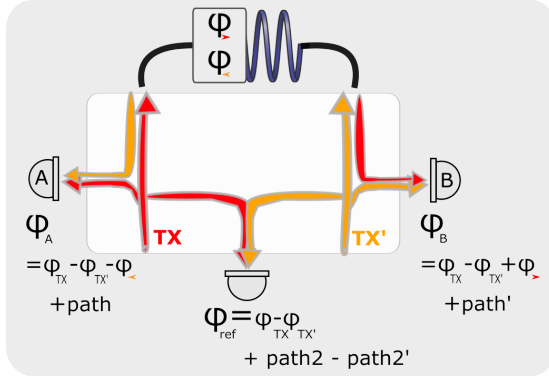
Combinations of all three interferometers reveal the non-reciprocity via:

$$\varphi_A + \varphi_B - 2 \cdot \varphi_{\text{ref}}$$
$$= -\varphi_{\leftarrow} + (\varphi_{\text{TX}} - \varphi_{\text{TX'}})$$
$$+ \varphi_{\rightarrow} + (\varphi_{\text{TX}} - \varphi_{\text{TX'}})$$
$$- 2 \cdot (\varphi_{\text{TX}} - \varphi_{\text{TX'}})$$
$$= \varphi_{\rightarrow} - \varphi_{\leftarrow} = \varphi_{\text{non-rec}}$$

Fig. 1.7.: Simplified drawing of the experiment by R. Fleddermann and the calculations to extract the non-reciprocity from the measurements. The pathlength contribution cancel by assuming path=path' and path2=path2'.

noise in LISA by up to 2 orders of magnitude, based on a requirement set in [Ger+19] compared to recent temperature measurement in the former laboratory of R. Fleddermann. Suppressing this backscatter in the laboratory environment thus enables studying solely the Backlink implementations. Backscatter suppression at the TX-fiber is implemented via an R=95 % attenuator behind the TX-fiber, comparable to the LISA-telescope beamsplitter, and a Faraday Isolator behind it.

All three Backlinks use different techniques to overcome the other primary noise source, the backscatter from the Backlink fiber connection. These are explained jointly with the extraction of the critical parameter, the non-reciprocity, in the next section.

1.5.1 Non-Reciprocity and Phase Reference

Due to the strict requirement of the pathlength stability in LISA, any unsymmetrical noise created in the Backlink fiber is undesirable. Thus, the differential pathlength or phase stability for the counter-propagating beams must fulfill the LISA requirement of $1 \frac{\text{pm}}{\sqrt{\text{Hz}}}$. This can be measured by sending light counter-propagating through a Backlink and tracking the phase differences on both sides. In the previous experiment on a single optical bench, this non-reciprocity was measured as schematically depicted in Figure 1.7. The two measurement interferometers A and B, on the left and right side, detect the phases between the interfered local and Backlink beam each. This phase consists of the laser frequency and fiber noise of the TX- and the TX'-beam and the phase contribution of the light propagating in one of the Backlink directions. The phase collected on the path between fiber coupler and interferometer for both beams is also included. A third interferometer, shown at the bottom, interferes the two local beams without the Backlink in between. It measures the TX- and TX'-noise and another path on the optical bench. The non-reciprocity $\varphi_{\text{non-rec}} = \varphi_{\rightarrow} - \varphi_{\leftarrow}$ is extracted by combining the measurement of all three interferometers. The phases collected on the bench are equal and cancel due to the symmetric design. The reference interferometer measures the noise term, $\varphi_{\text{TX'}} - \varphi_{\text{TX}}$, which is dominated by the noise created in the feed-through fibers. It is subtracted as shown in Figure 1.7, leaving only the desired non-reciprocity $\varphi_{\text{non-rec}}$. Without the reference measurement, the measurement would be limited by $\varphi_{\text{TX}} - \varphi_{\text{TX'}}$. In contrast, the 3BL lacks a stable reference due to its two-bench design, and its solution is presented in the following.
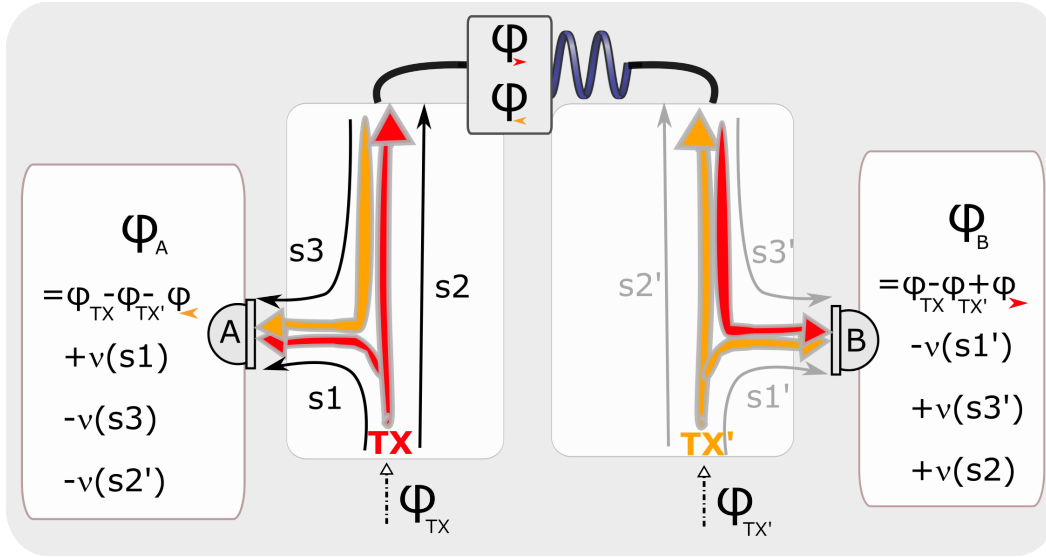
Fig. 1.8.: Phase contributions for the measurements in the DFBL in a simplified sketch of the 3BL. The pathlength on the optical benches are assumed to be equal because of the mirror-symmetric design. The laser frequency and fiber noise and the desired phase noise in the counter-propagating directions of the Backlink are measured on the PRs on both benches. The measured phases are combined in Equation 1.10.

The Direct Fiber Backlink - DFBL

The Backlink implementation of a Direct Fiber Backlink (DFBL), in older documents also referred to as "classic Backlink", consists of a fiber, like in the experiment by R. Fleddermann. It does not use any noise reductions for the Backlink's backscatter, and the Power ratio of backscattered (BC) light to nominal light at the frequency of the local laser (TX) is expected to be

$$\frac{P_{\mathrm{TX}}^{\mathrm{sc}}}{P_{\mathrm{TX}}} = \mathrm{BC} \cdot f_{BC} \cdot \mathrm{bs} = 3.5 \cdot 10^{-6}, \tag{1.9}$$

which is based on a fiber backscatter f_{BC} of $7\,\mathrm{ppm/m}$, see Section 4.1 and two 50/50 beamsplitter (bs). Not only the amount of backscatter, but its coupling mechanism into the phase measurements are critical for the Backlink's performance. Because the Faraday Isolator suppresses the TX-backscatter, the DFBL enables studying the noise couplings inside the Backlink fiber, like the influence of thermal couplings on the measured non-reciprocity.

In this implementation, the non-reciprocity is extracted similarly to the previous section. Figure 1.8 shows details of the different phase contributions. The pathlength on the optical bench s_i and $s_{i'}$ with $i \in \{1, 2, 3\}$ are sketched and with their contribution to the phase in $\nu(s_i)$. Because of the mirror-symmetry and when neglecting construction uncertainties, these pathlengths are equal, $s_i = s_{i'}$. The phases φ_{TX} and $\varphi_{\mathrm{TX'}}$ and the phases in both directions of the Backlink $\varphi_{\leftarrow}$ and $\varphi_{\rightarrow}$ are comparable to 1.7. These phase terms are measured on both PR on the left and right benches,

respectively. By adding the phase signal from both PRs, the terms $\nu(s_i)$ and $\nu(s_i')$ cancel because of their equal pathlength:

$$
\begin{aligned}
&\varphi_A + \varphi_B \\
&= \underbrace{\varphi_{\text{TX}} - \varphi_{\text{TX'}} + (\nu(s1) - \nu(s3) - \nu(2')) - \varphi_{\leftarrow}}_{\varphi_A} \\
&\quad + \underbrace{\varphi_{\text{TX}} - \varphi_{\text{TX'}} - (\nu(s1') + \nu(s3') + \nu(2)) + \varphi_{\rightarrow}}_{\varphi_B} \\
&= \varphi_{\rightarrow} - \varphi_{\leftarrow} + 2 \cdot (\varphi_{\text{TX}} - \varphi_{\text{TX'}}) = \Phi_{\text{DFBL}}
\end{aligned}
\tag{1.10}
$$

The final combination, Φ_{DFBL}, contains the non-reciprocity of the DFBL, $\varphi_{\text{non-rec}}^{\text{DFBL}} = \varphi_{\rightarrow} - \varphi_{\leftarrow}$. Since the two-bench implementation does not allow for a reference interferometer, also the term $\varphi_{\text{TX}} - \varphi_{\text{TX'}}$ remains. Combinations with the other Backlinks are necessary.

The Free-Beam Backlink - FBBL
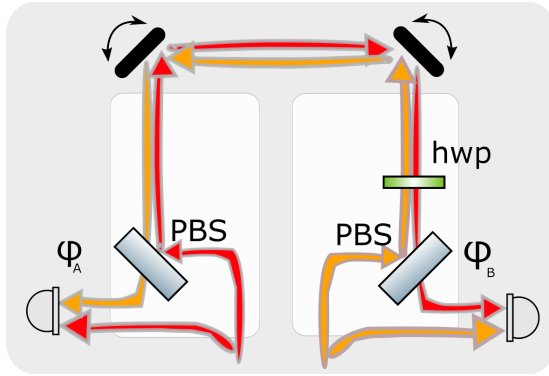
Combinations of the left an right FBBL interferometer reveals:

$$
\begin{aligned}
&\varphi_A + \varphi_B \\
&= -\varphi_{\leftarrow} + \varphi_{\text{TX}} - \varphi_{\text{TX'}} \\
&\quad + \varphi_{\rightarrow} + \varphi_{\text{TX}} - \varphi_{\text{TX'}} \\
&= \varphi_{\rightarrow} - \varphi_{\leftarrow} + 2 \cdot (\varphi_{\text{TX}} - \varphi_{\text{TX'}}) \\
&= \Phi_{\text{FBBL}}
\end{aligned}
$$

Fig. 1.9.: A simplified sketch of the implementation of the FBBL. The light is split via a pbs and a half-waveplate (hwp) on one bench and adjusted via off-bench steering mirrors.

The Free-Beam Backlink (FBBL) eliminates fiber backscatter from the Backlink fiber completely by not using a fiber connection but a free-beam laser link. Two steerable mirrors are controlled by a control loop based on the technique of Differential Wavefront Sensing (DWS) using Quadrant Photodiode (QPD). This compensates for the optical bench's rotation necessary for telescope pointing. Details of the implementation are given in Section 3.5.

The measurement principle is shown in Figure 1.9, where the pathlength contributions are neglected for visibility. This is equivalent to the DFBL and thus presented in less detail. The measurements on both benches are combined to Φ_{FBBL},

$$
\begin{aligned}
\Phi_{\text{FBBL}} &= \varphi_A^{\text{FBBL}} + \varphi_B^{\text{FBBL}} \\
&= \varphi_{\text{TX}} - \varphi_{\text{TX'}} + \nu(\text{ path}) - \varphi_{\leftarrow}^{\text{FBBL}} \\
&\quad + \varphi_{\text{TX}} - \varphi_{\text{TX'}} - \nu(\text{ path}) + \varphi_{\rightarrow}^{\text{FBBL}} \\
&= \varphi_{\rightarrow}^{\text{FBBL}} - \varphi_{\leftarrow}^{\text{FBBL}} + 2 \cdot (\varphi_{\text{TX}} - \varphi_{\text{TX'}}),
\end{aligned}
\tag{1.11}
$$

including the desired non-reciprocity $\varphi_{non-rec}^{\text{FBBL}}$ and the noise term $(\varphi_{\text{TX}} - \varphi_{\text{TX'}})$.

This layout is not limited by backscatter at the TX-fiber by design. The two polarizing beamsplitter and the one half-wave plate in Figure 1.9 separate the path of the beams, and a negligible amount

of residual light due to imperfect polarization separation reaches the TX-fiber. The Faraday Isolator will suppress residual s-polarized light by more than 10^{-6} [Win17]. Combined with the other optics and the fiber-backscatter, the ratio of the nominal Backlink beam to the backscattered beam is in the order of 10^{-16}. P-polarized reflections at the *pbs5* are below 2% of the impinging beam. Only a fraction of 10^{-17} to the nominal light can reach the interferometer after being backscattered at the TX-fiber.

This Backlink implementation is influenced by the actual telescope-pointing optical bench rotation and thus suffers from Tilt to Length (TTL) coupling, which depends on the quality of the optical bench construction. More details are given in Section 2.3.7.

An experimental prototype was used to test critical functions of the FBBL, for example, the piezo-driven steering mirror actuation via DWS and the rotation of the benches. An interferometer built from off-the-shelf components and the steering mirrors for the 3BL has been set up, and a control loop was implemented. It showed a control bandwidth of 80 Hz. Further details can be found in [Isl18; Isl+18; Bis18]. This experiment successfully proved the feasibility of a free-beam connection between two rotating optical benches. Its design was similar to Figure 1.9, including the dominant noise term $\varphi_{\mathrm{TX'}} - \varphi_{\mathrm{TX}}$, and, by design, the pm-requirement was not reached. Contrary to Figure 1.9, the implementation in the Pre-Experiment did not use polarization separation, which additionally resulted in a high amount of backscatter at the TX- and TX'-fibers. The rotation of the benches increased the backscatter coupling into the phase measurements. During this rotation, significant oscillations in the phase were caused by the step-wise motion of the bench's rotation. This required an update of the read-out implementation, which is presented in Section 3.1.3.

A similar approach to testing the feasibility of a free-beam connection between two benches was done at the University of Florida, [Chi19]. The experiment was then updated with a second free-beam Backlink to enable reference measurements and probe the non-reciprocity at the pm-level. When this experiment and the 3BL reach a sufficient sensitivity, their comparison will provide an increased understanding of a free-beam Backlink. Compared to the in-field pointing strategy introduced in Section 1.1, the steering mirror in the FBBL has a considerably less stringent requirement. The in-field pointing steering mirror is part of the telescope, whose magnification increases the required actuation range [Koe18].

The Frequency Separated Fiber Backlink - FSFBL

The introduced IQ-demodulation read-out scheme extracts a signal only at the nominal beatnote frequency. Interference at other frequencies will thus, in first order, not interact with the measurement. This fact is used in the Backlink implementation of the Frequency Separated Fiber Backlink (FSFBL). Each optical bench uses an Additional Local Oscillator (ALO), thus an additional laser with a new frequency. Figure 1.10 shows how these ALOs are first interfered with the local TX-beam and then exchanged with the Backlink fiber. Afterwards, they interfere with the TX'-beam of the second bench. The light that is backscattered at the Backlink fiber is at a different frequency than the local reference beam or the beam from the adjacent bench. Therefore, no fiber backscatter due to the nominal beam path happens at the read-out frequency. With a FSFBL specific reference
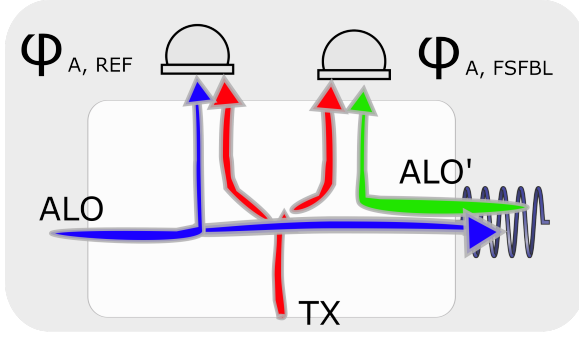
For the FSFBL, four interferometers in total are compared:

$$
\begin{aligned}
(\varphi_{\text{A,FSFBL}} &- \varphi_{\text{B,FSFBL}}) + (\varphi_{\text{A,REF}} - \varphi_{\text{B,REF}}) \\
&= -\varphi_{\leftarrow} + (\varphi_{\text{TX}} - \varphi_{\text{TX'}}) + (\varphi_{\text{ALO}} - \varphi_{\text{ALO'}}) \\
&\quad + \varphi_{\rightarrow} + (\varphi_{\text{TX}} - \varphi_{\text{TX'}}) - (\varphi_{\text{ALO}} - \varphi_{\text{ALO'}}) \\
&= \varphi_{\rightarrow} - \varphi_{\leftarrow} + 2 \cdot (\varphi_{\text{TX}} - \varphi_{\text{TX'}}) \\
&= \Phi_{\text{FSFBL}}
\end{aligned}
$$

Fig. 1.10.: A simplified sketch of the implementation of the FSFBL is shown for the left-side bench. The TX-light is not send through the backlink, but interfered with the Backlink beam and the ALO which is exchanged via the Backlink fiber between the benches.

interferometer, the noise terms $\varphi_{\text{ALO}} - \varphi_{\text{ALO'}}$ are canceled, and the term Φ_{FSFBL} is extracted. The pathlength contributions are neglected completely for simplicity:

$$
\begin{aligned}
\Phi_{\text{FSFBL}} =&(\varphi_{\text{A,FSFBL}} - \varphi_{\text{B,FSFBL}}) + (\varphi_{\text{A,REF}} - \varphi_{\text{B,REF}}) \\
=&\varphi_{\text{TX}} - \varphi_{\text{ALO'}} - \varphi_{\leftarrow} - (\varphi_{\text{TX'}} - \varphi_{\text{ALO}} - \varphi_{\rightarrow}) \\
&+ \varphi_{\text{TX}} - \varphi_{\text{ALO}} - (\varphi_{\text{TX'}} - \varphi_{\text{ALO'}}) \\
=&\varphi_{\rightarrow} - \varphi_{\leftarrow} + 2 \cdot (\varphi_{\text{TX}} - \varphi_{\text{TX'}}).
\end{aligned}
\tag{1.12}
$$

Combined Non-Reciprocity

In the last sections, the Φ-combinations from the phase measurements of the three Backlink implementations have been derived:

$$
\begin{aligned}
\Phi_{\text{DFBL}} &= 2 \cdot (\varphi_{\text{TX}} - \varphi_{\text{TX'}}) + (\varphi_{\rightarrow}^{\text{DFBL}} - \varphi_{\leftarrow}^{\text{DFBL}}) \\
\Phi_{\text{FSFBL}} &= 2 \cdot (\varphi_{\text{TX}} - \varphi_{\text{TX'}}) + (\varphi_{\rightarrow}^{\text{FSFBL}} - \varphi_{\leftarrow}^{\text{FSFBL}}) \\
\Phi_{\text{FBBL}} &= 2 \cdot (\varphi_{\text{TX}} - \varphi_{\text{TX'}}) + (\varphi_{\rightarrow}^{\text{FBBL}} - \varphi_{\leftarrow}^{\text{FBBL}})
\end{aligned}
\tag{1.13}
$$

By combining them pairwise, the joint noise term cancels and the differential non-reciprocity for two Backlinks is extracted, as exemplary for DFBL and FSFBL:

$$
\begin{aligned}
\Phi_{\text{DFBL}} &- \Phi_{\text{FSFBL}} \\
&= 2 \cdot (\varphi_{\text{TX}} - \varphi_{\text{TX'}}) + (\varphi_{\rightarrow}^{\text{DFBL}} - \varphi_{\leftarrow}^{\text{DFBL}}) - 2 \cdot (\varphi_{\text{TX}} - \varphi_{\text{TX'}}) - (\varphi_{\rightarrow}^{\text{FSFBL}} - \varphi_{\leftarrow}^{\text{FSFBL}}) \\
&= (\varphi_{\rightarrow}^{\text{DFBL}} - \varphi_{\leftarrow}^{\text{DFBL}}) - (\varphi_{\rightarrow}^{\text{FSFBL}} - \varphi_{\leftarrow}^{\text{FSFBL}}) = \varphi_{non-rec}^{\text{DFBL}} - \varphi_{non-rec}^{\text{FSFBL}}.
\end{aligned}
\tag{1.14}
$$

Either both Backlinks perform equally, or this measurement is dominated by the worse one. In both cases, at least one of the Backlinks is at or better than the resulting noise floor, assuming uncorrelated noise. Therefore, the Backlinks act as reference measurements for each other, replacing the reference interferometer in the experiment by R. Fleddermann. The non-reciprocity is always measured pairwise, as discussed further in Section 3.2.

All three Backlink implementations are needed to disentangle their individual performances, assuming their limiting noise is not correlated. This is an essential design choice of the experiment. Three different Backlinks are compared, contrary to comparing them to a reference or a second, identical Backlink. This allows the possibility of studying the coupling mechanism and noise sources that can appear different in each Backlink. From the previous Backlink experiment and further backscatter measurements, a preliminary understanding of the DFBL is already present, which can be compared to the noise couplings in the other fiber Backlink and further to the noise couplings in the Free-Beam Backlink. As discussed in Chapter 3, this theoretical concept for disentangling the non-reciprocal behaviors of each Backlink performs as expected.

The measurements include the non-reciprocal effects inside the backlink and backscatter that couples into the interferometers as a non-reciprocal effect. Additional various noise sources in the experiment are caused, for example, by the read-out electronics, temperature coupling, or laser frequency stabilization. These terms can not be disentangled experimentally. The goal is to reduce the noise terms and their coupling until the non-reciprocal effects are isolated. Modeling and data analysis can provide insight into the different couplings and causes of the non-reciprocal effects. Noise analysis and suppression are discussed in this thesis in Chapter 2.

1.5.2 Experimental Design

The optical benches for the 3BL were designed with the C++ library IfoCAD by optimizing the design for the influence of stray light and backscatter by K.-S. Isleif in her PhD thesis [Isl18]. The resulting layout is shown in Figure 1.11. The two benches are identical but mirror-symmetric with one exception; one bench includes an additional waveplate in the free-beam arm. The two quarter-waveplates in the original design were changed to a half-waveplate because of the undesired reflection of circularly polarized light on the steering mirrors.

Light is injected from the lower corner by a Fiber Injector Optical Sub-assembly (fios). The first component behind it is the attenuator, followed by a pbs to clean the polarization. A *Faraday rotator* combined with a waveplate and another pbs form an isolator for back-reflected light. The following beamsplitter, *bs1*, guides the light downwards to the DFBL. It is split again for sending light through the DFBL-fiber and towards the local DFBL-interferometer. There it interferes with the beam from the other bench, which propagates the Backlink fiber.

Behind *bs1*, the beam is separated once more towards the FBBL. The light is split between the local interferometer and the Backlink connection. The beam passes the half-wave plate in the Backlink path for the latter. It is turned to the p-polarized state to pass the pbs on the adjacent bench, after which another half-waveplate rotates the light back to s-polarization, and it interferes with the local beam.

Finally, the main beam is guided to the two interferometers on the top side of the bench, the FSFBL and REF interferometers.

The ALO is guided on the optical bench by *fios4* at the upper side of the bench. It is attenuated and sent to the local REF interferometer and towards *fios3*, where it propagates to the other bench with the second fiber-based Backlink. Light incoming from *fios3* is sent to the FSFBL-interferometer and interferes with the local TX-beam. Each interferometer is equipped with a PD at each port to enable π-measurements and balanced detection. Several small beamdumps on the optical bench
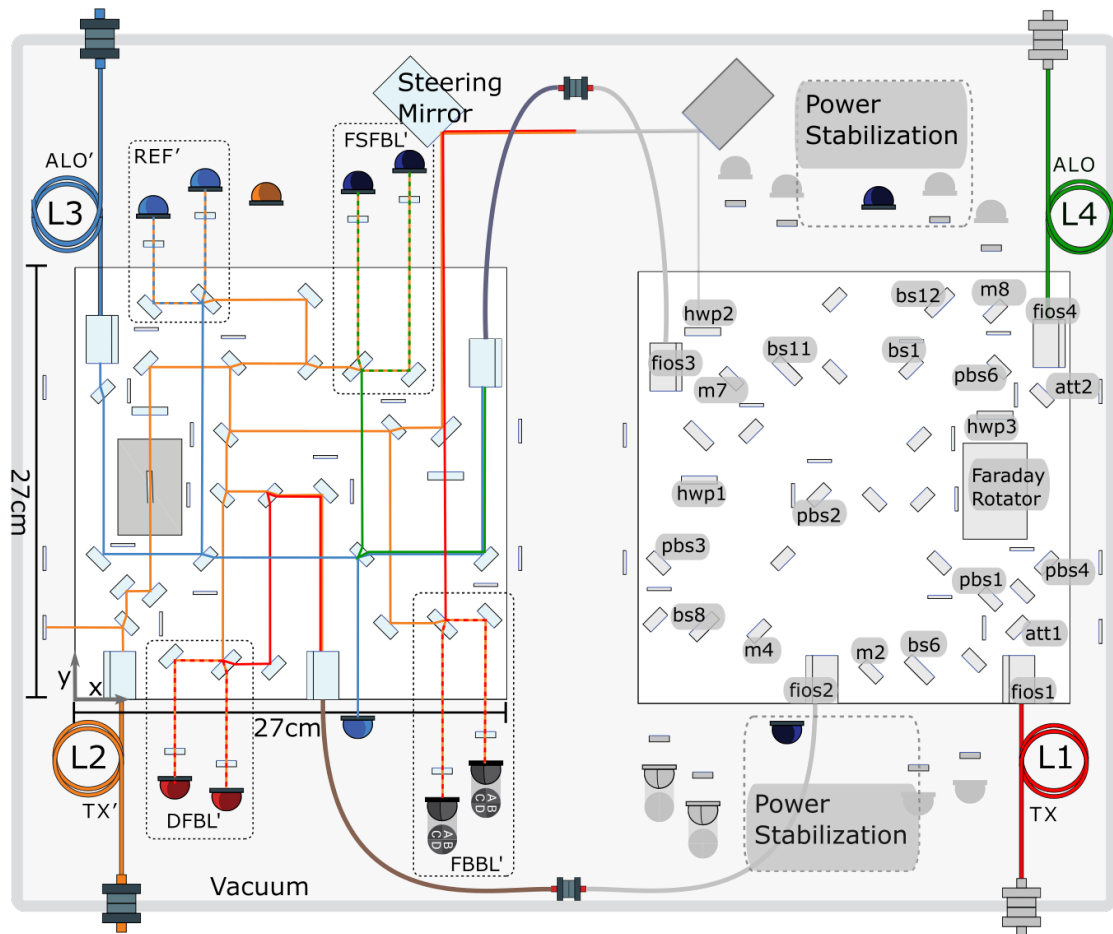
Fig. 1.11.: The optical design of the 3BL's benches in a schematic of their implementation inside the vacuum chamber. Relevant components are labeled and the beam path are shown. The benches are integrated opposite to the original design by [Isl18]. Figure based on [Isl18].

block spurious beams.

In summary, about 40 components, four interferometers, and two beam couplings into a Backlink fiber are required on each bench. Each interferometer uses the local fios's beam, resulting in an entanglement of many construction parameters. This requires sophisticated alignment strategies for the different components. The following Chapter 2 describes the complex construction process of these two demanding optical benches.

Quasi-Monolithic
Optical Bench Construction

<div align="right">

2

</div>

The construction of quasi-monolithic optical benches that operate with pm-stability is a key challenge when investigating LISA instrumentation. Only a limited number of these optical benches have been built so far; examples are the LPF benches [Rob+13], the Hexagon-Experiment [Deh12], the previous Backlink Experiment [Ste08], and the LISA Optical Bench Testbed [Chw+16]. The 3BL represents an especially complicated design with over 40 components per bench, forming eight interferometers and requiring four couplings into two Backlink fibers. The demands for the different parts of the optical design are partially coupled. Because of the use of eight quasi-monolithic, thus not later-adjustable, fiber couplers, the alignment is especially challenging. Previous experiments like the first Backlink experiment built by F. Steier [Ste08] and the first implementation of the Hexagon [Deh12] were built with commercial, adjustable couplers, which cause higher tilt-to-length noise. The 3BL is the first glued experiment of this scale at the AEI in Hannover, while the concept of gluing and its pm-stability was proven in [Ger+17].

The challenging design of the 3BL was translated to the two actual optical benches in the frame of this thesis. Besides the construction, sophisticated strategies and alignment techniques have been developed and are presented.

A key parameter of the optical bench construction is the alignment of the beams relative to the optical bench and relative to each other for interference and fiber coupling. A tool for measurement and alignment of the beams, the Calibrated Quadrant Photodiode Singleton (CQS), was developed and characterized based on the existing technique of a Calibrated Quadrant Photodiode Pair (CQP) [Fit+13]. The idea and design are credit to D. Penkert, while the throughout investigations of its quality presented in Section 2.1 have been performed by the author.

The beams are guided onto the optical bench by the beam couplers, the so-called quasi-monolithic Fiber Injector Optical Sub-assembly (fios), allowing beam propagation and beam parameter alignment during their construction on the optical bench. They are assembled using UV-glue, which is also used for the other optics, here referred to as "components", introduced in Section 2.2.

The construction of the 3BL was planned thoroughly to ensure that all entangled demands could be fulfilled. The finalized construction is presented in Section 2.3. Five alignment strategies have been developed for the especially challenging components and are applicable for future optical bench constructions. These construction strategies have been investigated and improved over extended time frames, and only the final optimized strategies are presented.

The optical benches were successfully assembled and are characterized and examined in Section 2.4. Starting at the end of 2017 till the finalization in August 2021, it took about four years of technique development and construction to finalize the two 3BL benches. Many people joined the team for different amounts of time. The author of this thesis constantly worked on, and eventually led, the construction and was supported by O. Gerberding, K.-S. Isleif, D. Penkert (Ph.D. student), S. Ast,
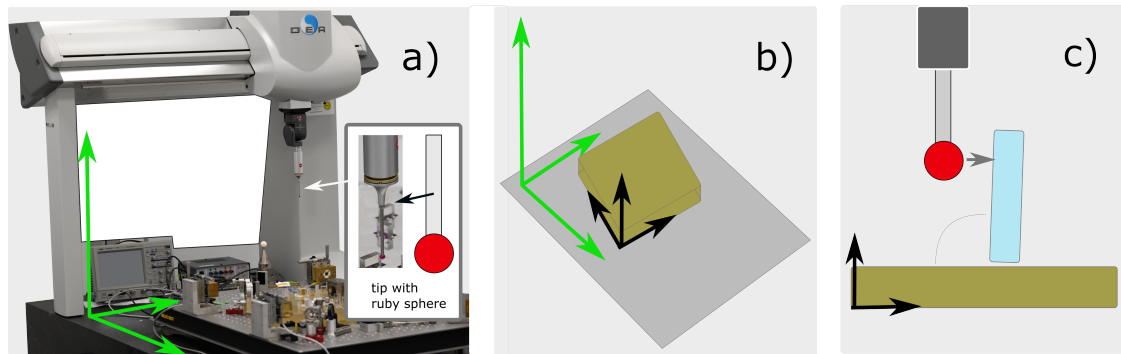
Fig. 2.1.: a) CMM photograph with the ruby sphere tip at the arm. CMM's coordinate system in green. b) the optical bench with its own coordinate system in black on the CMM table. c) The surface of a component is measured with the ruby tip. The AEI's CMM is the model *GLOBAL Advantage* by the company *Hexagon Metrology GmbH*.

J. v. Wrangel (master's student supervised by D. Penkert), N. Knust (master's student supervised by the author), D. Jestrabek (master's student supervised by the author), J. J. Ho Zhang (Ph.D. student partly supervised by the author). With further consultation from G. Heinzel, J. Reiche and colleagues at the University of Glasgow, especially by D. Robertson and A. Taylor.

2.1 Measurements of Beam Positions with μm Precision - Calibrated Quadrant Photodiode Singleton (CQS)

Precisely aligned beams in absolute relation to the optical bench are necessary for the optical bench's construction. Accordingly, a method that can provide measurements and alignments with this precision is required to ensure sufficient contrast and fiber-coupling.

This alignment is supported by a **Coordinate Measurement Machine (CMM)**, see Figure 2.1, that measures absolute distances in a pre-defined coordinate system with the uncertainty in the order of 1 μm. A coordinate system based on the optical bench is shown in black in Figure 2.1 b) with its origin at the left front corner. It enables the beam alignment relative and absolute to the optical bench's surface. A component is probed in this coordinate system by probing its surface with the ruby tip of the CMM, also illustrated in Figure 2.1 c). The CMM is controlled via a script in the software *PC-DMIS*, written by D. Penkert and adjusted by the author.

The technique for beam measurements and alignments used in this thesis is the new technique of a Calibrated Quadrant Photodiode Singleton (CQS). It measures a beam position by combining these μm precise position measurements of a CMM with beam centering on a Quadrant Photodiode (QPD). The idea and the naming are based on the existing Calibrated Quadrant Photodiode Pair (CQP) ([Fit10; Deh12; Fit+13]). The following Section 2.1.1 introduces both techniques in more detail before the working principle, and the calibration are introduced in Section 2.1.2. After investigations on the measurement uncertainties of these Calibrated Quadrant Photodiode Singleton (CQS) in Section 2.1.3 their repeatability and stability are characterized in Section 2.1.4. The three Calibrated Quadrant Photodiode Singleton (CQS) were compared to each other in Section 2.1.5.
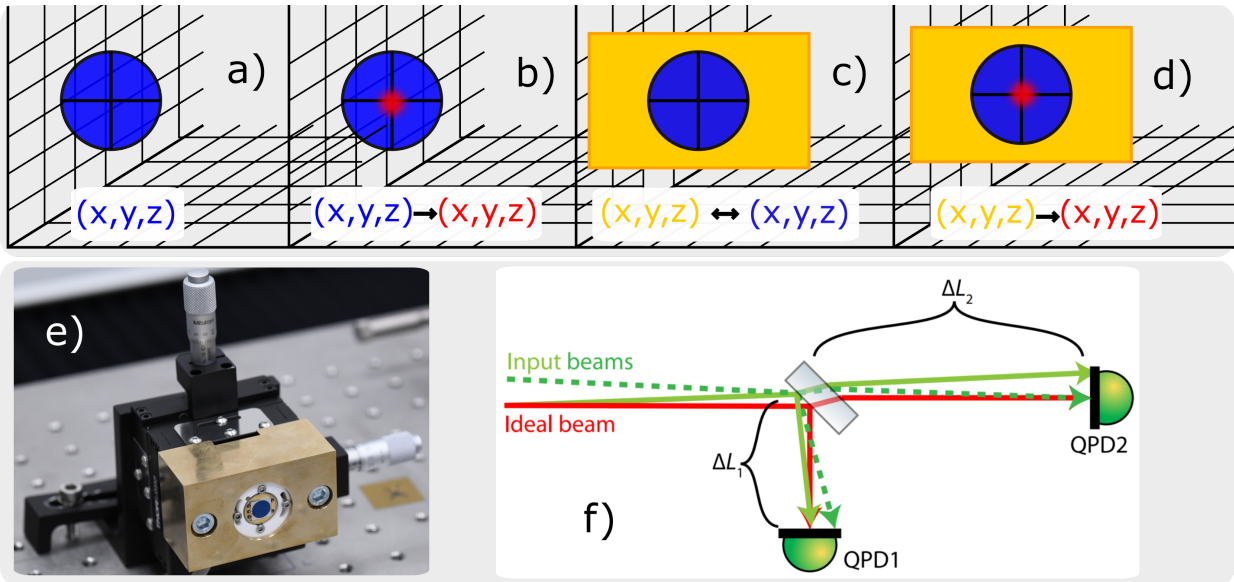
Fig. 2.2.: CQS Principle a)-d) and photograph in e). CQP basics picture from [Deh12] in f).

2.1.1 Overview on Beam Alignment and Measurement Tools

The CQS as a beam measurement and alignment tool was created by D. Penkert and previously described in [Fit10]. It was further investigated and tested by the author in this thesis.

In Figures 2.2 a)-d) the idea of a CQS is illustrated: When the position of a QPD's center is known in the coordinate system of the optical bench, a), the position of a beam is determined by centering it on this QPD, b). This is realized by calibrating the center of the QPD to its mount, and the assembly is then called CQS c). Its center is known relative to the coordinate system, and when a beam is centered on the CQS's QPD, the measurement of the CQS's housing reveals the beam's position, d).

By repeating this at a second position, two points determine the beam's propagation vector. Accordingly, with a CQS, two measurements are done successively along the beam, and their exact positions can be adapted to the set-up. In contrast, in a Calibrated Quadrant Photodiode Pair (CQP), these two measurements are done simultaneously with two PDs. A stable housing holds a beamsplitter, and two QPDs with different distances to the beamsplitter, see Figure 2.2 f). The beam can only be centered on both QPDs in a particular orientation, which is known after a calibration procedure. Mounting the CQP on a device like a Hexapod allows to adjust all necessary degrees of freedom to align the QPDs. With this procedure, absolute measurements of a beam in the μm and μrad range can be accomplished ([Fit+13]). Furthermore, the CQP can be used as a reference to bring the beam to a predefined propagation vector. This requires the CQP to be aligned to the desired orientation and centering the beam accordingly. Different CQPs in literature are mentioned in Section 2.1.6 and they are naturally a valuable tool for precise interferometer construction. However, it was not used in the 3BL for several reasons. a) no CQP was directly available at the beginning of the construction, but an improved version is currently under development (O. Gerberding, D. Penkert). b) A Hexapod or a similar device needs significant space on the CMM and effort when needed at a different interferometer output port. Contrarily, the CQSs are more compact and flexible. With two CQS measurements at different output ports of the interferometer, a constellation like in a CQP is created. Therefore, the basic idea of the CQP was used to develop the CQS, described and analyzed in the following sections.

Another technique for precise beam measurements and alignments developed at the AEI is a method called CMM-Assisted Beam Alignment and Measurement (CABAM) [SMH14]. This technique works without a calibration or stability requirements of a mounting structure. Its basic concept is to use the ruby sphere tip of the CMM head working as a spherical lens. A QPD behind it will see no changes between with or without the sphere if centered perfectly in the beam. The CMM position of the ruby sphere reveals the beam's one-point position. This simple but elegant method was originally planned to be used in the 3BL construction. However, it was found unsuitable for constructing a fios, which can be adjusted in nearly all its coupled degrees of freedom. Therefore a live beam observation at two positions is required, as, for example, the CQP provides, but CABAM does not. The CQS, needing two measurements for a beam characterization, does neither. However, a different strategy of live measuring the beam by using two interferometer output ports (and emulating the features of a CQP) was developed and is described in Section 2.3.3.

As with the CQP, a CQS can be used to measure the propagation vector of a beam and reach a required beam alignment, as described in the alignment strategies in the later sections.

Three CQSs have been used and characterized in the process of the 3BL construction. They are named *CQS1green*, *CQS2red*, and *CQS3blue*. The combination of numbers and colors aims to reduce mix-ups due to typing errors or misunderstandings.

2.1.2 Working Principle and Calibration

After introducing the general idea of a CQS, more details are provided in the following. In the CQS, the QPD *QP50-6 TO* by *First Sensor* is used with removed protection window to minimize back reflections which would disturb the measurement [Fle12]. A ring made of MACOR® encloses the QPD and minimizes thermal and electrical transmissions. The main mount is a block of $65\,\text{mm} \times 40\,\text{mm} \times 25\,\text{mm}$ Brass to provide an extended surface for the CMM probing. This mount is fixed on two linear translation stages (*SDS Low-Profile, Single-Row Ball Bearing Stainless Steel Linear Stages by Newport Corporation*). A 5-pin Lemo cable connects this CQS with a Transimpedance Amplifier (TIA) box (*qpd_switchable-gain* by J. M. Rohr), which, in turn, is connected to a PicoScope® 2000 Series by *Pico Technology*. This small oscilloscope uses PC-based software that allows for live calculations during the measurement and is used to create a read-out screen tailored to the CQSs. It was developed together with D. Penkert, who created the finalized version.

The beam is centered on the QPD by using its power center [Fit10], thus equalizing the signal on each quadrant using Differential Power Sensing (DPS). For a perfect Gaussian beam TEM00 mode, the horizontal DPS signal is extracted from the power levels in Quadrants A-D:

$$\text{horizontal} = \frac{P_\text{left} - P_\text{right}}{P_\text{sum}} = \frac{P_A + P_C - P_B - P_D}{P_A + P_C + P_B + P_D} \tag{2.1}$$

and respectively for the vertical axis [Wan+12]. To reduce the effect of ambient light on the Silicium-PDs, an amplitude modulation with $1\,\text{kHz}$ is added by using an electrically controlled fiber-based attenuator, the *variable optical attenuator* by *OZ Optics*. The PicoScope® is used for the demodulation and normalization. Its output is customized to the read-out screen shown in Figure 2.3a, which is called the **grid**. The horizontal DPS is applied on the x-axis and the vertical on the y-axis. The resulting grid's divisions are proportional to the QPD surface and illustrate the
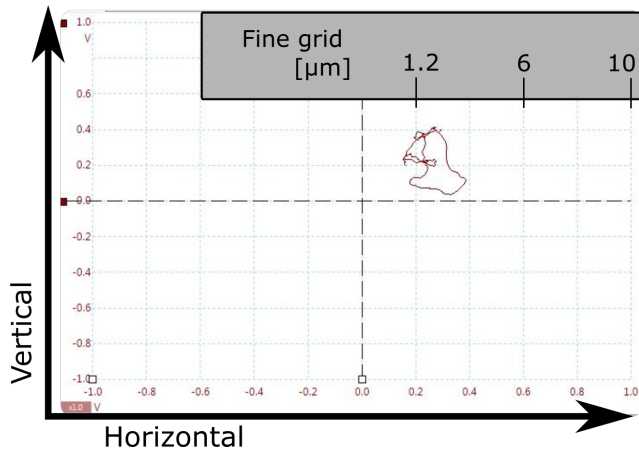
(a) Read-out grid screen, where the vertical and horizontal DPS signal is applied to each axis. The size of the divisions was determined experimentally.
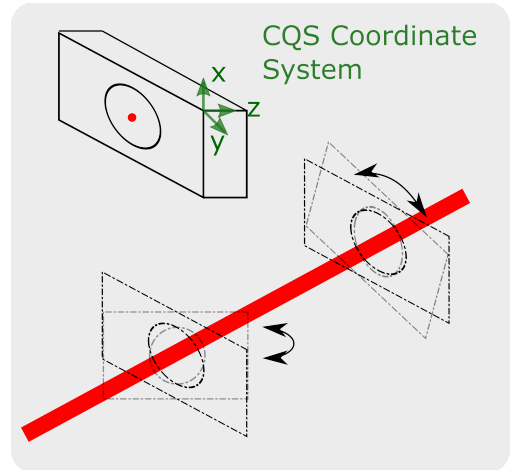
(b) Calibration process with CQS orientation changed towards the beam.

Fig. 2.3.: Fine grid for the CQS readout. The full grid is shown in Appendix B.4. Schematic of the calibration process wit a stable beam shown in red.

position of a beam's center by a cloud of points. Its dimensions are determined by the signal-to-noise ratio of the detected power and the beam size. Two additional, more rough scales are shown in Appendix B.4. With the translation stages attached to the CQS, it is straightforward and intuitive to center the beam on the QPD by centering the cloud of points in the grid on the PicoScope®. This enables centering the beam but also measuring the deviation of the beam to the CQS position and doing a calibrated offset measurement. Furthermore, this can be used to place the CQS at a specific position by using the beam as a reference.

A better grid calibration in the future can allow using the CQS more independently of the CMM. For example, a CQS with a more precisely characterized grid can be used to align and measure the distance of collinear beams without additional CMM measurements. Furthermore, the CQS can serve as a diagnostic tool to observe beam stability and pointing based on this grid.

A calibration process is required to link the center of the QPD to the Calibrated Quadrant Photodiode Singleton (CQS) housing. For the CQS it is similar to the CQP's, which is explained in detail in [Fit10] and [Deh12]. The fundamental idea is to measure a particularly stable beam with a CQS in several different positions and orientations, as illustrated in Figure 2.3b.

The surfaces of the CQS's mount define a coordinate system with the origin at the right, front upper corner. Starting from there, the halved dimensions of the mount provide the theoretical position of the QPD's center. A fitting algorithm combines the beam point measurements in different orientations to extract the correct relations. Additionally, the script provides the standard deviation of the fit, which is written in *Matlab* by D. Penkert. The standard deviation of the calibration results is given in Table 2.1 and appendix B.1 provides an example output of the script and the detailed results for all three CQS.

The CMM script includes the calibration parameters. Thus the fitted distances from the mount outside to the QPD's center and thus provides the one-point position of the measured beam.

Since this measurement is very precise, deviations of the resistor values in the channels of the TIA circuit and the PicoScope® become relevant. As a solution, the calibration is done for one specific TIA setting, PicoScope® scale, and the related power range ($2.4\,\text{mW}$ to $0.4\,\text{mW}$). One additional

calibration for lower power levels was done for one CQS to extend the range of possible beam measurements.

2.1.3 CQS Uncertainties

Estimating the measurement uncertainties of the measurement tool, the CQS, is necessary for evaluating the beam measurements. This section analyzes the different contributions.

Three types of uncertainties that influence the measurements with the CQS are included: The CMM measurement uncertainties, the uncertainties that appear when the beam is centered in the CQS grid, and the standard deviation that is extracted from the calibration fit.

CMM Uncertainties

Different internal uncertainties of the CMM measurements influence the final result. They are studied and presented in great detail in [Deh12] and are calculated accordingly in Appendix B.2.1. The resulting uncertainties from the machine u_m, sampling u_s, temperature u_t and datum error u_d are included.

QPD Centering Error

- **Electronically:**
  The channels for each of the four quadrants can have different gains caused by deviations in the resistor values in the TIA box and the PicoScope®, causing an unknown static offset. It is estimated roughly and conservatively in Appendix B.3 to an upper limit of $50\,\mu m$. Unchanged channel and setting are used for each CQS, to avoid changes in the static offset.

- **Gap on the QPD:**
  The gap of the QPD with a width of $42\,\mu m$ does not influence the position of a perfectly centered beam. Simple *Matlab* calculation indicates that a $10\,\mu m$ offset towards the center causes a $0.5\,\mu m$ position error in the read-out for a beam with $500\,\mu m$ radius. Typically, a beam can be centered more precisely, and the error is negligible. (This error influences a beam's position measurement performed with the grid, but at the moment, the CQS is not optimized for this purpose and the uncertainty of the grid dominates the uncertainty.)

- **Human alignment error:**
  Depending on the spot size, the centering of the beam on the PicoScope® grid is more or less unambiguous. The spot size depends on the laser power and on the beam size, which can not always be optimized. Typical alignments are below the first division around the center (see Figure 2.3a), and thus an uncertainty of $u_h = 0.5\,\mu m$ is assumed.

	CQS1green	CQS1green higher gain	CQS2red	CQS3blue
std dev [µm]	1.485	3.066	2.629	1.514
u_{CQS} [µm]	2.57	3.71	3.36	2.58

Tab. 2.1.: Standard deviation in the calibration process for each Calibrated Quadrant Photodiode Singleton (CQS) and uncertainties u_{CQS} for CQS position measurements based on the different standard deviations.

The Standard Deviation

The *uncorrected sample standard deviation* s_N is a result of the fitting process in the *Matlab* script. It is influenced by the quality of the measurements and the stability of the reference beam. It differs for each CQS, see Table 2.1 in a range of $1.5\,\text{µm}$ to $3\,\text{µm}$. The external influences on the measurements naturally also influence the measurements of the calibration process itself.

Uncertainty in a Beam Position Measurement

The exact uncertainty determination is non-trivial due to the effects influencing the standard deviation and the later measurements. However, a reasonable estimate of the CQS uncertainty can be reached by combining the components mentioned above according to the so-called "law of propagation of uncertainty" [JCGrr], as discussed with details in the Appendix B.2:

$$u_{\text{CQS}} = \sqrt{u_{\text{m}}^2 + u_{\text{s}}^2 + u_{\text{t}}^2 + u_{\text{d}}^2 + u_{\text{h}}^2 + s_N^2}. \tag{2.2}$$

The uncertainty for each CQS varies with their standard deviation and is given in Table 2.1. The uncertainty calculated with the mean value of the CQS's standard deviations is:

$$u_{\overline{\text{CQS}}} = 3.02\,\text{µm}. \tag{2.3}$$

This value will be used for CQS measurements throughout this thesis when the specific CQS is either unknown or irrelevant.

Conclusively, a beam position measurement $\vec{p}$ is accompanied by an uncertainty sphere with radius $u_{\overline{\text{CQS}}}$ for a 68% confidence interval.

Uncertainty in a Beam Vector and Angle Measurement

The propagation direction of a beam is determined by two measurements along the beam and described by $\vec{b} = \vec{s} + \gamma \hat{e}$ with the basic vector $\hat{e}$ along the propagation direction and the variable γ. Each component of the beam vector is accompanied by an offset u_{offset} and an uncertainty u_b for each axis x, y and z. The uncertainty is calculated in Appendix B.2 with the result:

$$\vec{b} = \begin{pmatrix} bx \\ by \\ bz \end{pmatrix} + \begin{pmatrix} u_{\text{offset}} \\ u_{\text{offset}} \\ u_{\text{offset}} \end{pmatrix} + \begin{pmatrix} u_{bx} \\ u_{by} \\ u_{bz} \end{pmatrix} = \begin{pmatrix} bx \\ by \\ bz \end{pmatrix} + \begin{pmatrix} u_{\text{offset}} \\ u_{\text{offset}} \\ u_{\text{offset}} \end{pmatrix} + \begin{pmatrix} \sqrt{3.02\,\text{µm} + \gamma^2 \cdot 16.78\,\text{µm}} \\ \sqrt{3.02\,\text{µm} + \gamma^2 \cdot 13.84\,\text{µm}} \\ \sqrt{3.02\,\text{µm} + \gamma^2 \cdot 13.84\,\text{µm}} \end{pmatrix} \tag{2.4}$$
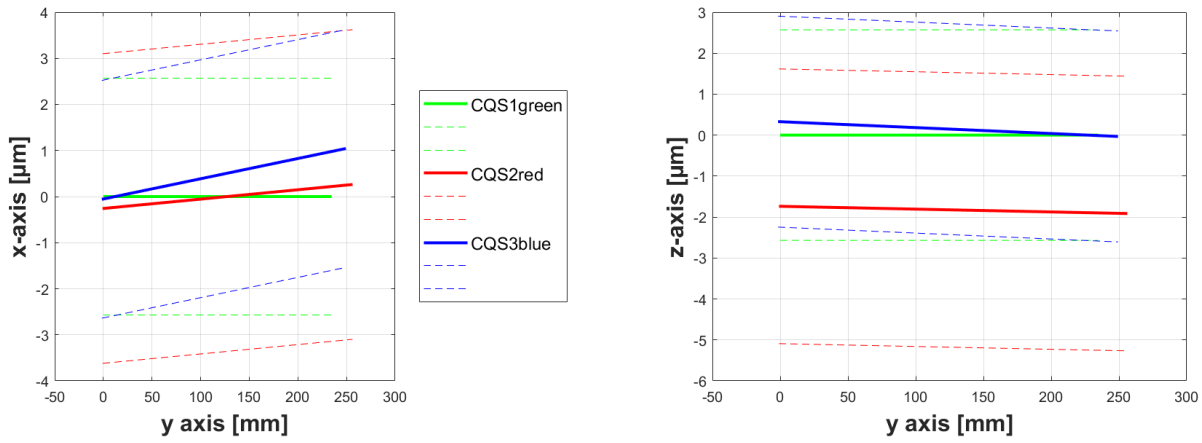
(a) Measurement differences along the x-axis.

(b) Measurement differences along the z-axis.

Fig. 2.4.: One measurement set of the same beam along y-axis, with 3 CQSs, including their individual uncertainties indicated with the dashed lines. In both cases, all three measurements agree in their uncertainty range.

dependent on the position along the beam, given by γ. A measurement distance of 60 cm and a beam parallel to the x-axis are assumed.

The beam's angle towards the baseplate can be calculated by simple trigonometry. The corresponding uncertainty is given by $u_\alpha = 7.12\,\mu rad$, see Appendix B.2. For calculating the angle between two beams, the uncertainty depends on the applied formula, discussed in Appendix B.2, and is $u_{\alpha_A} = 23.73\,\mu rad$ or $u_{\alpha_B} = 10.1\,\mu rad$.

2.1.4 Repeatability and Stability of the CQS

Experimental investigations of the repeatability were performed by measuring a beam several times at the same position. The repeatability of a beam measurement was found to be about 1 µm in the orthogonal axes and less than 1 µm along the beam propagation axis. The associated measurements are discussed and illustrated in the Appendix B.5.

Changes in the position of a CQS over several hours have been observed, which can be related to a movement of the CQS's translation stages. Furthermore, the position of the CQS is defined relative to the optical bench's coordinate system, which is re-defined every morning. Suppose the optical bench's position is changed, for example, by thermal expansion of its mount, the measured CQS position changes. A discussion, including the related measurements, is presented in Appendix B.6. It concludes an upper limit for the CQS stability of 4 µm for the height, 2 µm along the axis orthogonal to the beam, and 1 µm along the beam's propagation vector.

2.1.5 Comparison of three CQS

When using two CQS to measure one beam at different interferometer output ports, it is essential that these CQS are in good agreement to create a valid beam measurement. To probe this, all three CQS have been used to measure the propagation of the same beam. This beam can not be

perfectly stable but is influenced by residual thermal instabilities of its coupler or the aluminum breadboard. A clear distinction between the thermal effects and the CQS differences is not possible, but an overall limit is presented.

The comparison was performed thrice over the last years (2018-10, 2019-03, 2020-8), with slightly different results. In Figure 2.4, the newest measurement of 2020 is shown with the specific uncertainty range of each CQS from Table 2.1. An estimated offset is not included because only the offset's difference would appear in the measurement. All three measurements agree on both axes. In the x-axis, an increased deviation at the position further away from the beam's coupler is visible, indicating a beam pointing during these measurements. On the z-axis, an offset of about 2 µm is visible between the measurements. The older measurements are presented in Appendix B.7, and the one from 2019 are also in agreement, except for an outlier of the CQS1green in the x-axis, which deviates by about 2 µm. A misalignment of the beam during this measurement is possible. The shape of the deviations in both axis in the measurement runs from 2020 and 2019 are different and indicates a statistical error instead of a systematic offset. The measurements from 2018 only agree on the position close to the beam's coupler and show a significant angular difference. This is presumably caused by a pointing of the beam's origin which is in agreement with the unstable beam coupler and the low experience level during these measurements. Overall, the CQS have been concluded to be sufficiently agreeing and can be used jointly in the beam measurements.

2.1.6 Comparing the CQS to Existing Beam Alignment Methods

The technique of the CQS is compared quantitatively to the already mentioned alternative techniques. The CQP developed at the University of Glasgow has an accuracy of $\pm 4\,\mu\text{m}$ and $\pm 20\,\mu\text{rad}$ [Fit+13]. A CQP constructed at the AEI has a similar accuracy of $\pm 4\,\mu\text{m}$, and $\pm 30\,\mu\text{rad}$ [Deh12]. With a slightly less strict requirement, the CQP from [Li+19] reaches $\pm 10\,\mu\text{m}$ and $\pm 50\,\mu\text{rad}$. The method CABAM, also developed at the AEI, was shown to have an accuracy of $\pm 3\,\mu\text{m}$ and an angle accuracy better than $\pm 10\,\mu\text{rad}$ [SMH14].

The here presented CQS were investigated for their uncertainty, repeatability, and stability. Measurements can be done with an averaged uncertainty range of $\pm 3.02\,\mu\text{m}$ and angular measurements of $\text{u}_{\alpha_B} = \pm 10.1\,\mu\text{rad}$. The repeatability is about $1\,\mu\text{m}$, and the stability over $24\,\text{hours}$ are below $5\,\mu\text{m}$ in all axes. Conclusively, the CQSs are comparable with the existing beam measurement devices for precision interferometry alignment.

2.2 Component Alignment

To fulfill the demands of the interferometer, the optics, here called components, must be placed accurately. Optical bench designs, like Figure 1.11 in Chapter 1 assume nearly perfect parallelism between beams and optical bench plate and are therefore depicted in the plane horizontal to the optical bench. This is a valid assumption in bonded interferometers, where the component tilts are below $10\,\mu\text{rad}$ [Ell+05]. As discussed later in Section 2.4.5, this assumption does not hold in a glued interferometer; thus, the actual beam height in the z-axis gains additional importance. This has to be considered during the alignments of the component. This section provides an overview of the

components in the 3BL with a focus on the beam injector, the fios. It introduces the glue and the alignment process and provides an overview of the procedure for gluing a component at the end.

2.2.1 Components

The ground plates of the 3BL are made of *Clearceram HS* by *OHARA GmbH* with a low Coefficient of Thermal Expansion (CTE) of 10^{-8} /K and dimensions of $27\,\mathrm{x}27\,\mathrm{x}3.6\,\mathrm{cm}^3$ [Isl18]. Most of the optics, here referred to as *components*, are made of *fused silica* (CTE of 5.5e-7 /K [Isl18]). The two exceptions are the *Faraday rotator* (its mount is specially designed to compensate for thermal expansions of the material, [Isl18]), and the waveplates. Their mounts are either made of the nickel-iron alloy *invar* (CTE10^{-6} /K [DL92]) or, due to the small distance to the *Faraday rotator*'s magnet, of *Titanium* (CTE 8.610^{-6} /K [DL92]).

Each bench consists of about 40 components: 4x fios (Fiber Injector Optical Sub-assembly, the quasi monolithic fiber couplers, described in the following), 1x *Faraday rotator*, 6x pbs (polarizing beamsplitter (pbs) of which four are used to clean the polarization after each fiber, and two are part of the FBBL separation), 8x mirrors, 12x 50/50 -beamsplitter (bs) (including four interfering bs), 2x bs with a ratio of R/T $= 95/5$ and 3(2)x waveplates (the first bench is equipped with one more half-waveplate for the FBBL separation). Additionally, about 25x so-called beamstops (of the material *KS5* by *Union Optics*) are placed to block spurious beams in the interferometers.

The Fiber Injector Optical Subassembly - fios

Stable optical benches also require a stable beam collimator that guides the beam in the interferometers. The 3BL uses a quasi-monolithic Fiber Injector Optical Sub-assembly (fios). It was designed by D. Penkert based on his previous work with D. Schmelzer [Sch15], [Pen16]. A picture of a partly assembled and a finalized fios are shown in Figure 2.5. The fiber in its ferrule is placed in the Fiber Mount Assembly (FMA) with a girder on its side, and, separately, the lens is glued in its holder. The fios is constructed on the optical bench from these two pieces. The lens holder is attached to the girder via UV-glue, as is the FMA to the optical bench. Both parts are placed in the BEam Alignment Support Tool (BEAST), which is also shown in Figure 2.5. This alignment tool was designed (by D. Penkert) for the special needs of the fios alignment. It allows moving the two components with eight micrometer screws. A very detailed description based on the work by D. Penkert including the pre-assembeling of the fios part, is given in [Knu20]. The alignment of the fios and its output beam is central part of the optical bench's construction and addressed in Strategies 1,2 and 4 presented in 2.3.3, 2.3.4 and 2.3.6.

The fios parts are manufactured from *Fused Silica*. The lens is the model *355110 -C* by *Thorlabs* and the fibers are *Nufern* PM 980-XP. Part of the pre-assembling is the alignment of the fiber inside the FMA with a polarization analyzer by *Schäfter + Kirchhoff GmbH*. An overview about the reached parameters for each fios are given in Appendix A.
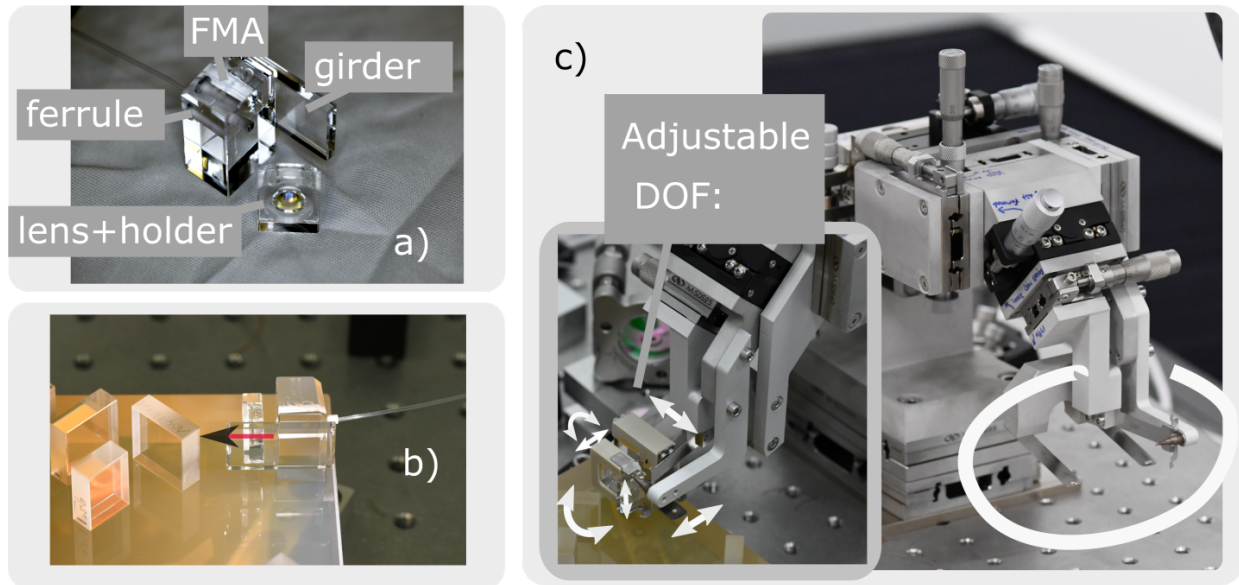
Fig. 2.5.: a) Separate fios parts, b) finalized fios guides the beam onto the optical bench. c) BEam Alignment Support Tool (BEAST) that aligns the FMA and the lens holder. The several degrees of freedom are controlled with micrometer screws.

2.2.2 Glue

The choice of the gluing technique in the 3BL is based on its sufficient stability compared with high flexibility and is re-evaluated in Section 2.5. The 3BL was built by the use of an adhesive that is cured when illuminated with ultraviolet (UV)-light, *Optocast 3553*, and the UV-lamp *Norland Opticure LED-200*. The fused silica components transmit its wavelength of 365 nm. The glue allows for an alignment time of about six hours before it can either be cured with UV-light, or the construction step is aborted because of an insufficient alignment. The limit of six hours was set after observing contamination of the glue layer for longer alignment times, as discussed in Section 2.4.6. To reduce contamination in the first place, the construction was carried out in a cleanroom at the AEI. The metal mounts have been glued with the two-component epoxy *Hysol EA9461*. The metal components can not be glued with UV-glue because of their and the baseplate's non-transparency to UV-light. An equal glue layer of about 100 µm in the two-component epoxy is ensured by mixing it with a 4% weight of ceramic balls. Pressure from above was provided by a simple mounting of a nylon screw to ensure better curing.

Other commonly used techniques like *hydroxide-catalysis* bonding or *optical contacting* were introduced in Chapter 1 and suffer from alignment times of less than 1 min [Deh12]. A recent technology developed at the *University of Florida* [Kul+20] uses adjustable mirror mounts anchored in an ultra-low expansion glass plate. This increases the possible adjustments but also the required space, compared to the small 7x15x20 mm³ components that are used in the 3BL.

2.2.3 Alignment

Components that can tolerate placement inaccuracy up to 100 µm can be placed using a **template**, typically deflection mirrors or transmitting optics. The manufacturing precision for the aluminum template defines the achievable placement accuracy. Figure 2.6 shows the template's pockets for
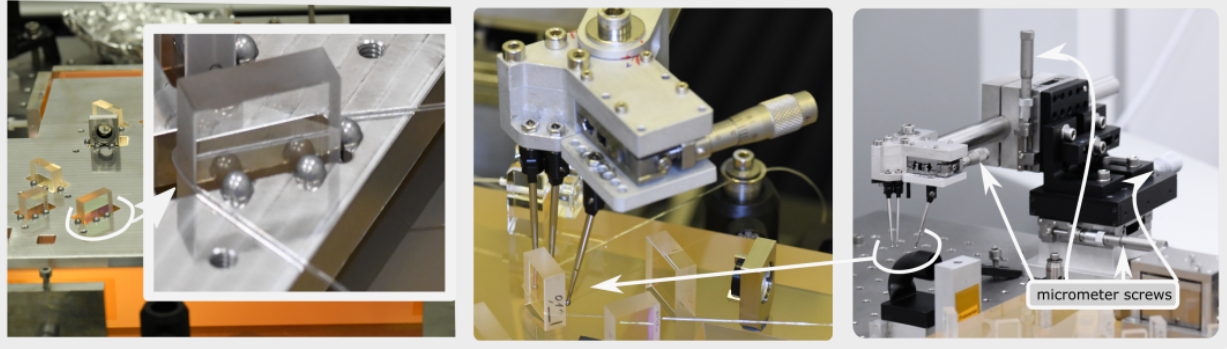
Fig. 2.6.: Left: Template with pockets for the components and the spheres for the three-point contact, fixed with a rubber band. Right: Pointing Fingers that are aligned with four micrometer screws.

each component, with three small pockets for spheres with 4 mm diameter, providing three-point support. The component's position is fixed by applying a rubber band to ensure contact with these spheres. Template components can be glued time efficiently, typically in 1-3 h in total per component, but without further alignment. Another alignment tool are **Pointing Fingers**, which are also based on three spheres as contact points to define a component's position. Three metal rods with spherical tips are connected to translation stages that enable moving and tilting of the component, designed by D. Penkert [Pen16], shown in Figure 2.6. A component can be adjusted while its reflected beam is tracked in real time. Accordingly, laser beams must be available for the construction, and a **laser preparation** is installed on a separate optical table. It starts with one NPRO-laser that can be modulated in phase and amplitude and provides two beams with variable optical power via fibers to the CMM table. A fiber circulator in one of these fibers is used to track fiber couplings during construction. The schematic set-up can be found in Appendix A.1.

2.2.4 The Process of Gluing

The following procedure is applied to place a component with the mentioned alignment methods. In the first step, the component is inspected in a simple optical reflectivity measurement to verify its optical properties. This is essential because the components can not be removed from the bench after the glue is cured. Afterwards, the components and the baseplate are cleaned with *isopropanol* to remove any visible dust contamination and residuals of water. The UV-glue is applied with a pipet *Pipetman* by *Gilson*, with an amount depending on the component's surface size. The bachelor's thesis of B. Haase [Haa14] found $0.005\,\mu L/mm^2$ with a combination of a low force to get a uniform glue layer of $5\,\mu m$ thickness without contamination of air bubbles. The pipet has limited portions of $0.5\,\mu L$ and for the 7 mm x 15 mm components, $1\,\mu L$ instead of $0.53\,\mu L$ was used. During the alignment, the component is moved over several mm, and a significant amount of glue remains on the optical bench. The increased amount of glue guarantees a glue layer covering the surface of the whole component. The details about the amounts of glue for the different components used during the 3BL construction are presented in [Knu20] and Appendix A.

After placing the component, its glue layer is investigated with a lamp with no partial UV contribution in the emitted LED light (e.g. *PSX501 Mini Light* from *Thorlabs*). If any contamination or air bubble are observed, the component is removed, cleaned, and the process is repeated. For components placed with pointing fingers (Section 2.2.3), the component is afterwards adjusted until its alignment

is sufficient or the six-hour alignment time is over. When the alignment and the glue layer are adequate, the UV-lamp is activated for at least 4 min to cure the glue. This is based on measurements presented in [Knu20] and extends the curing time of 1 min suggested by [Haa14].

2.3 3BL Construction

More than 40 components assemble each 3BL bench, and not all can be presented with much detail. One of the general challenges was caused by thermal and mechanical instabilities, presented in Section 2.3.2. The following Section 2.3.1 summarizes the steps for all components as a shortened construction plan. The general challenge lies in the finality of assembling with glue. Once the glue layer is cured, the component can not be removed or adjusted. Each component has thus to be placed by taking care that the previous alignment does not limit any subsequent component.
The Sections 2.3.3 to 2.3.7 describe five strategies, strategy 1-5, for aligning quasi-monolithic optical benches developed during this thesis. They are formulated abstractly to be used in future optical bench constructions. Each strategy starts with a short description of the overall goal and the details of the procedure. An example in the 3BL is given, including the results in the alignment of both benches. The strategies were developed while constructing the first bench, which is the left bench in the original design by [Isl18] and is described in great detail in the master's thesis of N. Knust [Knu20], supervised by the author. Since both benches are mirror-symmetrical, the construction experience accelerated the second bench's fabrication.

2.3.1 Construction Overview

1. A trench on both optical benches was laser machined by the *Fraunhofer Institute for Laser Technology* for the *Faraday rotator*. The template is aligned accordingly around this trench and parallel to the bench up to a few 1 µrad.

2. Alignment uncritical components are placed with the template starting with the one on the upper edge to keep space for the rubber bands. Metal components are cured with pressure from above over weekends.
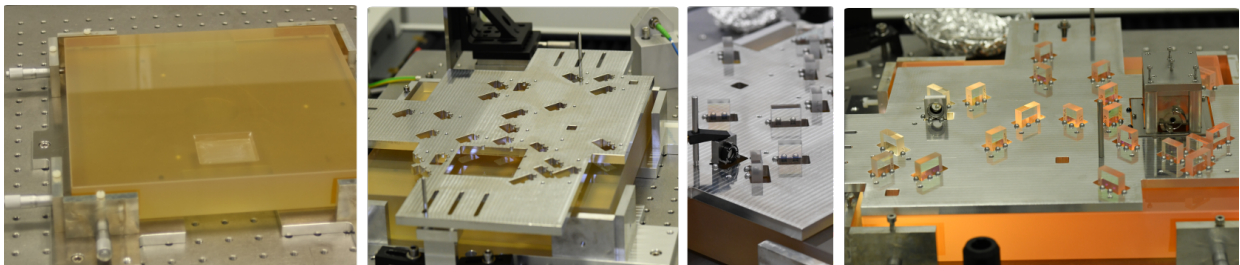
Fig. 2.7.: Empty optical Bench with trench and with template on top of it (Step1). A metal component is placed with additional pressure from above and the template is completely assembled (Step 2)

3. The waveplate behind the *Faraday rotator* is aligned for s-polarized light in the interferometers by using a polarisation analyzer. This needs to be done before the application of Strategy 1

(see 2.3.3) in Step 4 because the rotation of the waveplate introduces a misalignment in the µm range.

4. Strategy 1 (2.3.3) aligns the *fios1* and the *Faraday rotator*. The *fios1* beam requires an absolute beam height of 15 mm and horizontality. Its proper alignment is essential because nearly all other components will be placed subsequently relative to the *fios1* beam. The *Faraday rotator* detours the beam and their coupled demands require a complex alignment procedure that is performed in one step.
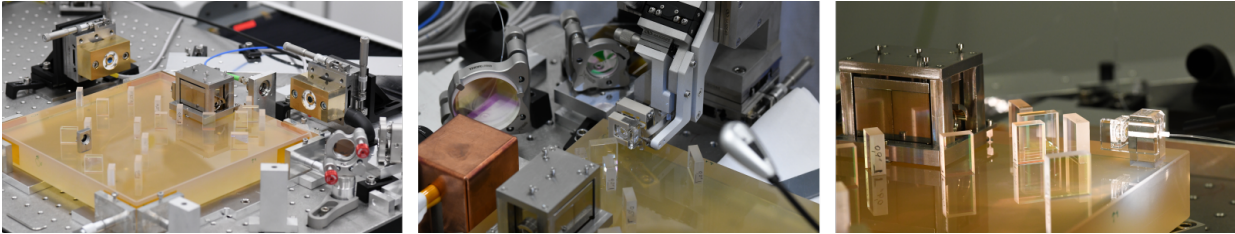
Fig. 2.8.: The *fios1* and *Faraday rotator* preparation and their final aligment are done in Step 4. A Picture of the finalized *fios1* is shown.

5. Strategy 2 (2.3.4) is applied to place *pbs6* and *fios2*. Light is coupled into *fios2* by *fios1*, and thus this fios has to be placed to maximize the incoupling and adjusting the beam parameters. A starting point for the coupling is provided by the strategy. The alignment includes a sufficient in-coupling and adjustment of the beam parameters, which are important to enable sufficient interference with the *fios1* beam in the next step. If the coupling or the contrast are very weak, slight changes in the fios parameters caused by operation in the vacuum might potentially become critical. Accordingly, a coupling and contrast of at least 50% was targeted.

6. *m2*, the mirror to create interference in the DFBL, is aligned with Strategy 3 (2.3.5) by optimizing the contrast. An intentional beam tilt by the component was necessary on both benches to reach a contrast of about 50%.

7. *m3*, the deflection mirror that guides the already interfered beam on the second DFBL-interferometer port is aligned with *pointing fingers* and low precision in the 0.1 mm range.
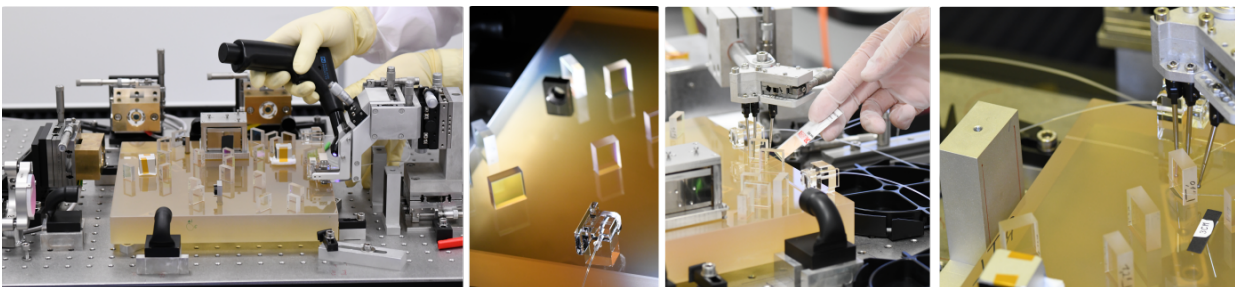
Fig. 2.9.: *fios2* is aligned with the support of CQS and shown while cured and finalized (Step 5). *m2* (Step 6) and *m3* are aligned with *pointing fingers* (Step 7).

8. Strategy 4 (2.3.6) is used to implement the FSFBL consisting of *fios3, fios4, bs11* and *bs12*. The entanglement of all four components with each other and the *fios1* beam makes this a challenging and time consuming alignment step. The fios can not be placed simultaneously,

thus the alignment of *fios4* has to guarantee that the incoupling into *fios3* and the interference from its beam with *fios1* can still be accomplished afterwards.
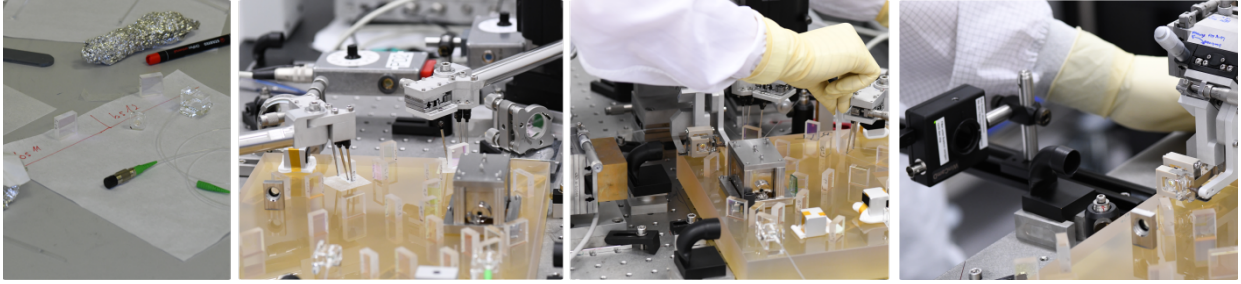
Fig. 2.10.: *bs11, bs12* and two fios are constructed in one step. Two PRs and two *pointing fingers* during a pre-alignment on lens-tissues are shown. The real alignment of the fios and the components, and the measurements with a WinCam are shown.

9. *m7* and *m8*, the deflection mirrors for the FSFBL-meas and FSFBL-ref interferometer are aligned with *pointing fingers* and low precision in the 0.1 mm range.

10. *hwp2* is aligned for p-polarisation towards *pbs5* (just on the first bench) and *hwp1* to turn the light back to the s-polarisation state. Misalignment of these polarization axis will result in spurious interference.

11. With Strategy 5 (2.3.7), the alignment of the FBBL is prepared. Two counter-propagating beams have to be overlapped in the range of a few 10µm and 10µrad range. This is not only a challenge to align but also to verify for this precision. After evaluation of different approaches and possibilities, the requirement was relaxed by an order of magnitude and the here presented strategy was developed, based on the CQS with an angular uncertainty of 10.1 µrad.

12. Strategy 3 (2.3.5) is used to align the interferometer of the FBBL with *m4* with absolute distance of collinear propagating beams by using the CQS's grid. The preparation of the beams in the previous step needs to be stable for this step, thus a sophisticated alignment plan for the finalized execution of steps 12 and 13 is needed. A misalignment of *m4* or of the beams that were aligned in step 12 during the *m4*-alignment would cause an increased TTL coupling and potentially degrade the performance of the FBBL.

13. *m5*, the deflection mirror in the FBBL, is placed with pointing fingers and low precision in the 0.1 mm range.

14. As last construction step, beamstops are placed behind the mirrors, pbs, unwanted bs ports and next to nominal beams where ghost beams by secondary reflections are expected.

15. The benches are fully assembled and ready for their careful transportation to the laboratory were the measurement infrastructure is prepared.

2.3.2 Thermal and Mechanical Stability of the Construction Set-up

In the complex construction steps presented in the strategies in Sections 2.3.3 to 2.3.7, the set-up of the optical bench was extended with commercial mirrors, for example, to create an artificial beam. Their alignment in the µm-range needs to be stable because of the high demand for stability
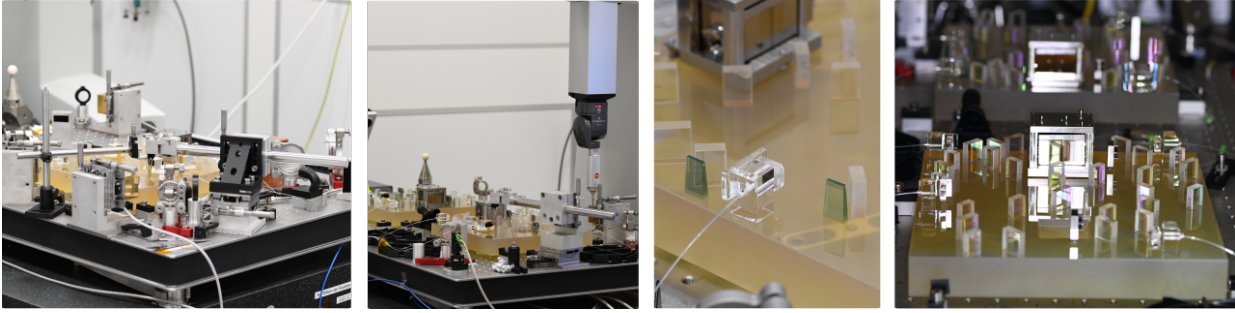
Fig. 2.11.: The alignment and its preparation for $m4$ requires many components and CQS for alignment and beam pointing observation. The beamstops are placed behind most components to reduce backreflections. The two finalized benches are shown.

during construction. The preparation of single alignment steps typically took several days or weeks, with successive alignments during which the influence of temperature changes up to $2\,°C$ became apparent. The AEI's cleanroom is not equipped with specially fine-tuned air conditioning but is part of the system for the whole laboratory building. It is also coupled to the ambient temperature outside to reduce energy consumption. Stable stainless steel Polaris® mounts from *Thorlabs* and a non-adjustable collimator (TC06APC-1064 by *Thorlabs*) in a non-adjustable mount (designed by D. Penkert) were used to reduce temperature influences. Furthermore, the optical bench's mounting was optimized in terms of material, as shown in Figure A.1b.

Mechanical instabilities also affect the alignment of the off-bench components. Changing the weight load of the CMM's breadboard miss-aligns a beam by some micrometer due to the finite rigidity of the breadboard and the translation stages holding the CQS sink during the construction day, see Section 2.1.4.

The influence of the weight load is reduced by placing every component softly and avoiding any additional vibrations. Finalized construction strategies ensure no high load is added after fine adjustments or measurements. The misalignment due to component settling or thermal expansions is tracked using two Quadrant Photodiodes (QPDs) to detect beam misalignment in the 1µm range. Either the observed misalignment is tolerable, or the alignment is repeated, depending on the extent of the misalignment. Tracking this misalignment is thus an essential strategy to guarantee precise alignments.

2.3.3 Strategy 1: Absolute Alignment of a fios Beam

A beam can be required to have an absolute orientation in the coordinate system of the optical bench. In the case of a fios, a straight-forward alignment of its output beam to this orientation is unfeasible. The reasons and the solution in the form of the here presented strategy are given in the following. A rough overview "in a nutshell" is provided before the steps are explained in detail.

The strategy in a nutshell: In preparation for placing a fios, its geometrical alignment is done firstly with an easily adjustable **alignment beam**, which is created by an external beam collimator and two deflection mirrors. Its benefit is explained below. CQS measurements determine the beam's geometrical path, which is then aligned by applying the **target alignment method**. When the alignment is satisfying, it is **saved**, and the beam's path is re-created with the actual fios.
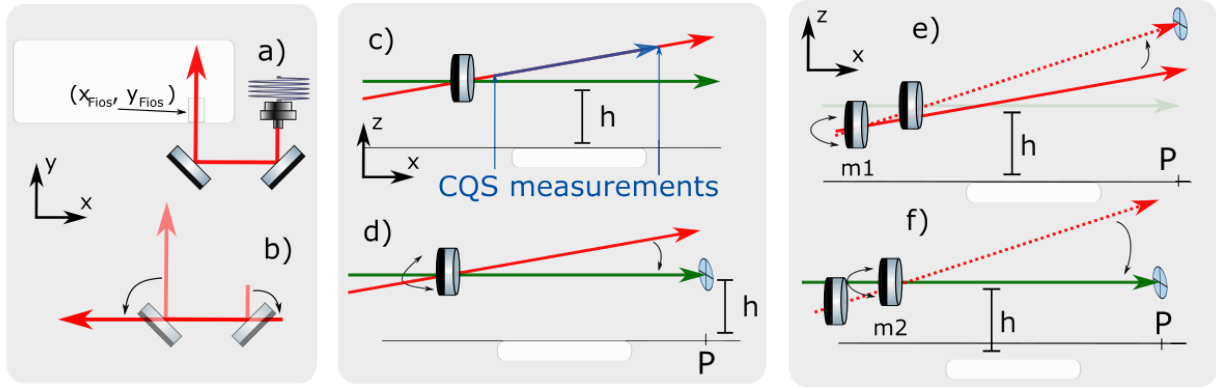
Fig. 2.12.: Overview about the *alignment beam* and the target alignment method. a) *alignment beam* created by two mirrors and a stable beam coupler. b) the beam is unfolded to a two-dimensional representation. c) xz view on the beams, the slightly tilted mirror indicates the position of the mirror. Comparison between alignment and *goal beam*. d) the mirror brings the *alignment beam* to its goal orientation, a CQS serves as target. e) a second mirror is needed to create the starting condition. f) the beam is overlapped with the *goal beam* by m2 equivalent to d).

As a result, the fios's beam is aligned to a predefined, absolute orientation defined by two CQS measurements. The alignment is typically possible up to $1\,\mu m \pm 3.02\,\mu m$ and $4\,\mu rad \pm 7.12\,\mu rad$ deviations from the predefined beam. The separate steps are explained in detail in the following.

This strategy aims to create an output beam from the fios that agrees with a simulated, or otherwise pre-determined, beam in its beam parameters and propagation direction. This beam is called the *goal beam* in the following.

It is unfeasible to have an iterative process for the alignment of a fios's beam. As described in Section 2.2.1, the fios consists of several parts, and its final assembling is done on the optical bench, allowing to align the lens's position relative to the fiber's end and tailor the beam to the need in the experiment. Any slight movement of one of eight micrometer screws in the alignment tool, the BEAST, changes the beam waist and the geometrical alignment. This is not reproducible because of the coupling between the axes and creeps in the springs of the screws. Furthermore, the fios can only be aligned with glue between the surfaces, which leaves a few hours before the glue has to be renewed, and no successive alignment over several days is possible. Accordingly, it is not feasible to successively align and measure the beam with two CQS measurements, which need about 10 min each time. Furthermore, also the beam waist has to be tracked simultaneously and aligned to its target parameter.

The here presented strategy separates the steps of measuring and aligning the beam. The CQSs play a key role and serve in several different tasks. As described in Section 2.1, they measure a beam's propagation vector in the optical bench's coordinate system with two position measurements. Furthermore, the CQS can fulfill the functionality of a target for the beam's alignment, then referred to as target-CQS. By placing a target-CQS at a pre-defined position and centering the beam on it, the beam is crossing this position. A pre-defined propagation vector is created by placing two target-CQS along the beam. This pre-defined beam orientation is given by its requirements, for example, from simulations. Typically the beam is horizontal in the bench's coordinate system and at a height determined by the components, which is at 15 mm above the baseplate in the 3BL. Finding the positions of the target-CQSs by fulfilling these requirements is the first part of the strategy and is done with an *alignment beam*, as presented in the following. Theoretically, the CQS could be placed directly at the two positions of the *goal-beam*'s propagation vector in the

bench's coordinate system. However, the tilts of involved components are unknown but affect the propagation. Therefore, the alignment beam is required.

1. The ***alignment beam*** is created by three simple components placed outside the bench; a fiber coupler and two adjustable mirrors. This is shown in Figure 2.12 a). The so-created beam is aligned to fulfill the geometric properties of the *goal beam*: the horizontality and the beam height. The fios naturally emits the beam at the goal height, so this is an additional but uncritical condition for the *alignment beam*, as discussed in the following. The propagation vector of the *alignment beam* is brought to overlap the *goal beam*'s propagation vector with a method that is called the *target alignment method*.

2. The goal of the ***Target Alignment Method*** is to align the geometrical path of the fios's beam to the predefined *goal beam* by using the target-CQS. The *alignment beam* is injected into the interferometer at the position $(x_{\mathrm{fios}}, y_{\mathrm{fios}})$ of the to-be-placed fios, as shown in Figure 2.12 a). At the first output port of the interferometer, the beam is measured at two positions with a CQS. This determines the beam's propagation vector. The following alignment is based on geometry and the two pivot points of the involved mirrors. The three-dimensional beam is transformed into a two-dimensional view by unfolding it at its reflection points, as visualized in b) of Figure 2.12. The view is changed from the xy-view to the xz-view in picture c), where the measured beam is illustrated by a two-dimensional propagation vector shown in blue, which is extrapolated to the red beam. The *goal beam* is shown in green; it is defined with a beam height h horizontal above the optical bench in its coordinate system. The green and red beam cross at the pivot point at one mirror in their joint path. A target-CQS is placed at the *goal beam*'s height of 15 mm at a position P, as shown in picture d). By aligning the mirror, the *alignment beam* is tilted around the pivot point and centered on this target-CQS. As a result, the red and the green *goal beam* have overlapping propagation vectors and agree accordingly in their geometrical path.

   One additional step has to be added in reality, where the crossing point and pivot point are unlikely to match, as shown in picture e). The preferred starting condition with the *alignment beam* crossing the pivot point of the second mirror, called m2, is illustrated in the dotted beams. It is created by fitting a line between the pivot point of the first mirror, m1, and the point where the *goal beam* crosses the surface of the second mirror. Thus, the first step is to align the *alignment beam* to this dotted beam. With the existing knowledge of the distances between the mirrors and geometry, the height of the dotted beam at position P is calculated. This is described in more detail in [Knu20]. A target-CQS is placed at this height, and m1 is aligned to center the *alignment beam* on it. The situation in d) is re-created in picture f), and m2 is used to align the *alignment beam*'s propagation vector with the *goal beams* orientation. Two CQS measurements along the final *alignment beam* follow this procedure to examine the alignment result. Typically several iterations are needed until a satisfying alignment is reached, mainly because the beam is not exactly hitting the pivot points of the mirrors.

3. **Saving and re-creating a Beam Alignment:**
   The successful application of the *target alignment method* creates an *alignment beam* which serves as a model for the fios's beam. To align the fios accordingly, a third way of using the CQSs is required; to save a beam's orientation. Accordingly, the CQS are called saving-CQS for this purpose. The finalized *alignment beam* is measured at two output ports relative
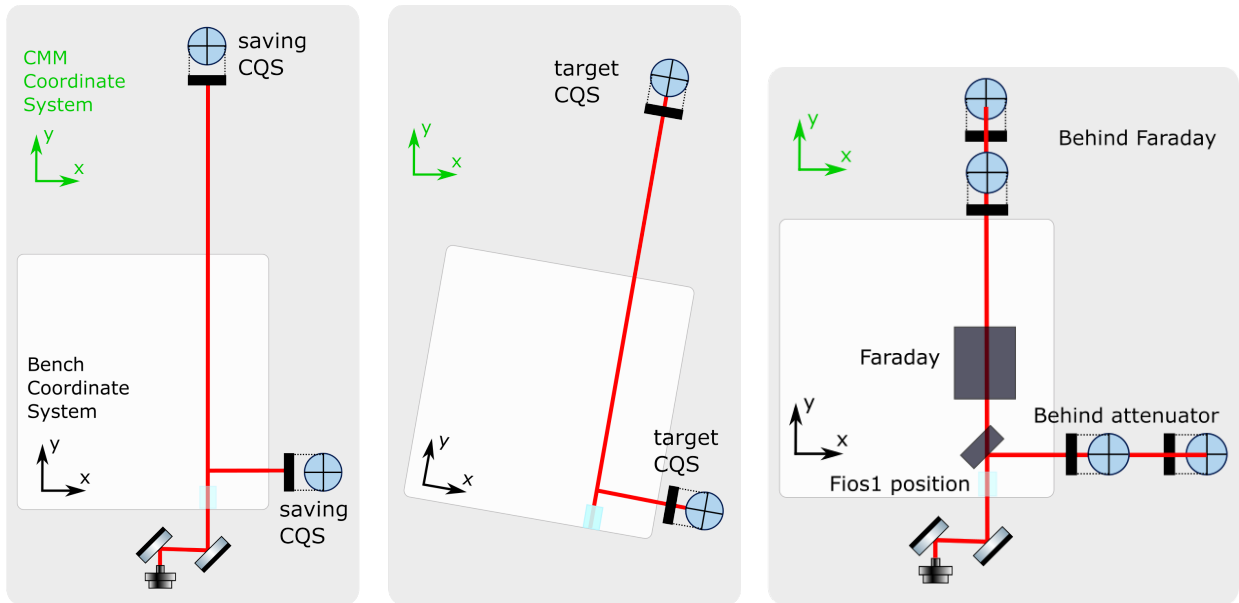
(a) When the beam is saved with two saving-CQS, microscopic or macroscopic movements of the bench are uncritical. As long as the target-CQS are aligned in the coordinate system of the optical bench, the beam can be re-created.

(b) While constructing *fios1*, measurements behind the attenuator for the beam height and behind the *Faraday rotator* for the horizontality were needed.

Fig. 2.13.: Details about the beam saving method and the re-creation of the saved beam in a) and a schematic of the set-up used to place *fios1*.

to the optical bench, as shown in Figure 2.13a (a). (A set-up similar to a CQP is created, see Section 2.1.1). A beam centered at these two CQS automatically fulfills the geometric requirement reached with the *alignment beam*. Even after moving the whole optical bench, the beam is re-creatable by placing the saving-CQS at the same positions in the optical bench's coordinate system, as also illustrated in Figure 2.13a a).

4. **Placing the fios**
   In the second picture of 2.13a a), the two saving-CQS now serve as target-CQS. If the bench or the CQS were moved in between the steps, they are placed by using the characterization of the grid in Section 2.1.2 to bring each saving-CQS exactly to the position determined in the previous step. Then the *alignment beam* is replaced by the actual fios. By centering its beam with the BEAST on the two target-CQSs, the geometrical path of the *alignment beam* is recovered, and thus the requirements can be reached in a comparatively short time frame. As a last strategy part, a beam profiler like a *WinCam* by *DataRay* is used to measure the beam's diameter at an additional port. The fiber of the fios can not be adjusted; it is fixed to a height of 15mm $\pm 50\,\mu$m given by the manufacturer. Nearly all other degrees of freedom are flexible, especially the lens that can be moved vertically along the beam axis and tilted around a horizontal axis. This allows for small height adjustments. Furthermore, the lens' position also defines the beam waist; thus, the beam position can not be changed independently of the beam waist. Conclusively, it is essential to monitor the two saving-CQS and simultaneously the beam waist on the *WinCam*. The alignment is, accordingly, time-consuming and takes several hours.

Example

Strategy 1 was developed to place the first fios, labeled *fios1* in Figure 1.11. It distributes beams in all four local interferometers and provides the light through two Backlinks to the second bench. Accordingly, the subsequent components are placed relative to this one, and *fios1* requires a good starting alignment. The requirements are a beam height of 15 mm within a few µm, a horizontal distribution along the bench within a few µrad, and a beam waist of 0.5 mm at 0.5 m distance. Strategy 1 required slight changes, as described in the following.

Before being distributed in the interferometers, the *fios1* beam is transmitted through the *Faraday rotator*. Its optical path consists of a crystal in the shape of a parallelepiped. As measured by [Win17], this crystal is not perfectly aligned in its mount, and the planes of the parallelepiped are not perfectly aligned to each other either, causing beam tilts bigger than 30 µrad. O. Gerberding designed a thermally compensated mount that allows for height, rotation around the beam axis, and angle alignment to compensate for the mismatch in the crystal [Isl18]. However, this alignment is limited; thus, the *Faraday rotator* was aligned jointly with the *fios1*. This ensures that the beam after the *Faraday rotator* still fulfills the horizontality at 15 mm. Therefore, Strategy 1 had to be slightly changed compared to the description above, illustrated in Figure 2.13b. Instead of only measuring at the attenuator reflection port, the beam after the *Faraday rotator* was also measured. (The pbs6 was not placed, and thus the beam was directly accessible.) The horizontality at 15 mm was probed, and the saving-CQSs were placed there. The attenuator port was used for verifying the 15 mm height at the fios position due to the proximity to the fios position. All four measurements are necessary for a target-alignment run and afterwards for checking the alignment and running possible iterations.

The achieved fios waists and their positions for both benches are $\omega_{1B} = 450\,\mu$m, $\omega_{2B} = 371\,\mu$m at $z_{1B} = 501$ mm and $z_{2B} = 450$ mm, for the first bench (1B) and the second bench (2B), respectively. For the first bench, the height at the fios position during the target alignment was 14.9937 mm $\pm(3.02\,\mu$m $\pm$ u$_{\text{offset}})$ and thus deviated less than 7 µm from the goal of 15 mm. Behind the *Faraday rotator*, an angle of 23.9 µrad ± 7.12 µrad in the vertical axis was achieved. Considering the FMA manufacturer uncertainty of $\pm 50\,\mu$m and the (later) observed beam tilts in the 300 µm range (see Section 2.4.5), this result is satisfying. On the second bench, the height at the fios position only deviated by 1 µm from the target 15 mm. The beam has an angle of 4 µrad ± 7.12 µrad and is about 10 µm $\pm(3.02\,\mu$m $\pm$ u$_{\text{offset}})$ lower than intended.

Strategy 1 was developed with D. Penkert, S. Ast, and O. Gerberding. The target alignment method was invented and implemented by D. Penkert in PC-DMIS for the specific case for *fios1* and later generalized by the author with N. Knust in a *Matlab* script to accelerate the calculations. With Strategy 1, an alignment procedure was developed to handle the coupling of several degrees of freedom. Without this strategy, the alignment of the fios would be unmanageable and presumably even impossible to a satisfying precision. Deducing the targets requires more than a day of alignment, and hitting the existing ones with the actual fios takes another day due to the cross-coupling of the degrees of freedom.

Appendix A.3.4 describes an additional step foreseen initially to speed up the beam mode alignment but was discarded due to infeasibility.

2.3.4 Strategy 2: fios-to-fios Coupling

The construction of the 3BL further includes the coupling of a beam into the Backlink fibers, which requires the beam coupling from the already placed fios into a new fios, placed relative to the first one. The coupling depends on matching the two beams in their modes and spatial alignment. As in the previous strategy, the number of degrees of freedom is both an advantage for a customized alignment and a disadvantage for a challenging and complex alignment.

The strategy in a nutshell: In preparation of a fios' beam alignment relative to an existing beam in the interferometer, the preparation is again done with an *alignment beam*, *saved* and then restored by the fios. By using a mirror under normal incidence, the existing beam is coupled back into its fios, creating a starting point for the to-be placed fios. As a result, a fios can be aligned relative to an already placed one with several components in between, and the existing beam is easily coupled into the new fios.

After one absolute beam is fixed in the interferometer, the others are aligned relative to it. This alignment can be sped up significantly with the here presented strategy. Figure 2.14 illustrates the following steps:

a) The *alignment beam* that was introduced in the previous strategy mimics the fios before its placement. This is done by a single mirror, m1, that is placed in the beam under zero degrees angle to reflect the beam back in itself, see Figure 2.14 a). The mirror has a wedged backside to prevent the creation of a cavity. A good overlap with the original counter-propagating beam is achieved by optimizing the incoupling in the beam's origin, the output *fios1* in this example. The incoupling is tracked on a fiber-coupled PR connected to a fiber circulator.

b) When a sufficient alignment is reached, two target-CQS at different ports of the interferometer *save* this beam alignment, as also introduced in the previous strategy.

c) The real fios is placed and centered on the target-CQS, which results in some amount of incoupling, which is afterwards optimized by aligning the fios. At the same time, another interferometer port is used for beam profiling WinCam measurements. The focus is on the optimized incoupling and the beam parameters, not the absolute overlap between the beams, which is discussed in Strategy 5 in 2.3.7.

d) The beam that is created in b) propagates through the interferometer at the same path as the final *fios2* beam will. It can be used to place components in this path before the actual fios is placed, as shown in Figure 2.14 d).

Examples:
This strategy was used to **place *fios2***, the DFBL-fios, which guides light in both directions through the Backlink fiber. No deflection mirrors are available, and only the fios can be adjusted to get the light of *fios1* coupled in. This required some starting point for the alignment, which was successfully found with this strategy. Since the design of the 3BL prevents light from coupling into *fios1* with the *Faraday rotator*, a polarizer was used to create a mixed polarization state that could partly be coupled back into *fios1* for step a).
This strategy is based on a technique for the alignment of parallel beams described by M. Dehne in
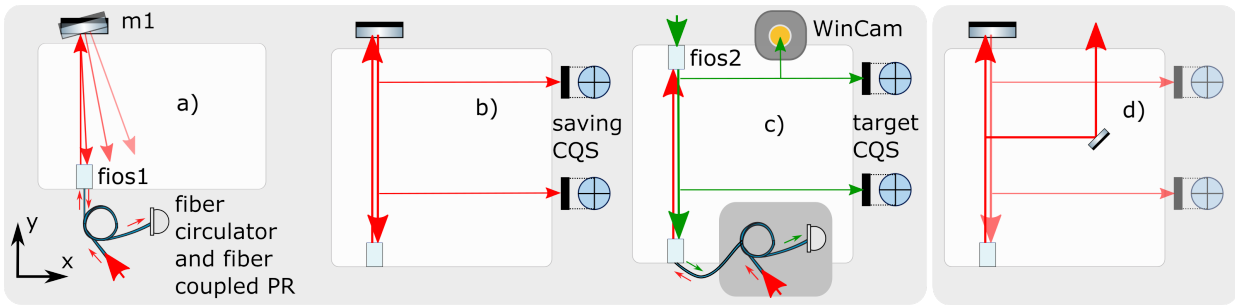
Fig. 2.14.: Steps of Strategy 2. a) mirror m1 reflects the beam back to *fios1*, the coupling is tracked on a PR. b) Two saving-CQS save the beam's alignment. c) The beam is replaced by fios, which is centered on the target-CQS. Its incoupling into *fios1* is optimized while its beam parameters are tracked with a WinCam. d) The strategy provides the mimicked beam to align components that depend on *fios2* before it placed.

her PhD thesis [Deh12]. It was extended because of the much more complex alignment of the fios in the 3BL.

The output beam of *fios2* has the additional constraint to be interfered with the *fios1* beam in the DFBL-ifo. During its construction, the BEAST blocked the beam path to the interferometer. Thus an alignment of both requirements simultaneously was impossible. Thus, the coupling into the fios was the driving alignment parameter. On both benches, a coupling of about 50% was reached and presumably limited by the non-adjustable height of the ferrule.

The polarizing beamsplitter **pbs6** was placed with Strategy 2, applied as in Figure 2.14 d). *pbs6* is placed in front of the beamsplitter that distributes the light in all interferometers. It needs to ensure all components are hit centered. One especially critical component is the waveplate *hwp1*, (shown in Figure 1.11), which has a small aperture of 7 mm in diameter. Due to its relatively long propagation path along the FBBL, the beam's radius is increased at this position, making it essential to hit the waveplate centered. Thus, the beam from the adjacent bench, which also needs to overlap with the local one (see also Strategy 5 in 2.3.7), is mimicked with this strategy and the alignment is completed.

Additionally, this strategy was used to place **_fios3_**. However, this fios is part of a more complex alignment strategy, presented as Strategy 4 in 2.3.6.

2.3.5 Strategy 3: Alignment of Collinear Beams and Introduction of Glue Wedges

After having two beams on the optical bench, these beams are overlapped in the interferometers to provide interferometric measurements. The 3BL design foresees the placement of the interfering beamsplitters with the template, and the overlap of the two beams is created by a deflection mirror in one of the two beams path.

The strategy in a nutshell: Two propagating beams that should be collinear are overlapped by using one horizontally alignable component. A tilt can be introduced to the glue layer below the component when a vertical alignment is necessary. Two different levels of precision are presented, either based on optimized contrast or absolute alignment. Beams can presumably be overlapped in
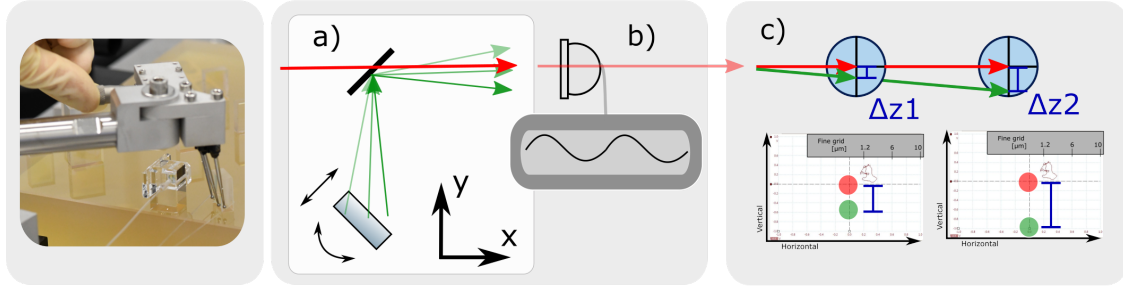
Fig. 2.15.: Strategy 3, two collinear propagating beams are superimposed by moving one deflection mirror a). The alignment is either tracked with a single PR to optimize contrast b) or on two CQS to optimize the spatial distance c).

the μrad range with this strategy, which could only be measured up to the CQS angle measurement uncertainty of 10.1 μrad.

Usually a pair of two mirrors is used to align all spatial degrees of freedom of a propagating beam in a so-called "beam walk" to overlap two beams for maximal interferometer contrast. Quasi-monolithic, complex interferometers are designed to achieve exceptional mechanical and thermal stability and optimize the usage of the available space and minimize the number of components. When, thus, only a single mirror is available for this procedure, the alignment of beams can only be done in two horizontal degrees of freedom; by tilting this component and moving it back and forth. A tool called the pointing fingers has been developed for this purpose in previous works, see Section 2.2.3. The two interfering beams are observed on a PD, and the contrast is optimized in the horizontal axis, see Figure 2.15 a).

The assumption of perfectly horizontally propagating beams and precisely vertically aligned interfaces of optical components do not hold in a glued interferometer. While bonded components have a tilt towards the baseplate of less than ± 10 μrad [Ell+05], glue introduces a tilt in the order of 300 μrad, see Section 2.4.5. While the non-zero thickness of the glue layer is part of the problem, the same can also be the solution. Applying a little force on one edge of the component introduces an intentional wedge in the glue layer. A simple construction, forming a "finger from above," can be used for this, see Figure 2.16a. Ideally, care should be taken to prevent these wedges in the first place because the different CTE's of the glue and the component can lead to thermally driven beam pointing, but turned out to be uncritical as shown in 2.4.5. However, this technique is only meant as a solution for unpreventable wedges.

In some cases, the alignment for optimal contrast might not be sufficient. Instead, the exact spatial overlap of the beams is essential. Simulations by [Isl18] for the Free-Beam Interferometer in the 3BL showed that a tilt of 20 μrad would only lead to a contrast change of 0.1%. The contrast can not be used to reach an overlap in the μm range, which is required for the FBBL, as discussed in Appendix C. Instead, it is possible to measure the misalignment with higher precision with the support of two CQS. This is illustrated in Figure 2.15 b). The fixed beam is split and centered on both QPDs in the near- and far-field. By observing the *alignment beam* on both QPDs, it is overlapped with the fixed beam up to the measurement uncertainties of the CQS position measurement of ± 3.02 μm. Residual misalignment can be extracted from the knowledge of the grid and the measurement distances.
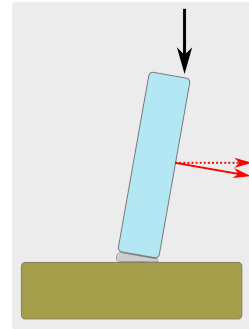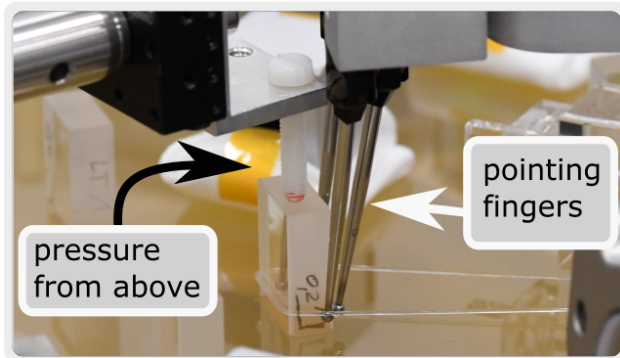
(a) Pointing fingers and pressure from above for slight vertical alignment. **(b)** Glue Wedge created by pressure on the front edge of the component.

Fig. 2.16.: Pressure from above creates an intentional wedge in the glue layer.

This version of the strategy is more time-consuming than the optimization of the contrast. However, the latter is automatically optimized this way, too. Opposite to other contrast optimization procedures, the geometrical overlap is explicitly extracted, and thus, it is known that no improvement can be made with further beam position alignments.

Examples:
The design of the 3BL includes one deflection mirror per interferometer for the DFBL and the FBBL to create the interferences. These mirrors, *m2* and *m4*, were glued in Strategy 3. *m2* needed a significant vertical tilt, afterwards measured to be $0.17°$ (see Section 2.4.5), in order to reach a contrast of 58%.

m4 was aligned using the CQS. This component creates interference in the FBBL-interferometer. It is more prone to Tilt to Length (TTL) coupling increase due to misalignment ([Isl18]) because of its lever arm. As discussed in Appendix C there was a recommended TTL requirement of $10\,\mu m/rad$, which was relaxed by one order of magnitude and best effort. As discussed in Strategy 5 in 2.3.7, a trade-off between the alignment before and behind the interfering bs8 was needed. Strategy 5 is about preparing for this m4 alignment and yields more information about the FBBL-interferometer construction. The resulting alignment with m4 of the collinear beams is in the horizontal axis 7.9 - 35 μm with vertical angles of 17 - 38 μrad. (The typical CQS uncertainties do not accompany these values because they were extracted as worst-case estimates from the CQS grid, see Section 2.1.2.)

2.3.6 Strategy 4: fios-to-fios Coupling and Contrast in two Interferometers Simultaneously

The strategy in a nutshell: The three strategies mentioned above are combined to place two fios and two interfering beamsplitters entangled with an existing fios.

This alignment strategy was employed to adjust the spatial parameters of two fios output beams with respect to a third local beam and achieve a fios-to-fios coupling, illustrated in Figure 2.17. Both fios and interfering beamsplitters must be constructed in the same step to guarantee good contrast and coupling efficiency. However, both fios can not be placed at the same time because
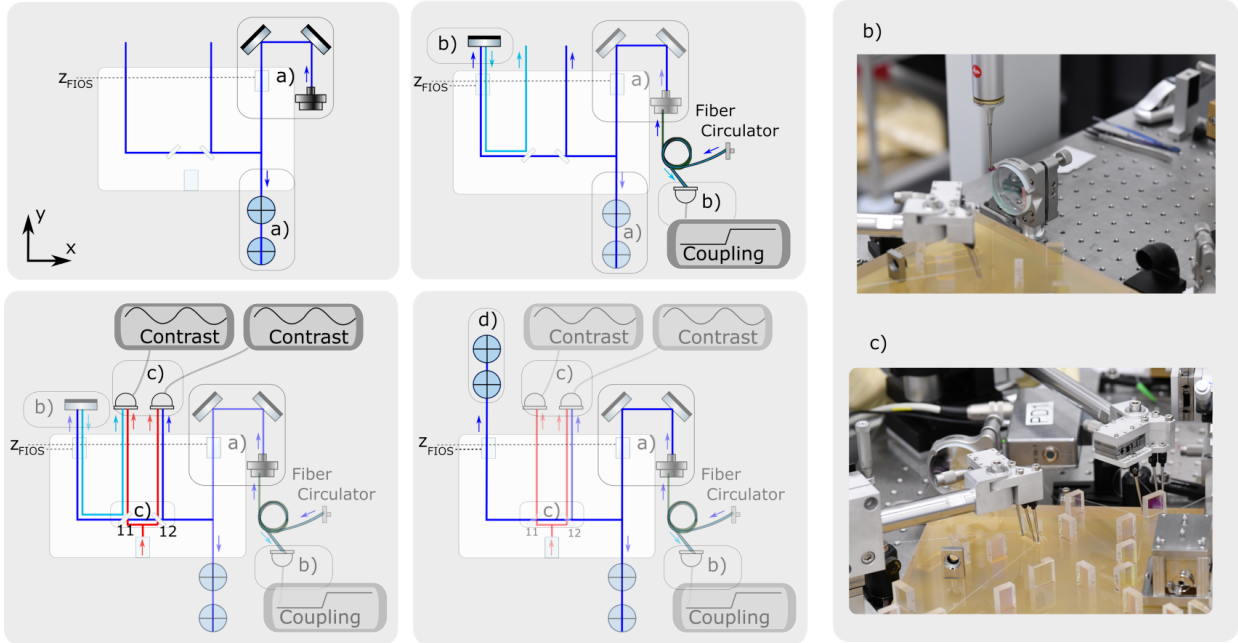
Fig. 2.17.: Schematics of Strategy 4. The different steps and requirements are circled. a) *fios4* beam is mimicked with an *alignment beam*, b) *fios3* is mimicked by a mirror that couples light back into the fiber circulator, c) two bs are placed to achieve contrast on a PD each d) the height at the *fios3* position is measured.

only one BEAST was available, and the simultaneous alignment of two fios would result in an extraordinarily amount of degrees of freedom.

This strategy was developed to construct the key parts of the FSFBL: *fios4*, that injects the additional local oscillator on the bench; *fios3*, that leads this light through the Backlink to the other bench; *bs12* that interferes the beams from *fios4* and the local *fios1*; and *bs11* that interferes a beam from the same *fios1* with one beam from *fios3* coming from the other bench. These create the FSFBL-Ref interferometer and the FSFBL-meas interferometer. The alignment of all four components (*fios4*, *fios3*, *bs12*, *bs11*) is entangled due to the superposition with the *fios1* beam. Due to the specifics of this strategy and because it merges the previously introduced strategies, it is explained jointly with the example.

Strategy and Example

The steps are shown in Figure 2.17:

a) The solution is based again on mimicking one fios, *fios4*, by an *alignment beam* with a stable mount and two mirrors, as in Strategy 1 (2.3.3). The attenuator's (att1) reflection in front of *fios4* enables calculating the beam height and the target alignment method. The beam is aligned to have a height of 15 mm at the fios position and be horizontal in the optical bench's coordinate system (Figure 2.17 a)).

b) *fios3* is mimicked by an *alignment beam* using a mirror, as in Strategy 2 (2.3.4), by coupling the *alignment beam* from *fios4* back in itself (Figure 2.17 b)).

c) When both beams are in place, the two interfering bs are placed (Figure 2.17 c)) with pointing fingers. They are aligned to maximize the contrast in the latter FSFBL-ref and FSFBL-meas interferometers but have no alignment in the vertical direction, as discussed in Strategy 3

(2.3.5). To avoid tilting the bs, small corrections are performed with the first *alignment beam* (dark blue) for the beams that interfere at the first bs, *bs12*. Immediately, the back coupled beam (cyan) is changed and needs correction to keep the backcoupling. The interference at the second bs, *bs11*, is affected by these corrections. The overall alignment is done with minimal adjustments and is very time-consuming. All four components are aligned until the four requirements are fulfilled: The beam height at the *fios4* position is 15 mm. The back-reflecting mirror couples light into the *fios4*-mimicking coupler. The contrast at *bs11* and *bs12* is at least 50%. The alignment includes target alignment, checking beam interferences on a viewer card, and modulating the incoupling by mechanically disturbing the mirror.

d) Then, the mirror is removed, and the fifth requirement, the height at the *fios3* position, is measured by two CQS measurements along the beam (Figure 2.17 d)).

When the beam height measured in d) is not 15 mm, the process is started again and typically needs several iterations until a good trade-off in the different requirements is found. If the result stays insufficient, a solution is to loosen one of these requirements. For example, the height at the second fios position. If the manufacturer can change the fios height by ablating some of the FMAs material, this is an easy solution that effectively keeps all requirements.

After the final alignment is done, the beams are saved with two sets of CQS positions, one for each fios. The alignment is recovered to place *fios4* and *bs12*, and without additional changes, *fios3* and *bs11* a few days later. *bs11* is not glued in the first step to keeping its alignment possibility during the *fios3* placement open. It is placed on UV-glue during the initial alignment but can remain uncured because of the very focused UV-lamp when *fios4* and *bs12* are cured. Removing it before curing would introduce too much shaking and, thus, misalignment on the optical bench.

This strategy was applied successfully on both benches for the FSFBL installation, with the results summarized in Section 2.4. During the alignment on the first bench, the beam at the *fios3* position was found to be too low by 390 µm $\pm (3.02\,\mu m \pm u_{offset})$. Shortening the fiber holder, the FMA, was possible and done by the company *Krombach*. On the second bench, the beam height at *fios3* of 14.980 mm $\pm (3.02\,\mu m \pm u_{offset})$ was in the FMA manufacturing uncertainty of $\pm 50\,\mu m$, and no change was necessary.

2.3.7 Strategy 5: Collinear Alignment of Counter-Propagating Beams

In the FBBL two beams are counter-propagating in a free-beam path, which requires a well-overlapped alignment.

The strategy in a nutshell: Like in Strategy 2 (2.3.4), the propagation vectors of two beams are overlapped. In this strategy, the beams counter-propagate, and the absolute angular and positional deviation between them are essential. The optical bench provides one beam, and an *alignment beam* is mimicked like in Strategy 2.3.3. Both beams' vectors are measured with the CQS, and the beams are aligned according to their mismatch. This strategy allows the overlap of counter-propagating beams down to the µm- and µrad-range, dominated by the CQS measurement uncertainty of beam angles up to 23.73 µrad.

Figure 2.18 describes the alignment process for steps a-c). Options I-III) are not illustrated
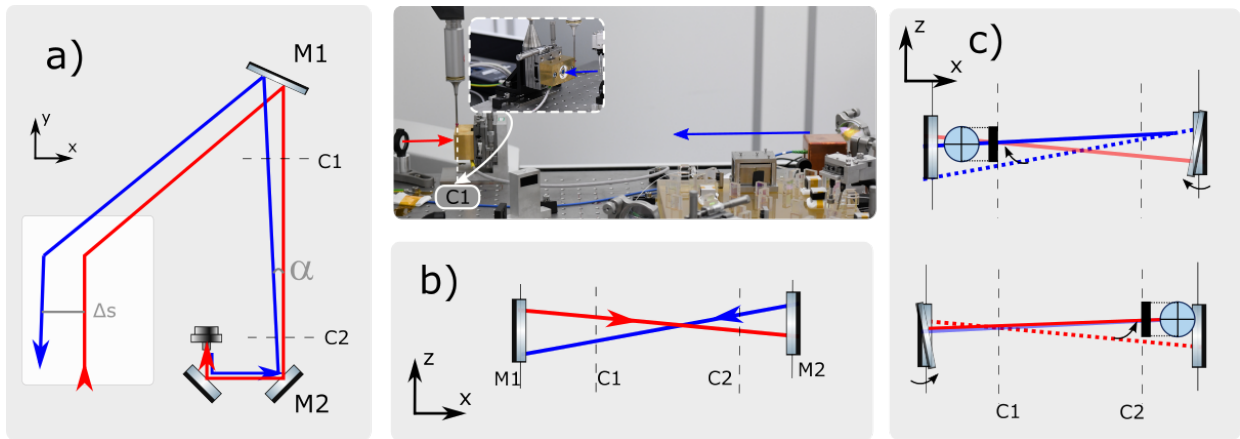
Fig. 2.18.: Strategy 5: collinear alignment of counter-propagating beams. a) The angle and the distance between both beams can be extrapolated after doing measurements at the positions C1 and C2, which is illustrated in the central photograph. Alignment techniques described in b) and c) are shown for an 2 dimensional extrapolated beam, as already in Figure 2.12.

in the Figure.

a) The situation is depicted in Figure 2.18 a). The CQS measures both beams in their particular direction at positions C1 and C2. The relative angle between the beams and, by extrapolation, their displacement anywhere along the beams are extracted. The alignment can be done by different approaches introduced and evaluated in the following.

I) The most straightforward approach for overlapping the two beams is the usage of two apertures, like the *variable Irises* from *Thorlabs*, placed at positions C1 and C2, and centered on the optical bench's beam. By iterative alignment of the *alignment beam* over a measurement distance of about 60 cm, an angle of 1.4 mrad ±10.1 µrad was reached.

II) Two orders of magnitude more precise is a strategy similar to Strategy 2 (2.3.4), where the target beam is coupled in the stable coupler with maximized coupling. For a perfect coupling, the mode of the incoming beam has to be identical to the coupler's output mode. This is similar to contrast optimization in an interferometer, meaning that the fiber coupling efficiency is not an accurate measure for beam overlap, as it changes by only 0.1 % for a 20 µrad tilt and behaves non-linear, as simulated in [Isl+18]. For completion, measurements about the dependency of the achieved incoupling to the angular mismatch are presented in Appendix C. Applying this technique, an angle of about 30 µrad between the beams was reached but not reliably reproducible.

III) Additional strategies were investigated for this problem and are shortly introduced in Appendix C.

b) By including the CQS in the alignment, a reliable precision in the µm and µrad-range can be achieved in the following simple procedure, which is illustrated in b) in Figure 2.18. The two beams are represented two-dimensional in the xz-plane, reflected by mirrors m1 and m2, with CQS measurements C1, C2 between the mirrors. The alignment is done at C1, where the CQS is facing the blue beam. It is aligned to the measured height of the red beam at that position. M2 is aligned to center the blue beam on the CQS. This procedure typically improves the angle between the beams but cannot improve the spatial displacement.

c) This approach can be expanded further. First, a good starting point is reached with one of the previously mentioned processes. The set-up is shown in Figure 2.18 c), where both mirrors, M1 and M2, are involved. After measuring the beam in both directions at positions C1 and C2, the CQS at C1 is centered on the red beam. M2 is used to center the blue beam on this target. The same is done on the other side. The CQS at C2 is adjusted to the position of the blue beam, and the red beam is centered there with M1. Typically, only one or two iterations are needed until the beam is aligned with deviations of $0.5\,\mu\text{rad} \pm 23.73\,\mu\text{rad}$ and $10\,\mu\text{m}$ $\pm 3.02\,\mu\text{m}$ over the relevant distance. It is essential to measure the beams in both directions at the same spots, C1 and C2, respectively, thus having the QPD itself always at the same spot. A deviation of 4mm along the beam's propagation axis will result in a mismatch of the targets of about $4\,\mu\text{m}$.

Example in the 3BL:

During the alignment of the Free-Beam Backlink, $m4$ is aligned to reach interference between the local beam and the Backlink beam. The local beam is aligned, while the beam coming from the Backlink is stable. However, the Backlink beam requires the control loop that keeps it in its well-overlapped position with the other, counter-propagating Backlink beam. The control loop depends on the interference that is not available without $m4$. This circle is broken by mimicking the incoming Backlink beam with an *alignment beam* and overlapping it with the outgoing Backlink beam. Thus, the here-discussed strategy is the first step in the $m4$ alignment, where the adjacency beam is prepared to be the reference in the interferometer. The beam preparation is very critical, motivated by simulations done by [Isl18], which formed a requirement based on the TTL-coupling in the FBBL-interferometer. The requirement is discussed in detail in Appendix C and was relaxed during the construction to $\pm 100\,\mu\text{rad}$ and $\pm 100\,\mu\text{m}$. The alignment of $m4$ was presented in Strategy 3 (2.3.5).

On the first bench, the *alignment beam* was created by a fiber coupler and a mirror pair, as introduced in Strategy 1 (2.3.3). Optimizing the latter's incoupling to the fiber coupler found a rough overlap with the outgoing Backlink beam. The final alignment was done with the method mentioned above in b).

The beam from the completed first bench was used for its alignment on the second bench. The first overlap was here reached by using the first bench's FBBL interferometer, where the outgoing beam from the second bench overlapped with the local beam. Afterwards, method c) was applied to overlap the counter-propagating Backlink beams.

During the alignment of the second bench, the previous alignment deviations on the first bench caused an additional requirement. Ideally, a perfect overlap of the counter-propagating beams results in an optimized overlap in the FBBL interferometer. Due to the alignment deviations during the first bench's construction, this was not fulfilled. A trade-off between a good overlap in the Backlink path and the FBBL interferometers on both benches was necessary. After several iterations, the two beams were overlapped within an angle of $27\,\mu\text{rad} \pm 23.73\,\mu\text{rad}$, and the distances at the interfering bs, $bs8$, was below $5\,\mu\text{m} \pm 3.02\,\mu\text{m}$ on both sides (see Appendix C.2), which is within the relaxed requirement. The alignment is thus believed to be sufficient. If, on the contrary, performance limitations in the FBBL are observed in the future, it is possible to adjust the DWS loop or use the DWS to do TTL coupling corrections in post-processing. Until the finalization of this thesis, no indication of a distorted control loop was found.

2.4 Bench Characterization

The optical benches of the 3BL were fully assembled according to the experiment's design. The finalized benches are presented in Figure 2.19. The different investigations and alignment procedures were formulated as five strategies that enable the construction of these complex benches. The second bench was built with a significantly more stringent time constraint and was realized within 30% of the time needed for the first bench. This was achieved due to the expertise and strategy development of the first bench's construction.

The constructed benches are analyzed in this section according to the achieved contrast, coupling, and beam parameters. They are evaluated in comparison to the simulated values. Discussing some observed back reflections and spurious beams further characterizes the benches. The measured component tilts due to uneven glue layers are discussed and summarized with lessons learned and a review of the gluing technique.

2.4.1 Contrast

The contrast depends on the heterodyne efficiency η, and the power ratio of the two interfered beams, as introduced in Section 1.2. During the construction, approximately equal beam powers were used while maximizing the contrast, and the achieved values are presented in Table 2.20. Calculations based on [WH14] including the measured beam parameters in Table 2.4 concluded that for perfectly aligned beams and equal powers, a contrast over 90% was theoretically possible in each interferometer. The actual contrast values between 52% and 90% are presumably, dominated by misalignment in the spatial overlap and small deviations in the measured power ratios during the alignment. The contrast values κ in the table can be seen as a lower limit for the heterodyne efficiency η by $\sqrt{\eta} = \kappa$, see Equation 1.5.

No comparable construction misalignment is introduced in the simulations of the 3BL by [Isl18]. The ideal heterodyne efficiency η is simulated at 0.89 for the FBBL and higher than 0.98 for the other interferometers. The achieved lower contrast levels can potentially be problematic in terms of the three noise sources; shot noise, electronic noise, and Relative Intensity Noise (RIN). Their coupling depends on the power levels and the heterodyne efficiency, as presented in [Isl18]. They were calculated for the 3BL interferences depending on the heterodyne efficiency, as shown exemplarily for the FSFBL-meas in Figure 2.20. The included RIN value of $3 \cdot 10^{-7} \frac{1}{\sqrt{\text{Hz}}}$ was measured in the laboratory, as presented in Appendix E.6. Even for a heterodyne efficiency of 0.1, these noise sources do not become problematic, thus the minimum contrast of 0.52, relating to a heterodyne efficiency of 0.27 is concluded as uncritical.

The contrast level also becomes relevant in the context of spurious light. As visible in Equation 1.7, the ratio $\sqrt{\frac{\eta_{SL}}{\eta_{\text{nominal}}}}$ of the heterodyne efficiencies between the spurious light and the nominal beam η_{SL} and between the two nominal beams η_{nominal} is essential for the phase error. If only η_{nominal} is reduced, the influence of the spurious light increases. However, it is impossible to quantify the ratios for the various possible spurious beams.
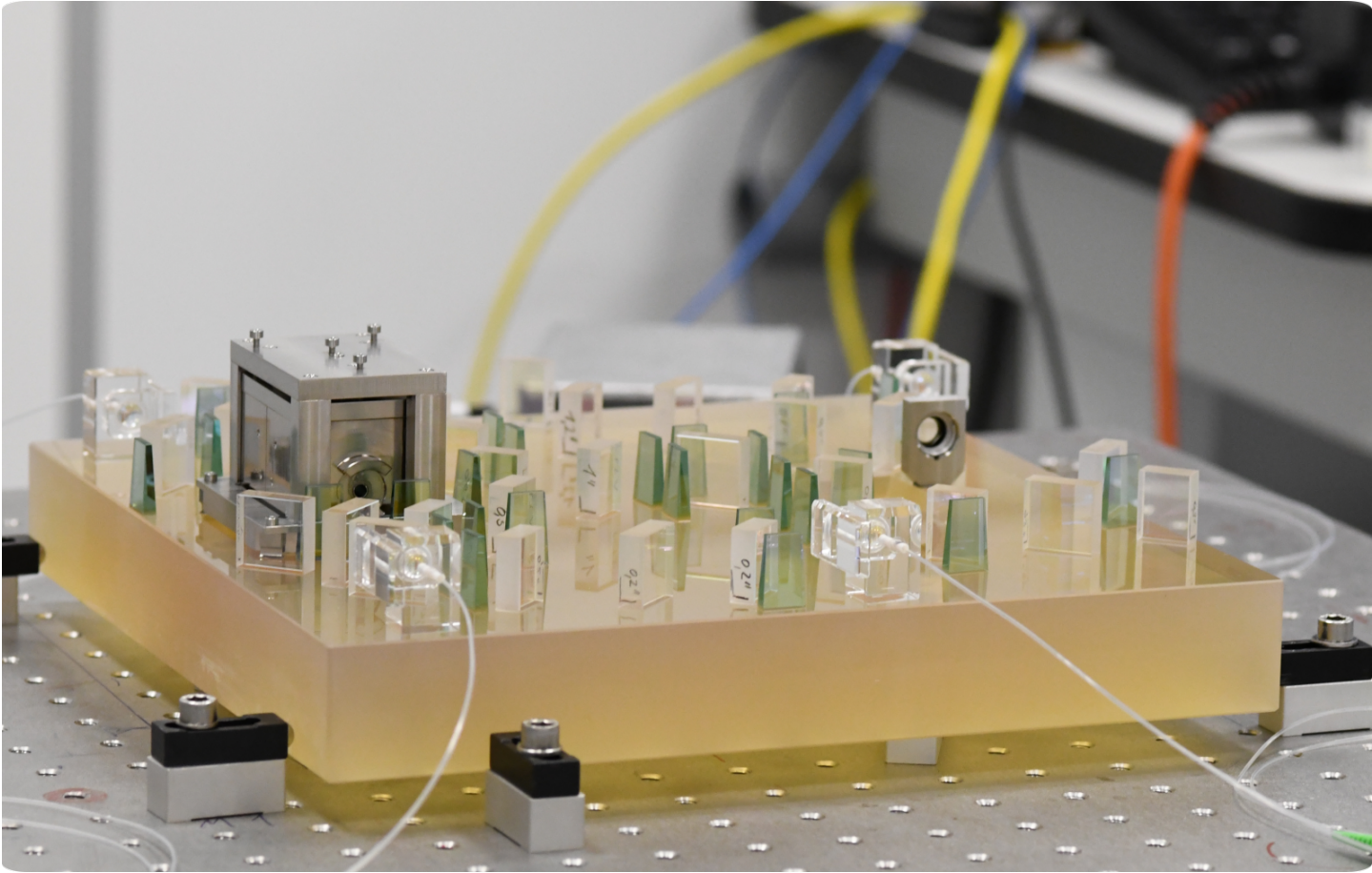
Fig. 2.19.: The fully assembled 3BL Benches.
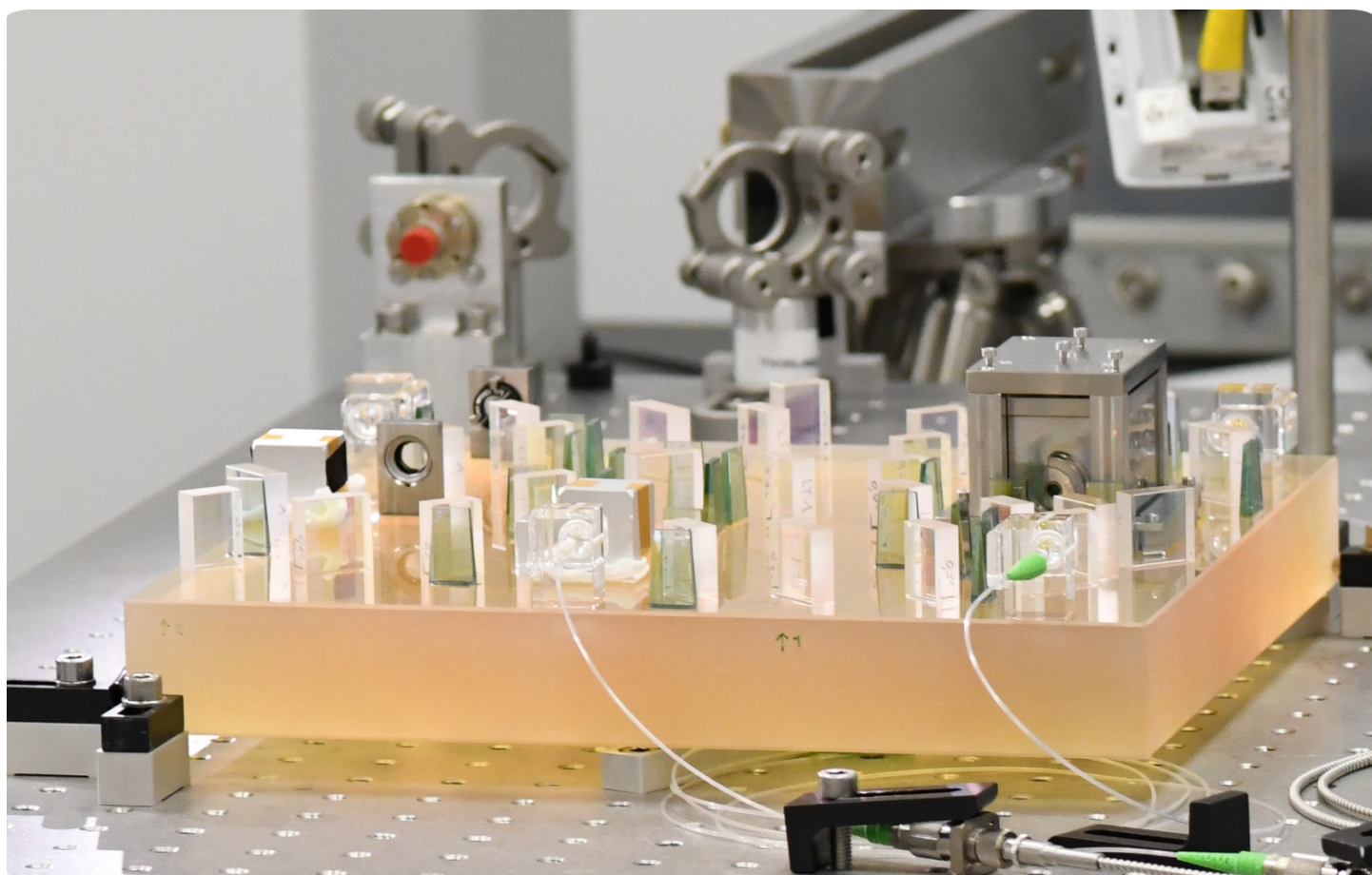
Interferometer		cleanroom contrast κ [%] (equal powers)
DFBL	1st	71
	2nd	58
FSFBL-meas	1st	52
	2nd	90
FSFBL-ref	1st	74
	2nd	83
FBBL	1st	$\approx 65*$
	2nd	$\approx 65*$
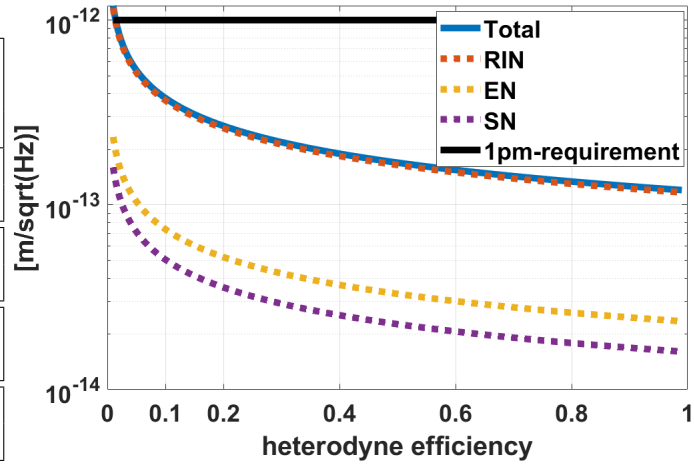
Fig. 2.20 & Tab. 2.2: Tab: Collection of the contrast levels reached in the 3BL construction. Given are the measured contrast values for approximately equal powers measured in the cleanroom. (* The FBBLs alignment depends on the steered beams and is not fixed like in the other interferometers. The measured values were achieved during its implementation.) Fig: Noise contributions calculated based on the measured contrast and RIN.

2.4.2 Coupling

The fios-to-fios couplings are key parts of the fiber Backlinks. The accomplished coupling efficiencies are collected in Table 2.3. Measurements during the construction in the cleanroom and after implementation in the vacuum chamber are shown. The powermeters by *Thorlabs* have an uncertainty of $\pm 7\%$ for a wavelength of 1064 nm [Tho22], which are included as uncertainty in the table. The values of both measurement runs agree, assuming a similar uncertainty for the powermeter measurements in the cleanroom. The exception is the coupling of the FSFBL on the second bench. Here, the coupling measured in the cleanroom is 26 % and thus significantly smaller than the 52% measured later in the laboratory. This deviation extends the scope of normal measurement errors or influences by fluctuating laser power. Possible explanations are slight changes in the alignment, for example, by creep over time in a not completely cured glue layer. Another option is the *Faraday rotator*, which could have undergone a slight misalignment during the shaking by transporting the benches from the cleanroom to the laboratory. However, this would also affect every local interferometer. Furthermore, the optical bench can bend slightly due to its finite stiffness. The three mounting spheres underneath it are differently orientated in the cleanroom compared to the vacuum chamber. Both coupling efficiencies were measured in air, thus a change in the refractive index is excluded. However, the measurements inside the vacuum chamber were done after evacuating the chamber once; thus if residual air between the glued surfaces was removed by the evacuation, this could cause misalignment.

The simulations by [Isl18] assumed a fiber-to-fiber coupling of 70%. Only the coupling of the FSFBL on the first bench comes close to this value with 68%, while the others are around 50% or lower. The reason is presumably the combination of the ferrule's non-adjustability with the components' horizontal tilts. In the 3BL simulation, maximal vertical tilts of 10µrad were assumed [Isl18]. They would be easily compensatable with the fios design, where the lens is adjustable. However, the vertical tilts of the components are one order of magnitude higher than expected. Since careful and persistent alignment was performed without any improvement above the $\approx 50\%$ coupling in *fios2*,

it was concluded that the height of the ferrule, the only non-adjustable degree of freedom, is the limiting factor.

The power levels in the interferometers do not change significantly with these coupling values, so no negative influence on the deviation from the target 70% is expected. It will be an interesting experiment in the future to alter the coupling efficiency and measure the Backlink's non-reciprocity in dependency of the fios-to-fios coupling. See also Section 3.11.

Backlink	Bench	fios	Cleanroom Coupling [%]	Laboratory Coupling [%]
DFBL	1st	fios1-fios2	52	46 ± 3.6
	2nd	fios1'-fios2'	50	48 ± 4.2
FSFBL	1st	fios4-fios3	68	76 ± 6.6
	2nd	fios4'-fios3'	**26**	**52** ± 4.1

Tab. 2.3.: Coupling values for the Backlink connections measured in the cleanroom and the laboratory. The values should not change between both measurements.

2.4.3 Beam Parameters

The target beam parameters given by the simulations by [Isl18] was a beam waist of 500 µm at a distance of 0.5 m towards the fios. The actual parameters are presented in Table 2.4 and vary from the target for different reasons but are all well collimated. *fios1* was placed on the bench first with a beam waist of 450 µm on the first and 371 µm on the second bench. The waists are located at 501 mm and 450 mm, respectively. The following fios were matched to *fios1*. *fios2* optimizes its parameters to maximize the coupling from the light of *fios1*. On the first bench, it has a beam waist of 578 µm at a distance of 207 mm. On the second bench, the waist is at 500 µm as targeted. Its waist position is within 5cm distance to the fios, and a more precise measurement was impossible. *fios4* and reached 529 µm at 210 mm and 426 µm at 512 mm, respectively with the priority on the interference with the *fios1* beam. *fios3* was then optimized for coupling of *fios4* and interference with *fios1*. Here, the beam waist on the first bench is 579 µm at a 647 mm distance and 350 µm at 550 mm on the second bench. The uncertainties depend on the distance measurement method (ruler or CMM) and the quality of the fit, which further depends on the number of measured points and how much of the beam's slope is covered. It is estimated for all fios to be in the order of 50 µm for the waist and 50 mm for its position.

Simple theoretical investigations about the influence of the changing refractive index during the operation in a vacuum were performed. They concluded a waist position change of about a few 1 cm, which is similar to observations during LISA fios construction at the University of Glasgow [Rob22]. Furthermore, the 3BL was operated successfully in vacuum.

2.4.4 Observed Backreflections and Spurious Beams

During the construction, some spurious light beams were observed. The most prominent or unexpected ones and an estimate of their influence are presented here.

fios		Beam Waist [µm]	Waist Location [mm]
fios1	1st	450	501
	2nd	371	450
fios2	1st	578	207
	2nd	≈ 500	very close to *fios2*
fios3	1st	579	647
	2nd	350	550
fios4	1st	529	201
	2nd	426	512

Tab. 2.4.: Beam waist and its location for the eight fios. The uncertainty is estimated for all fios to be in the order of 50 µm for the waist and 50 mm for its position

The fios showed a backreflection of 3% of the incoming light. This originates not at the lens but somewhere behind, in the FMA, ferrule or fiber. It has a misalignment towards the nominal beam; thus, its source is likely the FMA or the ferrule. This misalignment with the nominal beam differs for each fios, but it is mainly in the horizontal axis for all of them. The potential influence of this spurious beam on the measurement differs for the type of Backlinks.

Back-reflections at *fios2* are illustrated in Figure 2.21 a). The beams have the frequency of the local TX beam, and thus the interference with a TX'-beam enters the DFBL-interferometer at the nominal read-out frequency. This is, therefore, a critical stray light beam. There can be two cases. For an in-mode reflection with the nominal beam, the interference happens at the reflection point, and the spurious signal is removable with balanced detection, see Section 1.2.1. If this is not the case and the reflected beam is just propagating alongside the nominal beam, there is the possibility of them interfering at the interferometer. Then, the spurious signal would not be removable with balanced detection. However, no significant influence is expected because the spurious beam is close but not overlapping with the nominal beam, and thus the heterodyne efficiency η_{SL} is very low. According to Equation 1.7, the phase error will be negligible.

Backreflections at *fios4* are at the FSFBL-Backlink frequency, $f_{ALO'}$ and illustrated in Figure 2.21 b). The attenuator in front of *fios4* will reduce the back-reflection by 95%, and only the residuals enter the REF interferometer. There, the ALO and TX frequencies interfere nominally. This is the principle of the FSFBL; it protects the measurement from any spurious beams coming from *fios4* or *fios3*. The same is true for the backreflections caused by *fios3* at frequency ALO. Without an attenuator, most of the light will reach the FSFBL-meas interferometer, where ALO' and TX frequencies interfere.

The same spurious light beams do not appear in the FBBL, which dispenses a fiber Backlink to reduce backscatter and reflections from the fiber and the fios. Instead, a spurious beam is created by the **polarization separation**. The latter is realized by *pbs5* on each bench and a half-wave plate on the first bench. The residual light reflected at the *pbs5*, shown in Figure 2.21 c), measured in the cleanroom, is more than 1%. It is a combination of residual s- and p-polarization. The exact values were not investigated further because they likely change in the final commissioning of the experiment, where a different initial fiber coupling and, thus, a differently well-aligned start polarization is used. The suppression of this beam has been estimated in Section 1.5.1 for a pbs reflection of 2%, thus the observed spurious beam will cause a power ratio between nominal and

spurious beam after backscatter at the *fios1* fiber below 10^{-16}, which is uncritical.

By observing the Backlink beam in the FBBL on the first bench with a WinCam, a beam distortion was found at the outer edge of the beam profile. Its origin is somewhere on the first bench, and it might be caused by contamination of the waveplate or a cavity effect between the two waveplates. This is illustrated in Figure 2.21 d). They are slightly angled intentionally, but due to their small aperture, the angle of incidence of the beam is still close to zero. Furthermore, this effect was only visible on this bench, where two waveplates are placed and at no other interferometer port. This ghost beam would not vanish with balanced detection; thus, it should be remembered as a possible source of noise. (As before, no indication for a limitation of this distortion has been found in the measurements.)

The WinCam revealed another distortion in the **fios3 beams** on both benches but not in any other fios. It seems that a small, angled ghost beam accompanies it, as shown in Figure 2.21 e). This ghost beam was discovered with Wincam measurements, where it appeared as a distortion from the Gaussian shape. Rough estimations using the Wincam measurements and the distance measurements to the fios show that the angle from the ghost to the nominal beam is in the order of 0.2-0.3°. This distortion was investigated along the beam, especially at a position equivalent to the interfering bs' position. The beam showed a standard gaussian shape on the second bench at this position. However, the distortion was still visible on the first bench at a distance equivalent to the interferometer and might thus have an influence. However, the angle seems significant enough to prevent influences on the performance - and no evidence of a problem has appeared yet.

Some possible sources of back-reflection are investigated here shortly. The outcoupled beam of *fios3* creates its own spurious beam, which can happen by several reflections at the lens or the FMA surface, as shown in Figure 2.21 e), which creates a beam propagating in the same direction. These reflections are at power levels of $3.6 \cdot 10^{-6} \cdot P_{in}$ and $6.4 \cdot 10^{-5} \cdot P_{in}$, respectively. (Assuming a lens reflectivity of 0.19% (lens by *Thorlabs* 355110 -C) and reflectivity of the FMA's surface of 3.35%, based on its material's refractive index of $n_{\text{Corning 7980}}$=1.449 and the Fresnel equations). Since the beam was not observable without its nominal beam, it is impossible to estimate the real value. If this spurious beam is tolerable depends on the dynamics of its origin. The quasi-monolithic structure of the fios is presumable sufficient but can only be evaluated in the 3BL measurements. For the other observed spurious light beams created at the fios by an incoming beam, the lens was experimentally excluded as the point of backreflection. Instead, the measured 3% backscatter fit with the 3.35% reflectivity of the FMA's surface, which is likely the source of this spurious beam.

2.4.5 Component Tilts

The CMM allows measuring the perpendicularity between the coated surface of a component and the baseplate, the optical bench. Not every component was measured for two reasons. First, it is a time-consuming process and, more severe, the magnetic tip of the CMM should be kept away from the *Faraday rotator* to avoid misalignment, ruling out all components close to it for measurements. A sample of investigated template placed components have very scattered angle values with an average angle of 0.0216° (377 µrad), see Figure A.3a in the Appendix. The manufacturer guarantees
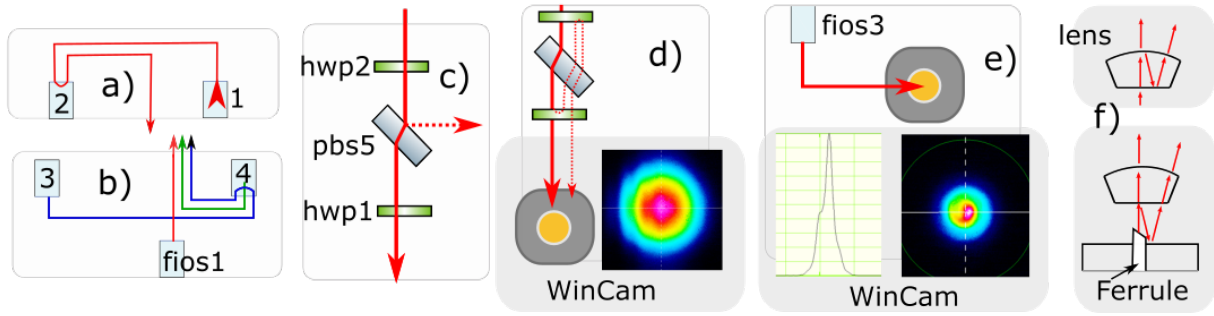
Fig. 2.21.: The different observed spurious beams: a) in the DFBL b) in the FSFBL c) caused by residual polarization in the FBBL, d) possible cavity effect on the first bench e) spurious beam in the nominal beam of *fios3* observed with a WinCam and f) possible points of reflections causing an angled backreflected beam.

a perpendicularity between coated surface and bonding surface up to 0.1"-1.7" (0.485 µrad-8.24 µrad). Clearly, the non-equal distribution in the glue layer is the dominant source of the components' tilt. They were observed after the construction of the first bench, and additional care was taken on the second bench to apply well-distributed pressure. However, the resulting misalignment was in the same order of magnitude. Therefore, the combination of 15 mm x 7 mm (or 20 mm x 7 mm) components with 6-10 nL/mm^2 glue results in component tilts of about 380 µrad.

Some components were slightly tilted when aligned with pointing fingers to compensate for limiting misalignment in the vertical axis. This effect was most significant for *m2*, where the beam had to be tilted by about 2°, measured with a ruler. CMM measurements confirmed that the component was tilted by 0.17° (2.97 mrad), corresponding to a wedge with a height difference of 21 µm.

The effect of this wedge on the geometrical TTL-coupling introduced by length changes due to temperature fluctuations is analyzed in the following. Assumed is a rotation axis at the edge of the bottom surface with the pivot point on that edge, as illustrated in Figure A.3b. The temperature-induced length change of the glue wedge's height is:

$$\Delta l = \text{CTE} \cdot \Delta T \cdot L = 1.155 \cdot 10^{-9} \text{m} \tag{2.5}$$

using a CTE of 55e-6/°C [Opt], the wedge height L=21 µm and a temperature change of 1 °C, which is in the order of magnitude of slow temperature changes inside the vacuum chamber. The corresponding tilt $\alpha = 1.65 \cdot 10^{-7}$ rad of the component results in geometrical TTL coupling, described by the lever arm and the piston effect, according to [Sch17]:

$$\Delta s_{\text{lever}} = \frac{\alpha^2}{2} d_{\text{pivot}} = 1.36 \cdot 10^{-15} \text{m}, \tag{2.6}$$

with the distance $d_{\text{pivot}} \approx 10$cm, between the pivot point and the PD, and

$$\Delta s_{\text{piston}} = 2\cos(\beta)(d_{\text{lat}}\alpha + d_{\text{long}}\alpha^2) = 4.95 \cdot 10^{-9} \text{m}, \tag{2.7}$$

with the longitudinal and lateral offsets between the point of rotation and the point of reflection, $d_{\text{lat}} = 15$ mm and $d_{\text{long}} = 7$ mm. Accordingly, the displacement caused by a 1°C temperature change is about 5 nm, resulting in a displacement coefficient by temperature fluctuation of about 5 nm/K. In [Isl18], this coefficient was calculated for the optical bench of the 3BL to derive the temperature requirement of 0.1 $\frac{\text{mK}}{\sqrt{\text{Hz}}}$ with a result one order of magnitude higher than the here derived coefficient.

Thus, even the significant wedge of 0.17° is tolerable under the environmental assumptions, which have been verified in the 3BL vacuum chamber [Isl18] of $10^{-5} \frac{\text{K}}{\sqrt{\text{Hz}}}$.

Conclusively, gluing without a sophisticated strategy for the perpendicularity results in components tilts in the order of 380 µrad. This is significantly more than the bonding flatness of ±10 µrad [Ell+05] achievable with hydroxide-catalysis bonding. The latter is critical to be that low because the tilt adds up with several components, and the technique does not allow for tilt compensations. For the gluing process, the glue causes the component to tilt and thus the beam angle. However, it is the solution at the same time. A wedge in one component can compensate for the tilts collected by the other components. As estimated above, even a significant wedge is not critical for thermal stability.

2.4.6 Glue

During the construction, drawbacks and problems caused by the UV-glue were observed and shortly presented in the following two sections in form of a lessons learned and a personal conclusion of the author about the application of UV-glue in general.

Lessons Learned

Several glue-related issues appeared during the construction and are shortly introduced in the following. The most important finding is to **never combine the techniques of *optical contacting* and glue**. Before the first coupling in a Backlink fiber was achieved, its feasibility was debated. To be on the safe side, one component in this path was placed with optical contact to be removable if an unforeseen problem arose. (This concern was unnecessary because the coupling worked well, presented in Section 2.3.4.) After successfully placing the remaining components of that beam path, the concern of instabilities due to the *optical contacting* occurred. Glue was applied around the component as additional fixation. This turned out to be a severe mistake, and the author would like to emphasize that this should never be done again. The expansion of the glue, either by curing or thermal expansion, destroyed the optical contact between the component and the bench. As a result, the component was neither stable nor easily removable. Since the glue was only applied to the component's outside, it was eventually removed after intensive use of the organic solvent *acetone*. The manufacturer also gave the information to use *Dynasolve®2000* or *Dynasolve®185* from *Versum Materials*, which was not tested. A similar problem also occurred in the triple mirror assembly of the laser ranging instrument in the GRACE Follow-On mission [Hei22][1].

Another problem is the combination of the solvent *octane* and UV-glue. One component was placed on *octane* to mimic its alignment with UV-glue but avoid unintentional curing while another component was cured. However, **octane was found to have a chemical influence on the glue**, preventing it from hardening (tested further by [Knu20]). The *octane* influenced the glue layer of the component in about 15 cm distance. Its glue was not cured. Further degradation of glue curing is caused by a degradation in the UV-lamp, which significantly increases the required illumination time. In response, simple glue and UV-lamp tests were performed before every gluing attempt.

---

[1] Private communication from G. Heinzel, 2022

Preventing the **contamination of a glue layer** is not trivial. Especially residual amounts of air or water appeared at some components' edges after some months. One component on the first bench, *pbs4*, has an especially bad glue layer, which is expected to introduce a significant tilt towards the baseplate. The component was placed at an early stage when not much experience has been collected. A more severe case of degraded glue layers happened during the fios construction on the second bench, where the glue layer looked fine during curing but degraded after some days. They got worse for a month until the state settled, which is shown in Appendix A. The fios are resistant to force applied by hand and thus apparently well attached. The cause for the disturbed glue layer is unclear and believed to be a combination of different circumstances. The alignment time of some of these fios was about ten hours. This is usually avoidable with a well-prepared gluing process and should be avoided in the future with the new limit of six hours. The humidity level in the cleanroom is very unstable and changes between 20% to 80% over the year. Thus, water and other contamination can creep into the glue layer during a long alignment. Additionally, the fios parts might have been incorrectly deployed in the BEam Alignment Support Tool, resulting in unequal pressure between the component and the optical bench over the component's surface. The disturbed glue layer appears on the opposite side of the center of mass, which is not in the center of the gluing surface. However, this and the problem of illuminating the whole gluing surface equally with the UV-lamp is entirely equal to the first bench where no such problem occurred. After applying some changes (one additional drop of glue, a 10x stronger UV-lamp, only six hours of alignment, and leaving the fios parts attached to the BEAST for a few days), the following fios was glued without any glue layer degradation. However, the last fios, *fios3*, showed a bad glue layer again, though a differently shaped one. Not the gluing process, but the optical bench may cause fios glue layer degradation. Both optical benches require a trench for the beam height exceeding *Faraday rotator*. The second bench houses two of these, caused by a manufacturing error. The optical bench's surface might have been damaged in this repeated process. Pictures of a selection of glue layers can be found in Appendix A.

Evaluating the Decision of Using the Gluing Technique

A quick personal evaluation by the author in favor of the gluing technique is presented. The decision between the different techniques of *optical contacting*, *silicate bonding techniques*, and UV-glue was made in favor of the latter. This was done before the 3BL's construction started and after the technique was tested in [Ger+17]. The author has also gained some experience with the *optical contacting* and *silicate bonding techniques* while supporting the construction of the ITAM-Experiment of D. Penkert and J. v. Wrangel [Wra19]. As presented throughout this chapter, the gluing technique has some disadvantages. In Section 2.4.6 degraded glue layers were discussed, likely caused by the glue's or the surfaces' contamination. However, these parameters are also essential for the other two bonding techniques. Another significant observation was the tilts of the components in Section 2.4.5. As discussed, even with care to apply equal pressure on the component, the component and thus beam tilts up to hundreds of μrad are unavoidable. This problem does not occur in the other two techniques, which are thus advantageous compared to UV-glue. However, if there is any additional angle in a silicate bonded interferometer, that technique does not allow any compensation, as it can be done with glue. The apparent advantage of glue is its long alignment times of several hours, allowing for strategies with long alignment and test procedures. For the

other techniques, the component has to be placed on an artificial ground (provided, for example, by a lens tissue or the chemical substance *octane*) during its pre-alignment. This ground can have a slightly different angle underneath the component than the final bond. Furthermore, for using glue, the surfaces of the components have to be slightly less polished, but no numbers are available on this topic.

One critical observation is the potential of some final creeps in the gluing layers, or changing alignments after some time in an evacuated vacuum chamber, as discussed in Section 2.4.2. More sophisticated investigations are necessary to make a comprehensive statement.

The gluing technique can evolve through a sophisticated control of the component angle. This would enable reducing the risk and uncertainties in the interferometer design, combined with the advantages of glue.

The best evaluation of the construction process is the operation of the experiment itself, as described in the following chapter. No influence of any of the mentioned problems (creep, degraded glue layer, or tilts) has been found to the present day. This is an essential conclusion because the first component was placed more than four years ago. The author believes that the glue technique is an excellent choice in a laboratory experiment without thermal cycling, based on the possibility of many test-runs, long alignment times during which the alignment properties like the contrast can be live tracked, and, so far, no critical disadvantage. In retrospect, the author would again decide to construct the 3BL based on UV-glue.

2.5 Conclusion
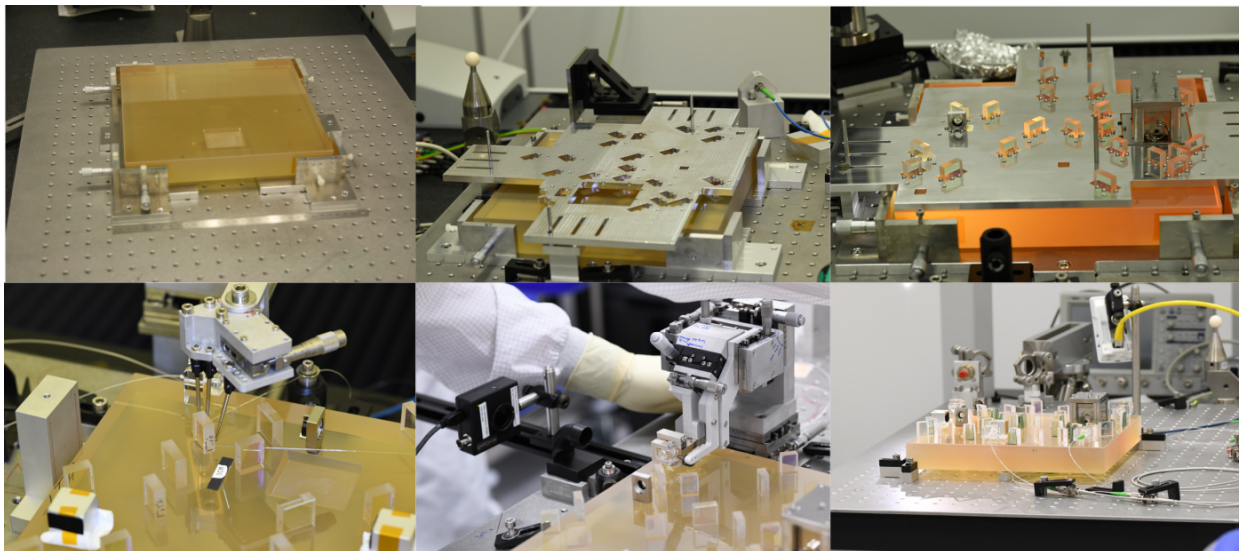
Fig. 2.22.: Photographs from the construction process illustrating the transmission between the blank optical bench with the trench for the *Faraday rotator* in the left upper corner to the completely assembled bench on the lower right side.

The challenge of constructing two optical benches, each containing four interferometers based on the same laser beam and two fiber couplings on each bench with an additional free-beam connection, requiring absolute beam overlap, was tackled in this thesis. The result is two completed benches that are assembled according to the design by [Isl18].

This chapter described the construction process, which is summarized in Figure 2.22, starting with

an empty optical bench which is assembled using the template, pointing fingers, and the BEAST for fios alignments to the finalized bench.

A new beam measurement technique, the CQS, was investigated and characterized for its uncertainty, stability, and agreement between several CQS. The CQSs provided an excellent CMM-based adjustment tool for precise beam alignment and measurements with an averaged uncertainty range of $\pm 3.02\,\mu\text{m}$ and angular measurements of $\pm 10.1\,\mu\text{rad}$. The further quality analysis concludes repeatability of about $1\,\mu\text{m}$, and stability below $5\,\mu\text{m}$ in all axes over several hours.

The CQSs were optimized for their use in the 3BL construction, but by further investigations, they can evolve to an even more sophisticated alignment tool. An alignment of collinear propagating beams with $1\,\mu\text{m}$ precision but without a CMM can be provided by a sophisticated grid characterization and the CQS.

With the discussed characterizations of contrast, coupling, and beam parameters, the construction of the 3BL was successful. Some parameters deviate from the simulated values as to be expected in such a complex interferometer, though their effect on the performance is estimated to be uncritical. The best characterization of the construction is the commissioning of the experiment itself, presented in the next chapter. When limiting noise sources appear in the measurements, it is advised to look at the construction details for possible explanations like the investigations of spurious beams in Section 2.4.4.

The process of UV-gluing components was investigated further by analysis of the components tilts towards the baseplate, which was concluded to be uncritical. The tilts were presumably the limitation of some construction parameters. One example is the height of the *fios2* ferrule, which is not adjustable, and the lens could only compensate for a vertical mismatch to achieve a coupling of about 50%. Future designs of optical benches can include these tilts in their simulations for further improvements. Sophisticated simulation of the 3BL could be repeated, including these tilts to test the understanding of the limited contrast. However, this is time-consuming and unnecessary as long as no construction-related limitation in the 3BL sensitivity is observed. Accordingly, the usage of glue is rated as a valid decision in retrospective.

Even though a second, identical version of the 3BL experiment is unlikely to be built, its strategies and technologies provide a valuable tool in varieties of interferometer alignment in the future. Strategies 1-5 in Sections 2.3.3-2.3.7 are described in an abstract way to make them applicable in future (quasi)-monolithic bench constructions with high complexity.

Three-Backlink Measurements

<div style="text-align: right; font-size: 3em;">3</div>

The optical benches for the 3BL were constructed to enable probing three Backlink implementations for their non-reciprocal behavior. The interferometric measurements on both benches each provide the phase information one-way through the Backlink. The non-reciprocity is extracted from their combination. Details and results of this process, including the non-reciprocal phase extraction, noise suppression, and analysis, are presented in this chapter.

After the finalized construction of the two 3BL-benches described in the previous chapter, they were integrated into a vacuum chamber. The experimental set-up is introduced, including the digital readout with a phase extraction device, commonly called a Phasemeter (PM). The data acquisition and evaluation of the measurements of the 3BL are introduced. The infrastructure was optimized with a Test-Interferometer (TIfo) prior to the 3BL implementation, and the results are presented. The first commissioning phase focused on the operation of the fiber Backlinks, including noise analysis and suppression. The implementation and optimization of the FBBL followed and enabled the complete operation of the 3BL - with all three Backlinks operating in parallel. A selection of the investigation and improvements of a full noise analysis is given, including the understanding of the remaining noise sources. Suggested strategies to reduce the noise in each frequency regime are included. The optimized non-reciprocity measurement and its interpretation for the three Backlinks' performances are given. They are followed by suggestions of measurements and investigations that can be done in the future to deepen the understanding of the LISA-Backlink.

Due to the scale of the experiment, the laboratory work was led by the author but carried out jointly with M. Ast, J.J.Ho Zhang (PhD student partly supervised by the author) and D. Jestrabek (master's student supervised by the author). Further support was provided by the other Backlink-team members at AEI; J.M. Rohr, M.J. Born, K. Rajasree, G. Heinzel, J. Reiche, the phasemeter team of T.S. Schwarze and C. Vorndamme, and the colleagues from the University of Glasgow, in particular D. Robertson and A. Taylor.

3.1 Experimental Set-up

The experiment requires a thermal and mechanical stable operation, provided by a vacuum chamber with temperature and vibration isolation. Furthermore, temperature sensors track the temperature environment. Many parts of this set-up were implemented already in a Pre-Experiment in 2016 [Isl18] and were completed and optimized in this thesis as described in Section 3.3.
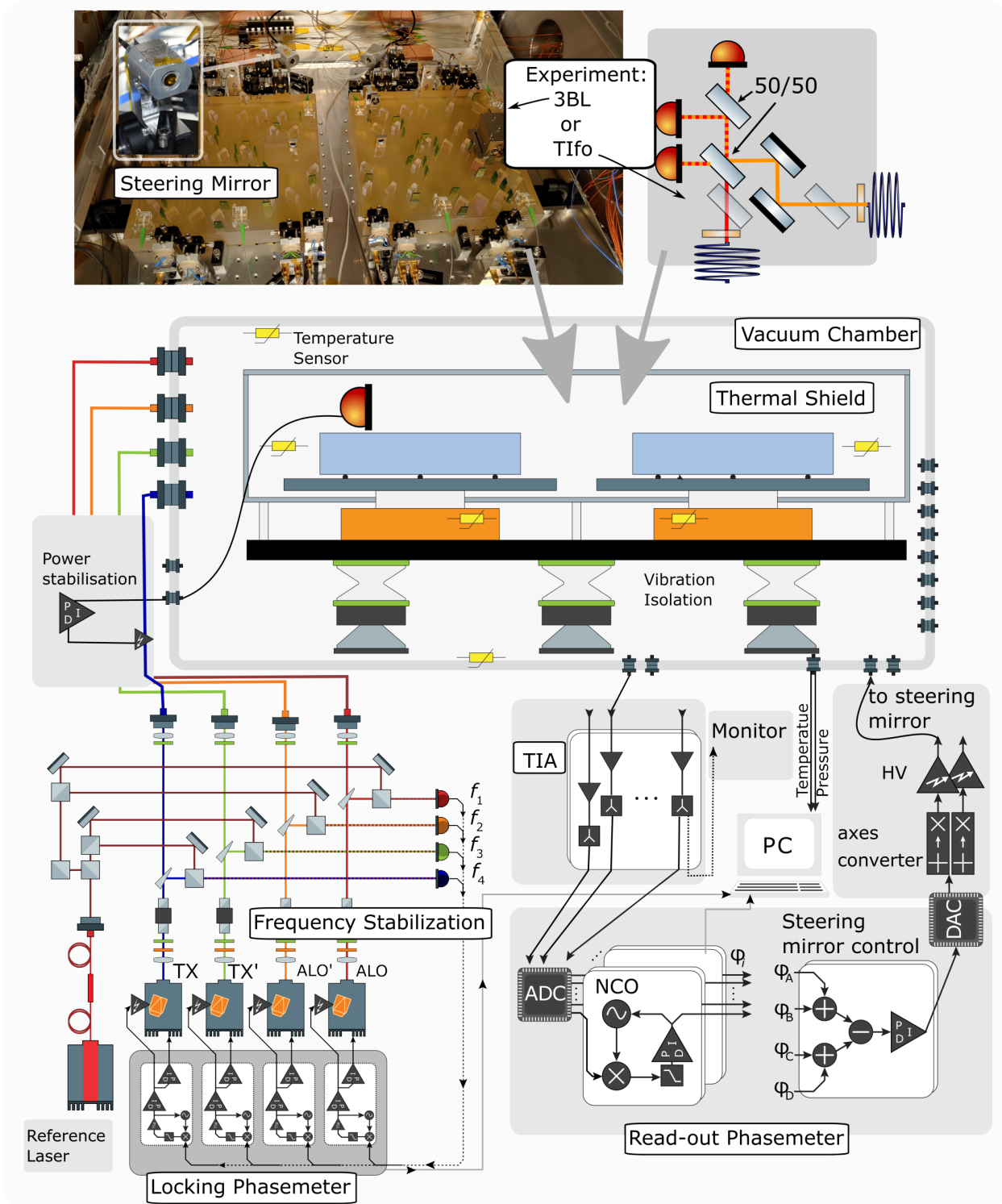
Fig. 3.1.: Overview of the experimental infrastructure, where first the TIfo and then the 3BL were implemented. The picture is a modified version of the related Figures 4.1, 4.4 and 4.8 in [Isl18].

3.1.1 Vacuum Chamber Infrastructure

The experiment integrated into the vacuum chamber and its infrastructure is shown in Figure 3.1. Both optical benches are placed on an aluminum breadboard, each holding the photodiode mounts. These breadboards are attached to the rotation stages that are placed centrally below them. Surrounding the experiment but excluding the rotation stages is a thermal shield made from aluminum wrapped in multilayer insulation foil. The rotation stages, URS50BPPV6 from Newport, are placed on a steel plate, isolated against vibration by vibration dumpers made from FKM (fluorocarbon-based fluoroelastomer materials). The vacuum chamber can be evacuated with the pre-pump *Pfeiffer Vacuum MVP 160-3* and to lower pressure levels around 10^{-6} mBar with the *Pfeiffer HiPace 700M Turbo Pump*. In the vacuum chamber, temperature sensors with a Positive Temperature Coefficient (PTC) resistor of the type PT10000 are distributed inside and outside the thermal shield. For thermal load reduction, the TIA of the PR are separated from the diodes. It is a modified version of the design *PD_khz_receiverBox_Backlink* by O. Gerberding, and placed outside the vacuum chamber. Most photodiodes are 1 mm diameter InGaAs LAPD-1-09-17-TO64 single element diodes. The control of the Free-Beam Backlink requires one Quadrant Photodiode (QPD) on each bench, the InGaAs GAP1000Q. The steering mirrors are the S-334 from Physik Instrumente. SEDs PC50 are used for observing the power levels of each laser used in the laser power stabilization. The analog control loop for this stabilization is the *modular servo* design by J. M. Rohr. A fiber-based variable optical attenuator (VOA) from OZ Optics is placed between the laser preparation and the feedthrough fiber and actuates on the passing power. The control loops use a P- and two I-stages for high and low frequencies.

As beamdump for the off-bench spurious beams, black foil is attached to the thermal shield at appropriate positions. This decision is discussed in Section 3.3.1.

Many parts of this infrastructure were already implemented in [Isl18] and were presented here for completeness.

3.1.2 Laser Frequency Locks

The 3BL requires four laser sources that are also shown in Figure 3.1. The frequency stability is required to be below $30\,\frac{\text{kHz}}{\sqrt{\text{Hz}}}$. This requirement assumes a maximal mismatch in the mirror-symmetry of both benches below 1 cm [Isl18]. Four NPRO *Mephisto* lasers by *Coherent* are operated in transponder mode and are stabilized to a common reference laser, a *Prometheus* laser by *Coherent*, which in turn is internally stabilized to an iodine cell. The stabilization was set up and characterized during the PhD thesis of K.-S. Isleif [Isl18] and the bachelor's thesis of the author [Bis15]. A Photoreceiver (PR) measures the heterodyne interference signal between each transponder laser and the reference laser. This signal is tracked by a digital Phasemeter (PM), which implements the feedback control loop of the laser frequencies in the digital domain.

The implementation enables the arbitrary choice of the beatnote frequency between the transponder lasers and the reference laser. It is set to

$$f_{\text{BN}} = 80\,\text{MHz}/2^4 + 80\text{MHz}/2^5 + n \cdot f_0 = 7.5\,\text{MHz} + n \cdot f_0$$

with a base frequency $f_0 = 80\,\text{MHz}/2^{13} \approx 9.8\,\text{kHz}$. The given constraints are caused by the readout phasemeter and are discussed in the next section. By choosing $n \in \mathbb{N}$ accordingly, the resulting BN between two stabilized transponder lasers can be easily adjusted. The 3BL is operated at kHz BNs, which enables the separation of PD and TIA of the PR and thus reduces the heat load inside the vacuum chamber. An observed influence of the chosen frequencies on the measurement is discussed in Section 3.4.1 and Section 3.7.1.

Locking Phasemeter

The locking phasemeter in the 3BL is called the **Ba**cklink-**Lo**cking PM (BaliLo), which was implemented by T.S. Schwarze and O. Gerberding. It uses an 80 MHz sampling clock that is synchronized with the readout phasemeter, described in the following section. The BaliLo's functionality can be explained in three steps:

The All Digital Phase-Locked Loop (ADPLL) tracks the digitized interference signal from the PR between the transponder laser and the reference laser. It is described with great detail in [Ger14] and serves here solely as a frequency sensor.

The piezo actuator lock is a control loop for frequency fluctuations in the kHz range of the laser. It takes the frequency tracked from the ADPLL and subtracts a reference value that the user sets. The difference serves as the error signal for the loop and is fed to the servo. The latter consists of two cascaded integrators. The gain of the individual integrators, I and II, can be set in steps of powers of two, and the overall gain can be fine-tuned with an additional multiplication factor. The resulting actuator signal is converted to an analog signal via DACs. This signal actuates the piezo attached to the laser crystal.

The gains of this loop have been optimized with two strategies (see Table E.1 in the Appendix). The systematic method measures the open-loop transfer function and aims for a phase margin of 25 deg. The other, more pragmatic version is increasing the gains until the system falls out of the lock and then using half that gain. The latter version resulted in much higher frequency stability and increased the UGF by about 1 kHz, but the phase margin reduced below 10 deg. The achieved UGFs are between 16-18 kHz and are comparable to the initial implementation in [Isl18].

The temperature lock interprets the piezo loop's actuator signal as an error signal. It is fed to the servo consisting of an integrator and finally drives the temperature of the laser's crystal via the DACs. It enables long-term stability of the overall laser frequency lock for a sufficiently tuned integrator gain. Without the temperature lock, the piezo actuator lock falls out of the lock typically after a few minutes.

3.1.3 Readout Phasemeter

The 3BL requires a readout phasemeter with a minimum number of 14 channels due to the necessity to read out 6x SEDs and 8x QPD-Segments. Additional 8 channels enable π-measurements and the post-correction via balanced detection (Section 1.2.1), where two PDs, one in each interferometer port, are required. Using QPDs in all interferometer ports in the future will require 64 channels in total. The PM needs to simultaneously extract the phase signal of five different frequencies in the kHz range, created by the four lasers, as mentioned in Section 3.1.2. The frequencies need to

(a) Plot of a CIC-filter with notches at frequency f_0. Figure based on a Figure by [Ris21].

(b) Phasemeter principle with the traces marking the IQ-demodulation (green) and the phase readout of the ADPLL implementation (orange). Figure based on a Figure by [Ris21].

Fig. 3.2.: The readout PM.

be sufficiently separated to reduce cross-coupling and distortions by harmonics. The choice was further constrained by the implemented CIC-filter in the readout PM, described in the following. The PM's readout noise has to be below the requirement of $1\frac{\text{pm}}{\sqrt{\text{Hz}}}$. The actuator signals for the FBBL require a DAC card with four channels to control both axes of the two mirrors of the FBBL. Finally, the PM needs to tolerate pathlength steps equivalent to about nine cycles, as these were observed during the step-wise rotation of the optical benches in [Isl18].

Two phasemeters are available that fulfill almost all of these requirements: A 16-channel phasemeter, called the **Ba**ckli**n**k-**R**ead-**o**ut PM (BaliRo), was used in the measurements presented in this thesis and prior in the Pre-Experiment [Isl18], [Isl+18]. In order to read out all interferometer ports the advanced **PM4** has been developed based on the BaliRo by the PM-team at the AEI and is described in [Ris21]. It currently has 32 channels and can be enlarged to track 64 channels. It includes all the features and requirements needed for the 3BL. It was originally commissioned during this thesis but is currently limited by strong cross-coupling between the channels. The investigation is explained in Appendix E.8.

An important element in the following explanation of the PM is a Cascaded Integrator-Comb (CIC)-filter, as shown in Figure 3.2a. It has a low-pass filter's shape and notches at frequencies f_0, which are implemented depending on the clock frequency f_{clock} by $f_0 = f_{\text{clock}}/2^{13}$ in the BaliRo and $f_0 = f_{\text{clock}}/2^7$ in the PM4. Its implementation in the FPGA is hardware-efficient [Ger14], and it is described in more detail, for example, in [Ris21].

Two readout schemes are implemented in the readout phasemeters, BaliRo and PM4: the first is an IQ-demodulation as introduced in Section 1.6. It is visualized in Figure 3.2b in the green traces. The input signal is split, mixed with the Numerical Controlled Oscillator (NCO), and filtered by a readout filter, here implemented by a CIC-filter. Its job is to low-pass second harmonics and other high-frequency components while performing decimation to a few Hz. The resulting I-

and Q-values enable the phase calculation according to Equation 1.6. This implementation is, for example, also used in the LISA pathfinder PM [Ger14]. Having a fixed NCO frequency and limited bandwidth, the IQ-demodulation is not capable of tracking the pathlength steps mentioned above. In the second scheme, the pathlength steps are tackled by a feedback loop for the NCO. As shown in Figure 3.2b in the orange trace, an ADPLL is implemented. The signal for the phase mixed with the NCO is filtered by a dedicated loop-filter, also implemented as CIC-filter. This architecture was chosen as a trade-off for efficient implementation and suppression of the second harmonics in the kHz range. While the envelope drops rather slowly, its suppression is maximized when the harmonics are at the frequency of one of the notches. This sets the aforementioned frequency constraints in Section 3.1.2. The influence on the chosen frequencies is discussed in detail in Section 3.4.1. The output of the CIC-filter is fed to the PI-controller. The gains of the integrator and the proportional stage, KI and Kp, respectively, have a fixed ratio of $Kp/KI = 2^{16}$ and can be set by a single parameter [Ris21], which will be called the *readout gain*. The control signal actuates the NCO's frequency to follow the frequency of the input signal. The controller signal is also accumulated and transformed to the phase measurement, called *phase offset*. Residuals of the Q value can be calculated, again according to Equation 1.6 and are stored in the *phase correction* term. The total readout *phase* consists of *phase offset + phase correction*.

The PMs can switch between both readout schemes for each channel individually. If the ADPLL is turned off, the servo output is set to zero and the *phase* and the *phase correction* are identical. For each channel, the *DC value*, the *heterodyne amplitude*, the *phase* and the *phase correction* are extracted by the phasemeter. Details about the included factors can be found in [Ris21].

The PM4 and the BaliRo use different ADCs with clock frequencies of 1 MHz and 80 MHz, respectively[1]. The sampling frequency and the frequency of the notches in the CIC-filter change accordingly; from a sampling frequency $80 \cdot 10^6 \,\mathrm{Hz}/2^{22} \approx 19 \,\mathrm{Hz}$ in the BaliRo and $10^6 \,\mathrm{Hz}/2^{16} \approx 15.3 \,\mathrm{Hz}$ in the PM4.

Free-Beam Backlink Control Loop

The control loop of the Free-Beam Backlink is implemented in both Backlink readout PMs. The operation of the FBBL requires two steering mirrors, shown in Figure 3.1, to ensure sufficient pathlength stability. They are controlled via a control loop based on Differential Wavefront Sensing (DWS). It is comparable to DPS, introduced in Equation 2.1. However, instead of comparing the power levels, an interfered beam is detected, and the phase contributions on both sides of one axis are compared. The DWS signal in the horizontal axis is calculated via the four quadrants labeled A-D by:

$$\mathrm{DWS}_{\mathrm{horizontal}} = \varphi_{\mathrm{left}} - \varphi_{\mathrm{right}} = (\varphi_A + \varphi_C) - (\varphi_B + \varphi_D) \tag{3.1}$$

This enables tracking the horizontal angle between two interfered beams on the QPD, and respectively for the vertical axis [Wan10]. The Phase Accumulator (PA) in Figure 3.2b carries the phase information for each channel. By combining these signals according to Equation 3.1, the DWS signals are extracted. The steering mirrors can be controlled in two axes each, requiring four control loops in total. The four DWS-signals for both sides and axes provide the error signals. They need

---

[1] The first iteration, the BaliRo, used an easily available 80 MHz ADC, while the PM4 was optimized further to the 3BL's needs.

to be decoupled and scaled to a mirror motion, as described in Section 3.5.1. Afterwards, they are fed to a servo, and the actuator outputs of the PM control them to zero. The steering mirrors use a coordinate system that is rotated by 45° compared to the system of the DWS signals. This mismatch is compensated by an analog circuit between PM and a high-voltage amplifier for the piezo-controlled mirrors, see also Section 3.5. The *DWS* values and the *actuator* and *error* signals are stored in files in the PC.

The FBBL has been integrated into a Pre-Experiment by [Isl18]. It was observed that the rotation of the benches induces significant phase jumps, which led to the implementation of the ADPLL scheme in the PM. In Section 3.5 the re-implementation and characterization of the FBBL in the 3BL are described.

3.2 Data Acquisition and Evaluation

The goal of the 3BL is to measure the non-reciprocity of the three Backlink connections. The basic principle and data evaluation of the related phase measurements are presented in the following.

3.2.1 Practical Measurement Description

The reciprocal behavior of the Backlink connections is extracted by comparing the phase measurements of the beams propagating through the Backlink in both directions. This phase information is gained by interference with a local beam, and its phase readout via a PM. Each interferometer has two accessible ports where the signal can be detected on a PD. Using both ports enables balanced detection and π-measurements in the data analysis but requires twice the amount of PM channels. The measurement in this thesis was performed with the BaliRo with 16 channels. Therefore, either two Backlinks with all their interferometer ports were operated or all three Backlinks simultaneously without the additional ports. While the latter is the goal of the 3BL to disentangle the non-reciprocities, the first is advantageous for noise analysis.

The data analysis was performed via *Matlab* and the LTPDA-toolbox, especially the *lpsd*-function for amplitude spectral densities. The phases of the measured signals are combined according to the calculations presented in the following to reveal the non-reciprocal phase noise. The measurements on each bench are referred to as "L" for "left" and "R" for right, based on a front view into the vacuum chamber and as in Figure 1.11.

3.2.2 Non-Reciprocity Extraction

The phase measurements on both benches are combined for the non-reciprocity extraction, as derived in Chapter 1 for each Backlink. For the DFBL, the phase readout of the PDs on the left side $\varphi_{\text{DFBL-L}}$ is summed up with the one on the right side $\varphi_{\text{DFBL-R}}$, resulting in the combination $\varphi_{\text{DFBL-L}} + \varphi_{\text{DFBL-R}} = \Phi_{\text{DFBL}}$. A similar term is extracted in the FBBL and subtracting both Φ-combinations from the two different Backlinks results in:

$$\text{non-rec}_{\text{DFBL\&FBBL}} := \Phi_{\text{DFBL}} - \Phi_{\text{FBBL}} = \varphi_{\text{non-rec}}^{\text{DFBL}} - \varphi_{\text{non-rec}}^{\text{FBBL}} =: \text{DFBL\&FBBL}. \qquad (3.2)$$

The notation DFBL&FBBL is used in the plots in this chapter and includes the $\varphi_{non-rec}$ for both Backlinks combined in one data set. It consists of physical non-reciprocal effects inside the fiber, backscatter that appears as non-reciprocal noise, and additional noise terms. The plotted dataset is therefore the combination of non-rec$_{\text{DFBL\&FBBL}}$ and noise. The goal of the following sections is to identify and reduce the noise so that the fundamental non-reciprocity effects of the Backlinks can be uncovered.

Combining the phase readout of the single interferometer channels differently reveals more information about the noise in the experiment. The phases on the left and right bench can be subtracted instead of summed up, and this combination is called the σ-combination. In this combination, the ν terms from the optical pathlength in Equation 1.10 do not cancel but appear twice, providing the opportunity to measure the LFN coupling in each interferometer. Furthermore, the collected phase in each Backlink direction is summed up; thus the pathlength noise of the Backlink, l_{DFBL}, is included in the σ-combination:

$$
\begin{aligned}
\varphi_{\text{DFBL-L}} - \varphi_{\text{DFBL-R}} &= -2\tilde{\nu}(\Delta\tau_{\text{DFBL}}) - (\varphi_{\leftarrow} + \varphi_{\rightarrow}) \\
&= -2\tilde{\nu}(\Delta\tau_{\text{DFBL}}) - l_{\text{DFBL}} =: \sigma_{\text{DFBL}}.
\end{aligned}
\tag{3.3}
$$

Similar combinations can be extracted for the FBBL and FSFBL, as presented in detail in [Isl18].

The measurements are evaluated over the interesting frequency range for LISA of $0.1\,\text{mHz}$ to $1\,\text{Hz}$ and additionally up to $10\,\text{Hz}$, limited by the sampling frequency of the PM. In the LISA range, the requirement is given by a displacement noise of $1\,\text{pm}/\sqrt{\text{Hz}}$ and the noise shape function:

$$
\text{req}(f) = 1\frac{\text{pm}}{\sqrt{\text{Hz}}}\sqrt{1 + \frac{(2.8\text{mHz})^4}{f^4}}.
\tag{3.4}
$$

The corner frequency of $2.8\,\text{mHz}$ is an outdated value, like also used in [Isl18] and in the plots in this chapter. The requirement has changed to a more conservative one with a corner frequency of $2.0\,\text{mHz}$ [AS+17]. The measurements presented in this chapter focus mostly on the high and center frequencies, and the requirement is not reached in the low frequencies with either noise shape curve. The $1\,\text{pm}$ displacement is equivalent to a phase of approximately $6\,\text{µrad}$ for the wavelength $1064\,\text{nm}$. This phase requirement is used in this chapter because the phase is the direct outcome of the measurements.

In measurements with only two Backlinks, like in the following Section 3.4, the non-rec$_{\text{DFBL\&FSFBL}}$ shows that either; a) both Backlinks are equally good or limited by the same source, or b), one Backlink is limiting the combined measurement, and the other one lies below it.

The disentanglement of the two cases is not possible; thus, the measurement has to be interpreted as the limitation for both. Only comparing all three combinations makes a statement of the single performance possible. Again, they can be limited by the same source or coupling (like in Subection 3.6.1) or limit each other in different frequency ranges (like in Subsection 3.10). This possibility for disentanglement is the essential design choice of the 3BL. It enables studying the different noise couplings in each Backlink. As discussed later in this chapter, this approach worked well and is an essential tool in noise analysis.

3.3 Noise Floor Investigations

Prior to the commissioning of the 3BL the noise floor of the infrastructure was analyzed and optimized in the master's thesis of D. Jestrabek [Jes22] under supervision by the author. After evaluating different beamdump options, a simple test interferometer, introduced in Section 3.3.2 was built, and so-called split measurements that probe the noise floor were performed. These investigations were performed in parallel to the construction of the benches in the cleanroom. The aim was to optimize the infrastructure and reduce the required time for commissioning the 3BL after its construction finalization. Many practical preparations like cable installation and re-commissioning programs like the readout for temperature and pressure have been done but are not presented here. An overview of the achieved noise floor in the split measurements is presented in Section 3.3.3 and two noise optimizations, the II-gain influence, Section 3.3.4, and the oscillations on the DAC card, Section 3.3.5, are presented.

3.3.1 Beamdumps

While the beamdumps on the optical benches, here referred to as beamstops, have been tested for their suitability for a few mW in [Isl18], a different solution is necessary for the light that is leaving the optical bench at the attenuators with a reflectivity of 95%. Powers of about $304\,\mathrm{mW}$, and $152\,\mathrm{mW}$ are dumped, respectively, behind *fios1* or *fios4* on each bench in full-power operation. Three different available beamdumps have been compared in [Jes22] under the requirement of low backscatter in the nominal beam and good thermal heat distribution: The standard beamdump used at the AEI, which is a bend copper tube that is painted black, a snail design by the University of Glasgow (the *Spiral Beam Dump* by M. Perreur-Lloyd), and a black foil from the company *Acktar*. Pictures are presented in the Appendix E.1, and more details about the measurement can be found in [Jes22]. The backscatter ratio under an angle of zero degrees was lowest for the standard tube beamdump ($3{\cdot}10^{-6}$) and similar for the *Acktar* foil ($5{\cdot}10^{-6}$). The snail design had a backscatter ratio of about $23 \cdot 10^{-6}$ of the incoming light and was thus discarded as a candidate.

Temperature measurement in vacuum of the standard beamdump absorbing $200\,\mathrm{mW}$ over three hours showed a temperature increase of about $4.5\,°\mathrm{C}$. Dissipating this heat inside the thermal shield is not trivial. Better temperature distribution is expected when the *Acktar* foil is used and glued directly onto the thermal shield. This approach is counter-intuitive to the typical goal of the thermal shield. However, it was concluded to be the best trade-off between a feasible and thermally sufficient solution.

The measured backscatter values allow estimating the influence of the beamdump on the non-reciprocal phase measurement in the 3BL. Backscattered light at the beamdump will propagate back to its origin fios, scatter in its fiber, and enter the interferometer where it interferes with the other nominal beam. The resulting phase error can be estimated with Equation 1.7:

$$\varphi_{\mathrm{error}}^{\mathrm{beamdump}} = \sqrt{\frac{\mathrm{P_{TX}} \cdot 0.95 \cdot \mathrm{BD_{sc}} \cdot 0.95 \cdot \mathrm{fiber_{sc}} \cdot 0.05}{\mathrm{P_{TX}} \cdot 0.05}} \cdot \sin(\Delta\varphi) \tag{3.5}$$

by including the numeric values for the initial power of the TX-beam $\mathrm{P_{TX}}$, the scatter value of the *Actar* beamdump $\mathrm{BD_{sc}}$, and the backscatter value of the fiber $\mathrm{fiber_{sc}}$. The latter is assumed

(a) Three types of split measurements: a) π-measurement, b) optical split and c) electrical split. The points of splitting are marked in red.

(b)
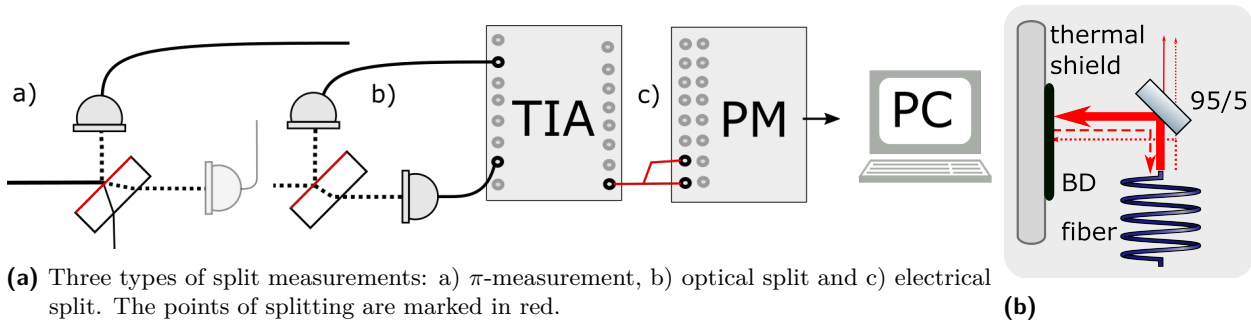
Fig. 3.3.: a) Split measurements. b) Backscatter at the beamdump enters the interferometer after being scattered again at the fiber.

to be $7\,\mathrm{ppm/m}$ for the $12\,\mathrm{m}$ feedthrough fiber, as discussed in Section 1.2.3. An approach for estimating $\Delta\varphi$ is based on the expansion of the thermal shield to where the *Actar* foil is attached to. Temperature noise $\tilde{t}$ were measured inside the vacuum chamber (see Section 3.9.1) and can be transformed to a length change Δl in the path of the backscatter. The $\mathrm{CTE_{Alu}}$ of aluminum and the thickness of the thermal shield d are combined to: $\Delta l = d \cdot \mathrm{CTE_{Alu}} \cdot \tilde{t}$. This is transformed further to a phase change with $\Delta\varphi = \Delta l \cdot 2\pi/\lambda$. The resulting noise curve is shown in Appendix E and is several orders of magnitude below the requirement. Conclusively, the backscatter from the beamdump that re-enters the interferometer after scattering at the fios is considered uncritical under this aspect for the 3BL measurements.

3.3.2 Test-Interferometer Measurements

A simple Test-Interferometer (TIfo) as shown in Figure 3.1 was built to investigate and optimize the noise floor prior to finalizing the 3BL construction. It uses two of the frequency-stabilized lasers that are interfered at a kHz BN and detected on PDs. The TIfo was later equipped with more bs to change the power ratios to 3BL-like levels and provide a specific power level for the laser power stabilization simultaneously. Electrical- and optical-split, and π-measurements tested the PM and the chain of PDs, cabling, and TIA boxes. These measurements are described in the following subsections.

Additionally, this set-up was used during the master's thesis by I. Rischkopf to perform the first optical tests with the PM4 [Ris21].

3.3.3 Split Measurements

Three types of so-called split measurements were performed to investigate the noise floor along the measurement chain, depicted in Figure 3.3a. The first one is the **electrical split measurement:** for investigations of the noise in the PM channels, an electrically or optically generated electrical signal is split, and the two identical signals are fed into two channels of the PM. When subtracting the two measured phases, only the PM channels' noise remains. This was done for the channels of the BaliRo, confirming that the phasemeter's readout noise is below the LISA requirement, as visualized by one representative measurement in Figure 3.4a.

The optical split measurement works with the same approach, but the splitting point is shifted to a bs splitting the interfered signal. The two identical optical signals are measured each on a PD.
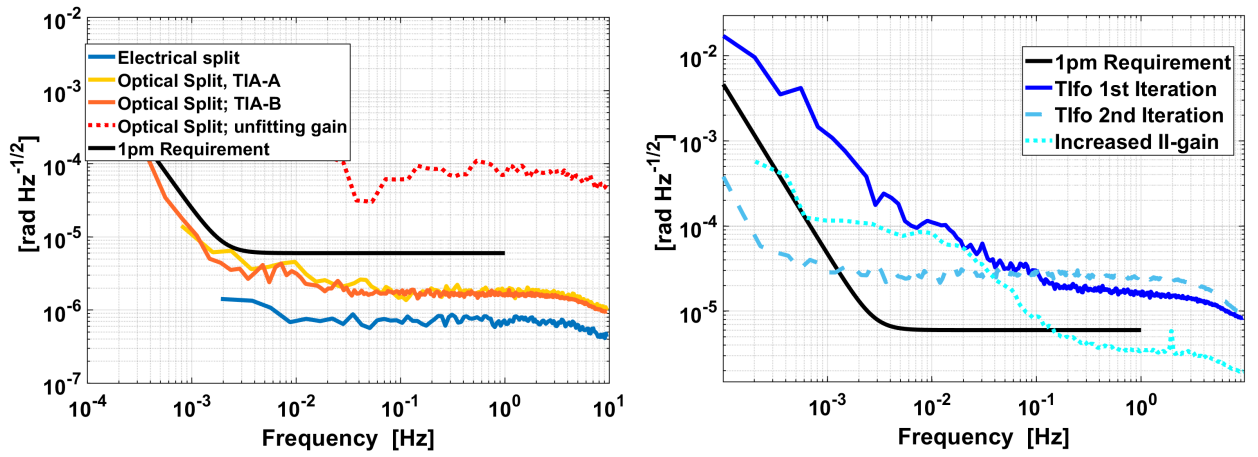
(a) The electrical and optical split measurements for both TIA boxes are shown with one representative measurement each. One optical split measurement with an unfitting *readout gain* setting is shown as demonstration.

(b) π-measurements in the first and second TIfo iterations. The noise level at low frequencies is reduced and slightly increased at high frequencies in the second iteration. A higher II-gain decreases the level below the requirement above 0.1 Hz but increases it at lower frequencies.

Fig. 3.4.: Noise floor investigations in the TIfo with split and π-measurements measured against the 1pm-Requirement.

Again, two ideally identical signals are measured in two channels. Any residual noise after their subtraction is caused by the chain of PDs, cables, and TIAs. Representative measurements also show the results in Figure 3.4a for two TIA boxes, TIA-A and TIA-B. These measurements were performed with the ADPLL scheme of the PM, and the importance of a correctly chosen *readout gain* is apparent by the performance violation shown in red dots that is caused by an insufficient gain setting.

The next step in the noise floor investigations is the π**-measurement** that was described in Section 1.2.1. At the interfering beamsplitter, the two ports have a phase shift of π based on energy conservation, and the AC-signals cancel when they are added up. Different noise sources do not experience this π-shift and stay as residual noise. The measurement results are shown in Figure 3.4b for both iterations of the TIfo, and an improvement in the second iteration is visible. A potential cause is the polarization control that was implemented via polarizers right behind the fibers in the second iteration. A further improvement is reached by increasing the II-gain, as described in the next section.

It should be noted that observation after the 3BL implementation suggests cross-coupling in the PM when additional signals are connected, and electrical split measurements were repeated in Section 3.8.5.

3.3.4 II-gain in the Laser Frequency Locks

Figure 3.4b shows how the π-measurements are influenced by the II-gain of the piezo actuator lock in the laser frequency stabilization. The gain settings were chosen based on the two different gain adjustment strategies discussed in Section 3.1.3. The higher frequency stability found by the pragmatic strategy reduces the noise in the π-measurements below the requirement above 0.1 Hz.

At the same time, the noise in the lower frequency range is increased. This behavior can be caused by the coupling of a spurious signal as a small phasor, as presented in Section 1.2.1. The changing dynamics in the frequency stabilization change the phasor's behavior and, thus, the noise's shape. However, there are various possible origins, and the exact coupling mechanism, which is often non-linear, is unknown. Since the optical set-up was about to change with the 3BL implementation, this noise was not further investigated.

The shape of the π-measurements with increased II-gain looks similar to later observed π-measurements in the 3BL, see Figure 3.20b. This indicates that the optical set-up (TIfo or 3BL) is not the source of this noise. Instead, it is potentially related to the laser frequency stabilization.

Noise sources in π-measurements can be, among others, related to spurious beams in the optical set-up. Since this was about to change by implementing the 3BL, the π-measurements were not optimized further, and the noise floor presented in Figure 3.4a was concluded to provide a sufficiently prepared infrastructure for implementing the 3BL.

3.3.5 Oscillations on the BaliLo's DAC-Card

Most preparation measurements operated with a 39 kHz BN because the same was used in the Pre-Experiment. During the early noise hunt, this BN appeared to be distorted. Spectrum analysis of the PR signal before the BaliRo revealed several peaks at around 40 kHz and multiples. These were found to be originating from sidebands in the optical interference. These sidebands were imprinted by the BaliLo, caused by oscillations in the Digital-to-Analog Converter (DAC) card, likely by the operational amplifiers. As a solution, the card was exchanged for one of the same type (design *FMC_DAC* by O. Gerberding) but with different capacitors and operational amplifiers, provided by C. Vorndamme. The kHz oscillations were removed at the cost of additional MHz oscillations. With a low-pass filter, these MHz peaks vanished, and the resulting BN is free from the sidebands.

With the here summarized preparation, the infrastructure was concluded to be ready to implement the 3BL's benches. More details about the infrastructure improvement can be found in the master's thesis by D. Jestrabek [Jes22] that was supervised by the author.

3.4 Commissioning of the Fiber Backlinks

The two fiber Backlinks were commissioned first because of the Free-Beam Backlink's higher complexity in commissioning (described in Section 3.5). Figure 3.5 shows the two benches placed on the aluminum breadboards. The light from the laser preparation is connected to the TX-fibers with mating sleeves via the feedthrough fiber. Both fiber surfaces were cleaned and inspected with a fiber microscope to prevent fiber damage. The PD signals travel through a vacuum feedthrough to the TIA box, the PM, and then to the PC. This section describes the first non-reciprocity measurements from this Backlink combination and a selection of applied noise hunting methods and conclusions.

The first measurement of the non-reciprocity of the two fiber Backlinks is shown in Figure 3.6 in green dashed lines and optimized by adjusted *readout gains* to the dotted curve. This is limited
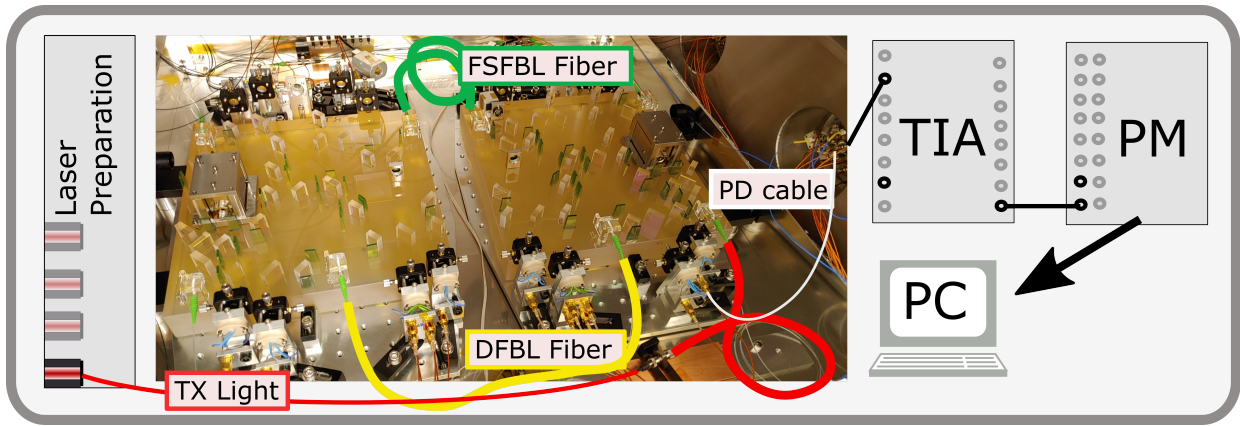
Fig. 3.5.: Integration of the fiber Backlinks. Laser light coming from the laser preparation is injected to the bench via the fios, exemplary shown for the TX-light. Both Backlink fibers are marked. One PD cable is exemplary processed through TIA and PM to be analyzed in the PC.

by a white noise level just below $10^{-4}\,\mathrm{rad}/\sqrt{\mathrm{Hz}}$ which is equivalent to $17\,\mathrm{pm}/\sqrt{\mathrm{Hz}}$ at frequencies above $0.1\,\mathrm{Hz}$. It is discussed in the next section. An increasing noise level is dominant below $0.1\,\mathrm{Hz}$, presumably dominated by effects caused by the air in the non-evacuated vacuum chamber in these measurements. The Φ-combination is shown in red for the DFBL and is above $0.1\,\mathrm{rad}/\sqrt{\mathrm{Hz}}$ in the relevant frequency range, illustrating the necessity of the reference subtraction by the second Backlink.

3.4.1 Beatnote Frequencies

Five different Beatnote (BN) frequencies appear in the 3BL. They are created by the different locking offsets of each transponder laser to the reference laser in the frequency stabilization, as described in Section 3.1.2. Figure 3.7a illustrates the beatnote creation in the different interferometers. By interfering the TX- and TX'-beams, which both have an offset f_1 and f_2 to the reference laser respectively, the difference frequency $f_{12} = f_1 - f_2$ arises. This frequency is used in the DFBL and FBBL. All interferences involved in the FSFBL are at a different frequency and different from the one used in the DFBL. Therefore five different beatnote combinations created from four laser frequencies are present in the 3BL and are listed in Table 3.1, as multiples of the basic frequency $f_0 \approx 9.8\,\mathrm{kHz}$. By combining all four frequency offsets f_1-f_4, the three multiples a, b and c can be chosen freely and the remaining factors are constrained by $d = b - a$ and $e = c - a$. Only multiples of f_0 are used for placing the harmonics in the notches of the CIC-filter, maximizing the suppression of higher harmonics in the PM, see Section 3.1.3.

A frequency set with the multiples (1,4,6,7,10,11) (for (a,f,d,b,e,c)) was suggested by [Isl18] and implemented first, but yielded a bad performance. Figure 3.7b shows the non-reciprocity measured for three additional frequency sets. Set C has a very high noise level, and its shape is comparable to the single channel phase measurements, suggesting insufficient common mode suppression between the Backlinks. Set B and D have a white noise shape above $0.1\,\mathrm{Hz}$ and set D with only even multiples performed best, at $4 \cdot 10^{-5}\,\mathrm{rad}/\sqrt{\mathrm{Hz}}$. The noise level depends on the chosen frequencies in the interferometers.

Since the FSFBL&DFBL combination involves all five frequencies to derive the non-reciprocity, detailed analysis and a flexible change of the single beatnotes was impossible. The later Section 3.7.1
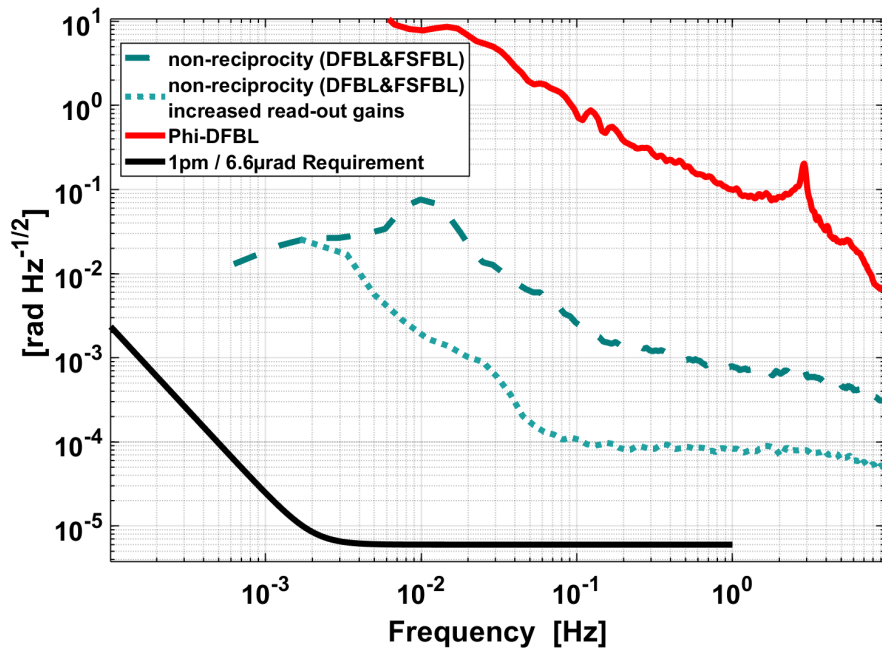
Fig. 3.6.: First measurement of the two fiber Backlinks in the 3BL and their combined non-reciprocity. DFBL without reference, meaning without FSFBL subtraction, is shown in the red curve to illustrate the importance of a reference. The following figures omit the term 'non-reciprocity'.
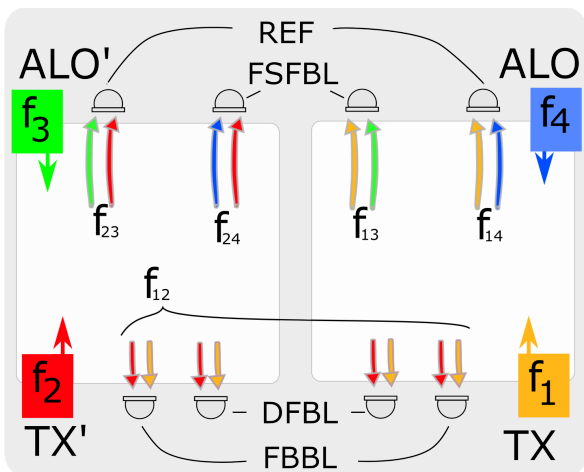
(a) Schematic of the four lasers creating five BN frequencies in the 3BL Experiment.
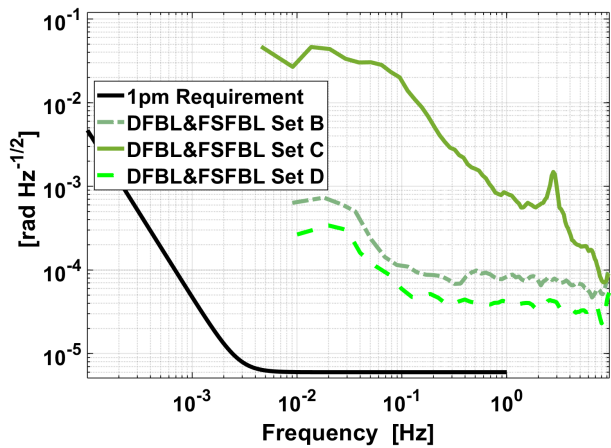
(b) Three different frequency sets. Set C including uneven multiples is performing worst while set D brings the best improvement.

Fig. 3.7.: Frequency sets as multiples of f_0: set B: $(4,6,8,10,12)$, set C: $(3,5,12,2,7)$ and set D: $(2,10,14,8,12)$.

discusses the further analysis of this correlation between beatnote frequency and noise based on measurements performed with the DFBL and the FBBL, that enable the operation with a single interference frequency.

	TX	TX'	ALO	ALO'
TX	-	$a \cdot f_0$	$b \cdot f_0$	$c \cdot f_0$
TX'	TX-TX'	-	$d \cdot f_0$	$e \cdot f_0$
ALO	TX-ALO	TX'-ALO	-	$(f \cdot f_0)$
ALO'	TX-ALO'	TX'-ALO	TX'-ALO'	-

(a) Combinations of the frequencies

TX-TX'	19.5 kHz
TX-ALO'	97.7 kHz
TX-ALO'	136.7 kHz
TX'-ALO	78.1 kHz
TX'-ALO'	117.1 kHz

(b) Example frequencies

Tab. 3.1.: Beatnote frequencies in the 3BL as created from the frequencies of the involved lasers (TX, TX', ALO and ALO'). The example frequencies for set D are given.

3.4.2 Set-up Optimization

Laser Frequency Locks

After implementing the laser frequency locks in [Isl18] and further optimization with the TIfo, the fiber Backlinks enable testing them in a pm-precise experiment. This reveals residual limitations in the laser frequency locks. They are sensitive to external noise sources like vibrations, for example, caused by the energetic usage of the laboratory doors. This was decreased by M. Ast and J.J. Ho Zhang by locating the mode-hop regions of the lasers and choosing operation points sufficiently far apart.

Readout Gain Setting

The gain of the readout ADPLL in the BaliRo, the aforementioned *readout gain*, depends on the amplitude of the input signal and can be set for each channel individually. For an insufficient gain setting, the phase readout becomes noisy, and the performance is distorted, as significantly visible in the first measurements shown in Figure 3.6. As the laser power naturally determines the input amplitude, a drift in the power level also causes gain changes. Stabilization of the laser's power is thus required for stable long-term measurements. It was implemented for the measurements with all three Backlinks, discussed in detail in Section 3.8.2.

Power Levels

The absolute power levels were not observed to influence the current state, and the 3BL is operated with TX-powers of 40 mW and ALO powers of 20 mW. Compared to the initial design powers of 320/180 mW in [Isl18], lower powers are preferred if it causes no disadvantage. It reduces the thermal load caused by the nominal 95% dumped on the beamdumps and any spurious beam. Low power reduces the danger of damaging a contaminated surface, for example, if a fiber connector is not perfectly clean. Besides a resistor change in the TIA box, it is easy to increase the powers if necessary in a later stage of the noise analysis.

Phase Drifts

The timeseries of the phase readout for each interferometer port show a drift, which typically points to a difference between the optical frequency and the readout frequency set by the user in the BaliRo. The expected optical frequency is extracted from the frequencies set by the user in the BaliLo. The actually created frequency deviates slightly by the phasemeter resolution, that is by design $80\,\mathrm{MHz}/2^{32} \approx 0.0186\,\mathrm{Hz}$. This has not been identified as a performance-limiting problem to the point of writing. This deviation is more severe for a less tight lock, as shown in Appendix E.4.

3.4.3 π-Measurements

Extracting the sources and couplings of noise to the non-reciprocity measurements is challenging because six interferometers are combined to extract non-rec$_{\mathrm{DFBL\&FBBL}}$. π-measurements probe each interferometer separately and support uncovering if the problem is caused by a particular laser, channel or Backlink. They are thus an important diagnostics tool. π-measurements require two PDs per interferometer, and because of limited PM channels, they can be performed simultaneously only with two operating Backlinks. The π-measurements of DFBL and FSFBL are shown in Figure 3.8a jointly with non-rec$_{\mathrm{DFBL\&FSFBL}}$. The π-measurements in the FSFBL-R and the REF-L show that achieving the pm-performance in the π-measurements is feasible. In all other interferometers, the requirement is exceeded, and the noise increases towards lower frequencies. The two DFBL π-measurements noise curves cross the requirement around $0.5\,\mathrm{Hz}$ and behave both very similarly. Their interferometers are operated with the same lasers and beatnotes. In the other interferometers, different laser combinations and beatnotes appear. No evidence was found that the different noise levels in the π-measurements relate to the chosen beatnote frequencies. The PM performance was tested in the TIfo measurements but can potentially see more cross-coupling effects in the 3BL caused by the increased amount of signals and frequencies. Other potential sources are the PDs and their cables, which have been tested by a small representing number in the TIfo measurements. Figure 3.8b additionally shows the π-measurement taken in the TIfo, Section 3.3.3, fitting well with the DFBL-R π-measurement. Accordingly, their noise seems independent of the optical interferometer (3BL or TIfo) and potentially comes from the lasers. This agrees with the different shapes for all FSFBL and REF interferometers. Varying performances in the laser frequency stability were observed and are still part of an ongoing investigation, as discussed later in Section 3.8.6.

3.4.4 Conclusion of the Fiber Backlink Commissioning

The optimized performance curve in this noise suppression iteration is presented in Figure 3.8a, and the focus lies on the high-frequency end. The first measurement with a noise level of about $1\,\mathrm{mrad}/\sqrt{\mathrm{Hz}}$ was improved by one order of magnitude by adjusting the *readout gains* properly. It was further reduced to $40\,\mathrm{\mu rad}/\sqrt{\mathrm{Hz}}$ which is equivalent to $6\,\mathrm{pm}/\sqrt{\mathrm{Hz}}$ by changing the frequency set. Further dependency on the laser frequency lock's quality became apparent. The absolute laser power level has no influence at the current state.

Diagnostic π-measurements below the requirement were taken in the experiment. They suggest a dependence on the laser frequency locks, and further optimization is necessary. The optical
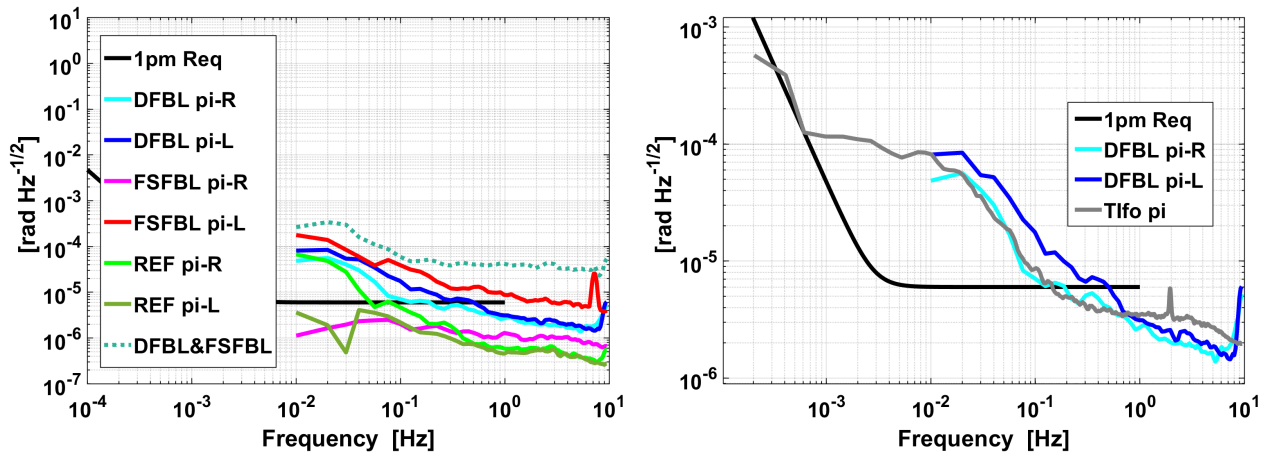
(a) π-measurements and non-reciprocities for the DFBL&FSFBL combination after the first noise suppression iteration.

(b) π-measurements of the DFBL compared to TIfo measurements. They have a common shape and comparable noise levels.

Fig. 3.8.: Non-reciprocity improvement and π-measurements for the fiber Backlinks. The peaks above $1\,\mathrm{Hz}$ are still under investigations and presumably related to the laser frequency locks.

set-up was concluded not to limit the π-measurements at the current state. Since the choice of the frequency set is a dominant parameter, the FBBL provides an excellent additional diagnostic tool because DFBL and FBBL operate at the same frequency. The next obvious step in the noise analysis is thus the commissioning of the FBBL, described in the following section.

3.5 Commissioning of the Free-Beam Backlink

The FBBL's implementation is illustrated in Figure 3.9 where the two steering mirrors exchange the light between the benches. Their interference with the local beam is tracked with a QPD. Its signal is sent to the PM after being transformed to a voltage with a TIA. The actuator signal, generated inside the PM, is aligned to the axis of the mirrors with an axis-rotation-stage and then given to the HV amplifiers that control the steering mirrors.

Even though the Free-Beam control loop operated in the Pre-Experiment [Isl18], it had to be re-installed and adapted to the new set-up. Its commissioning included the alignment of the steering mirrors, the determination of the coupling coefficients (Section 3.5.1), and the fine-tuning of the loops. This is presented in the following sections and in more detail in [Jes22]. Further characterizations include the performance of the DWS compared to a requirement based on the construction results in Section 3.5.2. The benches were not rotated, but the steering mirrors, which are placed in aluminum mounts on the aluminum plate, still require the control loop for sufficient stability.

3.5.1 Coupling Coefficients

The position of the steering mirrors is controlled in a closed-loop control system implemented in the PM. As sensors, two QPDs are used whose DWS signals are controlled to zero. This ensures two counter-propagating beams along the FBBL, according to the construction in Section 2.3.7.
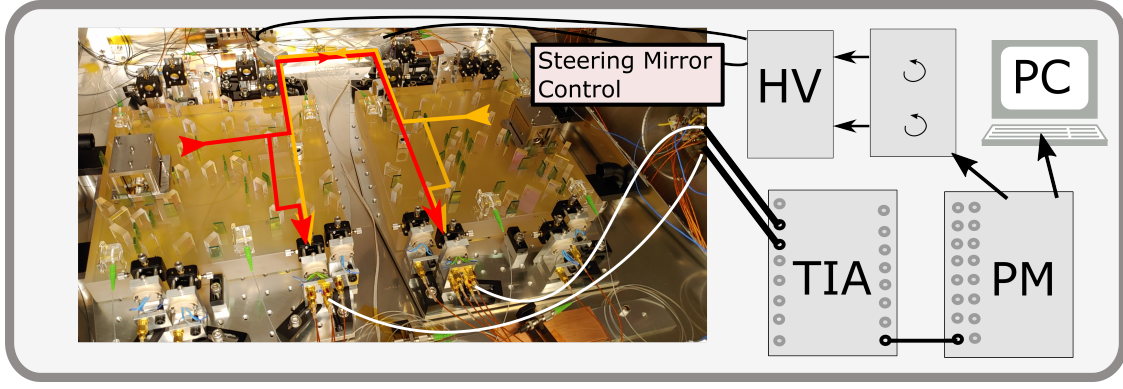
Fig. 3.9.: Integration of the Free-Beam Backlink. Light between the benches is exchanged with steering mirrors shown in the back and interfered on QPDs shown in the front. After processing with the TIA, the actuator signals are given from the PM to an axis transformation before they are input to the high voltage amplifiers (HV) which control the steering mirrors.

The translation between the movement of the four mirror axes to the four DWS values can be expressed with a coupling matrix K_{hh} with entries K1-K4. For horizontal mirror movements x_i and the DWS horizontal axis:

$$\begin{pmatrix} \text{DWS}_{\text{horizontal, L}} \\ \text{DWS}_{\text{horizontal, R}} \end{pmatrix} = \begin{pmatrix} K1 & K2 \\ K3 & K4 \end{pmatrix} \cdot \begin{pmatrix} x_{\text{L}} \\ x_{\text{R}} \end{pmatrix}. \tag{3.6}$$

And similar to the vertical axis with vertical motion in K_{vv} and the cross-coupled motions in K_{hv} and K_{vh}. Only K_{hh} and K_{vv} are integrated into the control loop. Lenses in front of the QPDs provide sufficient disentanglement between the different axis, as simulated in [Isl18]. The coupling coefficients are determined by exciting all four axes of the two control loops and observing the response of the four DWS signals on the two benches. Each axis is excited with a different frequency, and the DWS signals are demodulated accordingly. The coupling between each mirror axis to each DWS signal is determined and the reached coupling coefficient matrices K_{ij} found in [Jes22] are listed in Appendix E.5. Their absolute values are smaller than in the Pre-experiment [Bis18], which is caused by the changed geometry: the two optical benches are integrated into the vacuum chamber with switched orientation compared to the design by [Isl18]. This was done to increase the distance between the two strong magnetic fields of the Faraday rotators and reduce the effects or attraction between the magnets. Accordingly, the FBBL geometry is changed, resulting in a shorter pathlength, and the DWS response to the same mirror tilt is reduced. This differs from the original simulations but did not appear to cause a problem in the implemented control loops.

The quality of the decoupling between the axis is described by the condition number of each matrix, calculated with the maximal and minimal eigenvalues λ of K_{ij}:

$$cond(\text{K}_{ij}) \geq \frac{\|\lambda_{\text{max}}(\text{K}_{ij})\|}{\|\lambda_{\text{min}}(\text{K}_{ij})\|}. \tag{3.7}$$

[Isl18] simulated condition numbers of $cond(\text{K}_{\text{hh}})$=5.7 and $cond(\text{K}_{\text{vv}})$=5.4 for the horizontal and vertical axis. They were surpassed in the Pre-Experiment by measured values of $cond(\text{K}_{\text{hh}})$=3.4 and $cond(\text{K}_{\text{vv}})$=3.5 [Isl18]. In the current 3BL optimization, the $cond(\text{K}_{\text{hh}})$=5.07 and $cond(\text{K}_{\text{vv}})$=4.45 are slightly smaller than the simulation, indicating a better decoupling. The condition numbers depend on the beam radius on the QPD, and thus the position of the lenses [Isl18]. Presumably,
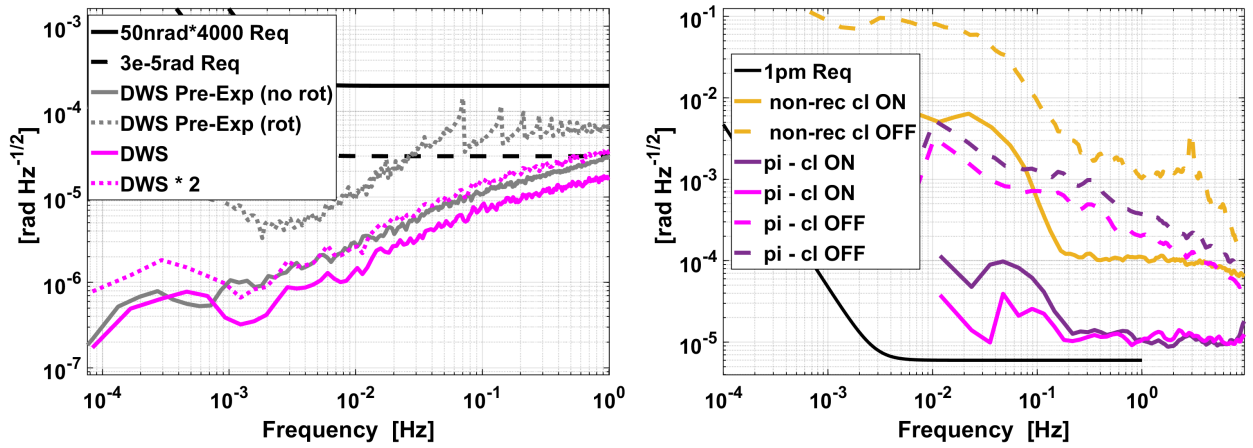
(a) DWS spectrums in the FBBL implementation lie underneath the original and the conservative requirement. Measurement from the Pre-Experiment with (rot) and without rotation (no rot) are shown and their ratio is used to scale a current measurement for estimating the performance during rotation.

(b) Influence of the control-loop (cl) on the non-reciprocity (non-rec), measured between FBBL and DFBL, and the π-measurements in the FBBL. The noise level decreases by about one order of magnitude for both measurements which are presumably limited by the BN-frequencies as discussed in 3.4.1.)

Fig. 3.10.: FBBL performance under the aspects of DWS measurements. The requirements are derived with a coupling coefficient of $4000\,\mathrm{rad/rad}$ by [Isl18] and in Appendix C.2. The effects of the control loop on the non-reciprocity and π-measurement are shown in (b).

the Pre-Experiment used a smaller beam size on the QPD, while the current implementation agrees with the simulations. No drawbacks from the changed geometry could be observed.

3.5.2 DWS Performance

The noise level of the DWS measurements for each side and axis is shown in Figure 3.10a. They lie below two requirements: The one calculated in [Isl18] as a solid line and the one derived in Appendix C.2 as a dashed line. The latter is based on a conservative interpretation of the construction results in Strategy 2.3.7.

The FBBL will experience a significant increase in its dynamics once the two benches rotate, as observed in the Pre-Experiment [Isl18]. To estimate this effect, two measurements from the Pre-Experiment are added to the plot in gray, comparing the same DWS signal with and without rotation. These measurements were taken during the measurements in [Bis18], and [Isl18] but were not published there. The noise increase by a factor of two at $1\,\mathrm{Hz}$ due to the dynamics caused by the rotation. Assuming that the noise increase is similar in the 3BL, a recent DWS measurement is scaled by this factor of two and shown in the pink dotted line. It is still below the strict requirement. The spikes in the rotation from the Pre-Experiment were caused by the discrete steps of the rotation stages. Their appearance in the 3BL will differ because of the changed mechanical weight load and will be studied when the benches are rotated in the future, see Section 3.11.

Conclusively, the DWS noise shows sufficient performance in its implementation in the 3BL. Compared to the Pre-Experiment, the improved DWS noise is explainable by its monolithic and more stable structure and precise alignment.

3.5.3 Free-Beam Backlink Conclusion

The FBBL is successfully implemented in the 3BL infrastructure, yet without rotation. Its control loop is stable and characterized by the decoupling numbers of the system that are comparable to the ones derived in the simulations. The gains of the mirror control loops were optimized with measurements of the open-loop transfer functions. They are presented in Appendix E.5, with UGF of 80 Hz and 35 degree phase margin and an identical behavior in all four loops. A new, conservative requirement for the DWS signals was derived for the specific alignments in the 3BL. It is based on an increased tilt-to-length coupling due to misalignment in the construction. The measured DWS signals stay below this requirement. Also, an estimated increase of the dynamics due to benches rotating is concluded to be uncritical.

The necessity of the FBBL's control loop, even with non-rotating benches, is illustrated in two early measurements in Figure 3.10b. The control loop was deactivated and activated, and the noise levels of non-reciprocity and π-measurements were reduced by about one order of magnitude. The steering mirrors are mounted off the quasi-monolithic bench and thus significantly decrease the pathlength stability in the FBBL if not operated in a closed-loop. This also illustrates the necessity of quasi-monolithic benches.

After successfully implementing the FBBL, the 3BL is ready to perform with all its three Backlinks.

3.6 Commissioning of the Three-Backlink Experiment

Following the previous preparations, the 3BL is operational in its design configuration - with all three Backlinks operating. The measurements presented in this thesis are performed without rotating the benches, which will introduce an additional noise source. Improvements in the noise curves of the non-reciprocity and understanding of noise couplings and limiting sources are discussed in the following. The frequency range of 0.1 mHz to 10 Hz is divided into the high, center and low frequencies discussed in separate sections where typically different noise sources are limiting. Slightly varying noise levels in the measurements are often caused by laser performance problems, as also discussed in Section 3.8.6.

This section introduces the first measurements and successively adds noise improvements and understanding.

3.6.1 First Measurement

The first measurement with all three Backlink implementations operating was performed on the 12th of January 2022 and is shown in Figure 3.11. All three combinations share the same shape indicating a joint limitation. The white noise floor at $5 \cdot 10^{-5} \frac{\text{rad}}{\sqrt{\text{Hz}}}$ or $1 \cdot 10^{-4} \frac{\text{rad}}{\sqrt{\text{Hz}}}$, which already limited the fiber Backlink measurements (Section 3.4.1), is limiting in the high frequencies above 0.2 Hz. The slight difference in the level presumably depends on an external dynamical source because it is not consistent for different measurements. This also explains the deviation from the optimized measurement with the fiber Backlinks. Below 0.2 Hz, the noise level rises to $10^{-2} \frac{\text{rad}}{\sqrt{\text{Hz}}}$ in all three combinations.

This measurement is the starting point for the noise analysis and suppression in the 3BL.
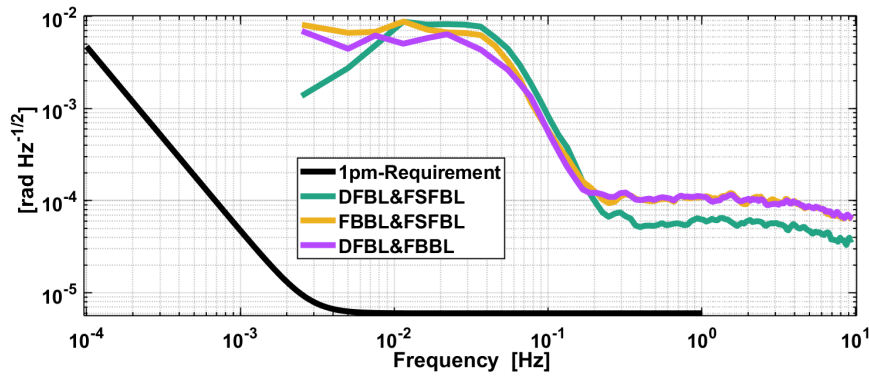
Fig. 3.11.: First Measurement with all three Backlinks operating. Above $0.2\,\text{Hz}$, a white noise floor at about $0.01\,\text{rad}/\sqrt{\text{Hz}}$ limits the non-reciprocities while an increase over two orders of magnitude limit at the frequencies below.

3.7 High Frequency Range

In this section, noise contributions found in the high frequency range are discussed. The high frequency range refers to frequencies above $0.3\,\text{Hz}$, where the previously mentioned BN frequencies and the ADPLL influence the non-reciprocity measurements.

3.7.1 Beatnote Frequencies

The chosen beatnote frequencies' influence was already found during the commissioning of the fiber Backlinks, Section 3.4.1, where different sets of frequencies were compared. This also limits the non-reciprocity measurements of all three Backlinks in the high-frequency range. With the implementation of the FBBL, two Backlinks use the same beatnote frequency and the performance of single beatnote frequencies is investigated.

The measurements are shown in Figure 3.12 where the different amplitude spectral densities and the noise level at $1\,\text{Hz}$ are plotted for multiples of the frequency f_0 between $2\,\text{x}$ and $30\,\text{x}$. The measurements were performed with the ADPLL setting of the BaliRo. The focus was on measurements of multiples of $f_0 \approx 9.8\,\text{kHz}$ because the idea was that this would maximize the CIC-filter's suppression, see Section 3.1.3. A clear trend of improved performance for higher multiples is visible in Figure 3.12a, and only for frequencies over $20\,\text{x}$ can the requirement be reached. Especially the measurement at $3 \cdot f_0$ has a very high noise level and is excluded from Figure 3.12b for visibility. The noise level dependence does not follow a strict function of multiples and likely external influences, like fluctuations in the laser frequency stability, vary for the different measurements. However, the overall trend of a monotonic decrease is evident. The increased noise level at $28 \cdot f_0$ might be an outlier or dominated by other noises because $30 \cdot f_0$ is again under the requirement. Analysis of the residual data, like the single-channel phase and heterodyne amplitude, shows no variation with the BN frequency. Measurements with multiples over $30 \cdot f_0 \approx 300\,\text{kHz}$ were not possible in this investigation, as this is the experimentally found limitation of the FBBL control loop. The measurements in Figure 3.12b distinguish between even and uneven multiples because this seemed to influence as shown in Section 3.4.1, but was not confirmed in the measurements presented here.
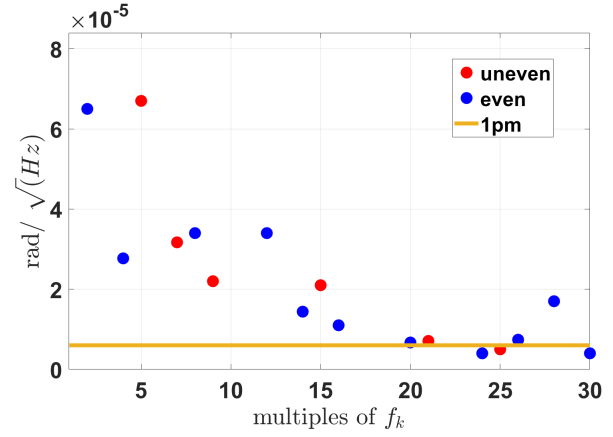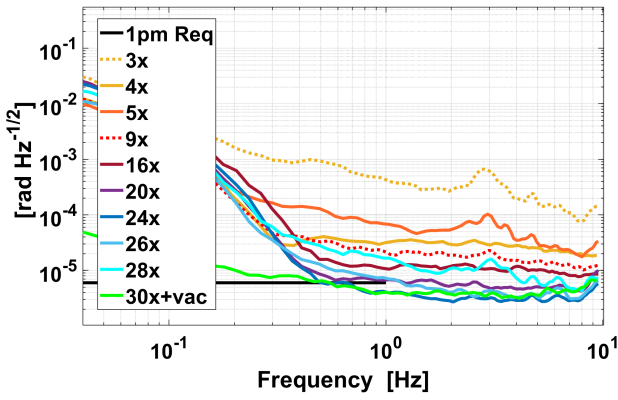
(a) Amplitude spectral density for the non-reciprocity of DFBL&FBBL at multiples of the frequency f_0.

(b) Noise level at $1\,\mathrm{Hz}$ for the measurements as shown in (a). A distinction between even and uneven multiples is made.

Fig. 3.12.: The frequency dependence of the noise floor in the non-reciprocity measurements.

This frequency-dependent behavior of the non-reciprocity measurements suggests that the non-reciprocity of a Backlink itself is, in fact, frequency-dependent. While some possible effects for this might exist, it seems more likely at the current status to expect the source to be in the experimental set-up instead of in the fundamental physics of a Backlink. The current understanding consists of several hypotheses that are presented in the following.

One investigation focuses on the single-channel behavior of the BaliRo. This measurement was performed by J. J. Ho Zhang and analyzed jointly with the author. No cable and thus no signal was connected to the BaliRo for these measurements. The readout frequency in the ADPLL-scheme was set to f_0 for one channel, and its output values were studied. No signal but only residual noise would be expected. Instead, a signal with a high heterodyne amplitude was observed. The readout frequency was set to multiples of f_0, and the heterodyne amplitude for each case was measured. The result is shown in Figure 3.13a. The signal only appears for uneven multiples. It is high for the base frequency, having an amplitude of $0.455\,\mathrm{V}$, and decreases for higher multiples until $10^{-6}\,\mathrm{V}$ is reached at $21{\cdot}f_0$.

Since this behavior was not found in the IQ-demodulation scheme, it can be caused by the ADPLL itself, potentially by the NCO locking to a parasitic tone. It is unclear what the origin is and how this couples only for uneven multiples. Alternatively, the signal can be at a frequency close to f_0, which is still tracked by the ADPLL but not by the IQ-demodulation[2]. Either way, deeper investigations like a spectral analysis of the BaliRo are needed for a complete picture in the future. The heterodyne amplitude correlation with the BN frequency fits well with the observed BN behavior of Figure 3.12. In both cases, the effect is reduced for beatnotes above $20{\cdot}f_0$. It is not entirely conclusive because the even multiples do not behave differently than the uneven ones in Figure 3.12, but do not appear in the open measurements. The underlying problem can be potentially solved by a more sophisticated filter or a shift of the CIC-filter's frequency in the future.

Another possible cause could be within the BaliRo. The decision to use multiples of a base frequency for the beatnotes is based on the notches of the in-loop CIC-filter (Section 3.1.3, Fig-

---

[2]The signal was not saved during these measurements, so a deeper analysis of the data, like the examination of a phase drift that would indicate a frequency offset are not possible, but will be repeated in the future.
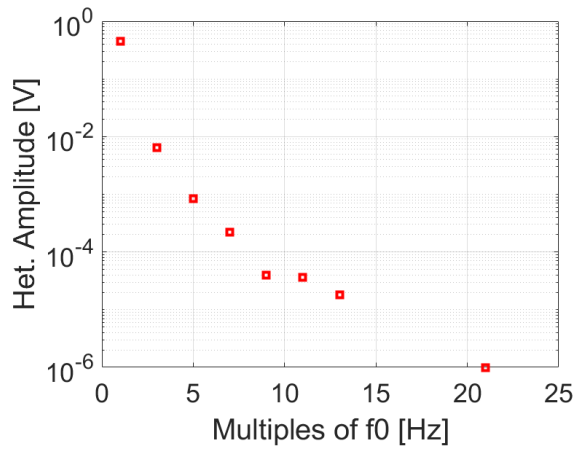
(a) Heterodyne amplitude measured without any signal connected to the PM at multiples of f_0. No signal was observed at even multiples.
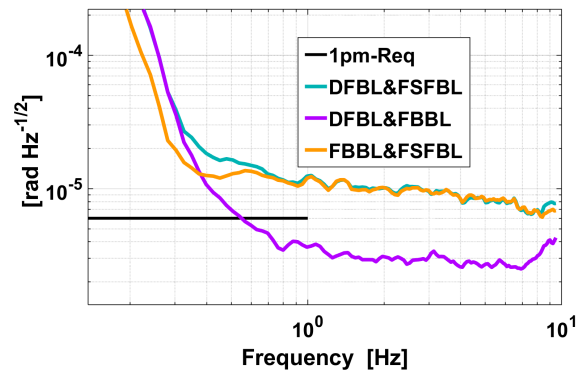
(b) Non-reciprocity measurement of all three Backlinks with the new frequency set, shown for the high-frequency end. The noise floor of DFBL and FBBL is below the requirement. The FSFBL is limited at about $10^{-5}\,\mathrm{rad}/\sqrt{\mathrm{Hz}}$.

Fig. 3.13.: Investigations on the frequency behavior and high frequency end with the current best frequency set.

ure 3.2a) where the harmonics are theoretically entirely suppressed. These notches have small tolerance for frequency changes, so the high phase dynamic of the input signal, as shown later in Figure 3.14b, will not be entirely suppressed by the notch. Instead, the fluctuations will appear on the two sides of the notch, where the suppression is much lower. Conclusively, they will appear downsampled and aliased in the measurement band. The envelope of the notch filter is a low-pass function, and accordingly, the suppression of signals next to the notch will get higher with higher frequencies. This fits the observed behavior in Figure 3.12a. It can be further investigated by repeating the measurements without the ADPLL, thus without the in-loop CIC-filter, where the behavior should be different.

Other possible explanations are based on the coupling of other types of parasitic signals. These can be oscillations imprinted on the laser locks by the electronics, similar to the oscillations found in the BaliLo's DAC card, during the laboratory preparations in Section 3.3.5. Similar kHz oscillations of components inside the TIA boxes can couple into the measurements. Cross-couplings typically increase with higher frequencies and are thus less likely. During the presented measurements, the other lasers were also activated, and hence additional BNs were present in the system. No influence of their presence was found in the following measurements. Acoustic signal coupling or Piezo resonances are other candidates that could cause kHz oscillations. Furthermore, the oscillations can also be caused internally by the BaliRo.

Another frequency-dependent noise source is the lasers' relative intensity noise (RIN) coupling. This noise is frequency dependent, and more information can be, for example, found in [Wis+22]. The RIN of all four transponder lasers was measured, and the noise level was found to be sufficiently low for the 3BL, as discussed in Section 2.4.1. Nevertheless, the relevant frequency range will be discussed here shortly. The measurements are shown in Appendix E.6 for a frequency range of $400\,\mathrm{Hz}$ to $10^8\,\mathrm{Hz}$. The frequency range between $10\,\mathrm{kHz}$ to $1000\,\mathrm{kHz}$, which relates to multiples between 1-100x, has two prominent peaks at $82\,\mathrm{kHz}{\approx}8{\cdot}f_0$ and $344\,\mathrm{kHz}{\approx}35{\cdot}f_0$. The level in-between is much lower, which agrees with the well-performing BNs between $20{\cdot}f_0$ and $30{\cdot}f_0$.

However, the frequency range of multiples below $8 \cdot f_0$ has a comparable noise level, which does not agree with the observations shown in Figure 3.12b. The correlation is thus not wholly conclusive.

To put it in a nutshell, four different hypotheses for the observed frequency dependencies were given: a spurious signal inside the BaliRo, residual signals next to the notches of the CIC-filter caused by the high phase dynamic, cross-couplings of kHz oscillations by electric components or coupling of RIN from the transponder lasers. Neither of the explanations is completely conclusive, and a combined effect seems likely. The spurious signals from Figure 3.13a can be investigated further to determine their origin, or the in-loop filter can be exchanged. Investigations will probe if the IQ-demodulation performance also depends on the frequencies. An operation at frequencies that are not multiples of f_0 in the future will provide deeper insights into the coupling. Modulating the laser's RIN can also further investigate its coupling.

This section concludes that the 3BL can measure with pm-precision in the high-frequency range, which is reached for the DFBL and the FBBL in Figure 3.13b. A beatnote frequency of at least $20 \cdot f_0$ is required, while no statements can be made for frequencies above $30 \cdot f_0$. However, due to the four lasers and five required BNs, frequencies outside this range must be chosen to operate the FSFBL. A temporarily acceptable frequency set was found with $(24, 52, 60) \cdot f_0$, whose performance is shown in Figure 3.13b. The white noise level is reduced compared to previous measurements, to about $10^{-5} \frac{\text{rad}}{\sqrt{\text{Hz}}}$. This level is still above the requirement, and the FSFBL limits its non-reciprocity combinations. This can be concluded because both combinations including it have a higher and equal noise level. At least one of the frequencies is not optimal, presumably for the reasons mentioned above. Further analysis will provide a better understanding of the involved noise couplings and presumably bring the FSFBL below the pm-requirement.

The analysis became further complicated because the white noise level is also influenced by the performance of the laser frequency lock.

3.7.2 Influence of the ADPLL in the BaliRo

As discussed in Section 3.1.3, the BaliRo operates either with an IQ-demodulation with limited bandwidth or an additional ADPLL that follows the phase dynamics. In the following measurements of the DFBL&FBBL the setting of the BaliRo was switched between both schemes for the DFBL channels at two different frequencies $8\text{x}f_0$ and $24\text{x}f_0$, presented in Figure 3.14a. In the measurements with the IQ-demodulation, the white noise level at high frequencies is at a level of about $5 \cdot 10^{-5} \frac{\text{rad}}{\sqrt{\text{Hz}}}$, while it reaches the 1pm-requirement for the active ADPLL with the frequency at 24x. Presumably, the phase dynamics in the single channels are too high to be sufficiently subtracted in the scheme without the ADPLL. Figure 3.14b shows the phase dynamics of the single channels, exemplarily shown for one DFBL-PD and one FBBL-PD, which do not depend on the readout scheme. They have a noise level of $0.03 \frac{\text{rad}}{\sqrt{\text{Hz}}}$ at $1\,\text{Hz}$ and are overlapping till about $5\,\text{Hz}$. The DFBL phase monotonously decreases, while the FBBL increases after $7\,\text{Hz}$.

As discussed before, the white noise level also depends on the chosen frequency, as visible in Figure 3.14a in the comparison of $8\,\text{x}$ and $24\,\text{x}$, for an active ADPLL. A dependency on the frequency is also observable for the IQ-demodulation, but it is inconclusive since only two different frequencies are compared. The IQ-demodulation dependency of the frequencies and an operation at frequencies
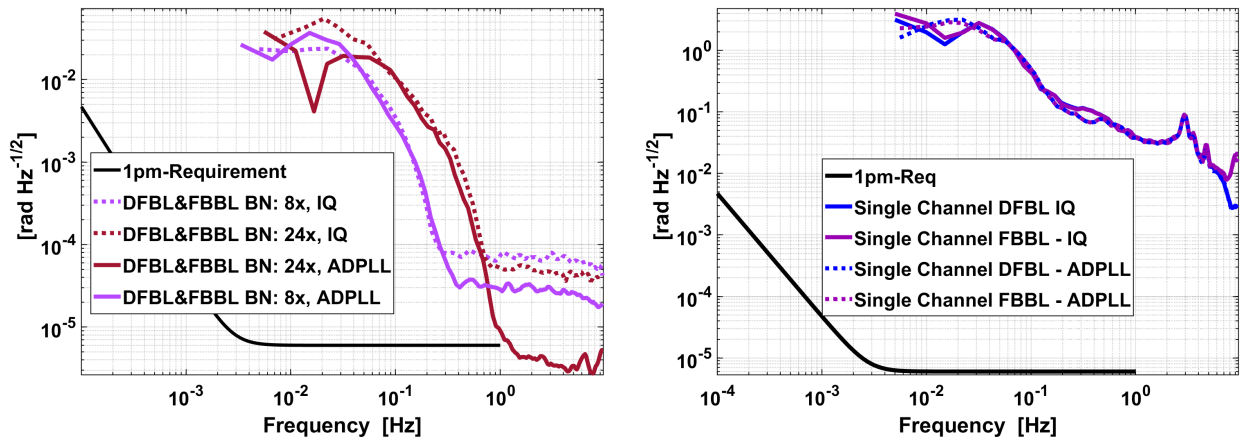
(a) Influence of the ADPLL on the non-reciprocity measurement for two BN-frequencies.

(b) Single channel phase noise with and without ADPLL.

Fig. 3.14.: Phase Dynamics and Influence of the ADPLL.

that are not multiples of f_0 in the future will provide deeper insights.

The different noise levels below $1\,\mathrm{Hz}$ are caused by varying thermal states at different measurement times because the vacuum chamber was not evacuated for these measurements.

Conclusively, the ADPLL readout is needed to reach the current implementation requirement, presumably due to its ability to cope with higher input dynamics.

3.8 Center Frequency Range

This section discusses noise contributions found in the center frequency range, which refers to frequencies between $0.3\,\mathrm{Hz}$ to about $10^{-2}\,\mathrm{Hz}$. The noise levels are reduced by commissioning the vacuum chamber and the laser power stabilization. Laser frequency noise was found to presumably couple via backscatter at the DFBL and is investigated and modeled. Furthermore, cross-coupling between phasemeter channels and fluctuating laser frequency performances presumably remain the limiting noise sources in this frequency range.

3.8.1 Vacuum

Figure 3.15 shows how the noise level of the non-reciprocity is reduced below $0.5\,\mathrm{Hz}$ after evacuating the vacuum chamber. Between $0.1\,\mathrm{Hz}$ and $0.01\,\mathrm{Hz}$, the noise level is lowered by two orders of magnitude. During the evacuation, at a pressure level below $10^{-4}\,\mathrm{mbar}$, no further dependency of the non-reciprocity level on the pressure was observed.

Fluctuations in the refractive index of the air appear as pathlength differences in the measurements [Fle12] randomly at different positions inside the interferometric path. This effect is not common mode between the two benches and thus does not cancel out. In agreement with that, the π-measurements that share a common interferometric path do not show comparable noise levels at the center frequencies (not shown here).
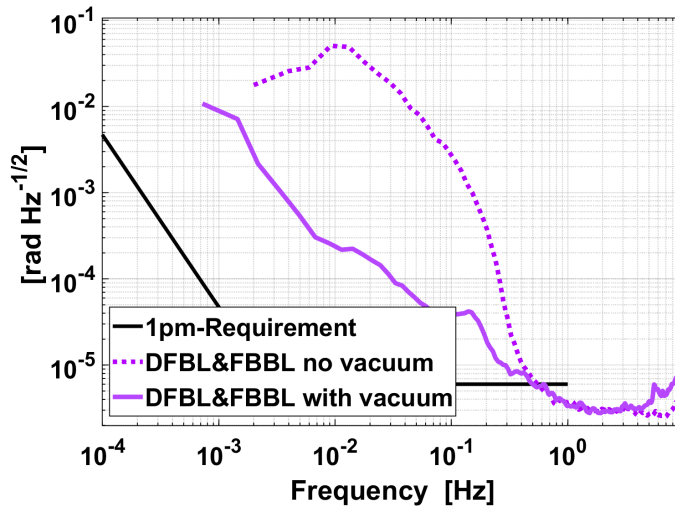
Fig. 3.15.: Influence of vacuum on the center frequencies. The noise level in the non-reciprocity is reduced and reveals a differently shaped noise source underneath.

Air fluctuations can cause this change in the refractive index [Fle12], which disappears when operating in vacuum. Furthermore, the refractive index of air changes with the temperature and humidity level [JK17]. Every time adjustments were performed inside the vacuum chamber, an experimenter needed to lean into the chamber, which caused breathing (even though masks were worn), human humidity vapor, and an increase in temperature. Here, the increase in the noise level could be clearly observed. For a simple estimation, a change in humidity and temperature is assumed on one bench along a geometrical length of s=10 cm. The resulting pathlength change Δl induced by the refractive index change Δn is given by

$$\Delta l = \Delta n \cdot s. \tag{3.8}$$

In [JK17], the changes of the refractive index with humidity and temperature are studied for light at 1550 nm wavelength and are used here for an approximation. A humidity change of 1 % affects the index of refraction by $9 \cdot 10^{-9}$. For a significant humidity change by breathing, an increase of 10 % is assumed, which causes a pathlength change of Δl=0.9 pm. The temperature causes a more significant change. 1 °C changes the index of refraction by $9.4 \cdot 10^{-7}$ and accordingly adds a pathlength of 9.4 nm. The temperature was not explicitly measured during alignments in the vacuum chamber but for an not-evacuated chamber, which is discussed later in Figure 3.25. A noise level of $10^{-2} \frac{°C}{\sqrt{Hz}}$ at 0.01 Hz is thus a conservative assumption. Combined with the coupling coefficient of $9.4 \frac{nm}{°C}$, a noise level of about $0.1 \frac{nm}{\sqrt{Hz}}$ is concluded. In Figure 3.15, the noise level at $5 \cdot 10^{-2}$ Hz is at $10^{-2} \frac{rad}{\sqrt{Hz}}$ which relates to $1.7 \frac{nm}{\sqrt{Hz}}$, which is one order of magnitude higher. Since the temperature noise is presumably higher with an experimenter aligning in the vacuum chamber, the model fits the observed noise curve as a simplified explanation. This very simple investigation conclude that the observed noise fits to a temperature noise inside the vacuum chamber.

(The noise increase at frequencies above 4 Hz appears in measurements with vacuum and might be caused by the vibrations or other influences of the active vacuum pumps.)

Conclusively, evacuating the vacuum chamber reduces the noise in the non-reciprocity measurements

of all Backlinks at the center and low frequencies. As expected and observed for similar experiments, the resulting noise curves are not limited by a pressure-dependent effect.

3.8.2 Influence of Laser Power Fluctuations

This section evaluates the fluctuations in the laser's amplitude or laser power. The term power is used here to reduce confusion with the heterodyne amplitude of the signal. Known coupling mechanisms from laser power fluctuations to phase noise are discussed, and the relative power in the single channel and their dependence on the power stabilization are analyzed. Its coupling in the non-reciprocity measurement is introduced and interpreted.

Power-to-Phase Coupling Mechanisms

A candidate for coupling of power fluctuations in the measurement phase is relative intensity noise (RIN), which is the relative power fluctuations of the laser and any modulation afterwards, divided by the mean power. Only RIN at the heterodyne BN frequency (called 1f-RIN) or at twice the BN (called 2f-RIN) couple directly into the phase measurements, as presented in [Wis+22]. Both couplings are not expected to limit the measurements above the requirement. The RIN was measured as shown in Appendix E.6 and is below $10^{-6}/\sqrt{\text{Hz}}$, which is sufficient as discussed in Section 2.4.1. Consistently, in the Backlink measurements by [Fle12], a stabilization at the heterodyne frequency yielded no performance improvement for the non-reciprocity.

Another candidate is RIN at frequencies around the DC level. This does not couple directly in the phase (as calculated in [Wis+22] and measured in [Sch18]) but indirectly over other effects like laser power-dependent temperature changes. One possible coupling mechanism point is at the photodiode. The temperature at the PD will change with the absorbed power, which changes the capacitance of the PDs [Fle12]. This effect would influence the performance at low frequencies due to the temperature dependency.

Power Stability in the 3BL

The DC readout of the BaliRo enables tracking the averaged beam power and its fluctuations around DC. The interfered beams and their combined power are discussed in the following. Thus the DC-RIN of the combined beams is monitored. First, their noise levels without stabilization are discussed briefly. Figure 3.16 shows the different shapes of this DC-RIN for the two reference interferometers (REF) exemplarily.

A white noise floor above $0.3\,\text{Hz}$ and a rising noise below is visible on the right bench, shown in dark green. The same measurement on the left bench has a similar noise level at low frequencies and a steeper slope above $0.3\,\text{Hz}$. In the figure, the involved lasers in both interferometers are labeled. The white noise appears in the interference of laser 2 (L2) and laser 3 (L3). By combining this with the measurements in the other interferometer, shown in Appendix E.7, L2 can be identified as the cause of this noise behavior. L2 is also the dominant noise contributor in the lower frequencies. This high noise contribution is presumably related to a polarization issue: At the pbs behind each fios, polarization fluctuations will couple to power fluctuations in the interferometer. In the first
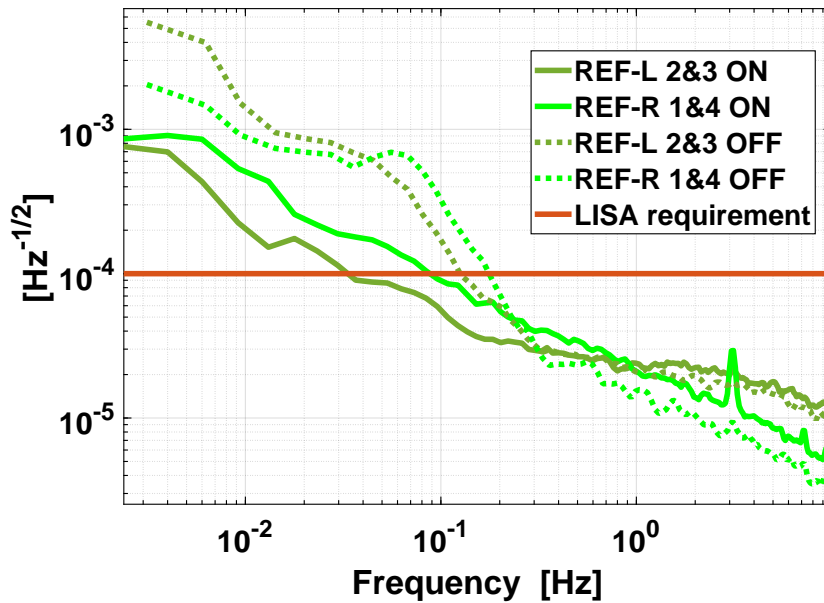
Fig. 3.16.: DC-RIN of the reference interferomters (REF) on the left (L) and right side (R) and the influence of the laser power stabilization (ON/OFF). The numbers of the two involved lasers is given for each signal. The requirement for the power stability in LISA in the frequency band between $3 \cdot 10^{-5}$ and $10\,\text{kHz}$ is included [Sho+19].

hours of operating L2, a significant power fluctuation in its pbs ports is observable while the laser is slowly getting into equilibrium. This indicates that the polarization coupling into this fiber is distorted. The fluctuations are reduced for a longer times operating laser, but they still indicate a significant alignment mismatch. An attempt to improve the axes matching with the waveplates in the laser preparation and a polarization analyzer was unsuccessful. The angle mismatch between the feedthrough and the fios fiber in the mating sleeve is presumably too significant. This problem must be kept in mind, and further investigation of the polarization alignment in the L2 fiber are advised. Fiber benches, like those implemented in [Sch18], might be the ultimate solution. The power stabilization can reduce the resulting power fluctuations in the interferometers but simultaneously increase the amount of light in the wrong polarization state because the ratio of wanted and unwanted polarization is unchanged. Polarizers in front of the PDs reduce the influence of the spurious interference caused by the unwanted polarization.

Improvement with Power Stabilization

As introduced in Section 3.1.1, a laser power stabilization is implemented for each laser to control the power levels inside the vacuum chamber. Its open-loop transfer functions were measured and optimized for a UGF around $800\,\text{Hz}$ and phase margins above 30 degrees.

Figure 3.16 shows the effect of the power stabilization on the combined DC levels of the two REF interferometers, which are only affected below $0.2\,\text{Hz}$. As a comparison, the requirement for the power stability in LISA in the frequency band between $3 \cdot 10^{-5}$ and $10\,\text{kHz}$ is shown at a level of $10^{-4}/\sqrt{\text{Hz}}$ [Sho+19]. This level is reached for frequencies above $0.2\,\text{Hz}$, even without stabilization. With the power stabilization, the noise level at $0.03\,\text{Hz}$ is reduced about one order of magnitude on the left bench and on the right bench by a factor of 2-3. This is in agreement with the above-
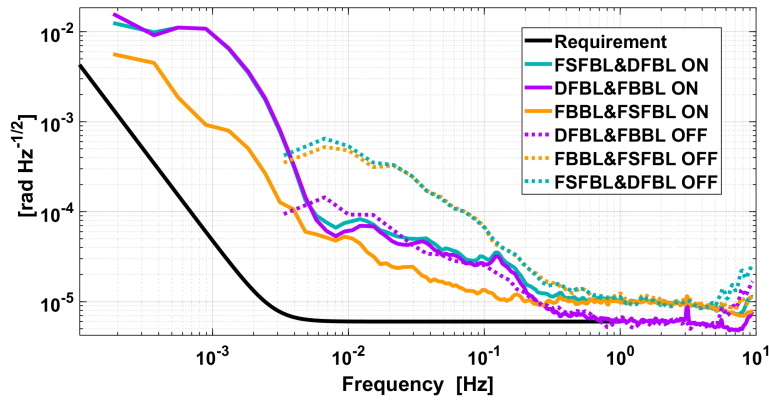
Fig. 3.17.: Influence of the laser power stabilization activated (ON) and deactivated (OFF) on the non-reciprocity measurements. The FSFBL noise is reduced by about one order of magnitude.

mentioned noise contribution from L2, which can also be seen in the measurements shown in the Appendix E.7. However, some channels are barely influenced but have an increased noise level at low frequencies. This can also be seen in REF-R above 0.3 Hz in Figuer 3.16.

The power stabilization was optimized regarding its gains using open-loop transfer function measurements to at least 800 Hz per laser. However, the DC noise levels are only affected in a range below 0.2 Hz by a factor between two and one order of magnitude.

Influence on Non-Reciprocity and Interpretation

The non-reciprocity measurements with and without power stabilization are shown in Figure 3.17. Without the stabilization, the FSFBL limits the combinations it is part of. It is the only Backlink that shows a visible effect to the activated stabilization. Its combination with the FBBL is reduced by about one order of magnitude, below the combination with the DFBL. With the stabilization DFBL&FSFBLis at the same level as the DFBL&FBBL with and without stabilization, which indicates that the DFBL is limiting these combinations. Accordingly, the DFBL is not influenced by the amplitude stabilization, the FSFBL's noise is reduced in the center frequency range, and no statement can be made for the FBBL, as it is not clear if FBBL&FSFBL is limited by either of the two.

The DFBL now dominates its non-reciprocity combinations in the center and low-frequency range. The noise at low frequencies is discussed in Section 3.9.1 and the shoulder at 0.12 Hz is discussed in Section 3.8.3.

The power stabilization only visibly improves the non-reciprocity of the FSFBL, even though it also reduces the DC RIN levels in each interferometer of the other Backlinks. As discussed in the beginning, the laser power fluctuations can couple via thermal fluctuations in the photodiodes material. This effect would accordingly scale with the number of photodiodes involved, which is higher in the FSFBL.

To evaluate if an improved power stabilization is necessary in the 3BL and to investigate the coupling mechanism from the power level to the noise floor in the non-reciprocity, a measurement with modulated powers is about to be performed as further analysis. A follow-up noise projection will test if the power stabilization limits the current non-reciprocity measurements.

Besides the performance improvement with the power stabilization, a more practical need for it became apparent during the commissioning. The chosen *readout gains* in the BaliRo depend on the signal's amplitude, and the performance of a measurement depends on the quality of these gains. Power drifts over time were thus affecting long-term measurements before the power stabilization was implemented.

3.8.3 Laser Frequency Noise

Laser Frequency Noise (LFN) is a potentially limiting noise source in interferometers with unequal armlength. It presumably appears in the center frequencies in the 3BL measurements and is modeled and discussed in this section.

LFN Coupling-to-Phase Measurement

In general, in a simple Mach-Zehnder interferometer, the frequency noise of the laser couples into the phase with the pathlength difference of the two interfered beam's travel path Δs. For a LFN $\tilde{f}$, the coupling into the phase is approximated by [Pac21]:

$$\Delta\phi \approx \frac{2\pi}{c} \cdot \Delta\text{s} \cdot \tilde{f} =: \nu(\Delta\text{s}). \tag{3.9}$$

The influence can either be reduced by an increased absolute laser frequency stability or a smaller armlength difference.

In each 3BL interferometer, two beams with potentially different LFN interfere. Since all lasers are locked to the reference laser it is a valid assumption to use $\tilde{f}_1 = \tilde{f}_2 = .. = \tilde{f}_{iod} = \tilde{f}$ so that Equation 3.9 can be applied. In the DFBL, the local beam travels a path s1, and the backlink beam the path s2 until the interfering bs. This includes the pathlength on the optical benches, the Backlink fiber of 2 m, and also the difference in the laser preparation and the feedthrough fibers. Since the latter are ideally identical and matched in the 1 cm range, they are negligible compared to the pathlength difference in the experiment. The LFN coupling in an interferometer on one bench is thus given by Equation 3.9:

$$\Delta\phi = \frac{2\pi}{c} \cdot (s2 - s1) \cdot \tilde{f}. \tag{3.10}$$

And equally on the other bench, with distances s1' and s2'.

To investigate the influence on the non-reciprocity measurements, the Φ-combination discussed in Section 3.2.2 is studied first. The LFN cancels in this combination for equal pathlength on both benches, but this assumption is dropped here. The pathlength s1 is not perfectly the same as s1' or as $s_{\text{simulated}}$ because of deviations in the construction, assumed to be in the order of 1 mm. Thus, the pathlength difference Δs presumably differs from the pathlength difference $\Delta s'$ on the other bench, and the Φ combination contains a term:

$$\Phi = ... + \frac{2\pi}{c}(\Delta\text{s} - \Delta\text{s'}) \cdot \tilde{f}. \tag{3.11}$$

The coupling of the LFN noise in Φ thus depends on the difference of the pathlength differences between both benches, $\Delta s - \Delta s' = \partial s_{DFBL}$. Pathlength differences between both benches that are seen by both beams, the local and also the Backlink beam, cancel. An example in the DFBL is a longer distance between *fios2* and the edge of the bench on one side.

A comparable difference of pathlength differences can appear for the FBBL with ∂s_{FBBL}. In the FSFBL, both interferometers can have a mismatch between the benches: $\partial s_{FSFBL} + \partial s_{REF}$. When combining the single Backlinks further to the non-reciprocity combination, only the difference between these differences of the benches pathlength remains for the LFN coupling:

$$\text{non-rec}_{\text{DFBL\&FBBL}} = \varphi_{non-rec}^{\text{DFBL}} - \varphi_{non-rec}^{\text{FBBL}} + \frac{2\pi}{c}(\partial s_{DFBL} - \partial s_{FBBL}) \cdot \tilde{f}. \tag{3.12}$$

And accordingly for the other combinations. The coupling of the LFN in the combined non-reciprocities thus depends on the difference of the differential length between the benches of the involved Backlinks.

LFN Coupling via Backscatter

LFN can not only couple via the nominal measurement, as discussed above, but also via backscatter. Especially the backscatter of the TX'-beam at the DFBL is a known source for phase errors. Its backscatter interferes with the counter-propagating Backlink beam at TX-frequency. LFN couples via the potential pathlength difference between these two interfered beams. The nominal TX-backlink beam and the TX'-beam that is about to scatter, enter the Backlink fiber from both ends with pathlength s2 and s2', respectively. Their pathlength difference thus depends on the difference between s2 and s2', and the position of the scattering center inside the fiber. The scattering happens at many points along the fiber and is here assumed to be a statistical effect with no correlation between the scattering in both directions. Thus, this is assumed to be a non-reciprocal effect. For setting up a simple model, the scattering is interpreted to happen for both sides at an effective pathlength difference Δs_{BS} and $\Delta s_{\text{BS'}}$, respectively. This value is in the following assumed to be between zero and $2\,\text{m}$, given by an effective scattering at the beginning or the end of the fiber. The resulting LFN coupling is given via:

$$\varphi_{\text{BS-LFN}} = \frac{2\pi}{c}\Delta s_{\text{BS}} \cdot \tilde{f}. \tag{3.13}$$

This interference between the nominal beam at TX-frequency and the backscatter at TX'-frequency creates a phasor that is added in the interferometer to the nominal one, like in Equation 1.7. Its influence on the nominal measurement is calculated with:

$$\varphi_{\text{BS-LFN-err}} = \sqrt{\frac{P_{\text{BS-TX}}^{\text{fiber}} P_{\text{TX'}}^{\text{fiber}}}{P_{\text{TX}}^{\text{ifo}} P_{\text{TX'}}^{\text{ifo}}}} \cdot \sin\left(\varphi_{\text{BS-LFN}}\right). \tag{3.14}$$

$P_{\text{BS-TX'}}^{\text{fiber}}$ is the backscattered (BS) power inside the fiber, which is based on a fiber backscatter of $7\,\text{ppm/m}$, thus $14\,\text{ppm}$ for the $2\,\text{m}$ fiber (see Section 1.2.3). $P_{\text{TX'}}^{\text{fiber}}$ is the power of the TX-beam inside the backlink fiber. The powers indicated with 'ifo' are the TX and TX' powers inside the interferometers, thus part of the nominal interference. Because the spurious interference happens before the bs in the DFBL-ifo, the phase noise will show up in the π-measurement. The same effects
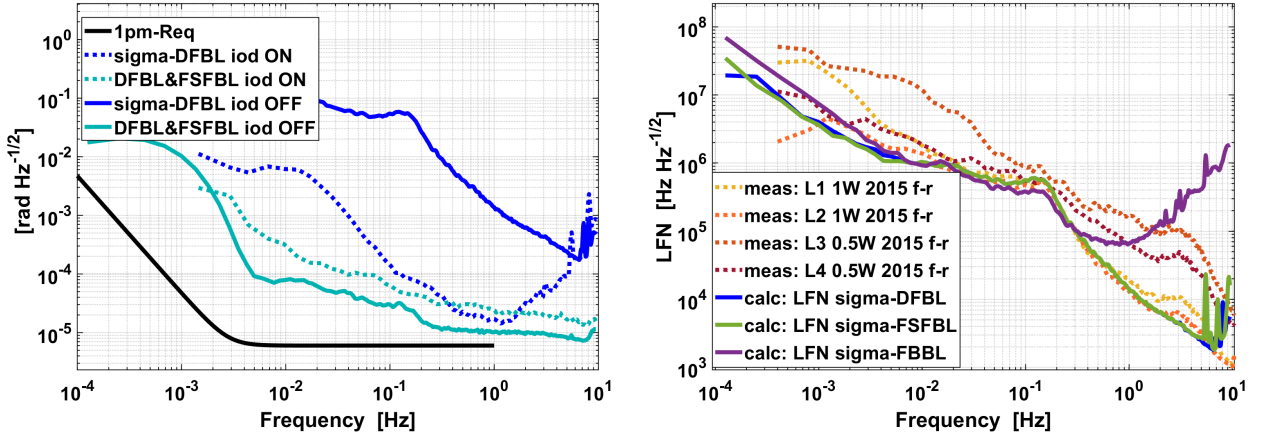
(a) Influence of the iodine stabilization of the reference laser on the σ-combination and the non-reciprocity. An additional noise is introduced to the non-reciprocity by the iodine stabilization.

(b) LFN measured (meas) in the Backlink laboratory in 2015 for Lasers 1-4 (L1-L4), free-running (f-r) [Isl18]. LFN calculated (calc) from the σ-combinations.

Fig. 3.18.: LFN measured in the σ-combinations and compared to LFN measured in the transponder laser.

happen on both benches. Even though no correlation between the scattered phases is assumed, the LFN that is investigated is still the same on both benches, $\tilde{f}$. Thus some amount of correlation is likely. To be consistent with the nominal coupling of LFN, it is assumed that the sum of both phase errors appear in the σ-combination and their difference in the non-reciprocity:

$$\sigma_{\text{DFBL\&FBBL}} = ... + \varphi_{\text{BS-LFN-err-left}} + \varphi_{\text{BS-LFN-err-right}} \tag{3.15}$$

and

$$\text{non-rec}_{\text{DFBL\&FBBL}} = ... + \varphi_{\text{BS-LFN-err-left}} - \varphi_{\text{BS-LFN-err-right}}. \tag{3.16}$$

The sign between the two sides depends on the phase relation.

The backscatter at the fiber is in first-order irrelevant in the other two Backlinks. For the FBBL, the waveplates are a potential additional source of backscatter. At *hwp2*, which only exists on one bench, the Backlink beams in both directions reflect at the same position, and because the reflection is not random as the fiber backscatter, the LFN mostly cancels because of the equal pathlength difference on both benches.

The reflections at *hwp1* are below 0.1% [B.H] and the *pbs5* transmits less than 0.1% s-polarized light [Las], assuming s-polarized backreflection. Accordingly, about 10^{-6} of the incoming light interferes at *pbs5* with the counterpropagating Backlink beam. The overlap between the beams is expected to be low. The pathlength difference is approximately the length of the free-beam path. This reflection happens on both sides of the benches, with approximately the same pathlength differences and power ratios. It is expected to be significantly lower than the DFBL backscatter contribution, which seems to be confirmed by the experimental investigations. As discussed in the following sections, it does not show up in π-measurements or balanced detection.

LFN Measured in the 3BL

While the LFN cancels in the non-reciprocity combination beside the noise in Equation 3.16, it is included twice in the signal combination called σ-combination (Equation 3.3), assuming it is equal on both benches. The imperfection in the mirror-symmetry of the two benches mentioned above is here again negligible because the pathlength difference for a single interferometer is larger by more than one order of magnitude. Figure 3.18a compares two measurements of σ_{DFBL} with and without the reference laser's stabilization. The level of σ_{DFBL} reduces by more than two orders of magnitude at $0.1\,\text{Hz}$ with the stabilization [Isl18], indicating that σ_{DFBL} is dominated by LFN coupling. With the stabilization, the reference laser's noise is reduced by about four orders of magnitude. Thus the resulting σ_{DFBL}-level is presumably dominated by its second term, the length noise of the Backlink, l_{DFBL}. The shown influence on the non-reciprocity illustrates why the measurements in this section were performed without the iodine stabilization of the reference laser. This stabilization introduces additional control noise that increases the noise level of the non-reciprocity. An initial malfunctioning of the stabilization was caused by a broken Peltier module that was successfully exchanged by colleagues. The remaining limiting noise in Figure 3.18a and its suppression are still under investigation.

Assuming accordingly that the LFN dominates the σ-measurement without stabilization, the σ-measurement can be combined with the LFN Equation 3.9. The assumed LFN noise that couples in the σ-combination are calculated inversely via:

$$\tilde{f}_\sigma = \frac{\sigma}{2} \cdot \frac{\text{c}}{2\pi} \cdot \frac{1}{\Delta\text{s}}, \tag{3.17}$$

with $\Delta\text{s}= 2.3\,\text{m}$ for the DFBL. The resulting frequency noise curves are shown in Figure 3.18b for each Backlink. Presumably, they are dominated by the frequency noise of the not-stabilized reference laser, as explained in the following. Previous measurements of laser frequency noise of the free-running NPROs in the 3BL's Laboratory are also plotted in Figure 3.18b. The frequency noise of the beatnote between the iodine-stabilized reference laser with the transponder NPROs was measured with the BaliLo. This was done in the past for a stabilized reference laser and not-stabilized NPROs, in [Isl18]. The frequency noise of the NPRO-lasers dominated this noise because the iodine stabilization was activated for the reference laser. The LFN of the stabilized reference laser is at about $100\,\text{Hz}/\sqrt{\text{Hz}}$ [Isl18], which is about four orders of magnitude below the LFN of an unstabilized NPRO, as shown in Figure 3.18b. In the measurements discussed in this section, the transponder lasers were locked, but the reference laser was not stabilized. The laser inside the iodine-stabilized Prometheus is an NPRO laser that is expected to behave similarly to the transponder lasers or any free-running NPRO. Conclusively, the frequency noise of all lasers, $\tilde{f}$ and, accordingly, the σ-combinations, are dominated by the frequency noise of the not-stabilized reference laser. The calculated LFN from the σ-measurement and the measured LFN from the free-running NPROs agree well, especially the shoulder at $0.14\,\text{Hz}$ is present in both. This agreement between calculated $\tilde{f}_\sigma$ and measured $\tilde{f}_{\text{NPRO}}$ gives further evidence that LFN coupling dominates the σ-combination. The used pathlength Δs for the calculations were extracted from the $2\,\text{m}$ fiber and the pathlength in Figure 1.11 and provided a nice overlap with the measured LFN without additional tuning.

The σ combinations for all Backlinks are shown in Figure 3.19a. The DFBL and the FSFBL overlap nearly in the whole frequency range, which agrees with their common pathlength difference of
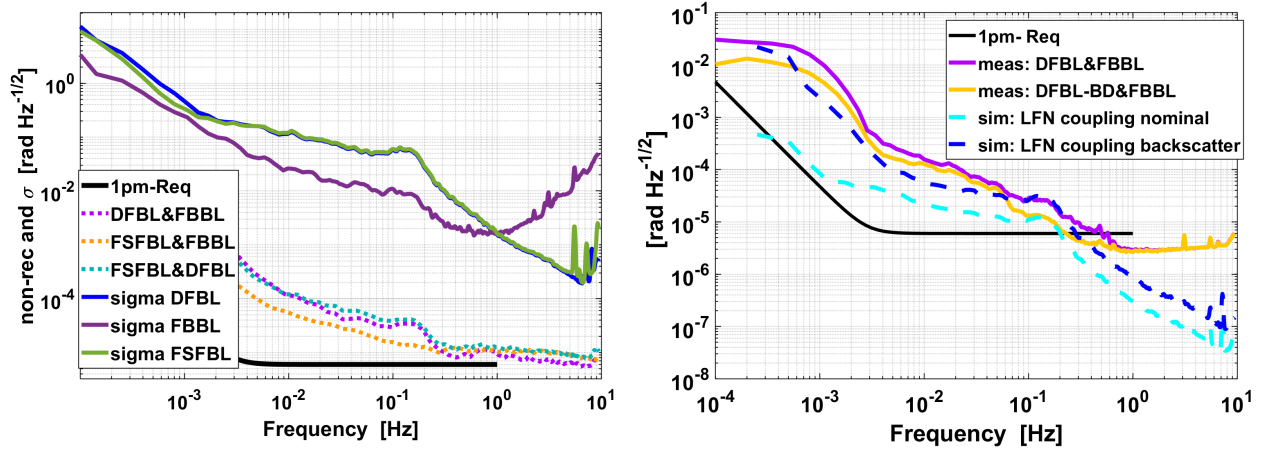
(a) σ-combination (sigma) and non-reciprocity measured for all three Backlinks. The combinations with DFBL show a similar shoulder at 0.14 Hz as the σ-combination.

(b) Modeled LFN coupling nominal and via backscatter compared to the measured non-reciprocity for DFBL&FBBL and balanced detection (-BD) applied to DFBL.

Fig. 3.19.: LFN coupling into the non-reciprocity and σ.

2.3 m and 2.4 m, respectively. The FBBL implementation has about 0.5 m pathlength difference. The noise shape is mainly the same for all three Backlinks till 0.3 Hz, but a factor of 5 smaller for the FBBL in the frequency range between $0.3 \cdot 10^{-4}$-0.3 Hz, which fits the ratio of the pathlength differences. At higher frequencies, the FBBL noise increases and σ_{FBBL} is presumably dominated by the pathlength noise of the free-beam connection, l_{FBBL}. The rotation between the benches was not activated during these measurements and will presumably increase this noise floor.

Conclusively, the σ-combination of all Backlinks is presumably dominated by LFN coupling in the frequency range from $0.3 \cdot 10^{-4}$ Hz to 0.3 Hz, and $\tilde{f}$ is dominated by free-running NPRO noise. Measurements of the LFN of the reference laser were not available.

Figure 3.19a also shows the non-reciprocity combinations of all three Backlinks. A prominent shoulder at 0.14 Hz is visible in the σ-combinations and the non-reciprocities, which include the DFBL. The implied hypothesis that the LFN couples specifically in the DFBL measurement is investigated in the next section.

Modeled Coupling of the Measured LFN into the Non-Reciprocity

Because of the prominent shoulder in the DFBL non-reciprocities, the coupling of LFN potentially works via backscatter at the DFBL's fiber. This is investigated with *Matlab* modeling. The nominal coupling is based on equation 3.12, and the backscatter coupling is discussed in the following. Equation 3.10 to 3.16 were combined with Equation 3.17 to simulate the LFN coupling via backscatter:

$$
\begin{aligned}
\text{non-rec}_{\text{DFBL\&FBBL}}^{\text{simu}} &= ... + \varphi_{\text{BS-LFN-err-left}} - \varphi_{\text{BS-LFN-err-right}} \\
&= ... + \sqrt{\text{Prl}} \cdot \sin\left(\varphi_{\text{BS-LFN-l}}\right) - \sqrt{\text{Prr}} \cdot \sin\left(\varphi_{\text{BS-LFN}-r}\right) \\
&= ... + \sqrt{\text{Prl}} \cdot \sin\left(\frac{2\pi}{\text{c}} \Delta s_{\text{BS-left}} \cdot \tilde{f}_{\sigma}\right) - \sqrt{\text{Prr}} \cdot \sin\left(\frac{2\pi}{\text{c}} \Delta s_{\text{BS-right}} \cdot \tilde{f}_{\sigma}\right).
\end{aligned}
\tag{3.18}
$$

The phase coupling was modeled on both benches based on the measured σ and with slightly different power ratios on the left $\sqrt{\text{Prl}}$ and the right $\sqrt{\text{Prr}}$ side. The pathlength difference Δs_{BS} for both sides was varied until an agreement between model and measurement was achieved. This is a simplified model, especially because scatter does not happen at one point, but throughout the fiber and Δs_{BS} is interpreted as an artificial effective pathlength difference. Furthermore, the behavior in both directions is assumed to be identical, only varied by the effective pathlength difference and the power ratio. The result is shown in Figure 3.19b and compared to the measured non-reciprocity of DFBL&FBBL, for $\Delta s_{\text{BS-left}} = 0.49\,\text{m}$ and $\Delta s_{\text{BS-right}} = 0.34\,\text{m}$. The values indicate that the backscatter is happening effectively in the first quarter of the Backlink fiber. The coupling efficiencies contributing to the power ratios are assumed according to Table 2.3 at $c_{\text{left}} = 0.5$ and $c_{\text{right}} = 0.52$. At $0.14\,\text{Hz}$, the shoulder in the model matches very well with the shoulder in the measurement. Above and below, the measurement seems limited by a different noise source. The high noise in the low-frequency range is presumably caused by temperature coupling and is discussed later in Section 3.9.1. The agreement of modeled and measured non-reciprocity in that region implies that the temperature also coupled into the σ-combination. The σ-combination was used to calculate the LFN because no direct measurement of the LFN of the reference laser was available. As mentioned before, this is a simplified model but fulfills the scope of understanding a possible coupling of the LFN and the backscatter behavior of the fiber.

Support for this assumed coupling can be found in the effect of balanced detection, shown in Figure 3.19b. Balanced detection was only applied to the DFBL because it can remove the fiber backscatter and, accordingly, the LFN coupling via this backscatter. The noise or coupling is reduced by a factor of two in the frequencies around $0.14\,\text{Hz}$. Balanced detection is studied in more detail in Section 3.8.4.

Additionally, Figure 3.19b shows the modeled nominal coupling of the LFN into the non-reciprocity according to Equation 3.12, for an assumed pathlength difference between the benches or asymmetry $\partial s_{DFBL} = 1\,\text{mm}$. It aligns with the residual noise shoulder at $0.14\,\text{Hz}$ of the non-reciprocity after applying balanced detection. This indicates that the noise below the LFN backscatter coupling is nominal LFN coupling. However, at the current state, no knowledge of the actual value of ∂s_{DFBL} is available, and this possible noise limitation has not been confirmed.

LFN in π-measurements

The described coupling of LFN via backscatter would also appear in π-measurements because the interference happens before the nominal interfering beamsplitter. Accordingly, the modeled noise on each bench in Equation 3.16, $\varphi_{\text{BS-LFN-err-left}}$ and $\varphi_{\text{BS-LFN-err-right}}$ model the noise in the π-measurements, when multiplied with a factor of two. This is shown in Figure 3.20a, where the model and measurement are compared. The π-measurements are assumed to have twice the noise as the model because of the two involved interferometer ports. However, the modeled noise levels only overlap with an additional factor of two, showing the limits of this simple model. With this additional factor, the curves overlap well in the center frequencies, and the π-measurements presumably show the LFN coupling via backscatter. This is further supported by Figure 3.20b. Shown are π-measurements for the DFBL without a stabilized reference laser (dashed) and with (solid). Again, the shoulder at $0.14\,\text{Hz}$ is removed with the stabilization. In the π-measurements of the FBBL (discussed later in Section 3.8.7), this shoulder is also not present, as expected.
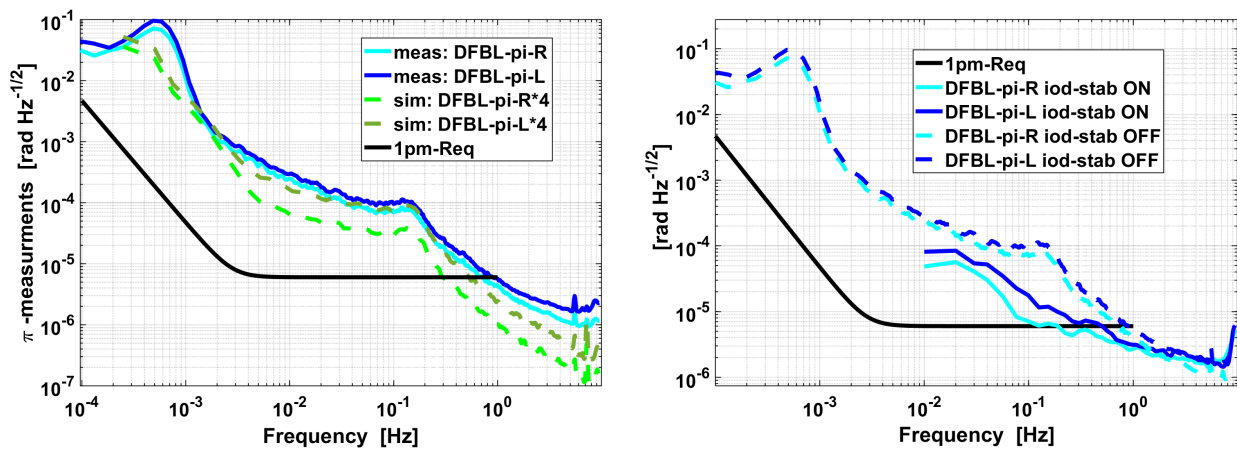
(a) π-measurements in the DFBL and the modeled LFN coupling via backscatter on both benches. The models are multiplied by 4 to be at a comparable level with the π-measurements.

(b) π-measurements in the DFBL with (ON) and without (OFF) reference stabilized (iod-stab). The noise at 0.14 Hz is reduced by one order of magnitude.

Fig. 3.20.: LFN coupling in π-measurements, measured and modeled and with the effect of the stabilized reference laser.
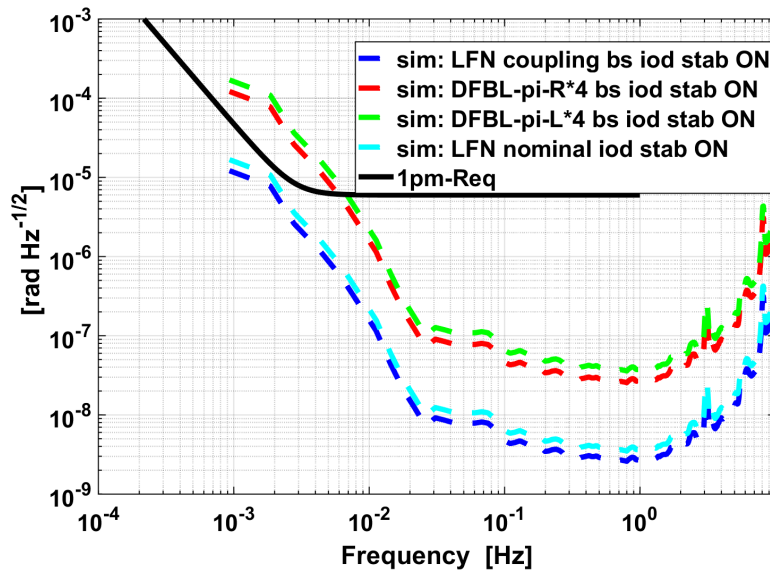
Fig. 3.21.: Modeled coupling of LFN to the non-reciprocity and π-measurements for a measurement with activated iodine stabilization (iod stab ON). For backscatter (bs) and nominal coupling.

Conclusion of LFN Coupling in the 3BL

To put it in a nutshell, the LFN is measured via its coupling into the σ-combination in the center frequencies and can be used to simulate its coupling into the non-reciprocity measurements. According to this model, the current performance of the DFBL is limited by LFN coupling via backscatter at the DFBL's fiber. It is suppressed with balanced detection by a factor of two at 0.14 Hz. The underlying noise source could be the nominal coupling of LFN for a 1 mm mismatch in the mirror-symmetry. To improve the noise floor, the LFN has to be reduced, which is possible with the iodine-stabilization of the reference laser. Compared to the here shown frequency noise of about $1\,\mathrm{MHz}/\sqrt{\mathrm{Hz}}$ at 0.1 Hz, a laser stabilized to an iodine cell performs below $100\,\mathrm{Hz}/\sqrt{\mathrm{Hz}}$ [Isl18]. The reason for its non-operation in the 3BL measurements were a technical issue and additional noise that couples into the system and limits the measurement of the non-reciprocity. To illustrate this, Figure 3.18a can be analyzed again. It showed two measurements with and without the activated stabilization. σ_{DFBL} is shown for both cases and reduced by two orders of magnitude at 0.14 Hz, removing the prominent shoulder. However, the stabilization introduces a higher noise floor in the non-reciprocity of FSFBL&DFBL. Experimental validation of the models in this section is thus not possible at the moment. However, the two orders of magnitude noise reduction in the LFN will presumably also significantly reduce the coupling into the non-reciprocity. This is stimulated by using a f_σ from a measurement with iodine stabilization and shown in Figure 3.21. Here, the $1\,\frac{\mathrm{pm}}{\sqrt{\mathrm{Hz}}}$-requirement can be reached in the non-reciprocity measurements. A low frequency-noise reference laser is thus needed to reduce the noise in the DFBL measurements.

Another possibility for LFN coupling, which was not investigated in detail, is its coupling via cross-talk between the channels in the BaliRo, see Section 3.8.5.

3.8.4 Balanced Detection in the Center Frequencies

Balanced detection (see Section 1.2.1) reduces specific noise terms by using the PD in each of the two interferometer ports. Some noise sources, like 1f-RIN [Wis+22] and spurious beams that have interfered with one of the nominal beams before the interfering bs can be reduced in post-correction. Backscattering at the DFBL's fiber is one of the associated noise sources. This specific spurious interference only happens at the DFBL because these backreflections are suppressed by design in the other Backlink implementations.

A set of short measurements presented here investigates the influence of balanced detection in the DFBL and the FBBL in the center frequency range. For this, the readout of the FSFBL was discarded such that all interferometer ports of the DFBL and FBBL could be connected to the limited number of channels in the BaliRo. Balanced detection was applied in post-processing in the *Matlab* analysis. First in all interferometers and then individually for both Backlinks to estimate their noise contributions. The result of three subsequent measurements is shown in Figure 3.22a. In the Figure, balanced detection is only applied in the DFBL, because it was found to have no influence when applied to the FBBL. This agrees with the hypothesis that the LFN couples via the backscatter at the DFBL. The noise levels of the data after applying balanced detection at 0.14 Hz are approximately the same, at $10^{-5}\,\frac{\mathrm{rad}}{\sqrt{\mathrm{Hz}}}$, while the raw data vary by a factor of two. This indicates that the reduced noise level is not limited by the balancing efficiency but by another noise source below. Nothing was changed between the measurements, and the different behavior is presumably
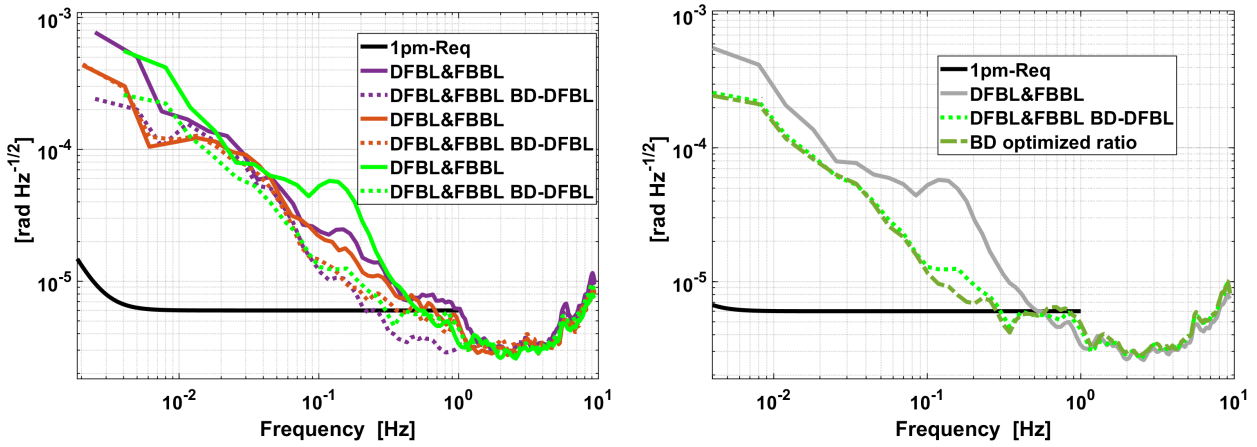
(a) Balanced detection (BD) effect on the non-reciprocity in different measurements. They also illustrate the varying noise levels that might be caused by fluctuations in the reference laser's frequency.

(b) Balanced detection using normalization and a changed ratioyielded little improvement in the center frequencies.

Fig. 3.22.: Balanced detection in the center frequencies, only applied to the DFBL.

caused by the varying noise behavior of the free-running reference laser.

Balanced detection is typically limited by the unequal signal amplitudes in both ports, caused by the non-perfect 50:50-ratio of a bs or by different PDs at each interferometer port (QPD vs. SED) [Ste08; Die13]. As a solution, the phasors that are created in post-processing are normalized before summation, and their ratio can be changed to optimize the noise suppression. More details are given [Ste08]. The normalization and the ratio changing were applied in the measurement presented here, with only minimal gain, as shown in Figure 3.22b.

Balanced Detection in the low frequency range is discussed later in Section 3.9.2.

3.8.5 Electrical Cross-Coupling

Electronic cross-coupling in the PMs is a potential noise source in the center frequencies and is introduced in this Section. Electronic split measurements in the BaliRo have been performed in the infrastructure-testing in Section 3.3.2 where only the signals required for the measurement were connected to the BaliRo. The measurements were repeated while optical signals were tracked in another channel simultaneously to investigate cross-coupling between the channels. The results from a measurement run performed by M. Ast are presented in Figure 3.23. The electrical split measurements are shown jointly with the noise level in the single channels. The measurement without an additional signal, shown in the green curves, performs similarly to the electrical split measurements in the TIfo. Next, the optical signals from the 3BL including all five possible BNs were connected to the BaliRo. These BNs were at the multiples of f_0; 25,52,60,28 and 36. Shown in the blue curve is an electrical split measurement that was performed at $42 \cdot f_0$. The single-channel measurements from the electronic split are no longer overlapping, and their combination, which is the electric split measurement, is significantly higher than for the case without an additional signal. Accordingly, the optical signal influences the electrical split measurement. This becomes more severe when the signal for the electrical split measurement uses one of the optical frequencies, as shown in the pink curve. The noise of the phase in the single channels is again higher, they do not overlap,
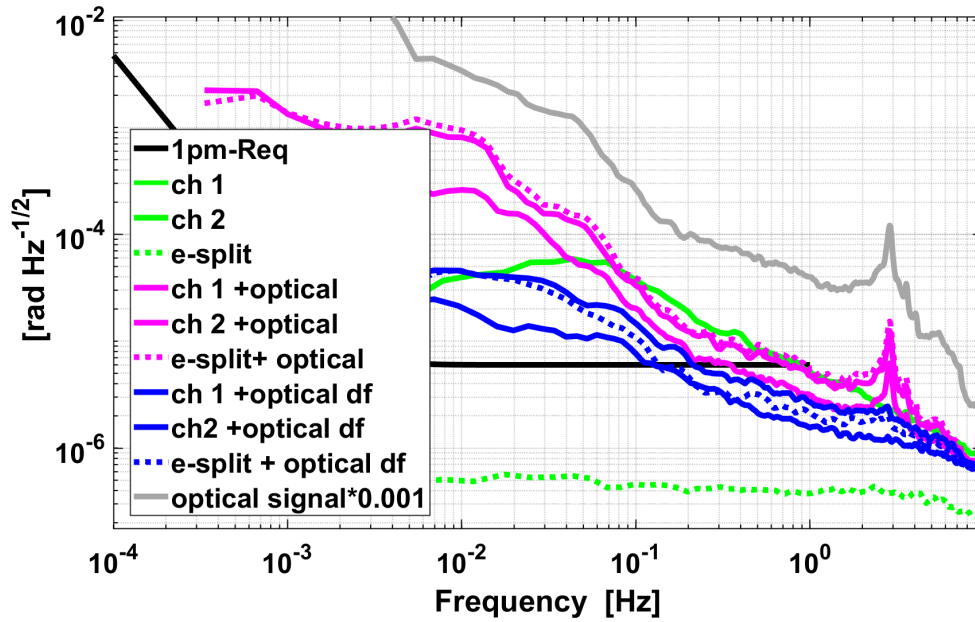
Fig. 3.23.: Electrical split (e-split) measurements with additional optical signals in the PM at the same frequency and at a frequency more than $50\,\text{kHz}$ apart (df). The cross-coupling increases when electrical and optical signal are at the same frequency and the features of the optical measurements couple into the single electric measurements.

and their subtraction is above the requirement in the whole frequency range. A peak at $3\,\text{Hz}$ is visible in the single channels of the electric split measurement. It also appears in the single channel measurement of the optical signal, which is shown with a factor of 0.001. These measurements conclude that the optical signals couple differently into the electronic split measurements. The coupling is less strong for signals at different frequencies but still limits the measurement above the requirement even with a spectral distance of six multiples to the closest optical frequency.

Using PM channels physically apart or on different ADC cards yielded no improvement. The rise in the slope of the observed distortion in the electrical split measurements in the center frequencies seems similar to the one observed in the non-reciprocity measurements. Especially when considering the utilization of 14 channels and five BN, hence more combinations for cross-coupling.

A residual cross-coupling between the PM channels is not surprising. The cross-coupling values of the 4-Channel ADCs are -90 dBc between near channels and -105 dBc for far channels [Adc] and -55dBc for the *4DSP-Abaco FMC116* ADC-card. The latter relates to a suppression of less than three orders of magnitude, which is not particularly strong.

Using the other PM, PM4, could not circumvent this issue, see Appendix E.8.

Accordingly, both PMs must be improved in cross-coupling, and these investigations are ongoing. If the electronic cross-coupling suppression reaches a limit, shifting the BN frequencies can be an option. This can be done by mixing the signals from the TIA boxes with an analog mixer to a different frequency. Further options are an optical pathlength difference stabilization or a fiber length stabilization, as implemented in [Fle12]. They reduce the system's dynamics and overcome the PM's non-linearity while the non-reciprocal behavior can still be studied. The dynamics and with them the cross-coupling will also be reduced by a lower LFN that can couple between the channels. As discussed in Section 3.8.3, the LFN needs to be reduced in any case in the future with a more stable reference laser.

3.8.6 Laser Frequency Influence

The quality of the laser frequency locks couples into the non-reciprocity by increasing the white noise level in the high frequencies and the noise level in the center frequencies. The exact coupling mechanism is currently unknown, and degradation in the laser frequency locks happens randomly, causing varying noise levels in otherwise identical measurements. Especially Laser 3, which is the ALO' in the FSFBL, suffers from instabilities in its frequency and complicates the capturing of long-term measurements with reliable performances. Its electronic chain (like the PR and BaliLo channel) was exchanged with the one of another laser. However, no improvement was found; accordingly, this laser 3 will be exchanged soon.

3.8.7 Conclusion for the Center Frequencies

The discussed effects of laser frequency locks and the PM's cross-coupling influence the non-reciprocity in the center frequencies, where also LFN couples via backscatter and less strong nominal around $0.14\,\mathrm{Hz}$ (see Section 3.8.3). A combination of these noises presumably limits the non-reciprocity measurements in all three Backlinks.

A hint for the origin of this noise at the center frequencies can be found in the π-measurements shown in Figure 3.24 for the DFBL and FBBL. The reference laser stabilization decreases the noise in the DFBL π-measurements, as already discussed in Section 3.8.3. A measurement with the TIfo and activated reference stabilization, as discussed in Section 3.3, is at the same level as one of the DFBL-π-measurements. The 3BL and the TIfo use different optical set-ups, and thus the remaining noise is presumably not caused by the interferometers. However, this is not in agreement with the π-measurement of the FBBL, whose noise levels are below the π-measurement of DFBL and TIfo even without the reference's stabilization. If the DFBL and TIfo are limited by the same source, the noise is either canceled in the FBBL, or something in the electrical chain is different for the involved channels. However, the limiting noise in the DFBL π-measurements with stabilized reference laser might not be related directly to the DFBL and is presumably reducible. A TIfo measurement without the stabilized reference laser is not available.

To disentangle the possible limitations, further noise investigations are necessary. The laser frequency can be modulated to further study its coupling in the non-reciprocity, and a stabilized reference laser can verify that its stability reduces the noise at the center frequencies as expected. Additionally, the investigations in the PM cross-coupling are ongoing.

3.9 Low Frequency Range

The final frequency range investigated are the frequencies below $10^{-2}\,\mathrm{Hz}$, referred to as low frequencies. The main contribution to the noise limitation in this frequency range is presumably temperature coupling.
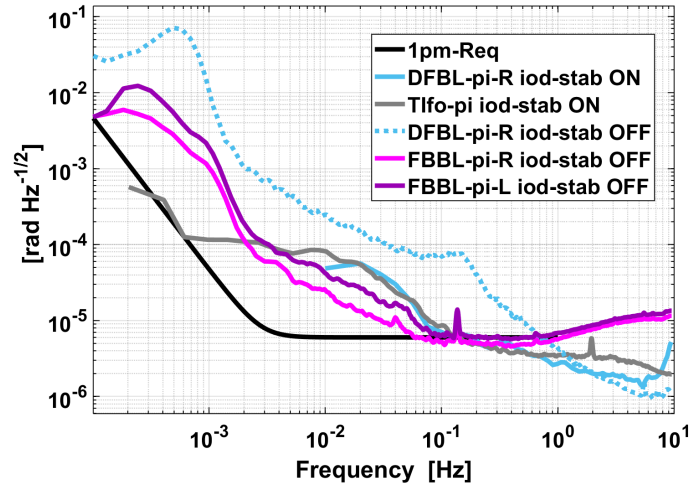
Fig. 3.24.: π-measurements for the DFBL,FBBL and TIfo. The reference laser was stabilized (iod-stab) in some measurements (ON/OFF).
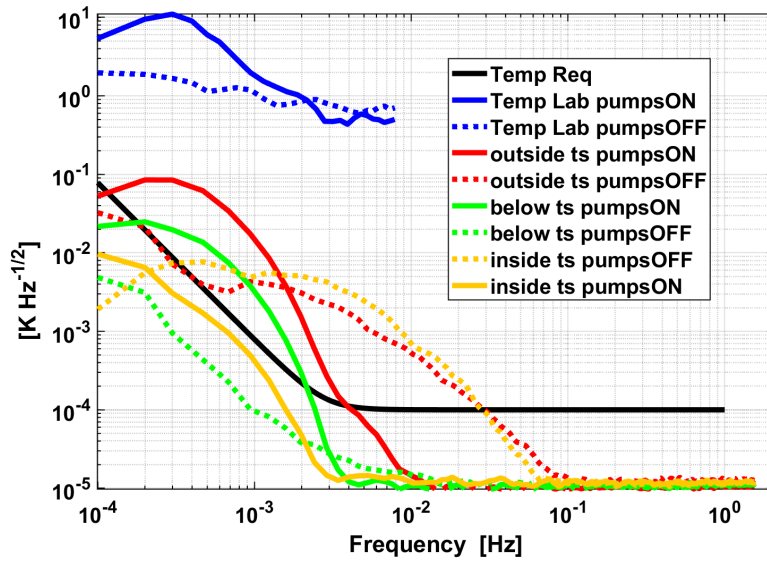
Fig. 3.25.: Temperature measurements in the laboratory (lab) and the vacuum chamber with and without the oscillations in the air conditioning, caused by the activated vacuum pump (pumpsON). The sensors are placed outside, below or inside the thermal shield (ts). Requirement $0.1\,\mathrm{mK}/\sqrt{\mathrm{Hz}}$ derived in [Isl18].

3.9.1 Temperature Coupling

In the frequency regime below $0.3 \cdot 10^{-2}$ Hz, temperature effects driven by the laboratories air conditioning are understood to limit the non-reciprocity of the DFBL. In this section, their origin and the modeling of the coupling are discussed.

Temperature Environment in the 3BL

A multisensor by Kentix GmbH attached to the laboratory wall enables continuously measuring of the laboratory's temperature. The temperature is not particularly stable and is influenced by outside weather conditions and the present heat load of laboratory devices. Inside the vacuum chamber, PTC resistor sensors, PT1000, are attached to the inner walls, the rotation stages, and inside the thermal shield. The thermal isolation, behaving as a thermal low-pass filter, does not prevent coupling from laboratory temperature to the inside of the thermal shield at low frequencies. The amplitude spectral densities of the temperature in the laboratory and the vacuum chamber are shown in Figure 3.25. As discussed in the following, the temperature behavior changes with activated vacuum pumps. The included temperature requirement of $0.1 \, \text{mK}/\sqrt{\text{Hz}}$ derived for the optical benches [Isl18], is based on the thermal expansion of the base plate material.

Coupling from Temperature to Phase

The change in the temperature of the fiber will lead to expansion and refractive index changes and, consequently, to a phase change. This was investigated by J. M. Rohr [Roh22], as shortly discussed in Section 1.2.3. A value of $50 \, \text{rad/K/m}$ was determined for fibers similar to the ones used in the 3BL. The feedthrough fibers of $12 \, \text{m}$ are mostly guided along the laboratory walls before entering the vacuum chamber. They are covered in plastic tubes and bubble-wrap to reduce the coupling of the laboratory temperature and movements due to airflow. The temperature couples via the coupling factor to the nominal phases inside the fibers. This coupling appears in the phases of the individual interferometers, because the coupling differs for both involved fibers. It should cancel in the non-reciprocity combinations, but residuals can appear if the common-noise suppression is insufficient. The coupling effect to the nominal interference in the Backlink fiber to the individual phases is much smaller because of the shorter fiber and the more stable temperature environment by about five orders of magnitude.

Additionally, the backscatter inside the fiber experiences the same temperature-to-phase coupling. This results in a phase error in the measured signal and is again described with the small vector formula discussed in Section 1.2.1:

$$\varphi_{\text{error}}^{\text{temp}} \approx \sqrt{\text{P}_{\text{ratio}}} \cdot \sin\left(\varphi_{\text{SL-temp}}\right), \tag{3.19}$$

with the relevant power ratio P_{ratio}, and $\varphi_{\text{SL-temp}}$ describing the phase dynamics driven via temperature. This coupling is again non-linear.
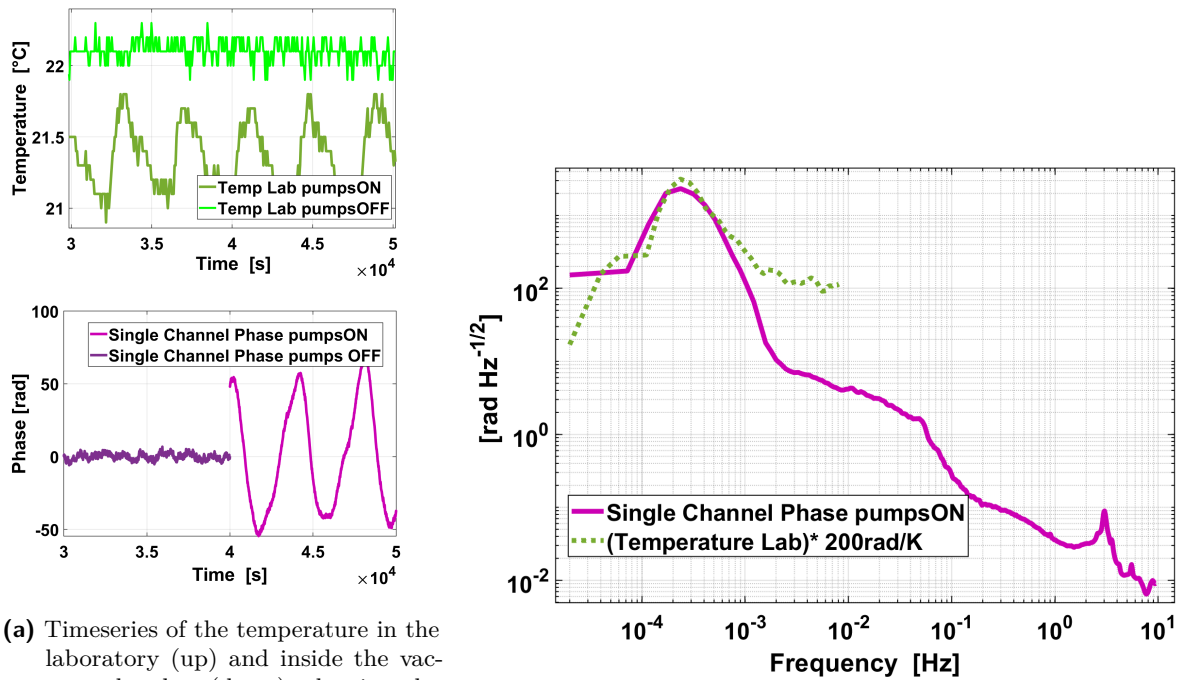
(a) Timeseries of the temperature in the laboratory (up) and inside the vacuum chamber (down), showing the difference between active/non-active vacuum pumps.

(b) Amplitude spectral density of a single channels phase and the laboratory temperature scaled with a coupling factor of 200 rad/K.

Fig. 3.26.: Influence of the vacuum pumps on the temperature and the temperature on the single channel phases.

Observed Temperature Coupling

The laboratory temperature depends on the present heat load, which is increased by about one order of magnitude when the vacuum pumps are active. It triggers an oscillation of the laboratory temperature with a frequency of about $0.3 \, \text{mHz}$ and a peak-to-peak amplitude of about $1 \, °\text{C}$, as shown in the upper left picture in Figure 3.26a. The corresponding phase measurements in one single channel are shown below it. The timeseries of the temperature and the measured phase in a single channel are each compared in two measurements with activated and deactivated vacuum pumps.

An increased noise around the corresponding frequency was observed in the single channels and in the non-reciprocity measurements. The coupling into the single-channel phases can be associated with the involved lasers and their fibers by disentangling the involved laser pairs. The coupling is strongest in Laser 2 (L2), followed by L4, L1 and L3. This is probably caused by slight differences in the wrapping quality and their exposure to air and the laser preparation table.

In the non-reciprocity measurements, the coupling is most prominently in the DFBL. As discussed in Section 3.8.3 for LFN, noise sources can couple via backscatter at this Backlink. In the following, temperature coupling via backscatter to the non-reciprocity is analyzed. The temperature also couples to the measurement via the nominal interference. However, this effect is not assumed to be part of the observed noise floor because it is expected to also be visible in the FSFBL, which is at a lower noise level compared to the DFBL.

Modeling of Temperature Coupling with Measured Data

The nominal coupling from temperature to the single channel measurements is modeled based on the temperature measured with the Kentix sensor. The single channel phase information contains the interference of two beams propagating through different fibers. The fiber ends on the preparation side are coiled up and placed on the optical table at different positions. Therefore, the temperature noise and the phase changes in the fibers are very likely uncorrelated, and no sufficient common mode subtraction is possible. This can be seen in Figure 3.26b. The temperature-to-phase coupling appears in the single channel's phases via:

$$\varphi_{\text{DFBL-L}}^{\text{temp}} = \tilde{t}_1 \cdot c - \tilde{t}_2 \cdot c \tag{3.20}$$

with the coupling factor c and the temperature noise $\tilde{t}_1$ and $\tilde{t}_2$. Since no temperature measurements of the single fibers are available, an effective coupling factor c_{eff} was determined by fitting the one dataset of laboratory temperature $\tilde{t}$ to the single-phase measurement via $\varphi_{\text{DFBL-L}} = \tilde{t} \cdot c_{\text{eff}}$. As shown in Figure 3.26b the measurement is modeled with a factor of $200\,\text{rad/K}$. This coupling is expected to vanish in the non-reciprocity combination, and only residuals of insufficient common mode reduction are expected to couple.

This nominal temperature-to-phase coupling also happens inside the Backlink fiber with a length of $2\,\text{m}$, and a much lower temperature noise at about $0.01\,\text{mK}/\sqrt{\text{Hz}}$ as shown in Figure 3.25. The associated phase coupling in the single channel is neglectable compared to the part of the feedthrough fibers.

A coupling via backscatter is presumed because of the prominent noise increase only in the DFBL. It is modeled in *Matlab*, similar to the case of the LFN in Section 3.8.3. The phase error is assumed to be completely dominated by the temperature noise. The models are based on Equation 3.19:

$$\varphi_{\text{error}}^{\text{temp}} = x \cdot \sqrt{\frac{P_{\text{BS-TX}}^{\text{fiber}} P_{\text{TX'}}^{\text{fiber}}}{P_{\text{TX}}^{\text{ifo}} P_{\text{TX'}}^{\text{ifo}}}} \sin\left(\varphi_{\text{SL-temp}} + y\right) \tag{3.21}$$

with the powers of the beams interfered inside the fiber $P_{\text{BS-TX}}^{\text{fiber}}$ and $P_{\text{TX'}}^{\text{fiber}}$, and the powers of the nominal interference inside the interferometer, $P_{\text{TX'}}^{\text{fiber}}$ and $P_{\text{TX}}^{\text{fiber}}$. The coupling from temperature to phase is happening in $\varphi_{\text{SL-temp}} = z \cdot c_{\text{temp-phase}} \cdot \tilde{t}$, with the measured temperature $\tilde{t}$, and the modeling factors x, y and z. They are introduced to model the measured temperature to the measured non-reciprocity in the time domain. The effect is again assumed not to be correlated between both sides, and to be consistent with Equation 3.16. Hence the difference appears in the non-reciprocity:

$$\text{non-rec} = \ldots + x \cdot \sqrt{P_{\text{L}}} \sin\left(\varphi_{\text{SL-temp-L}} + y\right) - x \cdot \sqrt{P_{\text{R}}} \sin\left(\varphi_{\text{SL-temp-R}} + y\right) \tag{3.22}$$

with the power ratios for the left and the right side denoted by $P_{\text{L/R}}$. For simplicity, the same modeling factors are included on both sides. Temperature measurements from two sensors inside the thermal shield were used to differentiate between the left and the right bench in the model. Accordingly, this is not a sophisticated model but a first approach to investigate the coupling mechanism. The modeling factors x, y and z were varied until the frequency and the order of magnitude in the amplitude of the model were comparable to the timeseries of the measurement, as shown in Figure 3.27a. Adjusting the square root of the power ratio of x=0.25 was necessary. Accordingly, the

assumed ratio is too high, which can be caused by a possible deviation in the assumed backscatter level of $7\,\text{ppm/m}$, in the included coupling of 0.5, or deviations of the parameters on the bench. y=445.5 is only a time shift but z=5.2 changes the coupling coefficient between temperature and phase. The 5.2 times higher coupling might be explainable by the additional wrapping of the fiber in FEP (Fluorinated ethylene propylene), because fibers in jackets have been found to have a higher coupling [LBJ81]. More sophisticated modeling will be necessary for a proper coupling analysis. Additionally, the modeled timeseries mainly agree in the frequency and the approximate order of magnitude with the measured non-reciprocity. This illustrated the challenge in modeling this non-linear coupling. Future modeling will focus on the separate parts of the non-reciprocity calculation.

The corresponding amplitude spectral densities for the model is shown in Figure 3.27b in red dotted lines, compared to the measured non-reciprocity of DFBL&FBBL in dark violet. The modeled noise shows a noise increase at the same frequencies but slightly sharper and higher. The simplified modeling indicates a coupling of temperature to the phase of the fiber backscatter, which is visible in the non-reciprocity measurements.

Conclusively, the noise in the non-reciprocity is expected to change in a more stable laboratory temperature. This is estimated with this model by using a temperature measurement without the activated pumps, also shown in Figure 3.27b. It still violates the requirement in the low-frequency range.

For further analysis, balanced detection has been applied in post-processing in the *Matlab* code and reduces the noise by nearly one order of magnitude in the low frequencies, see Figure 3.27b. A detailed analysis of the balanced detection in this frequency range is given in the following Section 3.9.2.

Conclusion and Outlook on the Temperature Coupling

The here described modeling aims to provide a first, primitive verification of the existing models of noise coupling to the non-reciprocity via experimental measurements. Non-linear couplings are not easy to model and the speckle behavior of the backscatter is an additional challenge.

Changes in its air conditioning system will increase the thermal stability of the laboratory. Furthermore, using the AEI's "house vacuum", measurements without the additional heat load of the vacuum pumps can probe the performance in a more stable environment. This will support the model investigation of the temperature coupling by providing additional measurements in a different temperature environment. Furthermore, it will reveal the underlying noise floor at low frequencies.

Conclusively, the current measurements in the low-frequency range are presumably limited by the backscatter at the DFBL, which couples to the non-reciprocity because of the high temperature noise. The known coupling from temperature to phase can be applied to model its appearance in the non-reciprocity in the 3BL. With balanced detection, this noise reduces, which is in line with the statement that the backscatter is the dominant source. The application of balanced detection is not necessary for future 3BL measurements because the problem can be overcome by eliminating the laboratory's temperature oscillations.
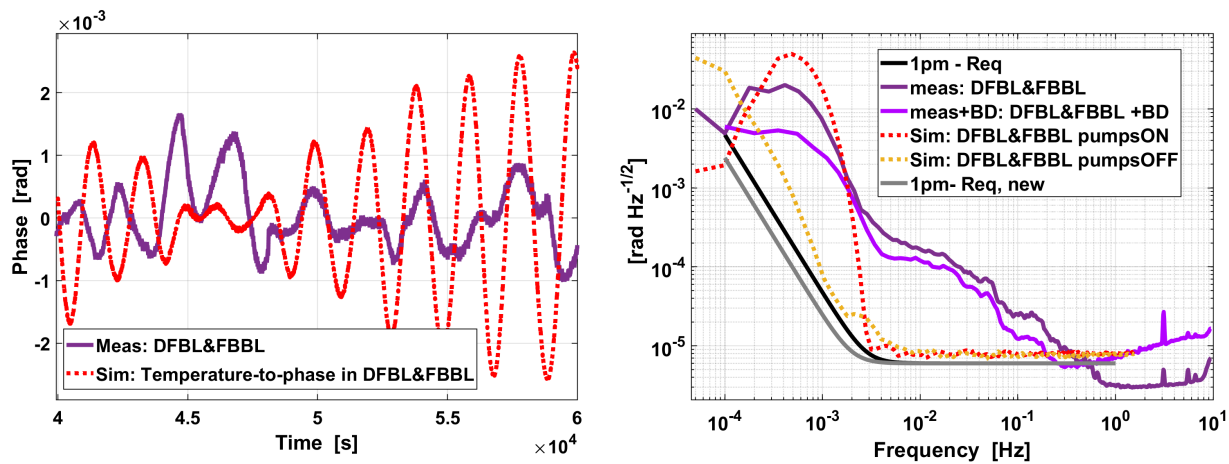
(a) Timeseries of the modeled coupling compared to the measured non-reciprocity

(b) Measured and modeled non-reciprocity, compared to balanced detection (+BD) and a model with low temperature environment. Also compared to the updated noise shape function as discussed in Section 3.2.2

Fig. 3.27.: Modeling of temperature coupling to non-reciprocal phase measurement with parameters x=0.25, y=445.5, z=5.2.

3.9.2 Balanced Detection in the Low Frequency Range

Based on the measured temperature noise and its coupling to the phase, the models in the previous section suggest that the fiber backscatter limits the non-reciprocity measurement of the DFBL. Figure 3.28a shows the influence of balanced detection in the non-reciprocity measurements of the DFBL&FBBL. The noise level is lower by nearly one order of magnitude in the low frequencies and is reduced over the whole frequency range. Balanced detection was also separately applied for the DFBL and the FBBL. Surprisingly, also the FBBL is affected by the balanced detection, though significantly less than the DFBL (comparing the green to the pink curve). Accordingly, some backscatter or residual polarization might influence the FBBL measurements. The FSFBL was not operated simultaneously because of the limited amount of PM channels, and no statement about the effect of balanced detection on it can be made. One possible source of backscatter in the FBBL are reflections at the waveplate *hpw2*, which is part of the Backlink path and only located on the right-sided bench. Reflections at this waveplate would lead to interference with the counter-propagating beam. The waveplate is supposed to be placed under an angle to reduce this problem; however, it has a small aperture that does not allow for a significant angle. The waveplate is fixed in its metal mount by a threaded ring. This metal mounting is more sensitive to noise caused by thermal expansion compared to the fused-silica optics. The previous section about LFN also discussed backscatter coupling, and the balanced detection, Section 3.8.4, showed no effect in the FBBL. This is not surprising because the LFN coupling via backscatter at *hwp2* cancels in the non-reciprocal measurement. The coupling of the temperature works differently and does not cancel. Other noise sources like RIN coupling that is also removed via balanced detection or cross-coupling effects can also not be excluded at this point.

A higher noise reduction was achieved by changing the ratio of the balancing amplitudes in *Matlab*. Figure 3.28b compares the non-reciprocity with the optimized balanced detection combination and a measurement with a different Backlink combination that does not include DFBL. If the latter is limited by fiber backscatter, the balanced detection applied noise curve is expected to be
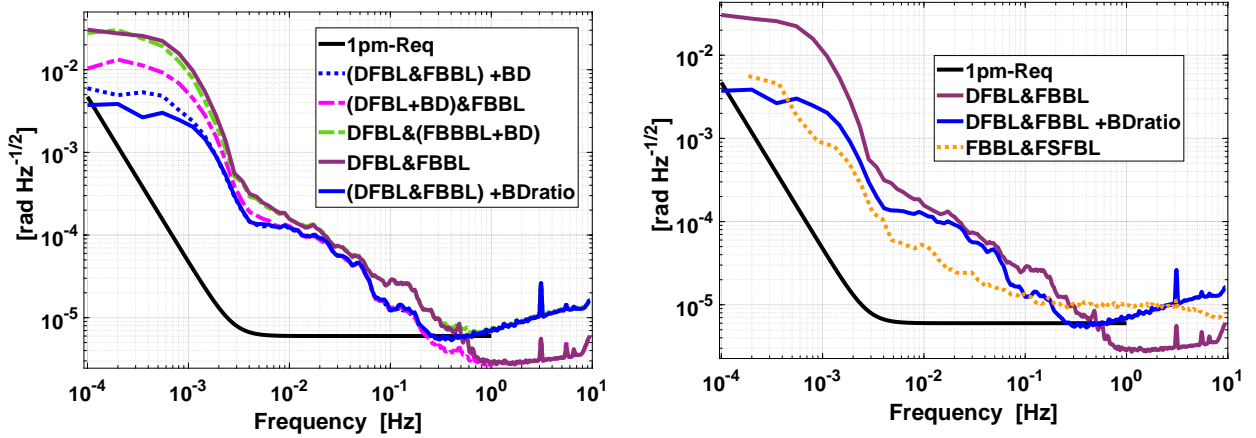
(a) Non-reciprocity without and with balanced detection (+BD), applied for the DFBL and FBBL separately and weighted (+BDratio).

(b) Comparison between the balanced non-reciprocity of DFBL&FBBL to the FSFBL&FBBL. The noise levels in the low frequencies are comparable.

Fig. 3.28.: Balanced detection influence in the low frequency range. The noise increase above 1 Hz is caused by the noise floor of the QPDs that are involved in the balanced detection calculation of the FBBL.

at a similar level as the FBBL&FSFBL measurement. This combination should not be limited by DFBL-backscatter. Since the noise levels are comparable in the low frequencies, it is possible that after the application of balanced detection, the residual noise is common in all three Backlinks in this frequency range.

3.10 Interpretation of the Best Measurement

After the first measurements, several noise analyses and improvements were applied, and the most important ones were presented in the previous sections. Figure 3.29 summarizes the main improvements. The noise floor in all three Backlink combinations is decreased significantly in the center frequencies when operated in vacuum, as described in Section 3.8.1. The choice of higher BN frequencies (see Section 3.7.1) improved the noise in all combinations in the high-frequency end, and the DFBL and the FBBL performances were decreased to the 1 pm-requirement. In the center frequencies, the noise of the FSFBL was reduced with laser power stabilization, presented in Section 3.8.2. In that frequency range, the DFBL presumably shows a coupling of LFN via backscatter in its fiber, as modeled and discussed in Section 3.8.3. This coupling can be reduced by a better stabilization of the laser frequency of the reference laser. Below this noise, cross-coupling in the PM and the effect of improper laser frequency stabilization of the transponder lasers is assumed to be limiting, see Sections 3.8.5 and 3.8.6. A similar noise presumably limits the FSFBL&FBBL combination. Their dominant noise lies below the DFBL. This is similar to the different levels in the π-measurements in Section 3.8.7 and might be caused by the same effect.

The final curves in Figure 3.29 show a slightly higher noise level in the DFBL-combinations with the FSFBL compared to the FBBL. Accordingly, the FSFBL performs slightly worse than the FBBL. The combination of FSFBL&FBBL is higher than the difference between DFBL&FSFBL and DFBL&FBBL, implying that the FBBL is also limited above the pm-requirement. Accordingly, the FBBL performs best in the center frequencies, followed by the FSFBL and the DFBL. In the
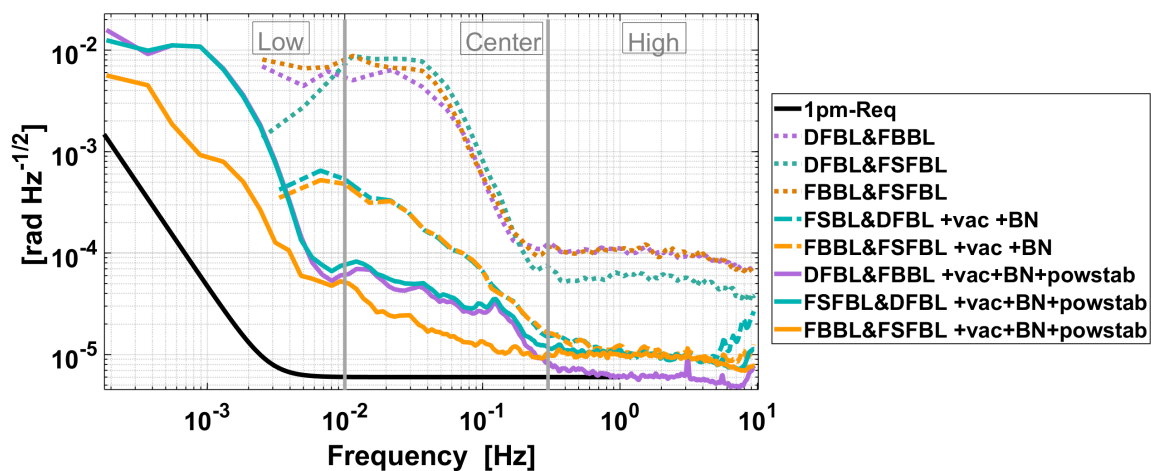
Fig. 3.29.: Noise improvements presented in this thesis decrease the noise from the first 3BL measurement to the optimized one, shown for the three discussed frequency ranges: in the high frequencies, the BN choice (BN) and in the center frequencies the vacuum (vac) and laser power stabilization (powstab). The remaining limiting noises are discussed and hypotheses and models presented in this thesis.

other frequency ranges, the upper two curves overlap and provide no conclusion about the relation of the two remaining Backlinks.

In the lower frequencies, the DFBL is limited by temperature couplings via backscatter, as modeled and discussed in Section 3.9.1.

Noise coupling via backscatter is observed in the DFBL, which is expected for this Backlink design. The observed coupling mechanism was caused by LFN and the temperature environment. Reducing these couplings by a more stable reference laser and laboratory temperature will reveal the noise sources below. The FBBL, which suffers most from TTL and the dynamic stray light with rotation, was not thoroughly investigated because the benches were not yet rotated. The rotation will be added as soon as the current limiting noise terms are removed. The FBBL shows promising behavior in a non-rotated environment and is so far the best-performing Backlink option. The FSFBL shows an improvement with the laser power stabilization and performs better than the DFBL, which indicates the suppression of backscatter coupling in this implementation is working. In π-measurements performed with only the fiber Backlinks in 3.4.3, the pm-requirement was reached for a REF and a FSFBL interferometer. They probe the pm-stability of the general environment, including the temperature and the PR-chain. Both interferometers operate with unique frequencies each, while the other two unique frequencies and the twice appearing DFBL-frequency have a higher noise level. This can point to a cross-coupling effect in the PM but also to additional noise contributions. It is presumably a matter of further noise suppression to reach the requirement in the non-reciprocities.

The final conclusion is an upper limit for the performance of each Backlink, shown in Figure 3.29 under the temperature stability discussed in Section 3.9.1. The temperature environment is at least $10^{-5} \frac{\text{K}}{\sqrt{\text{Hz}}}$, which is limited by sensor noise.

The different behaviors of the Backlinks are a huge advantage for analyzing the different noise contributions and couplings. A significant amount of work to understand and reduce the noise in an

experiment of this scale was to be expected. No fundamental limiting noise sources were discovered in any Backlink to the current date. The $1 \frac{\text{pm}}{\sqrt{\text{Hz}}}$-requirement was reached in the non-reciprocity above 0.3 Hz in the FBBL and the DFBL, while the FSFBL is limited at $1.7 \frac{\text{pm}}{\sqrt{\text{Hz}}}$ in this frequency range. The DFBL has the highest noise floor in the center and low frequencies, while the FBBL is currently performing with the lowest noise contribution at the center frequencies, between 0.3 Hz and 0.02 Hz. Conclusively, the 3BL provides an excellent tool to probe and compare three Backlink implementations and a preliminary upper limit for their performances. Non-linear couplings of LFN and temperature noise were investigated, and hypotheses and models were presented.

3.10.1 Performance Improvement Strategies

The Three-Backlink Experiment (3BL) was optimized in the course of this thesis until the noise floor discussed in the previous Sections was reached. Further noise reduction in the experiment's infrastructure is necessary to test the pm-performance of all three Backlink implementations. A selection of time-consuming next steps that would have exceeded the scope of this thesis is collected here.

The laser frequency noise exceeds the experiment's goal and couples into the measurements. Accordingly, the reference laser's stabilization must be repaired or replaced. The performance of the transponder Laser 3 is unreliable and consequently adds noise to the system or loses lock. After unsuccessful improvement approaches, this laser will be exchanged. The high-noise temperature environment will be reduced by improving the air conditioning and switching from the local pumps to the house vacuum. Investigations of the PMs will reduce the problem of the BN choice for the FSFBL and the current cross-coupling problem. If the latter can not be fixed because of limited cross-coupling suppression, a workaround by an analog frequency shift of the signals before the PM is possible. Its coupling values can be determined to further understand the different noise coupling mechanisms. The coupling from laser power modulation to non-reciprocity will enable a noise projection that determines whether the current laser power stabilization works sufficiently. Similarly, modulation of the reference laser's frequency determines its coupling into the non-reciprocal measurement. Inside the PM, the locked lasers' frequencies can also be modulated for probing if the current laser frequency stabilization is sufficient. After these improvements and analysis, other limiting noise sources will potentially be uncovered.

3.11 Future Measurements

The 3BL is expected to reach the 1pm-requirement after further improvement of the noise floor. It will enable making a statement about the performances of the single Backlinks and verify the feasibility of a Backlink for LISA for the first time between two separate benches and without post-processing.

After this accomplishment, the 3BL will remain a remarkably useful tool for investigating the Backlinks in more detail. This section gives an idea of valuable measurements of which measuring the non-reciprocity of a *Faraday rotator* and studying the dynamic range suppression of balanced detection were already presented in detail in [Isl18].

Rotation of the Benches

The motivation for the two-bench design of the 3BL lies in the telescope-pointing approach in LISA, where two optical benches in each s/c are rotated with a sinusoidal motion and an angle of $\pm 1°$. The 3BL's benches are placed on rotation stages to emulate this motion. Their operation will turn the two bench setup into an, even more, LISA-like test-bed. This presumably increases the dynamics of the FBBL significantly and allows studying its coupling into the non-reciprocity. The coupling of the dynamics to the fiber Backlinks will depend on the mounting of the fibers. The rotation stages are already part of the 3BL infrastructure and are ready for operation because they have already been operating in the Pre-Experiment [Isl18].

The rotation further enables to study the influence of a dynamic magnetic field on the fibers. The 3BL Benches are equipped with two *Faraday rotators* that introduce a magnetic field and imprint the Faraday effect on the Backlink and TX-fibers. While the influence in a stationary constellation is expected to be uncritical, it potentially increases with the rotation, by which the position of the *Faraday rotator* and thus the magnetic field changes.

Verifying the Combination of Fiber Measurements and Simulations

The two Backlink fibers consist of two separate fibers connected to each fios that are combined with a mating sleeve. Additional fiber types or fibers with varying fiber length can be inserted at this connection to test their influence on the non-reciprocity. These parameters have been studied for their backscatter values in single fibers ([Roh22; Ryb11]), and the results were used in simulations to predict the influence on the Backlink performance (see Chapter 4). Testing them directly in the 3BL enables their analysis in the Backlink path with the influence of the non-reciprocity. It will thus compare the results from separate measurements and simulations with the actual non-reciprocity measurement.

Similarly, the influence of temperature and motion, studied in [Roh22], can be investigated in an actual Backlink implementation. Modulating the temperature with a Peltier element or the motion with a Piezo actuator enables studying the increased dynamics in the non-reciprocity. This can be done for the Backlink and feedthrough fibers inside or outside the vacuum chamber.

Further testing of the backscatter model can be done with the FSFBL. By operating the two additional local oscillators (Lasers 3 and 4) at the same frequency, the backscatter suppression at the Backlink fiber is disabled, and its coupling can be studied.

Switching the Bench's Orientation

The FBBL can be further investigated when the benches are switched to their original orientation. The influence of the pathlength change and the different angles for the steering mirrors can be investigated. A thorough study of the magnetic influences between the *Faraday rotators* or the use of μ-metal for magnetic isolation is highly recommended beforehand to avoid damage by the strong attraction between the magnets.

Measuring the Stability of the fios

The optical benches and their quasi-monolithic fiber couplers, the fios, are expected to be very stable. However, stability tests of these fios have not yet been performed. By placing QPDs in several ports of the interferometer, this can be investigated in the 3BL. The movement between the bench and the unstable PD mounts can be disentangled. This way, the stability of the fios design by D. Penkert can be measured.

Including Attenuation in front of the Backlink Fiber

The DFBL implemented in the 3BL does not include methods of reducing the backscatter at its Backlink fiber. As discussed in the next Chapter 4, the noise level can potentially be decreased if the beam into the Backlink fiber is attenuated. To provide the possibility to test this assumption, the constructed 3BL benches vary slightly from their original design. *fios2* was placed closer to the edge of the benches to increase the space in front of it. This enables gluing two additional components at this position, an attenuator and an additional mirror, to compensate for the lateral beam shift. This was not implemented in the performed construction but can be implemented in the future.

Even more elaborate would be a solution that allows for a temporary placement of components to test different attenuation levels. This was done off-bench in [Hen13] for testing variable attenuators in front of the TX-fiber.

Furthermore, by introducing artificial misalignments, for example, by adding a transmitting optic, the influence of the coupling efficiency on the Backlink performance can be studied. It is expected to be uncritical, but a potential increase of backscatter or unconsidered effects might appear.

Investigating the Backlink Performance with MHz BNs

To operate the 3BL in a more LISA-like environment, the BNs can be shifted to MHz frequencies. The current operation at kHz BN is chosen to operate PRs with the TIA outside the vacuum chamber, reducing the thermal load. As long cables should be avoided for MHz signals, they would need to be combined in a new design. A reduction to the minimal required amount should be considered. Furthermore, the change of the PDs will presumably alter the coupling coefficients of the FBBL, and its loops need to be adapted. A readout PM capable of tracking MHz needs to be installed. The laser preparation already allows for the usage of MHz frequencies; hence there is no need for changes.

The Backlink - The Big Picture

<div style="text-align: right; font-size: 3em;">4</div>

This chapter aims to set the 3BL and its results into perspective by summarizing the work of many people investigating a Backlink for LISA. It concludes with a summary of the thesis presented here.

Previous experimental Backlink investigation have been introduced in Chapter 1 for the first LISA-like Backlink experiment that was investigated by R. Fleddermann [Fle12], F. Steier [Ste08] and C. Diekmann [Die13], as well as an updated experiment with TX-attenuators by J.-S. Hennig [Hen13] and a spin-off for first backscatter measurements by J. Rybizki [Ryb11]. The experimental investigations revealed that in the bidirectional path in a fiber Backlink implementation, backscatter in the fibers limits the non-reciprocity measurement. Two different actions evolved from this; further investigation of the backscatter and other fiber parameters, performed by J. M. Rohr [Roh22], which eventually led to a design of an engineering model for the LISA Backlink. And investigations on the trade-off of different possible Backlink implementations by [Die13], [Hen13] and [Isl18], as already discussed in Chapter 1, which led to the design of the 3BL.

4.1 Further Backscatter Understanding

Noise coupling via backscatter at the fibers was found to limit the non-reciprocity measurements in a direct fiber Backlink implementation. To further understand the exact coupling mechanism, these previous measurements were combined with the fiber backscatter measurements in simulations performed by K.-S. Isleif, O. Gerberding and E. Fitzsimons in [Ger+19]. They assume the temperature-to-phase coupling as the underlying coupling mechanism and combine it with the fiber backscatter ratio, both measured by [Roh22]. Based on these assumptions, models were investigated with which the measurements from the experiment by R. Fleddermann could be re-constructed by using the temperature environments of TX-fiber and Backlink fiber. The Backlink fiber was operated inside the thermally stable vacuum chamber, while the TX-fiber was exposed to the laboratory environment during the measurement with temperature fluctuations. Accordingly, the modeled noise floor is dominated by the TX-backscatter. The result agrees with the non-reciprocity measurements without post-corrections. For further verification, this modeling was repeated for the update of this experiment with attenuators by [Hen13], and the 3BL's Pre-Experiment [Isl18]. These measurements are also well modeled by assuming that the backscatter in the TX-fibers couples to the non-reciprocity measurements via the temperature-to-phase coupling. The comparably shorter Backlink fiber in a more stable temperature environment has a less critical noise floor. This result initiated reconsidering the implementation of a direct fiber Backlink in LISA with additional noise suppression by attenuation, discussed in Section 4.2.

4.2 A Backlink Design for LISA

The possibility of attenuation in front of the Backlink fiber was investigated again as a further improvement. This was already discussed, for example, in [Ste08] and [Fle12]. The theoretical investigation by K.-S. Isleif and O. Gerberding revealed the feasibility of the following approach in a fiber Backlink implementation. Figure 4.1a illustrates how the beam is split in front of the Backlink fiber and the interferometer. This beamsplitter's power splitting ratio can be changed. For a high ratio of R/T, like for example, 99/1, only a fraction of the light is sent to the Backlink, and the absolute backscatter level is reduced. At the same time, the local nominal power in the local interferometer is increased. The coupling (see Equation 1.7) of spurious interference to the phase error depends on this power ratio between backscattered light and the local TX-beam. This ratio decreases with the ratio of the beamsplitter. This attenuation can be implemented on the optical bench in LISA.

The most studied Backlink implementation is a direct fiber. It was experimentally tested in the past [Fle12] and analyzed in the simulations mentioned above [Ger+19]. Additionally, the separate fiber measurements by [Roh22] provide a further understanding of the involved dynamics. More practically, the DFBL is the most straightforward implementation regarding the number of components and mechanics and does not need an additional light source. The baseline for LISA is a fiber-based Backlink [LIG18], and the recommended implementation at the point of writing is a direct fiber Backlink. Its design includes a high reflective bs in front of the fiber, a reduction of the noise floor by a factor of 10 via balanced detection and a thermal requirement for the fibers. The TX-fiber requires a thermal stability of $300 \frac{\mathrm{mK}}{\sqrt{\mathrm{Hz}}}$ and the Backlink fiber of $1.4 \frac{\mathrm{mK}}{\sqrt{\mathrm{Hz}}}$ [Ger+19].

The 3BL experiment studies a direct fiber Backlink connection in comparison with two other Backlink implementations, which enables an entanglement of the noise couplings, better than could be achieved with only one or two Backlinks. It also includes features like the two-bench design and the operation with rotation, which enables a realistic study of the LISA Backlink. It will support the baseline design by investigating different aspects of the Backlink and verification of the existing noise models. Additionally, a more mission-oriented experiment, an Engineering Model (EM), is planned for verification of the baseline Backlink design. Its optical bench is similar to the first LISA Backlink experiment in Figure 1.7, but with the mentioned performance improvements. Additionally, it will be entirely quasi-monolithic, with LISA specifications for the fibers, most components, baseplate, and the bonding process. The design was made by E. Fitzsimons and schematically shown in Figure 4.1b. A redundant Backlink is indicated, which can potentially be added to the set-up to test a redundancy scheme for the Backlink. Furthermore, artificial motion can be added to the fibers, similar to [Roh22] for mimicking rotating benches. The optical bench's construction will be done at the University of Glasgow, and testing is planned to be performed by the Backlink team at AEI in Hannover.
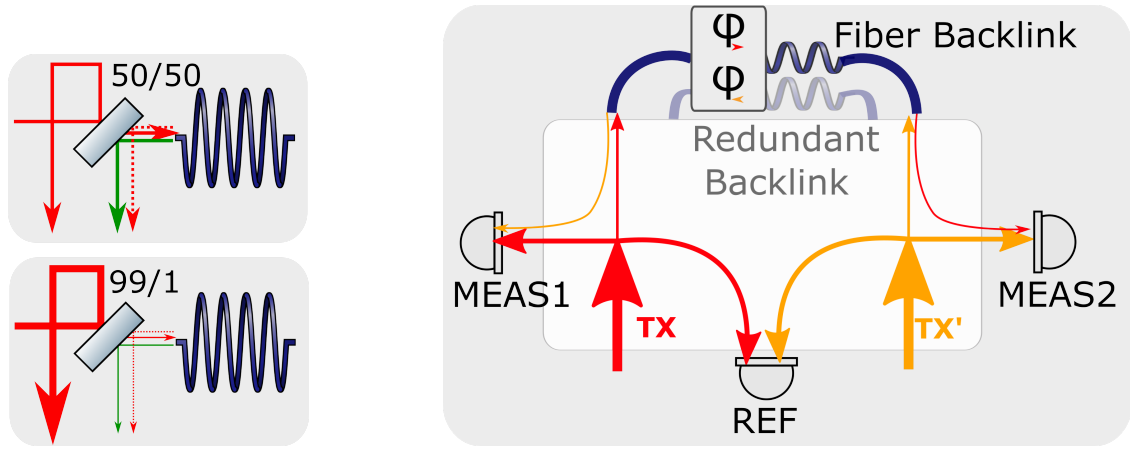
(a) The bs ratio of R/T determines the ratio between local beam and its backscatter at the Backlink fiber.

(b) Schematic drawing of the EM design for a direct fiber connection in the LISA Backlink, similar to the design by R. Fleddermann. The bs shown in (a) reduces the influence of backscattering at the Backlink Fiber. A second, redundant Backlink is indicated.

Fig. 4.1.: Schematic of the Backlink-EM design based on a high reflective beamsplitter in front of the backlink fiber and a design that is comparable to the one in [Fle12].

4.3 Backlink Studies with the Three-Backlink Experiment

As discussed in Chapter 1, the 3BL was designed according to different alternative Backlink implementations studied by [Isl18; Ste08; Hen13]. The 3BL compares the three implementations and studies their joint and different noise sources. The disentanglement of the three non-reciprocities, as discussed in Chapter 3, reveals information about each individual Backlink. The rotation stages will further enable studying the set-up with increased dynamics. The DFBL is a similar but worst-case version of the baseline in LISA (discussed in Section 4.2). It enables studying the backscatter of the Backlink fiber connection in detail. This is ensured by strongly attenuating TX-backscatter by the Faraday isolator. Furthermore, the 3BL can provide new insights into the behavior of a Backlink in a LISA-like set-up with two separate benches, which imprint a natural motion onto the Backlink fibers. This thesis provides the first measurements of a two-bench implementation of a LISA Backlink. Conclusions for different Backlink aspects and each Backlink implementation are presented in this section.

TX-Fiber Backscatter

Figure 4.2 compares the non-reciprocity measurement curves from the 3BL to those from [Fle12]. The thermal environments in both experiments are comparable, as shown for the inside of the vacuum chamber in Figure 4.3, and for the laboratory temperature based on the fact that both experiments were operated in the same laboratory. The influence of the backscatter coupling via temperature in both experiments is comparable. The shown performances of the three Backlinks are without the application of any post-corrections (balanced detection was applied in the previous chapter only for diagnostic purposes) and compared to the red dotted lines, showing the raw data from the measurements by R. Fleddermann. The noise levels in the three Backlinks are nearly two orders of magnitude lower in the high and center frequencies. This agrees with the understanding presented in Section 4.1, stating that the experiment from R. Fleddermann was
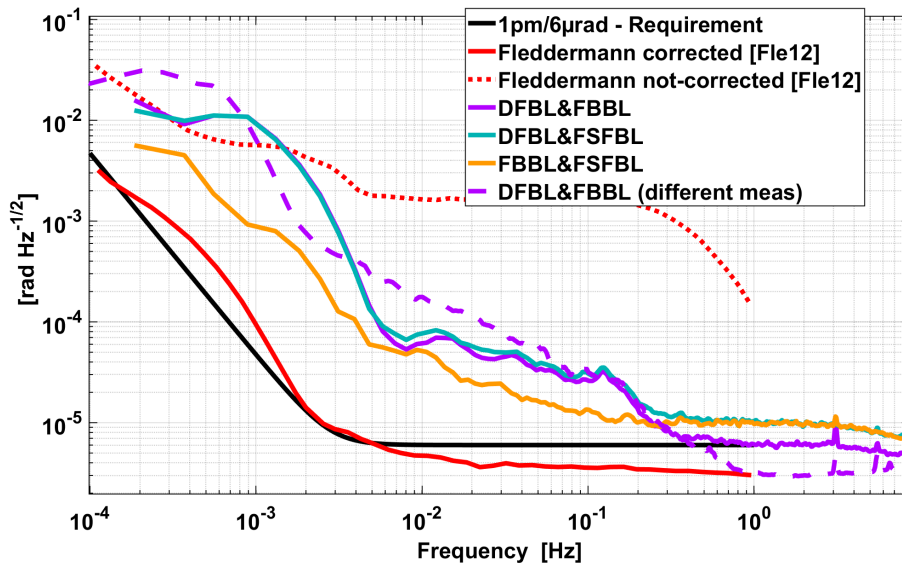
Fig. 4.2.: Non-reciprocity measurements of the three Backlinks in the 3BL and the results from R. Fleddermann [Fle12] without and with post-processing (Balanced Detection, DWS and temperature correction). The latter reaches the requirement while the non-corrected 3BL measurements are limited by noise in the center and low frequency range. An additional measurement for the DFBL&FBBL shows the varying noise levels in different measurements.
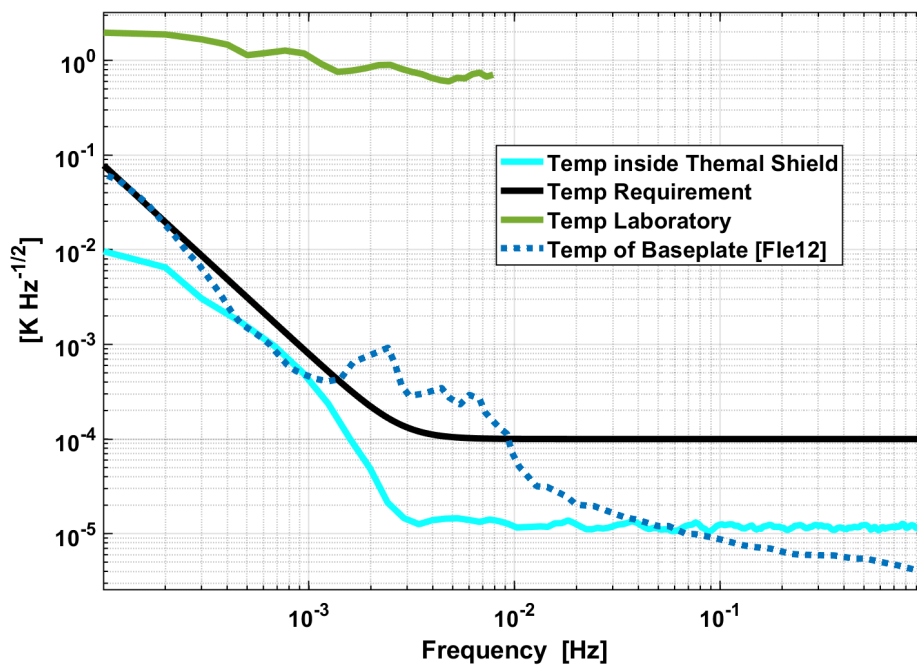
Fig. 4.3.: Temperature environment in the 3BL thermal shield inside the vacuum chamber and laboratory compared to the temperature measurements from R. Fleddermann (from [Fle12]) of the experiment's base plate.

limited by TX-backscatter. In principle, the DFBL implementation is the same in both experiments: the TX- and TX'-beams propagate through a fiber in both directions, with direct paths for the backscatter to enter the interferometers. However, the DFBL in the 3BL includes a Faraday isolator that suppresses the TX-backscatter significantly, leaving mainly the noise of the Backlink fiber backscatter. This is significantly lower than the noise coupling due to the backscatter at both fibers in R. Fleddermann. There are other differences in the designs and constructions of both experiments, like the quasi-monolithic fiber couplers in the 3BL. They are considered negligible in this argument because the influence of stray light in R. Fleddermann was nearly two orders of magnitude higher. This indicates that the design goal of the 3BL, to reduce the noise coupling from the TX-fiber backscatter, was successful.

Furthermore, it supports the existing model of the coupling of fiber backscatter into the non-reciprocity.

With applied post-processing techniques, the noise level by R. Fleddermann mostly complies with the requirement, as shown in the solid red curve. A comparable data set is not yet available for the 3BL because it aims to reach the requirement without suppression techniques. In the low frequencies, a noise increase in the R. Fleddermann data slightly violates the requirement. This seems comparable to the high noise in the 3BL low-frequencies, which is assumed to be temperature coupling via the backscatter at the Backlink fiber.

Probing Noise Coupling Models in the DFBL

The opportunity given by the 3BL to study the DFBL Backlink noise, mostly independent from the TX-backscatter, enables better coupling and model verification investigation. Noise investigation in Chapter 3 indicate that LFN and temperature noise coupling via fiber backscatter cause the current limitations.

These noise sources are reducible by improved frequency stability of the reference laser and a more stable temperature environment in the future to enable more precise measurements. However, the other way around, these couplings enable studying the Backlink's backscatter. Both couplings can be enhanced; the LFN by modulating the frequency and the temperature by active changes in the temperature environment. This thesis's measurements and first modeling provided the primary tool and showed the feasibility of these investigations. It further concludes that backscatter and its coupling appear according to expectations. So far, simple modeling for a direct fiber Backlink agrees with the measurements.

FBBL, FSFBL and three Backlink Disentanglement

The FBBL implementation shows no disadvantage compared to the other Backlinks in a non-rotatable set-up. It provides a stable interferometer over two quasi-monolithic benches controlled via two steering mirrors that minimize the DWS measurements between the local and the Backlink beam. The noise floor is reduced compared to the off-the-shelf component-based Pre-Experiment [Isl18].

The FSFBL demonstrates the concept of suppressing the fiber backscatter coupling to the non-reciprocity measurements by frequency separation. The remaining noise floor could be related to

fiber backscatter, but no verification was found to the current date.

The overall concept of the 3BL is the parallel operation of three Backlinks which can disentangle the noise of each implementation. The feasibility of this concept is visible in Figure 4.2, which enables a conclusion about the best performing Backlink. This is the FBBL at the moment because it is not limiting its combination in any frequency range, and it contributes less to its combination with the DFBL compared to DFBL&FSFBL. It is further applied in the investigation of LFN coupling, only found in the DFBL, which pointed to the DFBL backscatter as the most likely candidate.

Upper Limit for the Backlink Performance

The 3BL concludes that a non-reciprocity level shown in Figure 4.2 is achievable for a LISA Backlink without any post-corrections in the given temperature environment in Figure 4.3. The LISA 1 pm-requirement is reached in the high frequencies for two implementations, while the violation in the central frequencies below $0.3\,\mathrm{Hz}$ is about an order of magnitude and more than three orders of magnitude in the mHz-range

This noise level is expected to change with the temperature environment of the Backlink fiber. The requirement for the Backlink in LISA in [Ger+19] is at $1.4\,\frac{\mathrm{mK}}{\sqrt{\mathrm{Hz}}}$ but can be subject to change in the future. The temperature noise floor above $3\,\mathrm{mHz}$ in the 3BL is below the sensor noise of $10^{-5}\,\frac{\mathrm{K}}{\sqrt{\mathrm{Hz}}}$. Enhancement of the temperature stability around the Backlink fiber will enable probing the temperature coupling and verify the understanding of the mechanism in a fiber Backlink implementation, and enables testing the performance in a LISA-like temperature environment.

The remaining limiting noise in the 3BL can be explained by couplings and noise sources that are not fundamental limits for either of the three Backlink's implementations. The first attempts at modeling these noise couplings agree with the measurements. They provide a basis for more sophisticated model analysis with the 3BL.

Optical Bench Stability

No disadvantages of using UV-glue on the optical bench construction have been observed. Estimations about the effect of glue wedges on the length measurement caused by thermal coupling have been performed and concluded to be uncritical. The first components were placed four years ago, and the following components were subsequently aligned, indicating sufficient long-term stability.

4.4 Thesis Summary and Outlook

The 3BL is a complex experiment that exceeds the scope of a single PhD thesis. K.-S. Isleif initiated the design and planning of the 3BL [Isl18]. The here presented thesis concludes the implementation of the actual experiment by its construction, including developing the necessary alignment techniques. The experiment was commissioned, including noise analysis and noise reduction, with an understanding of the remaining noise sources. An upper limit for the Backlink's performance was discussed in the previous section and is given in Figure 4.2. The finalization of this

measurement by reaching the 1 pm-requirement and the further extraction of Backlink knowledge will be suspect for future work in the following PhD thesis.

The goal of the thesis was the challenging construction of the optical benches and the commissioning and noise reduction in the experiment. This provides the 3BL as part of the investigation for the LISA Backlink.

Quasi-Monolithic Optical Bench Construction

The design of the optical benches for the 3BL demands a sophisticated construction process, as described in this thesis's first part. The new technique of a CQS and its quality verification process was discussed in detail. A thorough investigation of the measurement uncertainty, repeatability, long-term stability, and agreement of different CQS in the 1 µm-range present the CQS as an excellent tool for beam measurements. Single beam positions are measured with an averaged uncertainty of ± 3.02 µm and beam angles within an uncertainty of $u_{\alpha_B} = \pm 10.1$ µrad.

The most complex steps of the 3BL construction were summarized in five alignment strategies. They describe the alignment of a fios beam through an absolute alignment of the beam's propagation vector or relative to another beam. The relative alignment for beams propagating in the same direction is described for two levels of precision and differs from the more demanding counter-propagating case. The strategies can be combined further to place components with entangled placement constraints. The CQS enables tracking construction misalignment, which is especially important in the FBBL alignment. The noise level requirement for the DWS signals in its control loop depends on the achieved alignment precision. The preliminary requirement based on simulations was re-evaluated for the actually achieved alignment and later reached in the commissioned experiment.

Several aspects characterized the two benches, including a fiber coupling of about 50% for most connections. The contrast in the interferometers is between 50% to 90%, depending on the geometrical misalignment and the beam parameters. The latter varies for the different fios, with beam waists radius around 450 µm and waist locations between nearly zero and 650 mm with respect to the fios' fiber interface. The deviation from the target parameters derived in the simulations was estimated, and no critical concern was found. A catalog of observed spurious beams is given to support future noise mitigation in the experiment. The finalized optical benches, as the result of the construction, are shown in Figure 4.4.

The commissioning of the experiment evaluates the construction of the optical benches. Until the writing of this thesis, no noise sources inherent to the construction or imprecision during its assembling were found.

Three Backlink Measurements

The second part of this thesis focuses on the commissioning and noise analysis of the 3BL in Chapter 3. The infrastructure was pre-analyzed with a simple test interferometer, with split and π-measurements, and the former complies with the requirement.

The FBBL control loop was implemented and characterized in terms of its control-loop parameters, and the achieved DWS measurements are below the requirement as mentioned above derived from the construction misalignment.

After the 3BL's commissioning, π-measurements in two interferometers were the first measurements
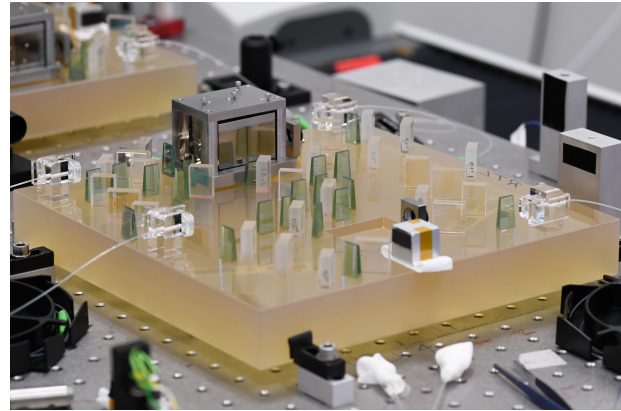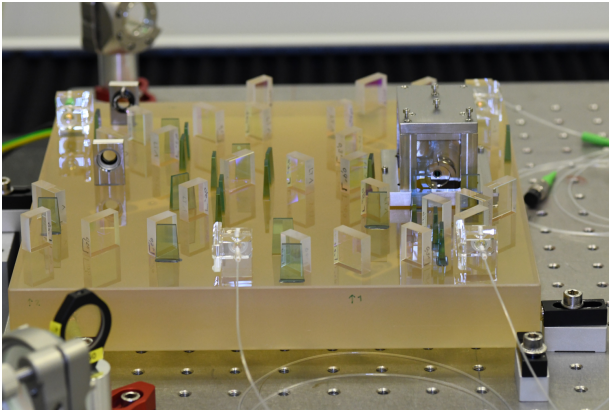
(a) First constructed bench that is implemented in the vacuum chamber on the right side.

(b) Second constructed bench that is implemented in the vacuum chamber on the left side

Fig. 4.4.: The finalized optical benches of the 3BL with their components and four fios each. The metal mount of the *Faraday rotator* and the beamstops wiith their greenisch material stand out.

with pm-precision. The noise floor in the non-reciprocity measurements of the three Backlinks was significantly reduced below $0.3\,\mathrm{Hz}$ by reducing the fluctuations of the refractive index of air at a vacuum level below $10^{-4}\,\mathrm{mBar}$. In the high-frequency range, above $0.3\,\mathrm{Hz}$, the non-reciprocity noise level was reduced with a better choice of BN frequencies and the 1pm-requirement compliant with the combination of DFBL&FBBL.

The FSFBL remains limited with a white noise level at about a factor of two higher. Stabilization of the laser powers decreased the noise level in this Backlink implementation in the center frequencies. The DFBL is expected to have a certain amount of fiber backscatter, which can be studied by the coupling of LFN in the center frequency range. Its coupling via the nominal and the backscattered light was investigated and compared to a model. Caused by a problem with the frequency stabilization of the reference laser, this coupling is presumably part of the noise floor in Figure 4.2, but can be reduced by an improved stabilization of or balanced detection in the future.

Backscatter coupling was further investigated via temperature at the fibers outside and inside the vacuum chamber and compared to modeling. This provides the understanding of temperature coupling to non-reciprocity in an active Backlink experiment. Again, active changes to the temperature environment and balanced detection can be applied to partially remove the noise, which is not included in Figure 4.2.

Further investigation revealed cross-coupling in the read-out PM, a significant influence of the transponder laser's frequency performance, and the necessity of an optimized ADPLL-setting in the PM.

The remaining noise floor in the non-reciprocity measurements in Figure 4.2 is assumed to be inherent to the experimental infrastructure, not the Backlink implementations. However, it can be interpreted as an upper limit for each Backlink performance in a temperature environment as shown in Figure 4.3 and without any post-corrections.

The combination of FSFBL&FBBL performs best, and the FBBL can be extracted as the best performing Backlink implementation at the current state with non-rotated benches. The DFBL has the highest noise floor that is limited between $0.3\,\mathrm{Hz}$ and $0.02\,\mathrm{Hz}$ below $6 \cdot 10^{-5}\,\frac{\mathrm{rad}}{\sqrt{\mathrm{Hz}}}$ (equivalent to $10\,\frac{\mathrm{pm}}{\sqrt{\mathrm{Hz}}}$), and at frequencies below $0.01\,\mathrm{Hz}$ below $3 \cdot 10^{-2}\,\frac{\mathrm{rad}}{\sqrt{\mathrm{Hz}}}$ ($5\,\frac{\mathrm{nm}}{\sqrt{\mathrm{Hz}}}$).

Big Picture

This last chapter provides an overview of the current status of the Backlink investigation. It introduces an engineering model whose design is based on previous direct fiber Backlink measurements, simulations, and separate backscatter and fiber investigations. The 3BL enables to probe models and understandings and verify for the first time a Backlink connection without post-processing between two benches close to the pm-requirement. The three individual Backlinks enable studying the individual influence in the here constructed, highly complex optical benches to expand the understanding of a LISA Backlink.

Outlook

The way forward for the 3BL is to remove limiting noise sources in the experimental infrastructure, investigate electrical cross-coupling, reduce the thermal oscillations, and identify possible remaining noise sources. Once the noise floor reaches the pm-level, the non-reciprocity of the three Backlink combinations will be studied. Disentangling the sole Backlink's performances provides conclusions about their advantages. Measurements like in Section 3.9.1 enable studying the model of temperature-to-phase coupling in a Backlink experiment. Jointly with the observed LFN coupling, the backscatter models can also be probed. The 3BL provides the possibility for multiple further investigations of the Backlink, as discussed in Section 3.11. An increased dynamic with the rotation stages is the most obvious one, providing an even more LISA-like test-bed. Adding additional components to the optical benches enables testing an implementation comparable to the LISA baseline and the EM. Different connectors and additional fibers can be attached to the Backlink fiber to investigate the expected increased backscatter. Shifting beatnotes in the experiment to MHz-frequencies requires an update of the read-out PM and PR but is feasible with the laser preparation and will be another step to a more LISA-like measurement.

This thesis provides a test-bed for the LISA Backlink on two separate rotatable benches. With three Backlinks, disentanglement of the noise sources and coupling mechanism is possible. The experiment's design reduces the influence of spurious lights, except for the DFBL, which enables studying the coupling mechanism of backscatter to the non-rec measurements in a direct fiber connection. Scattered and spurious light remains one of the critical challenges in the LISA metrology. This thesis is a further step towards implementing a Backlink in LISA.

Bibliography

[Abb+16] B. P. Abbott, Abbott R., Abbott T. D., et al. "Observation of Gravitational Waves from a Binary Black Hole Merger". In: *Phys. Rev. Lett.* 116 (6 2016), p. 061102 (cit. on p. 1).

[Abe+22] Homare Abe, Tomotada Akutsu, Masaki Ando, et al. "The Current Status and Future Prospects of KAGRA, the Large-Scale Cryogenic Gravitational Wave Telescope Built in the Kamioka Underground". In: *Galaxies* 10.3 (2022) (cit. on p. 1).

[AS+17] Pau Amaro-Seoane, Heather Audley, Stanislav Babak, et al. "Laser Interferometer Space Antenna". In: *arXiv* (2017) (cit. on pp. 1, 2, 10, 68).

[Ber+21] Diego Bersanetti, Barbara Patricelli, Ornella Juliana Piccinni, et al. "Advanced Virgo: Status of the Detector, Latest Results and Future Prospects". In: *Universe* 7.9 (2021) (cit. on p. 1).

[B.H] B.Halle. *Zero Order waveplates.* http://www.b-halle.de/products/retarders/retarders_zero_order.html. Accessed: 2022-09-01 (cit. on p. 92).

[Bis18] Lea Bischof. "An optical phase reference for LISA: Comparision of different solutions with picometer sensitivity". MA thesis. Institute for Gravitational Physics of the Gottfried Wilhelm Leibniz Universität Hannover, Max Planck Institute for Gravitational Physics (Albert Einstein Institute), 2018 (cit. on pp. 16, 78, 79, 148).

[Bis15] Lea Bischof. "Aufbau und Charakterisierung der Laservorbereitung für das 3-Backlink-Experiment". Bachelor's Thesis. Institute for Gravitational Physics of the Gottfried Wilhelm Leibniz Universität Hannover, Max Planck Institute for Gravitational Physics (Albert Einstein Institute), 2015 (cit. on p. 63).

[CM22] Craig Cahillane and Georgia Mansell. "Review of the Advanced LIGO Gravitational Wave Observatories Leading to Observing Run Four". In: *Galaxies* 10.1 (2022) (cit. on p. 1).

[Chi19] Andrew Chilton. "Technology Development for the LISA Mission". Copyright - Copyright ProQuest Dissertations Publishing 2019; Last updated - 2022-04-29. PhD thesis. University of Florida, 2019, p. 170 (cit. on p. 16).

[CKO21] Anja Knigge Christian Knothe and Ulrich Oechsner. "Perfectly coupled Making single-mode fiber coupling smooth and permanent". In: *Physics' Best* (2021) (cit. on p. 9).

[Chw+16] M Chwalla, K Danzmann, G Fernández Barranco, et al. "Design and construction of an optical test bed for LISA imaging systems and tilt-to-length coupling". In: *Classical and Quantum Gravity.* Classical and Quantum Gravity 33.24 (2016), p. 245015 (cit. on p. 21).

[Col+15] The LIGO Scientific Collaboration, J Aasi, B P Abbott, et al. "Advanced LIGO". In: *Classical and Quantum Gravity* 32.7 (2015), p. 074001 (cit. on p. 1).

[Deh12]   Marina Dehne. "Construction and noise behaviour of ultra-stable optical systems for space interferometers". PhD thesis. Institute for Gravitational Physics of the Gottfried Wilhelm Leibniz Universität Hannover, Max Planck Institute for Gravitational Physics (Albert Einstein Institute), 2012 (cit. on pp. 8, 12, 21–23, 25, 26, 29, 31, 42, 138, 149).

[Die13]   Christian Diekmann. "Development of core elements for the LISA optical bench : electro-optical measurement systems and test devices". PhD thesis. Institute for Gravitational Physics of the Gottfried Wilhelm Leibniz Universität Hannover, Max Planck Institute for Gravitational Physics (Albert Einstein Institute), 2013 (cit. on pp. 12, 98, 113).

[DL92]   editor-in-chief D.R. Lide. *CRC Handbook of Chemistry and Physics.* 71st ed. Boca Raton, FL, USA: CRC Press, 1992 (cit. on pp. 8, 30).

[Ell+05]   E.T. Elliffe, J Bogenstahl, A. Deshpande, et al. "Hydroxide-Catalysis Bonding for Stable Optical Systems for Space". In: *Classical and Quantum Gravity* 22 (May 2005) (cit. on pp. 29, 43, 57).

[Fit10]   Ewan D. Fitzsimons. "Techniques for precision interferometry in space". PhD thesis. University of Glasgow., 2010 (cit. on pp. 8, 10, 22–25).

[Fit+13]   Ewan D. Fitzsimons, Johanna Bogenstahl, James Hough, et al. "Precision absolute positional measurement of laser beams". In: *Appl. Opt.* 52.12 (2013), pp. 2527–2530 (cit. on pp. 21–23, 29).

[Fle12]   Roland Fleddermann. "Interferometry for a space-based gravitational wave observatory : reciprocity of an optical fiber". PhD thesis. Institute for Gravitational Physics of the Gottfried Wilhelm Leibniz Universität Hannover, Max Planck Institute for Gravitational Physics (Albert Einstein Institute), 2012 (cit. on pp. 7–9, 11, 12, 24, 85–87, 99, 113–116).

[Fle06]   Roland Fleddermann. "Komponentencharakterisierung für LISA Rauscharme Spannungsreferenzen und Reziprozität einer Glasfaser". Diploma Thesis. Institute for Gravitational Physics of the Gottfried Wilhelm Leibniz Universität Hannover, Max Planck Institute for Gravitational Physics (Albert Einstein Institute), 2006 (cit. on p. 11).

[Fle+18]   Roland Fleddermann, Christian Diekmann, Frank Steier, et al. "Sub-pm $\sqrt{(Hz)}^{-1}$ non-reciprocal noise in the LISA backlink fiber". In: *Classical and Quantum Gravity* 35.7 (2018), p. 075007 (cit. on pp. 11, 12).

[Geh19]   Martin Gehler. "LISA: observing gravitational waves from space (Conference Presentation)". In: *UV/Optical/IR Space Telescopes and Instruments: Innovative Technologies and Concepts IX*. Ed. by Allison A. Barto, James B. Breckinridge, and H. Philip Stahl. Vol. 11115. International Society for Optics and Photonics. SPIE, 2019 (cit. on p. 1).

[Ger14]   Oliver Gerberding. "Phase readout for satellite interferometry". PhD thesis. Institute for Gravitational Physics of the Gottfried Wilhelm Leibniz Universität Hannover, Max Planck Institute for Gravitational Physics (Albert Einstein Institute), 2014 (cit. on pp. 6, 64–66).

[Ger+19]   Oliver Gerberding, Katharina-Sophie Isleif, Ewan Fitzsimons, Michael Perreur-Lloyd, and David Robertson. *TN 1: Design Report.* Tech. rep. LISA-AEI-PRDS-TN1-2019. 2019 (cit. on pp. 12, 13, 113, 114, 118).

[Ger+17]   Oliver Gerberding, Katharina-Sophie Isleif, Moritz Mehmet, Karsten Danzmann, and Gerhard Heinzel. "Laser frequency stabilisation via quasi-monolithic, unequal arm-length Mach-Zehnder interferometer with balanced DC readout". In: *Physical Review Applied* 7 (Feb. 2017) (cit. on pp. 8, 21, 58).

[Haa14]   Björn E. Haase. "Characterisation and development of stable fibre couplers". Bachelor's Thesis. Institute for Gravitational Physics of the Gottfried Wilhelm Leibniz Universität Hannover, Max Planck Institute for Gravitational Physics (Albert Einstein Institute), 2014 (cit. on pp. 32, 33, 132).

[Har+21]   Peter Hartmann, Ralf Jedamzik, Antoine Carré, Janina Krieg, and Thomas Westerhoff. "Glass ceramic ZERODUR®: Even closer to zero thermal expansion: a review, part 1". In: *Journal of Astronomical Telescopes, Instruments, and Systems* 7.2 (2021), p. 020901 (cit. on p. 8).

[Har21]   Olaf Hartwig. "Instrumental modelling and noise reduction algorithms for the Laser Interferometer Space Antenna". PhD thesis. Institute for Gravitational Physics of the Gottfried Wilhelm Leibniz Universität Hannover, Max Planck Institute for Gravitational Physics (Albert Einstein Institute), 2021 (cit. on p. 2).

[Hei22]   Gerhard Heinzel. private communication. 2022 (cit. on p. 57).

[Hen13]   Jan-Simon Hennig. "Mitigation of Stray Light Effects in the LISA Backlink". MA thesis. Institute for Gravitational Physics of the Gottfried Wilhelm Leibniz Universität Hannover, Max Planck Institute for Gravitational Physics (Albert Einstein Institute), 2013 (cit. on pp. 12, 111, 113, 115).

[Isl18]   Katharina-Sophie Isleif. "Laser interferometry for LISA and satellite geodesy missions". PhD thesis. Institute for Gravitational Physics of the Gottfried Wilhelm Leibniz Universität Hannover, Max Planck Institute for Gravitational Physics (Albert Einstein Institute), 2018 (cit. on pp. 4, 6, 8, 12, 16, 18, 19, 30, 33, 40, 43, 44, 48, 49, 52, 53, 56, 57, 59, 61–65, 67–69, 73, 75, 77–79, 92, 93, 97, 101, 102, 109, 110, 113, 115, 117, 118, 139, 147, 148).

[Isl+18]   Katharina-Sophie Isleif, Lea Bischof, Stefan Ast, et al. "Towards the LISA backlink: experiment design for comparing optical phase reference distribution systems". In: *Classical and Quantum Gravity* 35.8 (2018), p. 085009 (cit. on pp. 16, 47, 65).

[JK17]   Yoon-Soo Jang and Seung-Woo Kim. *Compensation of the refractive index of air in laser interferometer for distance measurement: A review.* Seoul, 2017 (cit. on p. 86).

[JCGrr]   JCGM. "JCGM 100:2008 GUM 1995 with minor corrections, Evaluation of measurement data — Guide to the expression of uncertainty in measurement". In: *JCGM Publications* (Corrected Version 2010) (cit. on pp. 27, 139).

[Jes22]   Daniel Jestrabek. "Performance Optimization and First Measurements for the LISA Backlink Experiment". MA thesis. Institute for Gravitational Physics of the Gottfried Wilhelm Leibniz Universität Hannover, Max Planck Institute for Gravitational Physics (Albert Einstein Institute), 2022 (cit. on pp. 69, 72, 77, 78, 153, 154, 156).

[Kil06]   Christian J Killow. "Interferometry developments for spaceborne gravitational wave detectors". PhD thesis. University of Glasgow, 2006 (cit. on p. 8).

[Knu20]   Nicole Knust. "The Optical Benches of the Three-Backlink Experiment: Construction, Commissioning and Characterization". MA thesis. Institute for Gravitational Physics of the Gottfried Wilhelm Leibniz Universität Hannover, Max Planck Institute for Gravitational Physics (Albert Einstein Institute), 2020 (cit. on pp. 30, 32, 33, 38, 57, 132, 133, 135, 150).

[Koe18]   Harald Koegel. "Towards an Advanced LISA Payload Architecture Featuring In-Field Pointing and Spherical Proof Masses". PhD thesis. 2018 (cit. on pp. 3, 16).

[Kul+20]   Soham Kulkarni, Ada Umińska, Joseph Gleason, et al. "Ultrastable optical components using adjustable commercial mirror mounts anchored in a ULE spacer". In: *Appl. Opt.* 59.23 (2020), pp. 6999–7003 (cit. on p. 31).

[LBJ81]   N. Lagakos, J.A. Bucaro, and J. Jarzynski. "Temperature-induced optical phase shifts in fibers". In: *Applied Optics.* Applied Optics 20.13 (1981), pp. 2305–2308 (cit. on pp. 9, 105).

[LH09]   Ryan N Lang and Scott A Hughes. "Advanced localization of massive black hole coalescences with LISA". In: *Classical and Quantum Gravity* 26.9 (2009), p. 094035 (cit. on p. 2).

[Las]   Laseroptik. *Laseroptik / Coatings / Ranges / NIR 1030-1064 nm.* https://www.laseroptik.com/en/coatings/ranges/nir-1030-1064-nm. Accessed: 2022-09-01 (cit. on p. 92).

[Li+19]   Yupeng Li, Ya Zhao, Zhi-Jie Wang, Chao Fang, and Wei Sha. "Precision Measurement Method of Laser Beams Based on Coordinate Measuring Machine". In: *IEEE Access* PP (Aug. 2019), pp. 1–1 (cit. on p. 29).

[LIG18]   LISA-Instrument-Group. *DESIGN DESCRIPTION LISA Payload Definition Document.* Tech. rep. ESA-L3-EST-INST-DD-001. ESA estec, 2018 (cit. on pp. 3, 10, 11, 114).

[Liv+17]   J. Livas, S. Sankar, G. West, et al. "eLISA Telescope In-field Pointing and Scattered Light Study". In: *Journal of Physics: Conference Series* 840 (2017), p. 012015 (cit. on p. 3).

[Adc]   *Low Power Quad ADCs.* Datasheet. Linear Technology Corporation. 2009 (cit. on p. 99).

[Mar21]   Joseph Martino. *LISA Performance Model CBE and Allocations.* Tech. rep. LISA-LCST-INST-RP-003. LISA Consortium, 2021 (cit. on p. 11).

[MCB14]   C. J. Moore, R. H. Cole, and C. P. L. Berry. "Gravitational-wave sensitivity curves". In: *Classical and Quantum Gravity* 32.1 (2014), p. 015014 (cit. on p. 2).

[Ott15]   Markus Otto. "Time-delay interferometry simulations for the laser interferometer space antenna". PhD thesis. Institute for Gravitational Physics of the Gottfried Wilhelm Leibniz Universität Hannover, Max Planck Institute for Gravitational Physics (Albert Einstein Institute), 2015 (cit. on pp. 2, 10).

[Pac21]   Sarah Paczkowski. "Laser Frequency Stabilisation and Interferometer Path Length Differences during the LISA Pathfinder Satellite Mission". PhD thesis. Institute for Gravitational Physics of the Gottfried Wilhelm Leibniz Universität Hannover, Max Planck Institute for Gravitational Physics (Albert Einstein Institute), 2021 (cit. on p. 90).

[Pen16]   Daniel Penkert. "Hexagon - An Optical Three-Signal Testbed for the LISA Metrology Chain". Diploma Thesis. Institute for Gravitational Physics of the Gottfried Wilhelm Leibniz Universität Hannover, Max Planck Institute for Gravitational Physics (Albert Einstein Institute), 2016 (cit. on pp. 30, 32).

[Ris21]   Ira Rischkopf. "Development of a Multi-Channel Phasemeter forthe LISA Backlink". MA thesis. Institute for Gravitational Physics of the Gottfried Wilhelm Leibniz Universität Hannover, Max Planck Institute for Gravitational Physics (Albert Einstein Institute), 2021 (cit. on pp. 65, 66, 70).

[Rob22]   D. Robertson. "Optical Couplers for LISA". The 14th International LISA Symposium, Online Presentation. 2022 (cit. on p. 53).

[Rob+13]   D. I. Robertson, E. D. Fitzsimons, C. J. Killow, et al. "Construction and testing of the optical bench for LISA Pathfinder". In: *Classical and Quantum Gravity* 30.8 (2013) (cit. on p. 21).

[Roh22]   Johann Max Rohr. "Experimental investigations of fiber dynamics for the LISA back-link". PhD thesis. Institute for Gravitational Physics of the Gottfried Wilhelm Leibniz Universität Hannover, Max Planck Institute for Gravitational Physics (Albert Einstein Institute), 2022 (cit. on pp. 9, 102, 110, 113, 114).

[Ryb11]   Jan Rybizki. "LISA back-link fibre: back reflection of a polarisation maintaining single-mode optical fibre". Diploma Thesis. Institute for Gravitational Physics of the Gottfried Wilhelm Leibniz Universität Hannover, Max Planck Institute for Gravitational Physics (Albert Einstein Institute), 2011 (cit. on pp. 110, 113).

[Sal+09]   M Sallusti, P Gath, D Weise, M Berger, and H R Schulte. "LISA system design highlights". In: *Classical and Quantum Gravity* 26.9 (2009), p. 094015 (cit. on p. 3).

[Sch15]   Dennis Schmelzer. "Thermally compensated fiber injectors for the three-backlink and hexagon experiments". MA thesis. Institute for Gravitational Physics of the Gottfried Wilhelm Leibniz Universität Hannover, Max Planck Institute for Gravitational Physics (Albert Einstein Institute), 2015 (cit. on p. 30).

[Sch17]   Sönke Schuster. "Tilt-to-length coupling and diffraction aspects in satellite interferometry". PhD thesis. Institute for Gravitational Physics of the Gottfried Wilhelm Leibniz Universität Hannover, Max Planck Institute for Gravitational Physics (Albert Einstein Institute), 2017 (cit. on p. 56).

[Sch18]   Thomas S. Schwarze. "Phase extraction for laser interferometry in space : phase readout schemes and optical testing". PhD thesis. Institute for Gravitational Physics of the Gottfried Wilhelm Leibniz Universität Hannover, Max Planck Institute for Gravitational Physics (Albert Einstein Institute), 2018 (cit. on pp. 87, 88).

[SMH14]   Daniel Schütze, Vitali Müller, and Gerhard Heinzel. "Precision absolute measurement and alignment of laser beam direction and position". In: *Applied Optics* 53 (Sept. 2014), pp. 6503–6507 (cit. on pp. 24, 29, 142).

[Ses16]   Alberto Sesana. "Prospects for Multiband Gravitational-Wave Astronomy after GW150914". In: *Phys. Rev. Lett.* 116 (23 2016), p. 231102 (cit. on p. 2).

[Sho+19]   B. Shortt, L. Mondin, P. McNamara, et al. "LISA laser system and European development strategy". In: *International Conference on Space Optics — ICSO 2018*. Ed. by Zoran Sodnik, Nikos Karafolas, and Bruno Cugny. Vol. 11180. International Society for Optics and Photonics. SPIE, 2019, pp. 138 –151 (cit. on p. 88).

[Ste08]   Frank Steier. "Interferometry techniques for spaceborne gravitational wave detectors". PhD thesis. Institute for Gravitational Physics of the Gottfried Wilhelm Leibniz Universität Hannover, Max Planck Institute for Gravitational Physics (Albert Einstein Institute), 2008 (cit. on pp. 7, 8, 11, 21, 98, 113–115).

[Opt]   *Technical Datasheet OPTOCAST*. 3553-LV-UTF, 3553-LV-UTF-HW, 3553-LV-UTF-HM. Electronic Materials Inc. 2014 (cit. on p. 56).

[The+21]   The LIGO Scientific Collaboration, The Virgo Collaboration, The KAGRA Collaboration, et al. "GWTC-3: Compact Binary Coalescences Observed by LIGO and Virgo During the Second Part of the Third Observing Run". In: *arXiv* (2021) (cit. on p. 1).

[Tho22]   Thorlabs. *Thorlabs Photodiode Power Sensors (C-Series)*. https://www.thorlabs.de/newgroup page9.cfm?objectgroup_id=3328. Accessed: 2022-08-19. 2022 (cit. on p. 52).

[Tho95]   Kip S. Thorne. *Gravitational Waves*. 1995 (cit. on p. 1).

[van+08]   A.A. van Veggel, D. van den Ende, J. Bogenstahl, et al. "Hydroxide catalysis bonding of silicon carbide". In: *Journal of the European Ceramic Society* 28.1 (2008), pp. 303–310 (cit. on p. 8).

[VG12]   Herbert Venghaus and Norbert Grote. *Fibre optic communication : Key Devices, Springer Series in Optical Sciences*. Vol. 161. Berlin, Heidelberg: Springer, 2012 (cit. on pp. 5, 9).

[WH14]   G. Wanner and G. Heinzel. "Analytical description of interference between two misaligned and mismatched complete Gaussian beams". In: *Appl. Opt.* 53.14 (2014), pp. 3043–3048 (cit. on pp. 5, 8, 49, 149, 150).

[Wan10]   Gudrun Wanner. "Complex optical systems in space : numerical modelling of the heterodyne interferometry of LISA Pathfinder and LISA". PhD thesis. Institute for Gravitational Physics of the Gottfried Wilhelm Leibniz Universität Hannover, Max Planck Institute for Gravitational Physics (Albert Einstein Institute), 2010 (cit. on p. 66).

[Wan+12]   Gudrun Wanner, Gerhard Heinzel, Evgenia Kochkina, et al. "Methods for simulating the readout of lengths and angles in laser interferometers with Gaussian beams". In: *Optics Communications* 285.24 (2012), pp. 4831–4839 (cit. on p. 24).

[Win17]   Michael Winter. "Performance of optical components for the LISA backlink". MA thesis. Institute for Gravitational Physics of the Gottfried Wilhelm Leibniz Universität Hannover, Max Planck Institute for Gravitational Physics (Albert Einstein Institute), 2017 (cit. on pp. 16, 40).

[Wis+22]   Lennart Wissel, Andreas Wittchen, Thomas S Schwarze, et al. "Relative-Intensity-Noise Coupling in Heterodyne Interferometers". In: *Physical Review Applied* 17.2 (2022), p. 024025 (cit. on pp. 7, 83, 87, 97).

[Wra19]   Juliane Freiin von Wrangel. "Interferometer to measure temperature-dependent angular tilts and mode matching of fiber couplers". MA thesis. Institute for Gravitational Physics of the Gottfried Wilhelm Leibniz Universität Hannover, Max Planck Institute for Gravitational Physics (Albert Einstein Institute), 2019 (cit. on pp. 58, 135, 147).

A

Additional Construction Information

This Appendix provides further information about details of the gluing technique, the polarization alignment of each fios, step-by-step description of typical alignment steps and additional details about Strategy 2.3.3. It aims to be supporting future optical bench constructions.

A.1 Laser Preparation
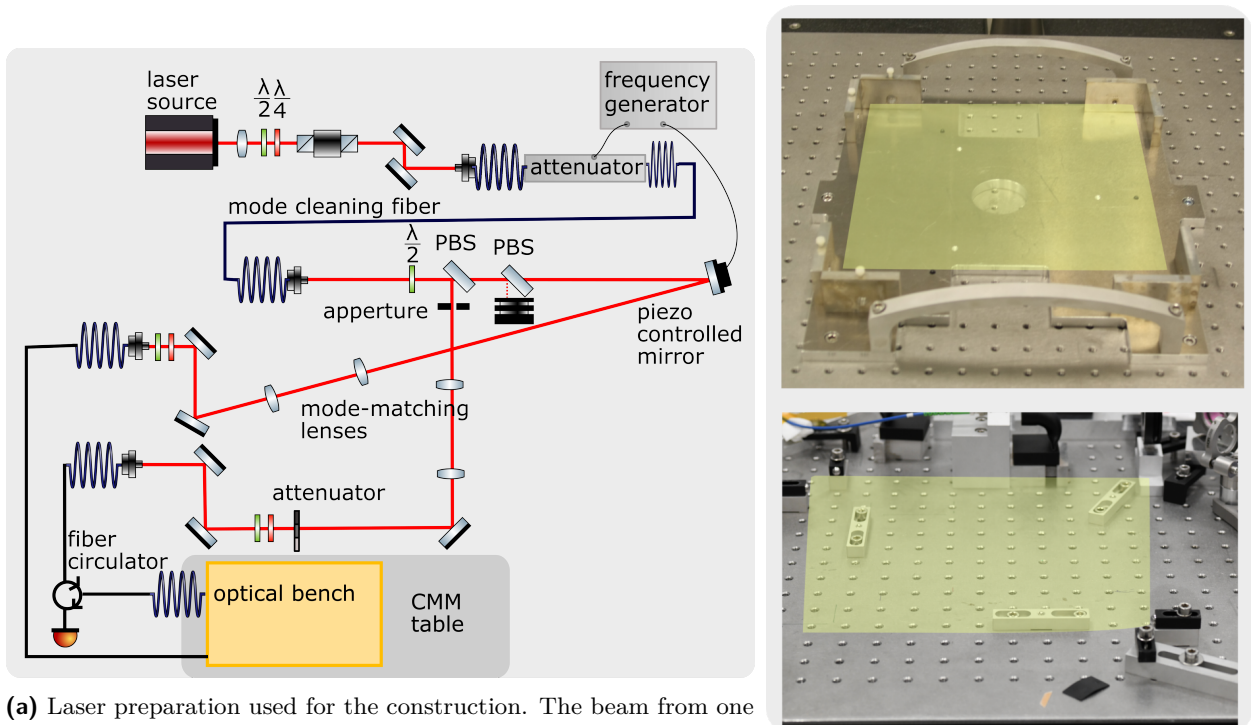
(a) Laser preparation used for the construction. The beam from one laser source can be amplitude modulated and is split in two arms, one of which can be phase modulated. The combination of pbs and waveplate and an attenuation wheel control the power ratio between the arms.

(b) Mounting of optical bench old (up) an new (down). Optical bench sketched.

Fig. A.1.: Laserpreparation in the cleanroom and the two iterations of the optical bench's mounting. The original aluminum mounting provided uncomplicated alignment underneath the template but suffered from several attached components with different CTE's, leading to misalignment with temperature-driven expansion. The new mounting by D. Penkert reduces the amount of material, ensures few defined contact points, and replaces the elastic peek spheres with stainless steel (CTE $10 \cdot 10^{-6}$/K).

The construction of the optical benches in the cleanroom requires alignment with a laser beam to ensure contrast and couplings into the fibers. A laser preparation creating two laser beams as shown in Figure A.1a is placed on a separate optical table. A piezo-controlled mirror imprints a phase modulation on one of the beams. To measure a beam position with the CQS (see Section 2.1) the laser's amplitude is modulated by an electrically controlled fiber attenuator. The required power ratio between the two beams differs for the construction steps and thus needs to be variable, which is achieved by a half-waveplate and a pbs. In one beam path, an attenuator wheel by *Thorlabs* (*Mounted Step Variable ND Filter*) can be used to reduce the laser power further. A quarter and a half waveplate further adjust the beam's polarization precisely to the polarization maintaining fibers' slow axis, which guides the light on the CMM table. In cases where a beam on the construction table is coupled back into these fibers, the level of back-reflected light is tracked with a fiber coupled PR behind a fiber circulator.

A.2 Glue

Information about the amount of glue used for the different construction steps and the glue layer problems discussed in Section 2.4.6 are presented.

A.2.1 Amount of Glue

The different surfaces attached with UV-glue have different sizes and demands. The chosen amount is based on the investigations by [Haa14] with further adaptations based on experience and the smallest possible amount of $0.5\,\mu L$. More information can also be found in [Knu20].

	Component	glue [µL]
Component that is attached to the optical bench	$15\,mm \times 7\,mm$	2×0.5
	$20\,mm \times 7\,mm$	3×0.5
	FMA	4×0.5
	beamstop	2×0.5
fios parts	lens into holder	4×0.5
	Ferrule to FMA	12×1
	girder to FMA	3×0.5
	lens holder to girder	2×0.5

Tab. A.1.: Amounts of glue used during the 3BL construction in the minimal available drop size of $0.5\,\mu L$.

A.2.2 Glue Layers

Degradations observed in the glue layers of the components have been discussed in Section 2.4.6. Photographs of a selection of glue layers are presented in Figure A.2. Picture a) shows the degraded glue layer of *pbs4* on the first bench. Contamination is visible in the form of bubbles that reflect the light and are visible as white dots. Picture b) visualizes an intended glue layer without contamination. The glue layers in c) and d) show specific shapes that might be related to a problem in the optical

First Bench · Second Bench

Fios1 · Fios2 · Fios3 · Fios4

Fios 1-4 on the second Bench
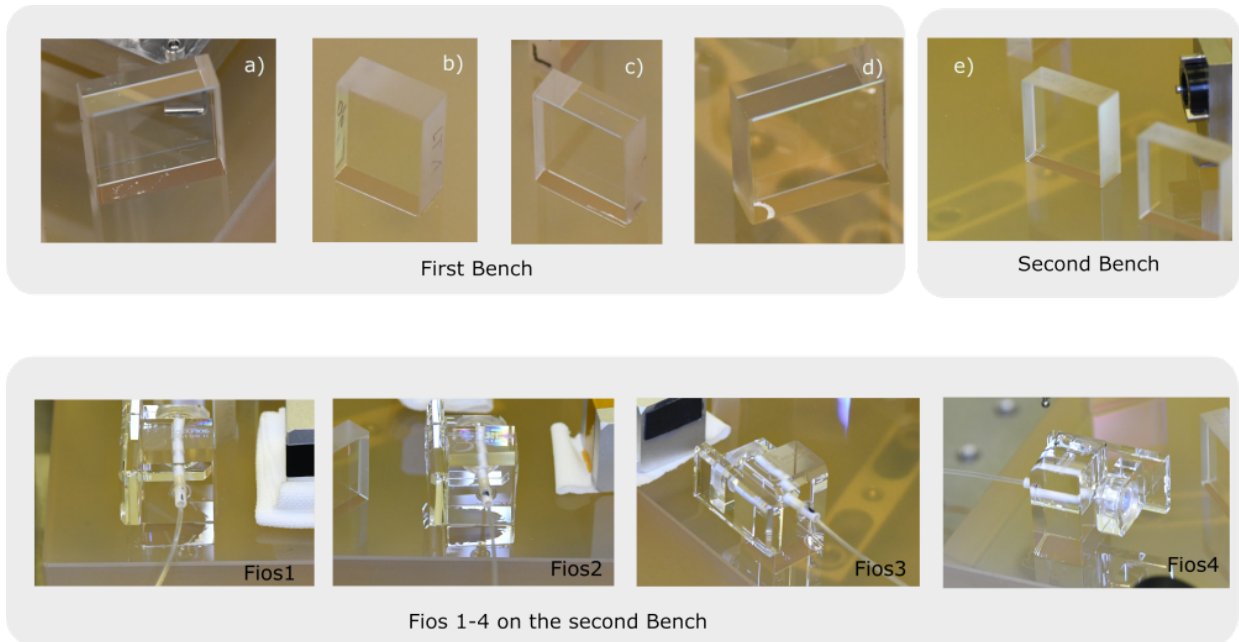
Fig. A.2.: Glue layers of different components. a) and d) are taken on the first bench and have very specific defects. b), c) and e) show more commonly observed glue layer appearances. The glue layer for all four fios on the second bench are shown, only *fios4* has a defect that is comparable to the common one in other components. The degradation was tracked over time and did not become more severe than shown in the presented pictures.

bench or components surface. Picture e) was taken on the second bench, and the glue layer is slightly distorted at the edges.

The glue layers of all four fios on the second bench are shown in the lower pictures. Their glue layers are particularly distorted, except for the one of *fios4*.

A.2.3 Component Tilts - Measurement

The measurements of the tilts for four components discussed in Section 2.4.5 are evaluated in Figure A.3a. Figure A.3b illustrates how the angle α is created by a change of ΔL in the wedge height L for the calculation of the thermal stability of the glue wedge.

A.3 Construction Steps

Besides the construction steps for the whole population of the 3BL benches in Section 2.3.1, construction steps for the Pre-assembeling of the fios parts and the individual steps for placing a fused silica or metal component are provided in the following. A description with more detail is given in [Knu20].

A.3.1 Pre-assembling Fios Parts

1. Glue the lens inside the lens holder.

(a) Average measurement for each component and the common average including the standard deviation.
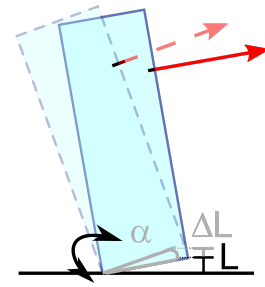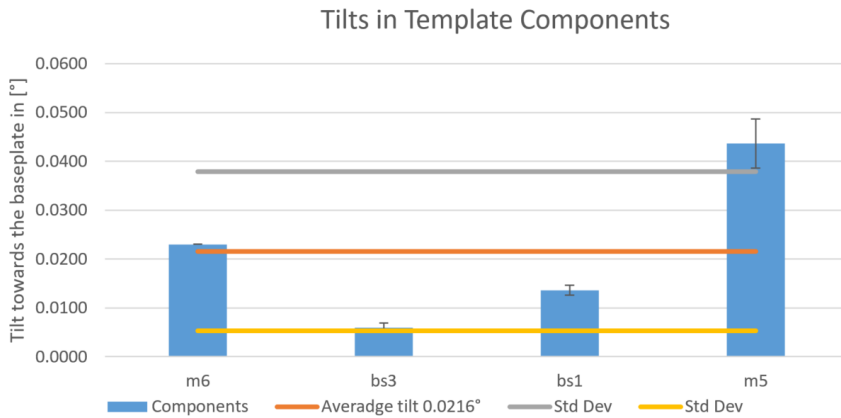
(b) Component with wedge of height L and tilts around the left corner caused by thermal expansion of the wedge.

Fig. A.3.: Component tilt measurement and the geometrical influence on a thermal expansion of the wedge.

2. Glue the Ferrule which is attached to the fiber inside the FMA. A polarization analyzer ensures a sufficient alignment of the polarization axis and measures the PER of the fiber. It is inspected with an IR-viewer to rule out damaged fibers.

3. Glue girder to the FMA side.

4. Assemble the finale fios with the BEAST. The lens holder is attached to the girder and the FMA to the optical bench.

A.3.2 Gluing a Component

1. Measure component's characteristics.

2. Clean component and optical bench.

3. Apply glue equally distributed.

4. Check glue layer and optical bench with inspection lamp.

5. Place component, mind the front side.

6. Apply slight, equal pressure with the thumb.

7. Wait about 30sec for the glue layer to distribute and settle.

8. Check glue layer for contamination.

9. Apply rubber band horizontally at the height of the pointing fingers or positioning spheres.

10. Align component if needed.

11. Check again the glue layer.

12. Radiate with UV-light.

13. Remove rubber band (and pointing fingers) and radiate again.

14. After a few hours, touch component with appropriate force to validate the curing.

A.3.3 Gluing a Metal Component

1. Clean component and optical bench.

2. Stir two-component epoxy and add the 4% weight ratio of glass beads.

3. Apply two-component epoxy equally distributed. A thin layer is preferred for small components to reduce the potential of gluing a wedge. The glue layer needs to be thick enough for larger components to ensure an even bond. (See [Wra19] for details.).

4. Place component, mind the front side.

5. Apply slight, equal pressure with the thumb.

6. Apply rubber band horizontally at the height of the pointing fingers or positioning spheres.

7. Align component if necessary.

8. Apply the "finger-from-above" (see Figure 2.16a) in a central position. This way, the component is additionally fixed to prevent creeping while the glue is curing, and the additional pressure supports the curing.

9. Leave untouched for a weekend.

10. Remove the rubber band.

11. After a few days touch component with appropriate force to validate the curing.

A.3.4 About Strategy 2.3.3

The original Strategy 2.3.3 included a sophisticated approach for the alignment of the beam's waist. Besides *saving* the spatial alignment of the beam (with the saving-CQS), the parameters of the waist and its position were planed to be saved, too. The idea is based on the fact that the coupling of a beam back in its own coupler is maximized when a mirror is placed under a zero degrees angle exactly in the waist of the beam. Accordingly, when a mirror is placed at the target position of the fios beam waist, the coupling can be maximized, and the beam inhibits the target parameters. By experimental testing this approach, the coupling was found to be an insufficient error signal. Additionally, the mirror under zero degrees formed a cavity with another surface in the path. This idea was discarded for this strategy but is described in more detail in [Knu20].

A.4 Fios - Polarization Axis Alignment

The fiber's alignment in the FMA is supervised by a polarization analyzer to ensure a s-polarized output state and a high PER. The resulting parameters are given in Table A.2.

Bench	fios	S/N	PER [dB]	Azimuth Angle [°]
First Bench	1	16	38.1	-2
	2	6	37.5	-0.1
	3	4	42.6	-0.1
	4	9	50.4	0.1
Second Bench	1	11	32.6	-0.2
	2	14	51.6	0
	3	1	48.6	0.2
	4	12	42.1	-0.3

Tab. A.2.: Parameters from the fios's construction, labeled with their serial number (S/N).

B

Additional CQS Analysis

This Appendix provides more details about the analysis of the CQS discussed in Section 2.1. After introducing the calibration results for each CQS, a thorough uncertainty calculation is presented, including the position uncertainty and the uncertainty of a beam's angle measurement. An estimate about the offset in the CQS measurements are given and the measurements about their quality in terms of repeatability and over-night stability are presented. The comparison between all three CQS is presented for two more measurements.

B.1 Calibration Results

The calibration is done via a fit in *Matlab* for each CQS separatly.

B.1.1 Example Output

The position of the QPD is given in the coordinate system of the CQS, which is different from the optical bench's coordinate system. It is placed at the upper right corner, as shown in Figure 2.3b. The x and y axis are orthogonal to the beam and the z axis is parallel to it. The output of the *Matlab* fit is given exemplary for the CQS1green in the following:

> FIT RESULT FOR CQS1GREEN:
> X POSITION OF QPD: 0.499955 PARTS OF THE QPD MOUNT'S WIDTH
> Y POSITION OF QPD: 0.308628 PARTS OF THE QPD MOUNT'S WIDTH
> Z POSITION OF QPD: -1.845786 MM
> SUM OF SQU. DIST.: 0.000037MM
> MAX. DISTANCE: 0.002582 MM
> MAX. OUTLIER: #12
> STANDARD DEVIATION: 0.001485 MM
> MEAN MOUNT WIDTH: 65.006617MM

which included a measurement of the mean mount width that allow for a compensation of thermal expansion in the mount. The x and y axis describe the QPD's position relative as parts of the mount, including the measured width, and the z-position is given in mm relative to the front surface.

B.1.2 Result for each CQS

	CQS1green	CQS1green low power	CQS2red	CQS3blue
X position of QPD in parts of the QPDs mount's width	0.499955	0.499984	0.496656	0.499397
Y position of QPD in parts of the QPDs mount's width	0.308628	0.308588	0.309713	0.310742
Z position of QPD in parts of the QPDs mount's width	-1.845786	-1.847186	-2.080190	-2.046180
std dev in μm	1.485	3.066	2.629	1.514

Tab. B.1.: Calibration results for the three CQS used in the 3BL construction. CQS1green is additionally calibrated for lower power.

Table B.1 summarizes the results of the calibration for the three CQS used in the 3BL experiment. These values are included in the CMM's script for the beam position measurements. CQS1green and CQS3blue have a similar standard deviation of about 1.5µm, while it is higher for CQS2red and the repeated calibration for CQS1green for lower powers. The deviation between the two calibrations of CQS1green is below 0.1%. The positional differences between the QPDs in the brass mounts are visible and highlight this calibration's importance.

B.2 Uncertainty Calculations

For truthful statements of the achieved precisions in the alignment, the knowledge of the uncertainty of the measurement device is crucial. Here, the uncertainty calculation for the CQS described in Section 2.1.3 is derived in detail.

B.2.1 CMM Uncertainties Based on the PhD Thesis by Marina Dehne

This section is based on [Deh12], where the different uncertainties for CMM measurements are derived and explained in great detail. Here it is applied to the case of a single position CQS measurement.

Machine Uncertainty

For a measurement piece of length L, the machine uncertainty is:

$$u_m = 1.5\mu\text{m} + \text{L[mm]}/333000. \tag{B.1}$$

The longest CQS side is L=65mm, which results in $u_m = 1.7$ µm.

Sampling Uncertainty

$$u_s = \frac{\sqrt{1.7^2 \mu m^2 + 2^2 \mu m^2}}{\sqrt{n-x}} \tag{B.2}$$

With x: number of required probing points, n: number of actual probing points. For the smallest probed surface, two measurement points were necessary, while 22 were taken. This results in an uncertainty of $u_s = 0.59\,\mu m$.

Thermal Uncertainty

The thermal expansion adds another uncertainty. The expansion of the optical bench is important because the coordinate system is based on it. However, this effect is negligible because of the CTE of 1e-8/K [Isl18]. The contribution by the brass mount with a length of 65mm and a CTE of $19 \cdot 10^{-6}$ is also low; a temperature deviation of 1°C to the optimal 20° results in a thermal uncertainty of $u_t = 0.09\,\mu m$.

Other candidates are the mounting of the optical bench, which was minimized in material and made of stainless steel and aluminum. Both have a lower CTE than brass and smaller dimensions; thus, they are also neglected here. However, the 80 cm breadboard made of stainless steel with a CTE of about $10 \cdot 10^{-6}$ results in a thermal uncertainty of $u_t = 0.8\,\mu m$, thus the final thermal uncertainty is $u_t = 0.89\,\mu m$.

Datum Uncertainty

This uncertainty is based in the reference frame that is created on the CQS mount. It is calculated like the sampling uncertainty, but now all surfaces are included. The first surface needing 3 probes, is probed 34 time, (2 vs 22 for the second and 32 vs 1 for the third). This results in:

$$u_d = \sqrt{(\frac{3}{6} \cdot 4.7 \cdot 10^{-7})^2 + (\frac{2}{6} \cdot 6 \cdot 10^{-7})^2 + (\frac{1}{6} \cdot 4.7 \cdot 10^{-7})^2} = 0.32\,\mu m. \tag{B.3}$$

B.2.2 Law of propagation of Uncertainty

The "Guide to the expression of uncertainty in measurement" by the *Joint Committee for Guides in Metrology* [JCGrr] introduces the so-called "law of propagation of uncertainty" [JCGrr, p.19] for the combination of uncertainties of input variables x_i to a result y, with a function $f(x_i)=y$ that describes the relation from x_i to y.

For N uncorrelated input variables with uncertainties $u(x_i)$, the uncertainty of y is determined by [JCGrr]:

$$u(y) = \sqrt{\sum_{i=1}^{N} (\frac{\partial f}{\partial x_i})^2 \cdot u(x_i)^2}. \tag{B.4}$$

The uncertainty for a CQS measurement according to Equation B.4, including the single uncertainties

from Section B.2 and the human error and the standard deviation discussed in Section 2.1.3, is given by:

$$u_{CQS} = \sqrt{u_m^2 + u_s^2 + u_t^2 + u_d^2 + u_h^2 + s_N^2} = 3.02\,\mu m. \tag{B.5}$$

B.2.3 Uncertainties of a Beam Vector

Two CQS measurements of the same beam result in the two positions $\vec{P1}$, $\vec{P2}$. The beam $\vec{b}$ can then be described by a position vector $\vec{s} = \overrightarrow{OP1}$, starting from the origin $\vec{O}$, and a direction vector $\hat{e} = \frac{\vec{P2}-\vec{P1}}{|\vec{P2}-\vec{P1}|}$, as $\vec{b} = \vec{s} + \gamma\hat{e}$, with $\gamma \in \mathbb{R}$.

According to Equation B.4, the uncertainty u_{bi} of each component b_i is given by

$$u_{bi} = \sqrt{(u_{si}^2 + \gamma^2 u_{ei}^2)}, \tag{B.6}$$

where u_{si} is given by the uncertainty of the position measurement $u_{si} = \Delta p = u_{CQS} = 3.02\,\mu m$. The uncertainty for the direction vector is calculated in the following:

$$\hat{e} = \frac{\vec{P2} - \vec{P1}}{|\vec{P2} - \vec{P1}|}$$
$$u_{e_i}^2 = \frac{\partial e_i}{\partial P_{a,j}}^2 \cdot u_{P_{a,j}}^2 \tag{B.7}$$

with $i, j \in \{1, 2, 3\}$, a $\in \{1, 2\}$. In an interferometer that uses only 90° reflections, the beam can be assumed to propagate along one axis, x, with deviations in the other two axis, y and z, in the µm range. Thus, without the loss of generality, $(P_{1x} - P_{2x})^2 \gg (P_{1y/z} - P_{2y/z})^2$ will be used in the following.

Starting with the uncertainty for the x-component, the result of Equation B.7 can be simplified to:

$$u_{e_x}^2 = \frac{4 \cdot \Delta p^2}{(P_{1x} - P_{2x})^4} \tag{B.8}$$

$$u_{e_x} = \pm 16.78\,\mu m \tag{B.9}$$

for a 60cm measurement distance between P_{1x} and P_{2x}.

The same assumption is also valid for the other two axes, which are given by:

$$u_{e_y} = u_{e_z} = \sqrt{2 \cdot \Delta p^2 \cdot \frac{(1 + (P_{1x} - P_{2x})^2)}{P_{1x}(P_{2x})^4}} = 13.84\,\mu m. \tag{B.10}$$

A beam determined by two CQS measurements can thus be described by combining the previous equations to:

$$\vec{b} = \begin{pmatrix} bx \\ by \\ bz \end{pmatrix} + \begin{pmatrix} u_{bx} \\ u_{bx} \\ u_{bx} \end{pmatrix} = \begin{pmatrix} bx \\ by \\ bz \end{pmatrix} + \begin{pmatrix} \sqrt{3.02\,\mu m + \gamma^2 \cdot 16.78\,\mu m} \\ \sqrt{3.02\,\mu m + \gamma^2 \cdot 13.84\,\mu m} \\ \sqrt{3.02\,\mu m + \gamma^2 \cdot 13.84\,\mu m} \end{pmatrix}, \tag{B.11}$$

dependend on the position along the beam, given by γ. Additionally, the potential offset in the CQS measurement is added to the starting vector and is discussed in Section B.3.

B.2.4 Uncertainties of a Beam Angle

Towards the Baseplate

For aligning a beam horizontal to the baseplate, the angle between the beam and the surface is needed. It can be calculated by simple geometry, and the uncertainty is again calculated according to Equation B.4:

$$\alpha = \arctan(\frac{\Delta z}{d}) \tag{B.12}$$

$$u(\alpha)^2 = (\frac{\partial \alpha}{\partial \Delta z})^2 \cdot u(\Delta z)^2 + (\frac{\partial \alpha}{\partial d})^2 \cdot u(\Delta z)^2 \tag{B.13}$$

$$= \frac{u(\Delta z)^2}{d^2 + \Delta z^2}. \tag{B.14}$$

Since the distance between two measurement points, d, is typically in the order of $60 \cdot 10^{-2}$m and $\Delta z^2 \approx 10^{-6}$m, a common uncertainty for an angle towards the baseplate is given by $u(\alpha)$=7.12 µrad.

Between two Beams

An angle between two beams can be extracted from the direction vectors via:

$$\alpha = \arccos \frac{\hat{e}_1.\hat{e}_2}{|e_1||e_2|}.$$

The corresponding uncertainty u_α is given by:

$$u_\alpha^2 = (\frac{\partial \alpha}{\partial e_{1x}})^2 \cdot u(e_x)^2 + (\frac{\partial \alpha}{\partial e_{1y}})^2 \cdot u(e_y)^2$$
$$+ (\frac{\partial \alpha}{\partial e_{2x}})^2 \cdot u(e_x)^2 + (\frac{\partial \alpha}{\partial e_{2y}})^2 \cdot u(e_y)^2.$$

Assuming u(e_x)=u(e_y) from Equation B.8 simplifies to:

$$u_\alpha^2 = u(e_x)^2 \frac{|\hat{e}_1| + |\hat{e}_2|}{|\hat{e}_1||\hat{e}_2|} \tag{B.15}$$

$$u_\alpha = \sqrt{2} \cdot u(e_x) = 23.73 \, \text{µrad}. \tag{B.16}$$

Another way of calculating this angle is by calculating the angles of both beams towards the baseplate. Their combination to the shared angle results in a smaller uncertainty of $\sqrt{2} \cdot u(\alpha)$ =10.1 µrad.

B.3 Offset in the CQS

Due to the mentioned electrical differences (cables, TIA channels, Picometer channels) in Section 2.1.4, the appearance of an offset in the CQS measurements towards the actual beam position is likely. Here, a rough approximation of a possible offset is given.

The offset $\vec{o}$ adds to a normal beam position $\vec{P}$ in the two-axis orthogonal to the beam. It cancels in all relative measurements, like in Strategy 2.3.5, where two beams were centered on the same
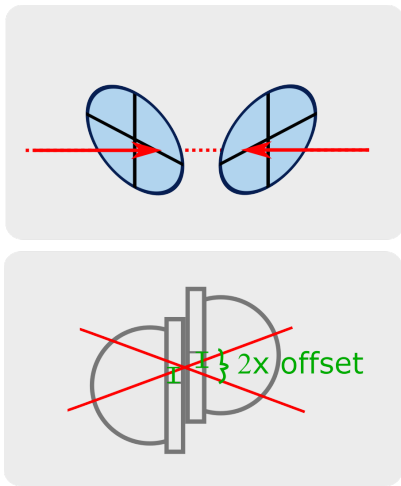
(a) Offset in the CQS when measuring two perfectly counterpropagating beams and the stategy to measure this offset for beams crossing on the QPD's surface.
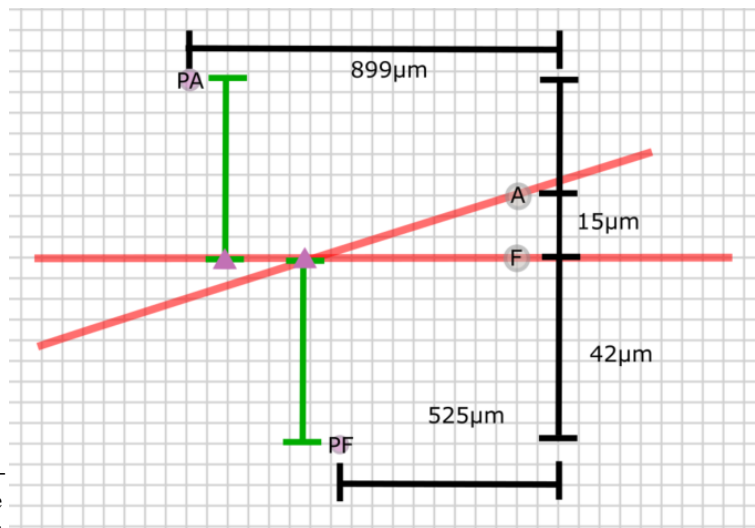
(b) Measurement for estimating the offset.

Fig. B.1.: CQS offset estimation

CQS. Also, the offset cancels for angle calculation between direction vectors or geometrically with the tangents. Contrary, the offset distorts the single beam position measurement, as is the starting vector for a beam description.

A measurement strategy to estimate this offset was developed and tested roughly. It is based on measuring in opposite directions, which will flip the sign of the statistic offset. Its principle is depicted in Figure B.1b a). In the first step, the ruby-sphere-based method CABAM (introduced in Section 2.1, [SMH14]) is used to cross two counter-propagating beams. Then, a CQS is used to measure each beam at this exact crossing point. The deviation between the CQS measurements will reveal twice the offset. This procedure was designed for a y-axis offset. For the z-axis, the CQS needs to be turned accordingly. However, this would change the probing points of the CMM and potentially lead to a higher deviation or makes a new calibration necessary. Accordingly, only the y-offset is investigated in the following.

This offset estimation measurement has been done once, but since it was a test run, it is limited by unprecise alignments, as depicted in Figure B.1b. Neither are both beams crossing precisely nor are the two CQS measurements done at the same x-position. The result is only a very rough estimate. Assuming that one of the beams, which was emitted by a fios, is very horizontally, the offset towards the ruby-sphere measurement is 42 µm. This is believed to be a very conservative estimate. A repetition of this measurement is recommended for a deeper characterization of the CQS.

The measurement was performed with CQS3blue and presumably vary for all CQS. However, since no significant differences appeared when measuring with one or the other CQS (see also Section 2.1.5), the same order of magnitude is assumed for all CQS and both axis.

As a result, the offset is assumed to be below 50µm, which is presumably highly overestimated. However, the absolut position measurement is mainly important for the alignment of the fios height, which is also given with an uncertainty of ±50µm by the manufacturer.

B.4 Grid Characterization

The grid was characterized with different extends several times for different beam powers and radii. Here, a typical grid characterization for a beam with 1142.9 µm radius and a power of 0.18 mW is presented in Figure B.2.
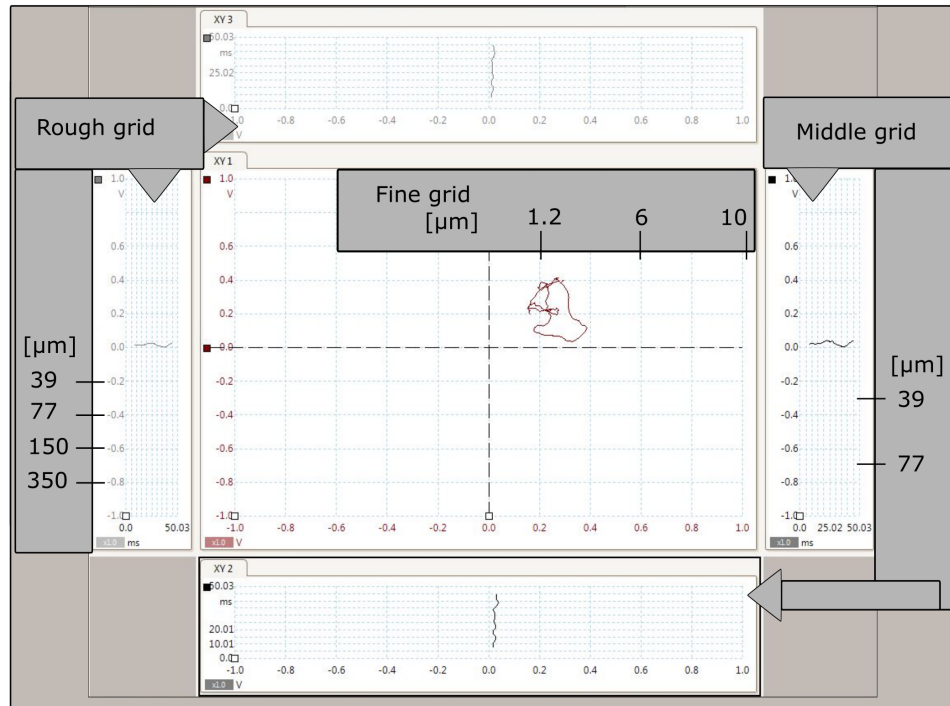
Fig. B.2.: The grid for the CQS measurements. The fine grid in the center, with the noise "*blob*" and the middle and rough grids on the sides, where the alignment is indicated by the brown lines. The division sizes were found with measurements and are not linear.

B.5 Measurements of the CQS's Repeatability

To evaluate the repeatability of the CQS measurements, the same position of a beam was measured several times after de- and re-adjusting the translation stages. The measurements are illustrated in Figure B.3 and given and discussed in the following. M0 was aligned by Person A, M1 by Person B and then alternating.

M0=[362.71192754, 385.40368572, 15.01734128];
M1=[362.71217606, 385.40381956, 15.01729281];
M2 =[362.71321952, 385.40348235, 15.01608426];
M3 =[362.71341154, 385.40341716, 15.01710919];
M4 =[362.71320018, 385.40337963, 15.01764393];
M5 =[362.71334057, 385.40360580, 15.0167694];
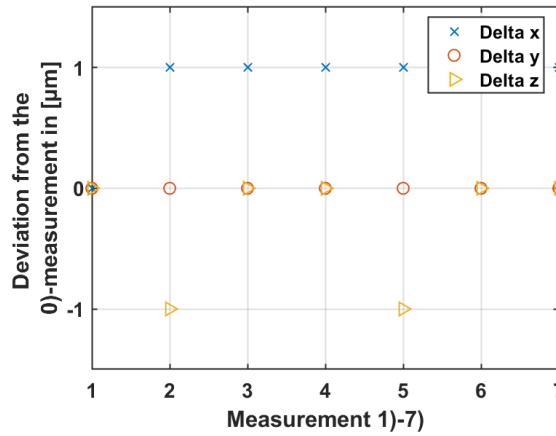
Fig. B.3.: Visualization of the repeatability measurements show μm deviations from the original measurement. The deviations are below the CQS measurement uncertainty of 3.02 μm.

M6 =[362.71292539, 385.40321469, 15.01754144];
M7 =[362.71304166, 385.40339309, 15.01720047];

In the y-direction, which is the beam propagation direction, the measurements deviate below 1 μm. The height along the z-axis oscillates between zero and 1 μm randomly. The x-direction is 1 μm off after the first measurement and stable afterward. This indicates a slight beam movement or breadboard distortion after the zero-measurement. In both cases, the deviations are within the measurement uncertainties of 3.02 μm. In conclusion, the repeatability of a beam measurement with the same CQS is about 1 μm in the orthogonal axes and less than 1 μm along the beam propagation axis.

These measurements are further influenced by the stability of the beam, which is limited by its coupler and the breadboard, both prone to thermal expansions by changing temperatures (as discussed in Section 2.3.2). A decoupling of the effects is not possible and the here present the behavior is representative for typical measurement times of a few hours.

B.6 Measurements of the CQS's Stability

During the construction process of the 3BL, positional changes of the CQS were observed over nights and collected here. The CQS's position was measured before and after the night without being moved. The mean position change is about 4.45 μm in height, 3 μm orthogonal to the beam, and 1.3 μm along the beam. The height change is presumably caused by the gravitational force of the heavy brass mount on the translation stage. Also, along the side orthogonal to the beam, the tension in the translation stage can move the CQS slightly. Along the beam, however, there is no movable axis. Instead, some thermal effects may cause a moment of the QPD's center. Even more likely is the influence of the CMM coordinate system. It is created relative to the position of the optical bench every day. If the bench is moved slightly in its mount (also due to thermal effects), this influences the effective CQS position. The same happens when the stainless steel breadboard expands, causing a changed relative position between the optical bench and CQS. Since the individual influences were not disentangled, the concluded CQS height stability is 4 μm, the

side stability 2 µm, and the position along the beam below 1 µm.

Fixing the locking screws on the translation stage improves the height stability by about a factor of 2. However, this tightening is prone to unintentional misalignment. It is also typically unnecessary because the CQS position is measured the next day again.

The height changes of the CQS have been observed over night (about 12 h) and are collected in Table B.2. Two measurements over lunch (ovl) for about 1.5 h are given, too.

Date	Δ height [µm]	Δ side [µm]	Δ along the beam [µm]
(2018-10-17)	(14)*	/	/
2018-11-28	5	/	/
	4.3	/	/
(2018-11-30) **	(24)	(4)	(6)
2018-12-04	3.4	1.4	1
2019-01-08	6	3.5	0.1
	5	2	2
2019-07-17	3	5	2
	$\bar{\Delta}h = 4.45$***	$\bar{\Delta}s = 3$***	$\bar{\Delta}b = 1.3$***
ovl 2021-08-16	4	1	/
ovl 2020-01-15	0	0	0

Tab. B.2.: Measurements to investigate the changes in the CQS alignment over night (and over lunch (ovl))
* this value is significantly bigger and does not fit the typical observations
** there where many measurements done in between the CQS measurements, therefore a movement of the optical bench and thus the coordinate system is more likely
*** excluding * and **

B.7 Measurements of the CQS Comparison

Further analysis of the CQS is provided by measurement of the same beam with all three CQS. The measurement from 2020 is presented in Figure 2.4 in Section 2.1.5, while the measurements of 2018 are given here in Figure B.4a and B.4b and for 2019 in Figure B.5a and B.5b.
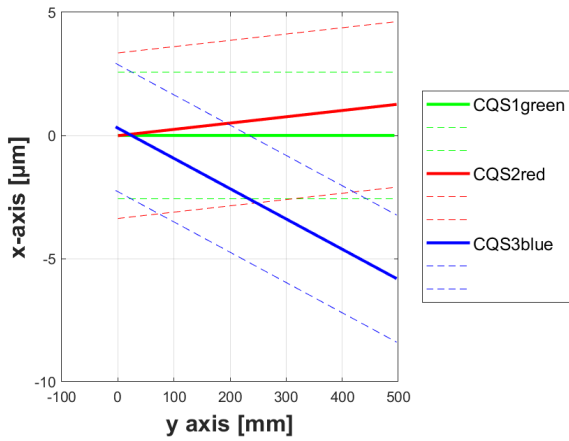
(a) Measurement differences along the x-axis.
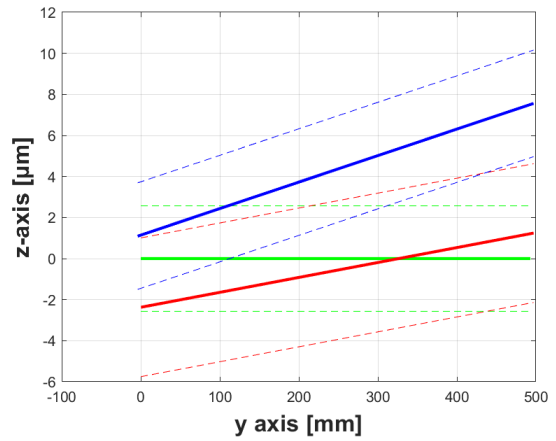
(b) Measurement differences along the z-axis.

Fig. B.4.: 2018 - Measurements of the same beam along y-axis, with three CQS, including their individual uncertainties. In both cases, all three measurements do not agree in their uncertainty range over the whole measurement distance. This is presumably caused by a moving beam, fitting the unstable fiber coupler used during these early measurements.
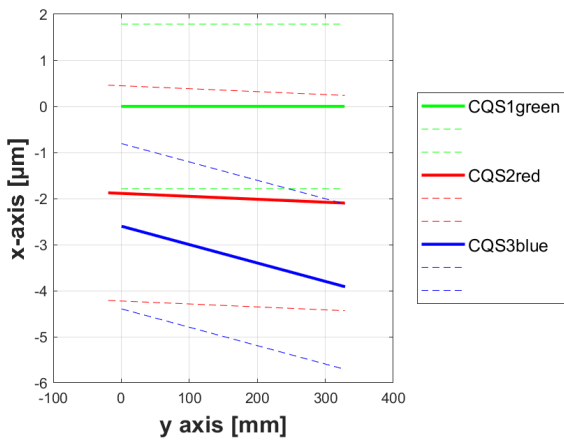
(a) Measurement differences along the x-axis.
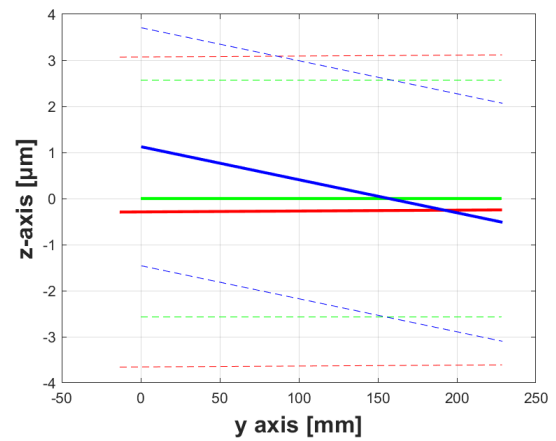
(b) Measurement differences along the z-axis.

Fig. B.5.: 2019 - Measurements of the same beam along y-axis, with 3 CQS, including their individual uncertainties. In the horizontal axis, the measurement with CQS1green is not agreeing with the other two. They, in turn, only disagree in a very small range at the end. In the z-axis, the three beams again agree nicely.

C

Fios and Free-Beam Stability Requirement

This Appendix discusses the requirement for the FBBL construction which is based on stability requirements and TTL-simulations. It concludes a requirement for the overlap of the two counter-propagating beams.

The requirement for the FBBL and the fios stability was determined by [Isl18] on the base of TTL coupling simulations. The FBBL has the longest pathlength and the highest dynamic and sets the upper limit for the TTL in all interferometers. Since the FBBL pathlength reduces in the switched benches configuration, the TTL coupling is expected to be even lower.

The TTL coupling was simulated with IfoCad depending on the amount of misalignment in $10\,\mathrm{\mu m}$ steps [Isl18]. By combining these results with the $1\,\mathrm{pm}/\sqrt{\mathrm{Hz}}$ as pathlength requirement and the coupling from phase to DWS assumed to be at least $4000\,\mathrm{rad/rad}$, the DWS requirement is given by:

$$\mathrm{Req}_{\mathrm{DWS}}(\mathrm{M}) = 1\mathrm{pm}/\sqrt{\mathrm{Hz}} \cdot (\mathrm{TTL\text{-}simulation}(\mathrm{M})[\frac{\mathrm{m}}{\mathrm{rad}}])^{-1} \cdot 4000\frac{\mathrm{rad}}{\mathrm{rad}}, \qquad (\mathrm{C.1})$$

depending on the misalignment M.

C.1 Fios Stability

The requirement for the stability of the fios is given by the first part of Equation C.1, and requires the beam tilt noise to be below:

$$\mathrm{Req}_{\mathrm{FIOS}}(\mathrm{M}) = 1\mathrm{pm}/\sqrt{\mathrm{Hz}} \cdot (\mathrm{TTL\text{-}simulation}(\mathrm{M})[\frac{\mathrm{m}}{\mathrm{rad}}])^{-1}$$

Dedicated measurements of the fios stability are planed in the ITAM experiment [Wra19], but have not been performed till the finalization of this thesis.

C.2 Free-Beam Requirement

Since a misalignment in the construction lead to an increase in TTL-coupling, the requirement for the DWS values depends on the achieved construction precision. The simulations by [Isl18] focus on a misalignment of $10\,\mathrm{\mu m}$ and $10\,\mathrm{rad}$, considered reasonable at that time. During the construction, it was found to be too strict, and a goal of $+/\text{-}100\,\mathrm{\mu m}$ and $+/\text{-}100\,\mathrm{rad}$ for a best-effort approach was set. Therefore a new evaluation of the TTL is necessary and provided in the following.

The simulations are based on a misalignment of the component *bs8*, the interfering bs in the FBBL interferometer. Since it was already placed with the template, the interpretation of the misalignment is shifted to the beams. The misalignment is further split into two parts, before and behind the *bs8*. The reason is the two different pairs of beams at those positions. Before *bs8*, the two counter-propagating Backlink beams have overlap. Behind the *bs8*, the Backlink beam and the local TX-beam are aligned. Misalignment in both positions form a worst-case estimate for the related *bs8* misalignment in the simulations.

During the construction of the second bench, the first bench was used to provide the actual Backlink beam. Therefore, the overlap in both interferometers was tracked simultaneously, and accordingly, only the reached performance in this combined measurement is analyzed here.

Equally to the simulations, a vertical tilt angle α_z and a horizontal displacement Δbs8 are analyzed.

	α_z [µrad]		Δbs8-l [µm]	Δbs8-r [µm]
before bs8	27*	27*	4.2	3.6
behind bs8	17	38	35	7.9
Sum	44	**65**	**39.2**	11.5

Tab. C.1.: Construction results in the FBBL alignment.
*same measurement for the two counter-propagating beams.

The results from the construction are summarized in table C.1. The values after bs8 are calculated from the CQS measurements, where only an upper limit was used. Thus, these values are a conservative worst-case estimate. The misalignment is below $70\,\mathrm{µrad}$ horizontally and $40\,\mathrm{µm}$ vertically. The TTL-simulations were only done up to $50\,\mathrm{µm/µrad}$ misalignment and showed a linear increase of the ordinate-intersect while the shape did not change [Isl18]. These simulations were done with the original bench orientation. The reduced pathlength caused by the switched benches presumably reduces the TTL-coupling. If assumed that the trend is valid for higher misalignment, the extrapolated TTL coupling due to $70\,\mathrm{µrad}$ on the local QPD is $13.8\,\mathrm{pm/µrad}$ and on the far one $34\,\mathrm{pm/µrad}$. The $40\,\mathrm{µm}$ misalignment results in a local response of $82.2\,\mathrm{pm/µrad}$ and a far response of $139\,\mathrm{pm/µrad}$. The horizontal effect is an order of magnitude higher and is thus used for the DWS requirement. For the worst case, the far QPD response is used and a DWS requirement of $3 \cdot 10^{-5}\mathrm{rad}/\sqrt{(\mathrm{Hz})}$ is extracted, given in Equation C.1. ($5 \cdot 10^{-5}\mathrm{rad}/\sqrt{(\mathrm{Hz})}$ for the close one). The measured DWS values in the 3BL, discussed in Section 3.5.2, are below the here derived requirement; thus, the increased misalignment compared to the initial requirement is not problematic. Additionally, one should notice that the estimations in table C.1 are also especially worst-case; thus, the real requirement is more relaxed. The DWS measurements from the Pre-Experiment ([Isl18], [Bis18]) are also presented in Section 3.5.2. They used the same control loop infrastructure, but a different pathlength, coupling coefficients, and a less stable or precise interferometer. The 3BL performance is significantly better. This is expected because the 3BL uses more stable collimators (monolithic fios instead of commercial, adjustable collimators), and the alignment is done with significantly more care. The DWS signals in the FBBL could also be used to compare the fiber coupler's stability in both experiments. However, it is not easy to disentangle the stability from the alignment and the misalignment in the Pre-Experiment is unknown.

D

Alternative Techniques for a Collinear Overlap

Alternative strategies in addition to Strategy 2.3.7 to overlap two counter-propagating beams are discussed in this Appendix.

Originally the alignment with CQS was believed to be insufficient, caused by the 10 µrad requirement and the high uncertainty of the beam measurements on the breadboard that did not provide a sufficient measurement distance. However, with the decision to relax the requirement, the CQS became the preferred option for two reasons. They are already part of the alignment process; thus, no additional technique has to be optimized. Additionally, they provide direct verification of the alignment. Other techniques would have needed reliable characterization. Some options which might be applicable for future optical bench constructions are presented in the following.

D.1 Fiber Coupler

A way of creating two collinear beams is to couple a beam in a fiber coupler with maximized coupling. This requires a perfect geometrical overlap. [Deh12] expected this approach to be limited by the perpendicularity of a component between the two involved couplers. However, it also requires a perfect mode overlap in the other beam parameters and an exact coupling measurement. Here presented measurements investigate the coupling's dependency from the angle between the beams.

Figure D.1 summarizes two types of measurements. First, a dedicated measurement in yellow circles and second a variety of measurements taken during the alignment investigations.

In the first one, the angle of one beam was misaligned stepwise, as shown with the yellow circles. It can be approximately fitted with the contrast calculation in [WH14], because the coupling in a fiber and the contrast for interference depend both on the overlap integral. Unequal beam parameters are assumed and the contrast is plotted over the misalignment of one of the beams. Additionally, a position mismatch was introduced to match the simulation with the measurements. A reasonable overlap between the simple modeling and the measurements can be concluded.

Second, the scattered measurement points have been taken as a byproduct of alignment measurements, and the dependency on the beam parameters and potential spatial misalignment became apparent. They were taken during different alignment iterations, and the beam parameters vary. Most measurements show a beam angle between 0-100 µrad but random coupling efficiencies between 0.7 and 0.35. This illustrates that a conclusion of an angle between the beams from the sole coupling value is not trivial. Because the coupling also depends on spatial misalignment or slight changes in
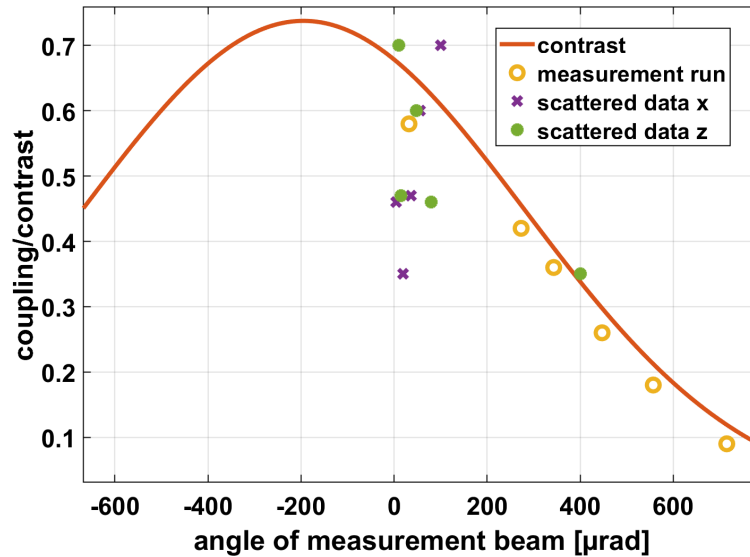
Fig. D.1.: Yellow circles show a measurement run with a step-wise angular change. The orange line models these measurement with a formula from [WH14]. Scattered measurement points in green and violet are shown from different alignment iterations, for the two axes orthogonal to the beam.

the beam parameters. Using a system of lenses can improve the mode overlap between the beams in both directions. However, misalignment via thermal changes would significantly impact the alignment due to a lens's enlarging nature.

D.2 A Sagnac Interferometer

A potential candidate for aligning two counterpropagating beams is a Sagnac interferometer. It consists of a 50/50 bs and mirrors that guide the two split beams in a circle to interfere again at the same bs. The number of phase jumps at the reflected surfaces results in a destructive interference at the open port of the bs while the beams interfere constructively at the port of the incoming beam. A perfect overlap between these counterpropagating beams is expected for a perfectly aligned interferometer.

Investigations with IfoCad simulations have been done by [Knu20] and the results are shown in Figure D.2. The Sagnac interferometer was created with different arm lengths (50 mm or 500 mm), and the bs was misaligned between 0 and 35 µrad. In this range, the interferometric contrast only changes from 100 % to 99.4 %, which is very challenging to measure. A photodiode placed at the dark port of the Sagnac interferometer measures residual powers caused by this misalignment. According to these simulations, 5 % of the incoming power appears on the PD when the misalignment is 30 µrad. A PR with sufficient gain can, in principle, detect this change. However, these simulations assume a perfect scenario. In reality, the bs will slightly differ from the 50/50 ratio, and spurious beams and potential polarization problems will appear. They might introduce a residual power leakage at the dark port that is not distinguishable from a misalignment. Furthermore, it is impossible to quantify the angle to a µrad level between the counterpropagating beams or between the beams at the dark port, because it is impossible to block one of them at a time. Based on these simulations,
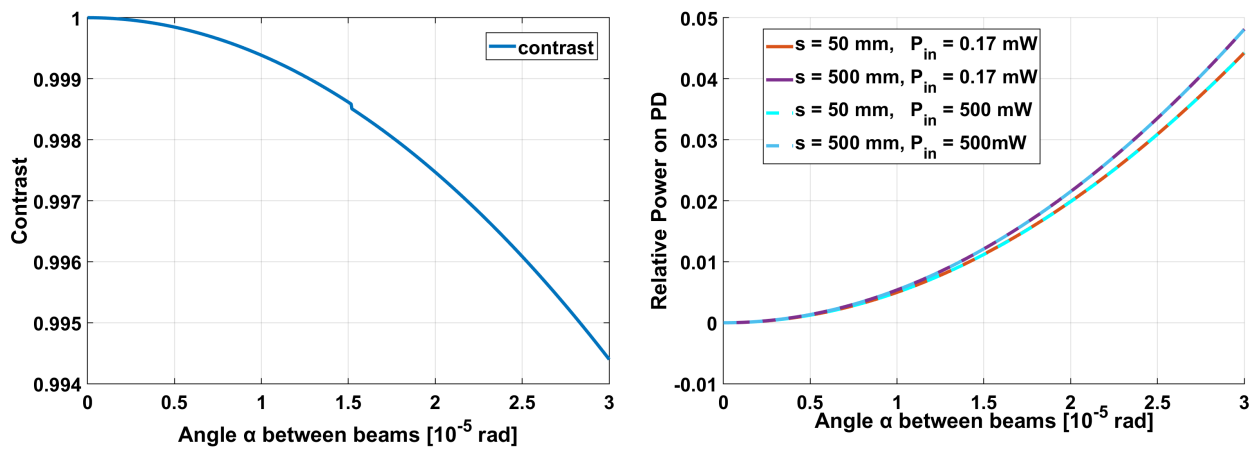
(a) Simulated contrast in a misaligned Sagnac interferometer.

(b) The power on the PD relative to the input power depends on the armlength of the interferometer. Simulated for 50 mm and 500 mm.

Fig. D.2.: Contrast and relative power in the Sagnac interferometer simulated in IfoCad for misalignments by α of the bs.

the Sagnac interferometer was excluded for the FBBL construction and therefore no further analysis was performed.

However, tuning the wavelength or the beam sizes together with more sophisticated simulations might be worthwhile. The advantage of a Sagnac interferometer as an alignment tool is, that an optimized quasi-monolithic Sagnac interferometer would allow alignment and alignment observation without a CMM. Furthermore, it allows the live tracking of the alignment. If the beam's orientation changes, for example, for thermal reasons, this will become evident immediately at the dark port.

D.3 A Cavity

Another idea by S. Ast for an external tool to overlap counterpropagating beams is the construction of a cavity. Its quality depends on the overlap between the cavity and beam's modes. Thus, the cavity must be tailored to the original beam, and its coupling into the cavity is optimized. For an optimal alignment, the back-reflected beam is expected to overlap with the incoming one. Again, a measurement of the actual angle is not feasible; thus, this approach was not investigated further.

E

Additional Details about the Laboratory Measurements

This Appendix provides some more details about the measurements in the Laboratory. It includes the beamdumps, the overview of the TIfo design, and the locking parameters of the laser frequency locks. The investigation on the phase drift and the details of the FBBL's control loop are given. Finally, the measurement of the RIN in all four transponder laser, additional measurements about the laser power and the cross-coupling measurements in the PM4 are presented.

E.1 Beamdumps

Fig. E.1.: Three different types of beamdumps, picture based on [Jes22]. a) AEI standard beamdump, b) textitspiral Beam Dump by M. Perreur-Lloyd, c) black foil from the company *Acktar*. d) Foil attached to the thermal shield and beam path sketched from *fios1* reflected by *att1*.

Picture of the beamdumps are presented in Figure E.1. The results of the calculation in Section 3.3.1, showing that the beamdump backscatter is unproblematic, are given in Figure E.2.
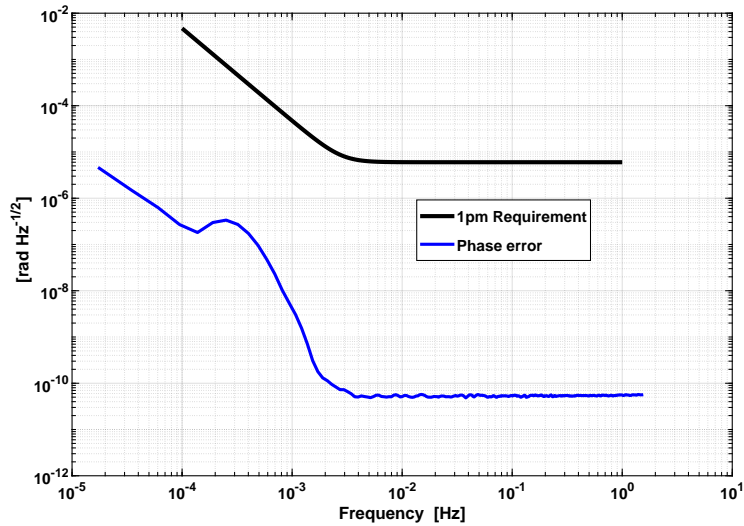
Fig. E.2.: Coupling of the backscattered light into a phase error based on the assumptions in Section 3.3.1.

E.2 Design of the TIfo

The design of the Test-Interferometer (TIfo) to investigate the noise floor in the 3BL's vacuum chamber is shown in Figure E.3.
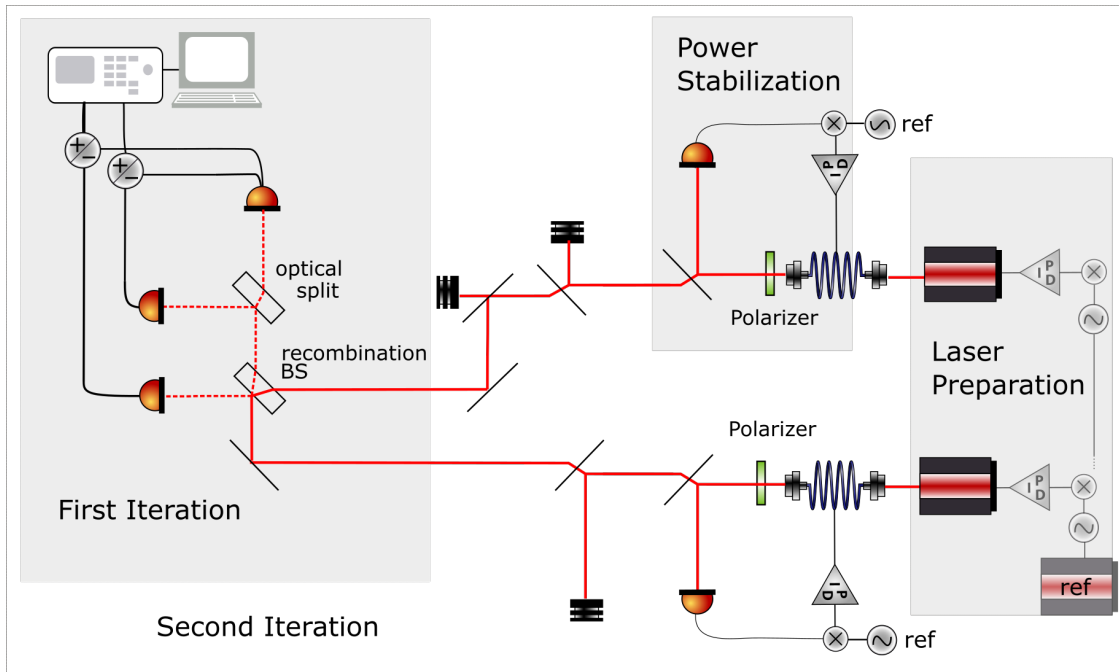
Fig. E.3.: Overview of the two iterations of the TIfo, based on the Figures in [Jes22]. The two lasers are frequency stabilized in the laser stabilization and brought to the vacuum chamber via feed-through fibers with a fiber-based variable optical attenuator in front of them. In the first iteration of the TIfo, the lasers interfere on an interfering bs, and the interference signal is split once for optical split measurements. Further addition of polarizers and bs for the power stabilization were added in the second iteration.

E.3 Laser Frequency Lock Parameter

The optimized gain parameters for the laser locks are given in Table E.1.

	Piezolock		
	I	II	k
Laser 1	42	7550	27
*	42	31	7550
Laser 2	42	27	8350
*	42	31	8350
Laser 3	42	18	7550
Laser 4	42	27	7950

Tab. E.1.: Parameters for the laser frequency locks; I and II and the fine-tuning parameter k. Determined by measuring the transferfunction and keeping a phase margin around 25°. With asterisk, the values for the pragmatic approach are marked.

E.4 Phase Drifts

The time series of the phases of each interferometer were observed to have phase drifts over several radians. Their origin was found in a mismatch of the actual optical frequency tracked in the locking PM and the read-out frequency set by the user in the BaliRo. This is shown in Figure E.4. The read-out frequency is set to the value equivalent to the expected BN based on the values set in the locking PM. The actual mean BN between the lasers and the reference laser is not precisely the frequency that is set as reference frequency in the locking PM. Instead, it deviates depending on the lock quality. E.g., for a lock with frequency fluctuation of several 10th of Hz, this deviation is about $580\,\text{Hz}$, and the observed phase drift in the BaliRo is $1.3\cdot10^6\,\text{rad}$ over $350\,\text{s}$. This corresponds to a frequency offset of $580\,\text{Hz}$, fitting the deviation in the locking frequencies. For an optimized frequency lock, the deviation and the phase drift are only in the order of the phasemeters resolution $80\,\text{MHz}/2^{32} \approx 0.0186\,\text{Hz}$. To the point of writing, this has not been identified as a performance-limiting problem.
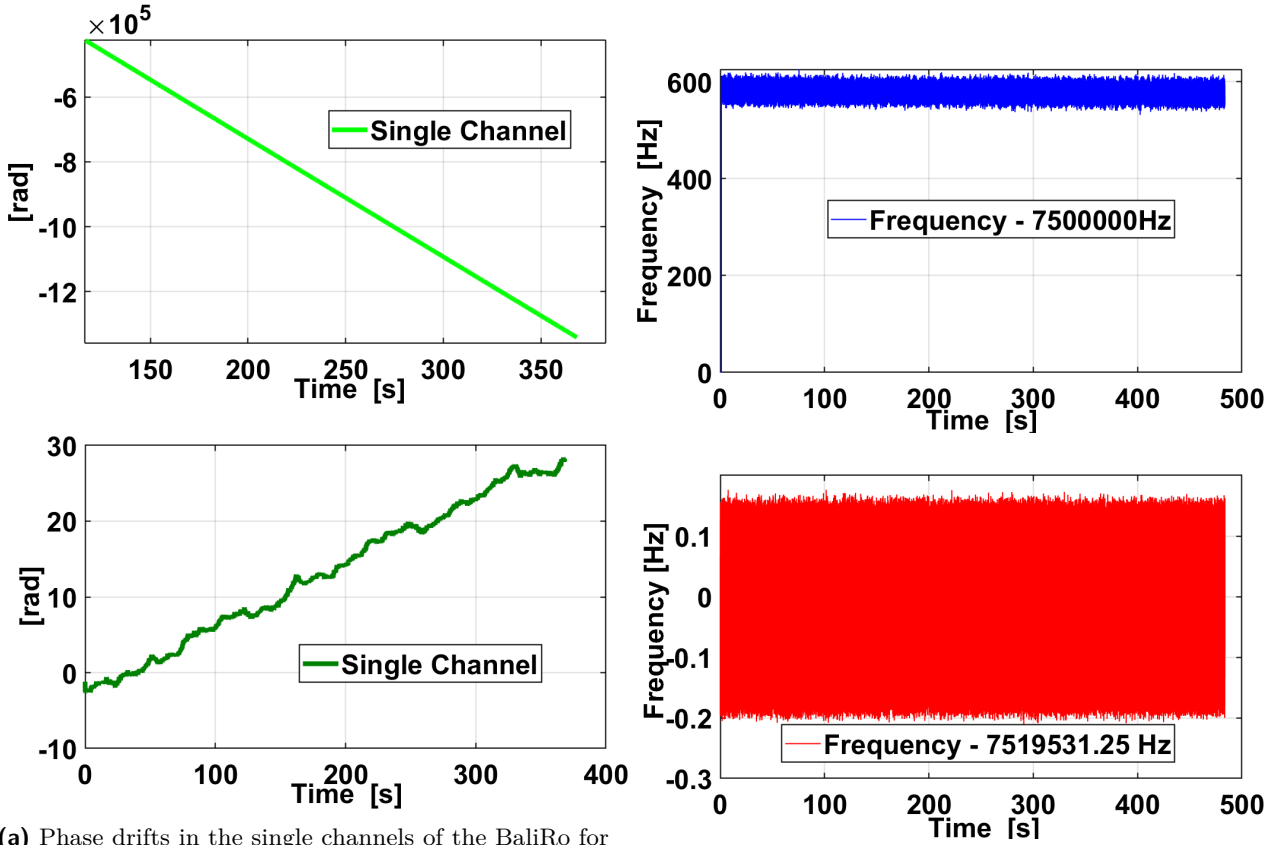
(a) Phase drifts in the single channels of the BaliRo for two differently stabilized lasers. Drift of 580 Hz and 0.012 Hz.

(b) Frequency read out by the BaliLo, the reference value set by the user is subtracted. The stabilization with less gain has a huge offser of about 580 Hz while the better stabilized on is about 0.018 Hz.

Fig. E.4.: Phase drift in the single channels and the related frequency offset.

E.5 Free-Beam Control Loop

The parameters of the optimized control loop discussed in Section 3.5.1 are collected here.

E.5.1 Coupling Matrices

In $\frac{\text{rad}}{\text{rad}}$:

$$K_{hh} = \begin{pmatrix} 3725.38 & 2756.02 \\ 2091.0 & 3447.42 \end{pmatrix}, K_{vv} = \begin{pmatrix} 2587.79 & 1763.01 \\ 1296.66 & 2297.87 \end{pmatrix}$$

$$K_{hv} = \begin{pmatrix} 277.99 & 473.87 \\ 30.54 & 72.10 \end{pmatrix}, K_{vh} = \begin{pmatrix} 67.11 & 195.47 \\ 224.10 & 426.34 \end{pmatrix}.$$

E.5.2 Transferfunction

The transferfunctions for each axis reached a unity gain frequency of 80 Hz with a phasemargin of 35°, as presented in [Jes22] and Figure E.5.
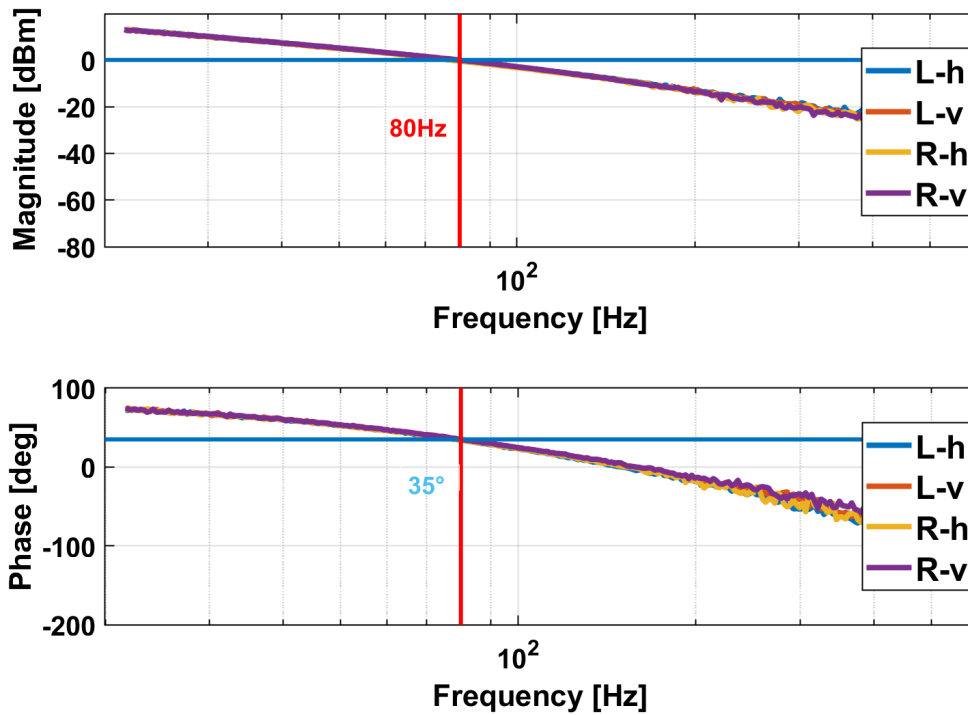
Fig. E.5.: Transferfunctions for the four steering mirror control loops. Left-horizontal (L-h), Left-vertical (L-v), Right-horizontal (R-h) and Right-vertical (R-v).

E.6 Measured RIN

The RIN levels of all four transponder lasers in the laboratory of the 3BL were measured by S. Ast and are shown in Figure E.6. The RIN for all four lasers is below $3 \cdot 10^{-7}/\sqrt{\text{Hz}}$ with prominent peaks at $82\,\text{kHz}$ and $35\,\text{kHz}$. The significant relaxation oscillation differs for each laser and lies between $1 \times 10^6\,\text{Hz}$ to $2 \times 10^6\,\text{Hz}$.

For the BN dependent measurements discussed in Section 3.7.1, the frequency range between $10\,\text{kHz}$ and $1000\,\text{kH}$ is interesting. The noise level decreases towards higher frequencies except for the high peaks at $82\,\text{kHz}$ and $344\,\text{kHz}$. The frequency range between $200\,\text{Hz}$ and $300\,\text{Hz}$, which performed optimal with the BNs, is marked, too. It is not significantly better than the level below $82\,\text{kHz}$.
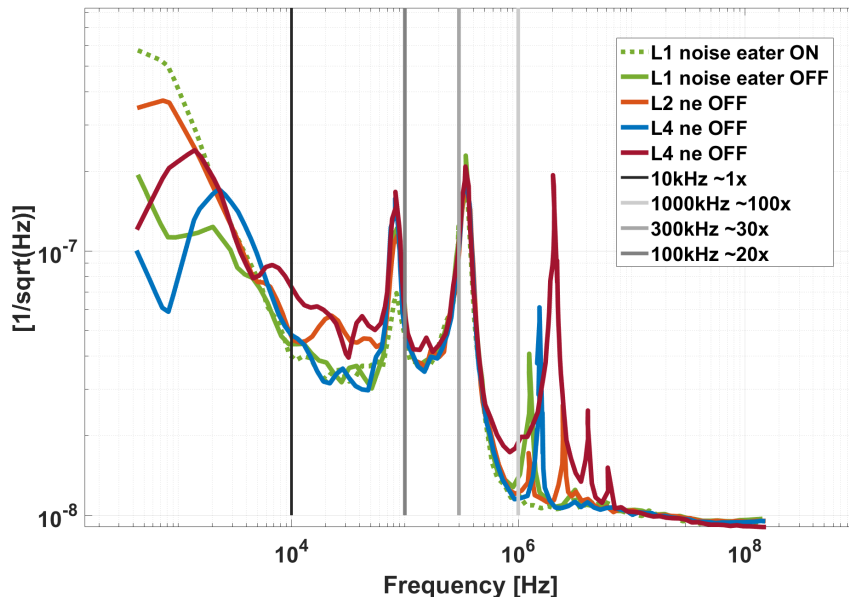
Fig. E.6.: RIN level measured for all four lasers in the 3BL. Noise eater (ne) ON shown for one laser exemplary, this reduces the relaxation oscillation between 1×10^6 Hz to 2×10^6 Hz.

E.7 Laser Power Measurements

The laser power and the influence of its stabilization were discussed in Section 3.8.2. The measurements of the remaining channels are presented in Figure E.7. The two channels of FSFBL-L and FBBL-R show a different and more noisy behavior. The cause for this is unclear and they are discarded in the analysis discussed in Section 3.8.2.
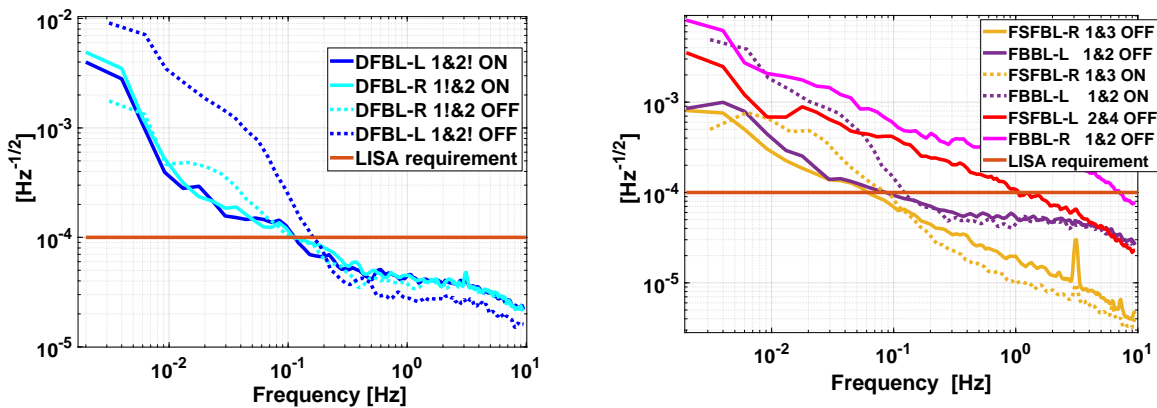
Fig. E.7.: DC-RIN of the different interferometers on the left (L) and right side (R) and the influence of the laser power stabilization (ON/OFF). The numbers of the two involved lasers are given for each signal. For the DFBL, the "!" markes the local laser that has by design an about five times higher power contribution.

E.8 Cross-Coupling in PM4
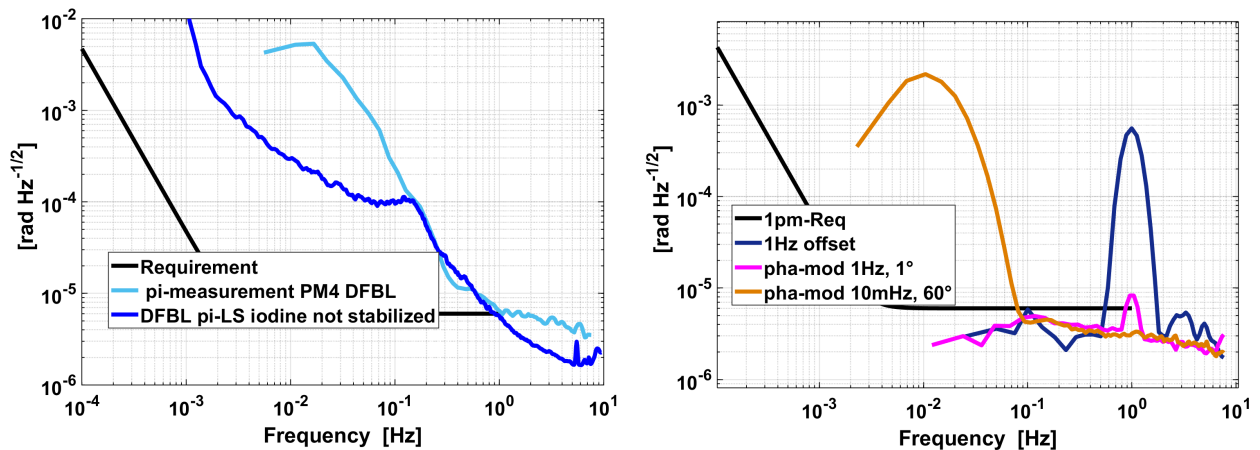
(a) π-measurements in PM4 and BaliRo with high rise towards lower frequencies.

(b) Electrical split measurements with an additional electrical signal that is shifted in frequency by $1\,\mathrm{Hz}$ or phase modulated (pha-mod).

Fig. E.8.: Cross-coupling investigations in the PM4 with π- and electronic split measurements.

The PM4 increases the available channels in the 3BL measurements and allows full operation including π-measurements in each interferometer. First π-measurements showed a substantial rise below $1\,\mathrm{Hz}$, as shown in Figure E.8a. Measurements with the BaliRo for the DFBL overlap till $0.1\,\mathrm{Hz}$, above which the BaliRo measurement is lower. Combination of different channels does not solve the problem in this PM either. Electrical split measurements with an additional electrical signal were performed and shown in Figure E.8b. The additional signal was shifted slightly in frequency, which allowed the difference of $1\,\mathrm{Hz}$ to appear in the electrical split measurement. Also, the coupling of a phase modulation at $1\,\mathrm{Hz}$ and $10\,\mathrm{mHz}$ appear at their modulation frequency.

Curriculum Vitae

Education

Since April 2018	**PhD student** at Leibniz University Hannover, working at the Max Planck Institute for Gravitational Physics (Albert Einstein Institute) area of research: *Investigations for an optimal Backlink candidate for the LISA mission* - Construction of two optical Benches in the cleanroom, with development of alignment strategies - Noise analysis and suppression
February 2018	**Master of Science**, Grade: 1.2 Thesis: *An optical phase reference for LISA: Comparision of different solutions with picometer sensitivity* Leibniz University Hannover
November 2015	**Bachelor of Science**, passed with distinction, Grade: 1.0 Thesis: *Aufbau und Charakterisierung der Laservorbereitung für das Drei-Backlink-Experiment* Leibniz University Hannover
July 2012	**General qualification for university entrance** (allgemeine Hochschulreife/**Abitur**) graduated as best of class, Grade: 1.3 Integrierte Gesamtschule Hannover-Linden, Germany

List of Publications

Publications

2021   Pau Amaro-Seoane, **Lea Bischof**, et al.
„LION: laser interferometer on the moon"
In: *Classical and Quantum Gravity* 38 (2021), p. 125008.

2018   Katharina-Sophie Isleif, **Lea Bischof**, Stefan Ast, et al.
„Towards the LISA backlink: Experiment design for comparing
optical phase reference distribution systems".
In: *Classical and Quantum Gravity* 35.8 (2018), p. 085009.

Acknowledgments